Synthesis of Amphiphilic Hyperbranched Glyco-Polydendrons for Potential Applications in Nanomedicine

Thesis submitted in accordance with the requirements of the University of Liverpool for the degree of Doctor in Philosophy by:

Andrew Bryan Dwyer

January 2016

UNIVERSITY OF LIVERPOOL

Acknowledgements

Firstly, I would like to thank my beautiful Jen for her constant support and encouragement throughout the last four years; her loving, warm, caring and bubbly personality has never failed to put a smile on my face, even during the difficult times of my PhD, providing me with the motivation to continue working hard. For that, I am forever grateful.

I would like to thank my parents, Brian and Barbara, for their constant love, support and guidance throughout my life; from an early age they have encouraged me to learn and have provided me every opportunity to do so. They are both lovely, inspiring people, and I hope that one day I can show the same level of love and support to my children as they have to theirs. I would also like to thank my two elder sisters, Lisa and Jenny, both of whom have shown me the level of commitment and hard work that is required to achieve academic success leading to rewarding careers.

I would like to thank my supervisor, Prof Steve Rannard, for the opportunity to study for this PhD within his research group. Not only has he provided continued support and guidance, he has provided a warm and enjoyable working environment for all members of his group to learn and develop. He possesses many attributes that make him a great supervisor; however, the great deal of time he dedicates to his group is something I admire most.

I would also like to thank all members of the Rannard group, past and present, with very special thanks to Dr Pierre Chambon; I'm very grateful for all his help and advice, and his investigative approach to his work is something I admire and have tried to adopt during my PhD. I'm also grateful to Adam Town for his help in the investigations of the *n*BuMA homopolymerisation study.

I would like to thank Prof Peter Myers, Dr Adham Ahmed, Dr Kevin Skinley and Dr Tom Wray, all of whom have helped me a great deal over the last eight years; without their help, I probably would not have had the opportunity to work with Steve during my PhD.

Finally, I would like to thank everyone who has been involved in the running of the Department of Chemistry at the University of Liverpool during my time here.

Abstract

The synthesis of amphiphilic hyperbranched glycopolydendrons bearing multivalent surface functionalities has yielded materials with potential nanomedical drug-delivery applications that may also be capable of actively targeting disease sites. The development of the hydrophilic surface functionalities (based on PEG, galactose and mannose moieties) and hydrophobic core functionalities (based on poly(*n*-butyl methacrylate)) are presented.

Despite methanol (MeOH) being widely regarded as an antisolvent for *p*(*n*BuMA), Cu-catalysed ATRP of *n*BuMA has been performed utilising anhydrous MeOH as the reaction solvent. Successful polymerisation was achieved at 60 °C and 25 °C using ethyl 2-bromoisobutyrate as the initiator, yielding well-defined polymers with high molecular weights (up to M_n = 75 880 g mol^{-1}) and low dispersities (as low as $Đ$ = 1.02). The effect of monomer co-solvency was investigated by determining the cloud point behaviour (upper critical solution temperature) of *p*(*n*BuMA) within the methanolic environment, and the effect of the ligand on the control of the polymerisation was also investigated. Successful polymerisation was also extended to RAFT, yielding low dispersity polymers that were analogous to those obtained by ATRP.

The methanolic polymerisation by Cu-catalysed ATRP was utilised to exploit the hydrophobic nature of *p*(*n*BuMA) as the core functionality of amphiphilic branched copolymer nanoparticles bearing PEG surface functionalities. The nanoparticles were prepared *via* a rapid nanoprecipitation approach, however, their small hydrodynamic diameters (D_n = 17 nm-27 nm) suggested nanoparticle formation by a solvent-switch rather than a nucleation/growth mechanism that is normally associated with this technique.

Dendritic ATRP initiators bearing multivalent protected galactose functionalities, also varying in generation number, were obtained by aza-Michael-type additions and used within the branched methanolic ATRP of *n*BuMA. Deprotection of the isopropylidene protecting groups was achieved under acidic reaction conditions using *para*-toluene sulfonic acid monohydrate; nanoprecipitation of the resulting galactosylated *hyp*-glycopolydendrons yielded charge-stabilised nanoparticles with D_z = 43-46 nm and highly negative zeta potentials. Comparisons to their protected equivalents were made.

Contents

Chapter 7 - Experimental

Abbreviations

ACUPA	2-[3-[5-amino-1-carboxypentyl]-ureido]-pentanedioic acid
ACVA	4,4'-azobis(4-cyanopentanoic acid)
AEMA	2-aminoethyl methacrylamide hydrochloride
AIDS	Acquired immunodeficiency syndrome
APAP	1-[*N*, *N*-bis(2-aminopropyl)-amino]-2-propanol
ART	Anti-retroviral therapy
ASGPR	Asialoglycoprotein receptor
ATRP	Atom transfer radical polymerisation
BAPA	bis(3-aminopropyl)amine
bis-MPA	bis(methylol)propionic acid
BPDMA	bisphenol A dimethacrylate
bpy	2,2-bipyridine
Caco-2 cell line	Human epithelial colorectal adenocarcinoma cell line
$CDCl_3$	Deuterated chloroform
CDI	1,1'-carbonyldiimidazole
Con A	Concanavalin A
COSY	Correlation Spectroscopy
CPBD	2-cyano-2-propyl benzodithioate
CTA	Chain transfer agents
CuAAC	Copper-catalysed azide-alkyne click
Đ	Dispersity
DC-SIGN	Dendritic cell-specific intercellular adhesion-molecule-3-grabbing non-integrin
DCM	Dichloromethane
DLS	Dynamic light scattering
DMAEMA	*N*, *N*-Dimethylaminoethyl methacrylate

DMAP	4-(dimethylamino)pyridine
DMF	Dimethylformamide
D_n	Number-weighted hydrodynamic diameter
DNA	Deoxyribonucleic acid
DOX	Doxorubicin
DP_n	Degree of polymerisation
DVB	Divinylbenzene
D_z	*Z*-average hydrodynamic diameter
EGDMA	Ethylene glycol dimethacrylate
EGFR	Epidermal growth factor receptors
EMA	European Medicines Agency
EPR	Enhanced permeability and retention
ESI	Electrospray ionization
$Et_3N^+Br^-$	Triethylammonium bromide
FDA	Food and Drug Administration
G1-6	Generation 1-6
Gal	*D*-galactose
GalNAc	*N*-acetylgalactosamine
GMA	Glycerol monomethacrylate
GPC	Gel permeation chromatography
HA	Hyaluronic acid
HBPs	Hyperbranched polymers
HBr	Hydrogen bromide
HeLa cell line	Human epitheloid cervix carcinoma cell line
HEMA	2-hydroxyethyl methacylate
HepG2 cells	Human hepatocellular liver carcinoma cell line
HER2 receptor	Human epidermal growth factor receptor 2
HIV	Human immunodeficiency virus
HPMA	2-hydroxypropyl methacrylate

HSQC	Heteronuclear single quantum coherence
Huh7.5 cell line	Human differentiated hepatocyte derived cellular carcinoma cell line
IFNγ	Interferon gamma
IND	Indomethacin
IPA	Isopropanol
LAEMA	2-lactobionamidoethyl methacrylamide
LCST	Lower critical solution temperature
Me6TREN	tris[2-(dimethylamino)ethyl]amine
MeOD	Deuterated methanol
MeOH	Methanol
MMA	Methyl methacrylate
M_n	Molecular weight
MPS	Mononuclear phagocytic system
MTT	3-(4,5-dimethylthiazol-2-yl)-2,5-diphenyltetrazolium bromide
NaCl	Sodium chloride
NaOH	Sodium hydroxide
nBuMA	*n*-butyl methacrylate
NGPE	*N*-glutaryl-phosphatidylethanolamine
NIPAM	*N*-isopropylacrylamide
NMR	Nuclear magnetic resonance
NO	Nitric oxide
PAMAM	Poly(amidoamine)
PBE	Poly(benzyl ether)
PdI	Polydispersity index
PEG	Poly(ethylene glycol)
PEG-*b*-*p*(GMA)	Poly(ethylene glycol)-*block*-poly(glycerol monomethacrylate)
PEG-*b*-*p*(*t*BA)-*b*-*p*(HEMA)	Poly(ethylene glycol)-*block*-poly(*tert*-butyl acrylate)-*block*-poly(2-hydroxyethyl methacylate)
PISA approach	Polymerisation induced self-assembly

PMDETA	*N*, *N*, *N'*, *N'*, *N''*-pentamethyldiethylenetriamine
PO	Propylene oxide
PPI	Poly(propylene imine)
proGal-OH	1,2:3,4-Di-*O*-isopropylidene-*α*-*D*-galactopyranose
PS	Poly(styrene)
PSMA	Prostate-specific membrane antigen
PTFE	Poly(tetrafluoroethylene)
PTSA	Para-toluene sulfonic acid monohydrate
RAFT	Reversible addition-fragmentation chain transfer
RDRP	Reversible-deactivation radical polymerisation
RES	Reticuloendothelial system
RI	Refractive index
RNA	Ribonucleic acid
ROMP	Ring-opening metathesis polymerisation
ROP	Ring-opening polymerisation
SARA ATRP	Supplemental activator and reducing agent ATRP
scFv	Single-chain antibody fragment
SCVP	Self-condensing vinyl polymerisation
SEM	Scanning electron microscopy
SET-LRP	Single-electron transfer living radical polymerisation
SiHa cell line	Human squamous cell cervix carcinoma cell line
SK HEP-1 cell line	Human endothelial liver adenocarcinoma cell line
*t*BOC	*N*-*tert*-butoxycarbonyl
*t*BuMA	*tert*-butyl methacrylate
TEA	Triethylamine
TEM	Transmission electron microscopy
tert-BuOH	*tert*-butanol
Tf receptor	Transferrin receptor
TFA	Trifluoroacetic acid

THF	Tetrahydrofuran
TLC	Thin layer chromatography
UCST	Upper critical solution temperature
VCAM-1	Vascular cell adhesion molecule-1

Chapter 1

Introduction

1.1. Conventional medicine

Conventional clinical medicine can successfully diagnose, treat, and prevent many forms of infection and disease; however, serious issues remain regarding the efficacy and economic viability of available treatments. One example is the cancer epidemic: according to Cancer Research UK, there were 14.1 million new cases and 8.2 million deaths worldwide in 2012 alone - of which the estimates for the UK were over 330,000 new cases and 161,000 deaths.[1] A 2011 Bupa report assessed the current and future costs of the diagnosis and treatment of cancer in the UK, and estimated that the annual costs may rise from £9.4 billion in 2010 to £15.3 billion in 2021 – a 63% increase over the decade – which implies that the average annual cost per patient is likely to rise from £30,000 in 2011 to £40,000 in 2021.[2] The report concludes that one of the key approaches to address this challenge is to find new and innovative ways of diagnosing and treating the disease. HIV/AIDS is another global epidemic with similar issues: it has been estimated that 37 million people worldwide were living with HIV in 2014, of whom only 15 million were receiving anti-retroviral therapy (ART).[3] The problems of economic viability - a particular issue in developing countries - are being addressed, with the estimated annual cost of ART medicines per patient falling from $10,000 USD in 2001 to $100 USD for first-line regimens in 2014.[4,5] However, serious issues remain regarding the efficacy of various treatments.

One key issue is the solubility of drugs *in vivo*. Drugs with poor solubility in blood are rapidly cleared from the systemic circulation primarily *via* renal clearance or through the reticuloendothelial system (RES), which consequently reduces their biodistribution and prevents an optimal therapeutic effect. This is compensated with high and frequent dosing, which exposes the patient to higher levels of cytotoxicity and risk of undesirable side-effects, often resulting in poor patient compliance to short, medium and long term dosing regimens. Ultimately, this renders such treatments expensive to implement and difficult to maintain.

To address these issues, research worldwide in both academic and industrial institutions is directed towards applying nanotechnology to medicine to provide economically viable, cost-effective, high-efficacy diagnosis and treatment of infection and disease.

1.2. Nanomedicine

Nanomedicine is an emerging field that applies nanotechnology to medicine. It involves the precise engineering of materials at the nanometre scale (1-1000 nm) so that the distinctive physicochemical properties of nanoparticles - such as high surface area-to-volume ratios, controlled shape and size, and unique optical properties - can be utilised to help overcome the problems currently associated with conventional medicinal treatments.[6] It is a field that is continuously expanding due to its great potential in therapeutic,[7] diagnostic and theranostic applications; the latter combines both therapeutics and diagnostics in a single nanomedicine formulation to enable detailed assessment of the biodistribution, pharmacokinetics and target-site localisation of a drug.[8,9] Given the vast scope of nanomedicine, only the therapeutic applications will be reviewed here.

1.2.1. Therapeutic applications

Using nanoparticles to transport and deliver drugs to disease sites has proved more advantageous than conventional administration for many reasons: they can improve the biodistribution of hydrophobic drugs that would otherwise exhibit poor solubility in blood, and also reduce immunogenicity and thus prolong the half-life of drugs within the systemic circulation. In addition, nanoparticles can enhance drug-efficacy and therefore reduce dosage and the frequency of administration, enhance cellular uptake and protect drugs from degradation. These advantages are particularly relevant for orally administered formulations that are subjected to the harsh conditions of the gastrointestinal tract. The release of drugs in a sustained manner, or in response to a stimulus, are also target opportunities being investigated and, the targeting of drugs specifically to disease sites when functionalised with cell-targeting ligands has been shown to reduce cytotoxicity and undesirable side-effects. As a result, there are currently more than 40 nanoparticle-based therapeutic products in clinical use after having gained approval from regulatory authorities such as the US Food and Drug Administration (FDA) and the European Medicines Agency (EMA), with many more in clinical trials and pre-clinical development.[10]

1.2.2. Clinically approved nanoparticle-based therapeutics

The FDA's Centre for Drug Evaluation and Research (CDER) – employing physicians, statisticians, chemists, pharmacologists, among other scientists - reviews (pre)clinical data to determine whether the health benefits of a therapeutic product outweigh its known risks; if deemed beneficial it will be approved for clinical use. Currently there are more than 40 nanoparticle-based therapeutic products that have gained approval from regulatory authorities,[10] the formulations of which include liposomes,[11] micelles,[12] polymeric drugs,[13] polymer-protein/aptamer conjugates[14] and antibody-drug conjugates.[15]

Doxil was the first liposomal-based therapeutic approved by the FDA in 1995 for the treatment of AIDS-related Kaposi's sarcoma – a cancer that can develop after infection with human herpes virus 8.[11,16–18] The transport and delivery of the anticancer chemotherapeutic drug, doxorubicin, was achieved after encapsulation into the internal aqueous phase of liposomes (consisting of phosphatidylcholine and cholesterol) - driven by a transmembrane ammonium sulphate gradient. Clinical trials found that this liposomal formulation dramatically prolonged systemic circulation of the drug, reduced cardiotoxicity and resulted in enhanced drug-accumulation in the tumour tissue compared to conventional treatment with doxorubicin. The formulation was later approved for clinical use in the treatment of ovarian cancer (1999) and multiple myeloma (2007).[19,20] The clinical success of Doxil in anticancer therapy is attributed to two general characteristics of nanoparticles: their size and surface functionality. Liposomes are self-assembled phospholipid vesicles with diameters typically between 80-200nm; this large size allows them to accumulate extensively in solid tumours *via* extravasation due to the enhanced permeability and retention (EPR) effect (Figure 1.1).[21,22] The effect exploits: (i) the disorganised 'leaky' tumour vasculature that exists because of angiogenesis (a process that involves the rapid and irregular formation of new blood vessels within the tumour microenvironment), and (ii) the impaired lymphatic system associated with tumours that is normally responsible for the drainage of macromolecules from the tissue. The greater permeability of the vessels and the poor lymphatic drainage thus enables the greater accumulation of liposomes in tumours than in healthy tissue.

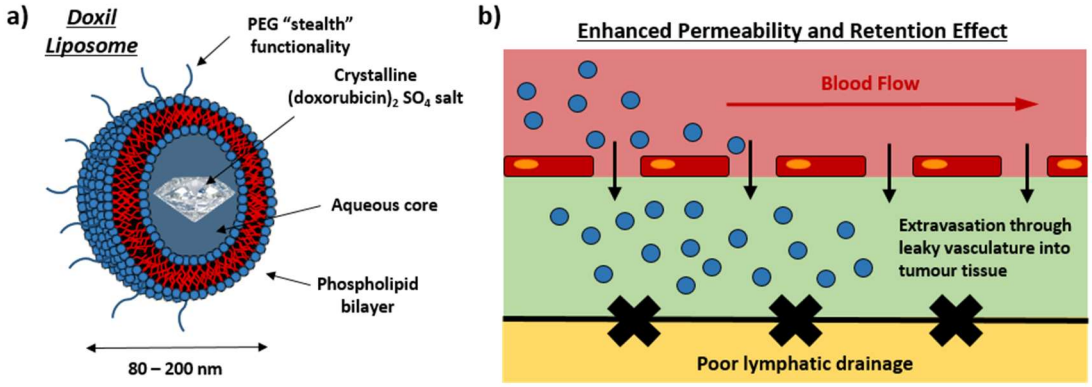

Figure 1.1. a) Graphical representation of the Doxil liposomal formulation encapsulating doxorubicin as a crystalline salt, with typical size of 80-200nm and PEG surface functionality; b) the enhanced permeability and retention (EPR) effect, showing the extravasation of liposomes through the fenestrations in the leaky tumour vasculature and their accumulation as a consequence of the poor lymphatic drainage.

Liposomes in their native form are rapidly cleared from systemic circulation *via* the reticuloendothelial system (RES) and the mononuclear phagocytic system (MPS) as part of an immune response; this can reduce their possible therapeutic effect.[23] To overcome this premature clearance, Doxil liposomes are functionalised with poly(ethylene glycol) (PEG) which reduces opsonisation and subsequent clearance, and therefore prolongs systemic circulation, which is vital to successfully utilise the EPR effect.[23–25] Despite its clinical success, however, there are two serious side effects associated with this treatment: (i) palmar plantar erythrodysthesia, and (ii) complement activation-related pseudo allergy.[11,26]

Currently, liposomes are the most clinically established *'nanocarrier'* structure in nanomedicine, with therapeutic applications that include the treatment of fungal infections, leukaemia, wet age-related macular degeneration, influenza, hepatitis A, anaesthesia and post-operative pain relief, (Table 1.1).

Polymer-protein/aptamer conjugates are another dominant platform in clinically-relevant nanomedicine (Table 1.1). They have been grouped together with polymeric drugs and polymer-drug conjugates to coin the term '*polymer therapeutics'*, to differentiate them from traditional nanocarrier drug-delivery systems (e.g. liposomes, micelles).[27]

Table 1.1. Clinically approved nanoparticle-based therapeutics

Product	Clinical Application	Admin.
Liposome		
Doxil/Caelyx	AIDS-related Kaposi's sarcoma, ovarian cancer, myeloma, breast cancer	i.v.
Abelcet	Fungal infection	i.v.
Ambisome	Fungal infection	i.v.
Depocyt	Malignant lymphomatous meningitis	i.t.
DaunoXome	AIDS-related Kaposi's sarcoma	i.v.
Myocet	Metastatic breast cancer	i.v.
Epaxal	Hepatitis A	i.m.
Inflexal V	Influenza	i.m.
DepoDur	Postoperative pain relief	Epidural
Visudyne	Age-related macular degeneration, pathologic myopia, ocular histoplasmosis	i.v.
Marquibo	Acute lymphoblastic leukaemia	i.v.
Micelle		
Estrasorb	Menopausal therapy	Topical
Taxol	Lung cancer, breast cancer, ovarian cancer, AIDS-related Kaposi's sarcoma	i.v.
Taxotere	Lung cancer, breast cancer, prostate cancer, stomach cancer	i.v.
Polymeric drug		
Copaxone	Multiple sclerosis	s.c.
Renagel	End-stage renal disease	Oral
Welchol	Type-2 diabetes	oral
Polymer-protein conjugate		
Adagen	Severe combined immunodeficiency syndrome	i.m.
Pegasys	Hepatitis C	s.c.
Neulasta	Chemotherapy-induced neutropenia	s.c.
Somavert	Acromegaly	s.c.
Oncaspar	Acute lymphoblastic leukaemia	i.v./i.m.
PEGIntron	Hepatitis C	s.c.
Cimzia	Rheumatoid arthritis, Crohn's disease	s.c.
Polymer-aptamer conjugate		
Macugen	Age-related macular degeneration	i.r.
Antibody-drug conjugate		
Adcetris	Hodgkin lymphoma, anaplastic large cell lymphoma	i.v.
Kadcyla	Breast cancer	i.v.
Albumin-bound nanoparticle		
Abraxane	Pancreatic cancer, breast cancer, lung cancer	i.v.

i.v. intraveneous, i.t. intrathecal, i.m. intramuscular, s.c. subcutaneous, i.r. intravitreous. Adapted from references 7, 10, 39 and 159.

Oncaspar (PEG-L-asparaginase) gained FDA approval in 1994 for clinical use in the treatment of acute lymphoblastic leukaemia.[28,29] Its phase I clinical trial showed that the conjugation of PEG to the enzyme, asparaginase, greatly increased its plasma half-life (357 h) compared to the native enzyme (20 h) by reducing opsonisation and subsequent clearance by the RES.[30] This therefore improved bioavailability, and enabled the hydrolysis of asparagine (an amino acid that is essential for tumour growth) into aspartic acid and ammonia before its removal from systemic circulation. Furthermore, the trial showed that the conjugation of PEG significantly reduced hypersensitivity reactions (e.g. anaphylactic shock) compared to the conventional treatment with asparaginase. Other polymer-protein/aptamer conjugates in clinical use include Somavert,[31] Cimzia,[32] Adagen,[33] Pegasys,[33] Neulasta,[34] PegIntron,[33] and Macugen,[35] the latter five also utilise PEG-conjugation to reduce immunogenicity and prolong systemic circulation.

Antibody-drug conjugates are a promising new class of nanomedicines that have the potential for active targeting (delivery of drugs to specific cells) owing to the specificity of the antibodies to relevant antigens.[36–38] Their therapeutic application is particularly promising for the treatment of cancers and aims to specifically interfere with molecular targets and pathways that are important for the proliferation of cancer cells; the drug is therefore selectively cytotoxic to tumours. Significant progress has been made in the pre-clinical development of these nanomaterials, with particular emphasis on the optimisation of antibody specificity, drug potency, linker design and site of conjugation. Currently, there are two antibody-drug conjugates that have gained FDA approval: Adcetris (2011) and Kadcyla (2013), used in the treatments of lymphomas and breast cancer respectively.[39]

1.2.3. Nanoparticle-based therapeutics under (pre)clinical evaluation

Since their approval for clinical use, nanoparticle-based therapeutics have been hugely successful in the field of medicine, particularly in the treatment of cancer. In this area, nanomaterials such as liposomes and polymer-protein conjugates have been developed to avoid recognition by the immune system and to accumulate in solid tumours by virtue of the EPR effect. This has resulted in enhanced drug-efficacy and reduced cytotoxicity; however, in anti-cancer therapy, even the application of nanomedicine

remains suboptimal. A key issue is the poor cellular internalisation of the nanoparticles after accumulation in the tumour tissue. Paradoxically, this is attributed to the stealth functionalities present on the periphery of the nanoparticles, which are required to utilise the EPR effect; this is known as the PEG dilemma.[40,41] Other issues include: (i) the high dependence on the degree of tumour vascularisation, which means that the efficacy of the therapy will vary considerably with tumour type and anatomical site;[42–44] (ii) the heterogeneity of tumour vasculature, which can severely affect the distribution of the nanoparticles within the tumour tissue;[43–45] and (iii) the heterogeneity in human cancer pathology.[43–45]

To address these issues, research is now heavily focused on the development of nanoparticle-based therapeutics that will promote entry of the drug-carriers into specific cells; a concept known as active targeting. It is achieved by functionalising the surface of the nanomaterials with targeting ligands (e.g. carbohydrates, peptides, vitamins, proteins, antibodies, aptamers and oligonucleotides) that have a high affinity for specific cell-receptors; the binding of these ligands to the relevant receptors triggers cellular internalisation *via* receptor-mediated endocytosis, enabling the intracellular delivery of the drug.

Two cellular targets can be distinguished for active targeting in anticancer therapy (Figure 1.2): (i) tumour cells (a direct approach), and (ii) tumour endothelium (an indirect approach);[46] targeting the former aims to increase internalisation of nanoparticles directly into tumour cells after accumulation within tumour tissue *via* the EPR effect. It is important to note that this direct approach cannot be achieved without passive accumulation of the nanoparticle within the tumour.[42] Target cell-receptors of interest include transferrin receptors,[47,48] folate receptors,[49–51] lectins,[52] and epidermal growth factor receptors (EGFR).[53,54] The second approach aims to remove the blood supply to the tumour by killing blood vessels that were formed as a result of angiogenesis. This starves the tumour of oxygen, nutrients, and growth factors that are vital for proliferation, consequently inducing apoptosis (cell-death) and causing shrinkage of the tumour tissue.

Targeting the tumour endothelium is interesting for a number of reasons: (i) extravasation of the nanoparticles into the tumour tissue is not required, thereby avoiding the problems caused by the high interstitial fluid pressures of tumours;

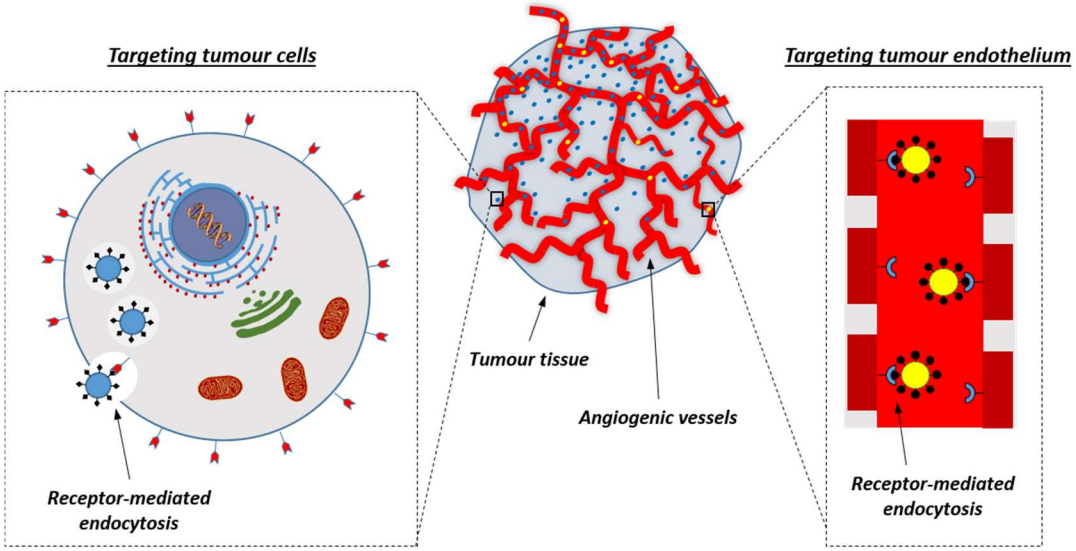

Figure 1.2. Graphical representation of the two cellular targets for active targeting in anticancer therapy: (i) targeting of tumour cells (a direct approach) after extravasation through leaky tumour vasculature, and (ii) targeting of tumour endothelium (an indirect approach).

(ii) endothelial cell markers are overexpressed in the majority of angiogenic vessels, which means that a targeted approach of this kind is not limited to particular forms of cancer, and can be effective in anticancer therapy in general; and (iii) the potential risk of tumours developing resistance to the anticancer therapy is reduced due to the genetic stability of endothelial cells compared to cancerous cells. This approach can be achieved by targeting vascular endothelial growth factors (VEGF) and their receptors,[55,56] $\alpha_v\beta_3$ integrins,[57,58] vascular cell adhesion molecule-1 (VCAM-1)[59] and matrix metalloproteinases.[60,61]

With regards to both direct and indirect active targeting, it remains important to avoid premature clearance by the RES and MPS; therefore, the degree of both targeting functionality and stealth functionality requires optimisation.

There are several nanoparticle-based therapeutics, utilising liposomes, polymeric micelles and polymeric nanoparticles, currently undergoing various stages of clinical trials that have been designed for the active targeting of tumours (Table 1.2). Once more, liposomes remain the dominant nanoparticle platform under (pre)clinical evaluation.

Table 1.2. Overview of actively-targeted nanomedicines under clinical evaluation.

Therapeutic	Payload	Ligand	Target	Clinical Application	Status
Liposomes					
2B3-101	Doxorubicin	Glutathione	Glutathione transporters	Brain metastases of breast cancer	Phase 1/2a
Anti-EGFR Immunoliposomes	Doxorubicin	Antibody fragment (scFv)	EGFR	Solid tumours	Phase 1
Lipovaxin-MM	Melanoma antigens and IFNγ	Single domain antibody (dAb) fragment (VH)	DC-SIGN	Melanoma vaccine	Phase 1
MBP-426	Oxaliplatin	Transferrin (Tf)	Tf receptor	Gastric cancer	Phase 2
MM-302	Doxorubicin	Antibody fragment (scFv)	HER2 (ErbB2) receptor	ErbB2-positive breast cancer	Phase 1
SGT-53	p53 plasmid DNA	Antibody fragment (scFv)	Tf receptor	Solid tumours	Phase 1b
SGT-94	RB94 plasmid DNA	Antibody fragment (scFv)	Tf receptor	Solid tumours	Phase 1
Polymeric Micelle					
BIND-014	Docetaxel	ACUPA	PSMA	Non-small-cell lung cancer, prostate cancer	Phase 1/2
SP1049C	Doxorubicin	Pluronic	P-glycoprotein	Advanced adenocarcinoma	Phase 2/3
Carbohydrate-based Nanoparticle					
CALAA-01	RRM2 siRNA	Transferrin (Tf)	Tf receptor	Solid tumours	Phase 1

Adapted from references 63 and 159.

MBP-426 is a liposome loaded with oxaliplatin, currently undergoing phase II clinical trials for the treatment of gastric, gastroesophageal and oesophageal adenocarcinomas. The surface of the liposome is functionalised with: (i) PEG – to reduce immunogenicity, and (ii) transferrin (Tf) – a glycoprotein that can actively target Tf receptors overexpressed on the surface of cancer cells. Initial *in vivo* studies in mice found that the encapsulation of oxaliplatin within Tf-PEG-liposomes significantly reduced binding to plasma proteins and erythrocytes (red blood cells), resulting in enhanced drug-systemic circulation and extravasation in colon 26 tumours. Results also indicated that the loaded Tf-PEG-liposomes were more effective at suppressing tumour growth compared to the free-drug, bare-liposomes and PEG-liposomes.[62]

Further development of the original formulation yielded a liposomal-therapeutic that not only actively targeted tumours but also acted in a stimuli-responsive manner. This was achieved by conjugating the Tf-ligand to N-glutaryl-phosphatidylethanolamine (NGPE) which caused disassembly of the liposome in a low pH environment; having localised in endosomal compartments after receptor-mediated endocytosis, the low pH environment caused the liposome to collapse and release the encapsulated oxaliplatin.

Another liposome nanocarrier under clinical evaluation for the active targeting of solid tumours is SGT-53, consisting of cationic lipids that encapsulate wild-type p53 plasmid DNA responsible for encoding vital tumour suppressor proteins.[63] These proteins play a critical role in two of the pathways involved in regulating tumour cell growth: apoptosis (cell-death) and the regulation of angiogenesis. However, they are absent in many human tumours. SGT-53 is therefore designed to deliver this plasmid DNA to tumours by actively targeting Tf glycoprotein receptors overexpressed on the surface of tumour cells; in this example, the targeting ligand is a single-chain antibody fragment (scFv). SGT-94 utilises the same Tf-targeted platform, but it encapsulates a gene that encodes the tumour suppressor protein RB94.[63] Without such ligand-targeted nanoparticle platforms, these genes are unable to pass through cell-membranes and consequently cannot reach the intracellular environment.

As already discussed, the binding of targeting ligands to specific receptors triggers cellular internalisation *via* receptor-mediated endocytosis; however, research has shown that the ligand density has a significant effect on the extent of internalisation. Polyvalent interactions provide simultaneous multiple binding of ligands to numerous cell-receptors, resulting in stronger cellular binding than corresponding monovalent interactions and increased probability of endocytosis (Figure 1.3).[64] Computational studies investigating the role of the physicochemical properties of coating ligands in receptor-mediated endocytosis found that both the density and rigidity of the ligand enhances their uniform distribution on the nanoparticle surface, and enable multivalent binding. This increases the probability of the nanoparticle being totally engulfed, leading to cellular internalisation.[65] Furthermore, *in vitro* and *in vivo* studies on various cancer cell-lines - using folic acid, transferrin and antibodies as the targeting ligand functionalities - also found that cellular uptake was enhanced with increasing ligand density.[66,67]

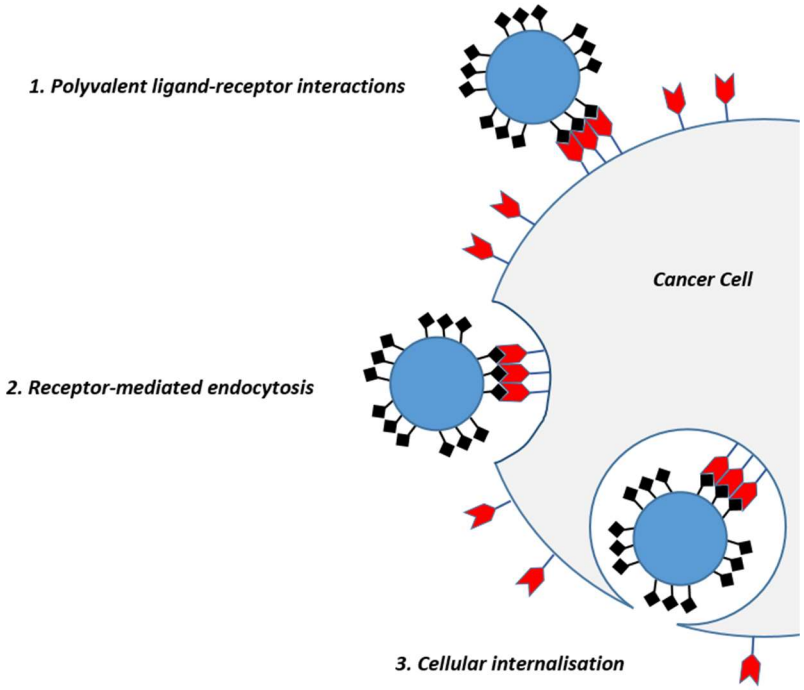

Figure 1.3. Receptor-mediated endocytosis of nanoparticles *via* polyvalent interactions.

As greater cellular uptake is generally achieved with higher ligand densities, dendrimers and polymers bearing multiple dendrons can be regarded as the ideal nanoparticle platform for active targeting in drug-delivery applications.

1.3. Dendrimers

Since their introduction in the late 1970's to mid-1980's, this unique class of polymeric materials have gained considerable interest owing to their potential in a variety of applications that include sensing, catalysis, molecular electronics and nanomedicine.[68–78]

The preparation and characterisation of these well-defined branched structures was first reported by Vögtle and coworkers in 1978, who referred to these materials as *"cascade molecules"*, obtained through an iterative synthetic procedure, (Scheme 1.1).[79] An iterative synthetic methodology was later adopted by Newkome *et al* [80] and Tomalia *et al*,[81] although they termed these well-defined branched constructs differently as "*arborol systems*" and "*dendrimers*" respectively. At present, the word dendrimer is the internationally accepted term for these materials – a word derived from Greek that describes a "tree-like" structure ("dendron" meaning "tree", and "meros" meaning "part").

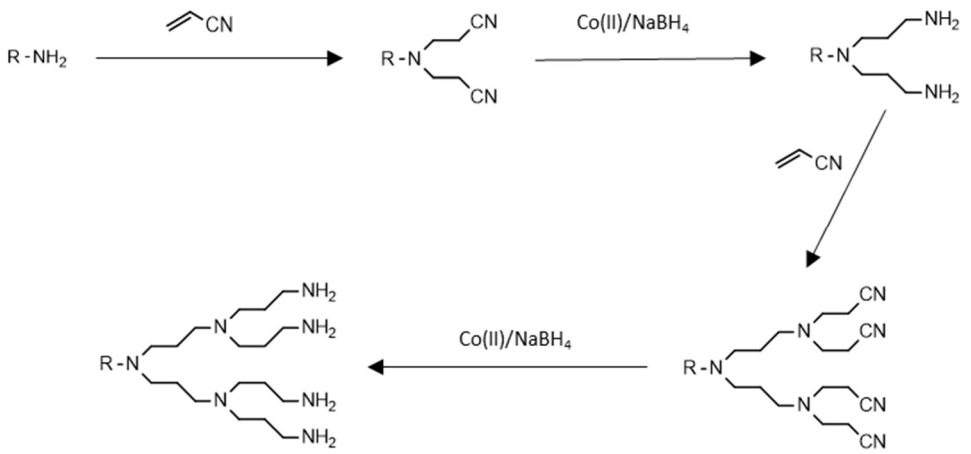

Scheme 1.1. Vögtle's synthesis of cascade molecules.[79] This iterative procedure involved: (i) Michael additions between amines and an excess of acrylonitrile, and (ii) activation by reduction using sodium borohydride.

Dendrimers are defined as perfectly branched, well-defined synthetic macromolecules obtained by a precise and step-wise process to yield monodisperse nanoparticles with a three-dimensional globular shape. Their unique architecture consists of three distinct domains: (i) a core-functionality, (ii) branching points, emanating from the core - the extent of which determines the overall generation of the dendrimer, and (iii) surface functionality - the degree of which increases exponentially with each generation, (Figure 1.4).

1.3.1. Synthesis of Dendrimers

Dendrimers are generally synthesised by one of two conceptually different routes: a divergent route or a convergent route. Both proceed *via* an iterative sequence of reactions that consist of a generation growth step followed by an activation step, with each iteration leading to a higher generation number.

1.3.1.1. Divergent Synthesis

Divergent synthesis begins from a multivalent central core extending outwards by the sequential addition of generational layers towards the periphery, (Figure 1.5).

The first example of divergent synthesis was the "cascade approach" described by Vögtle and coworkers (Scheme 1.1), whereby a series of mono- and di-amines were

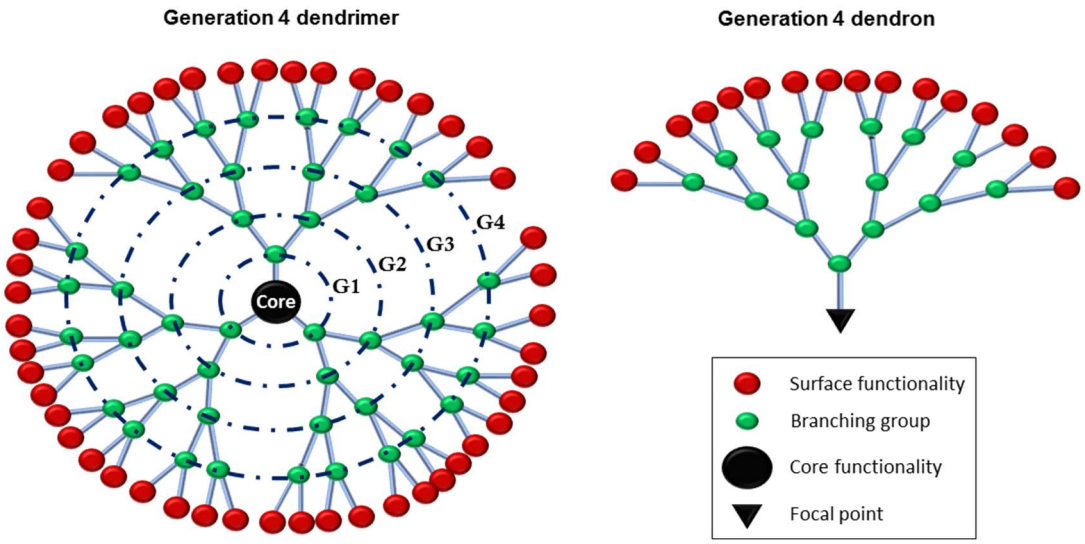

Figure 1.4. Graphical representation of: (i) a G4 dendrimer, showing the core functionality in black, the branched functionality in green, and the surface functionality in red; and (ii) the corresponding G4 dendron, with the focal point functionality depicted by a black triangle.

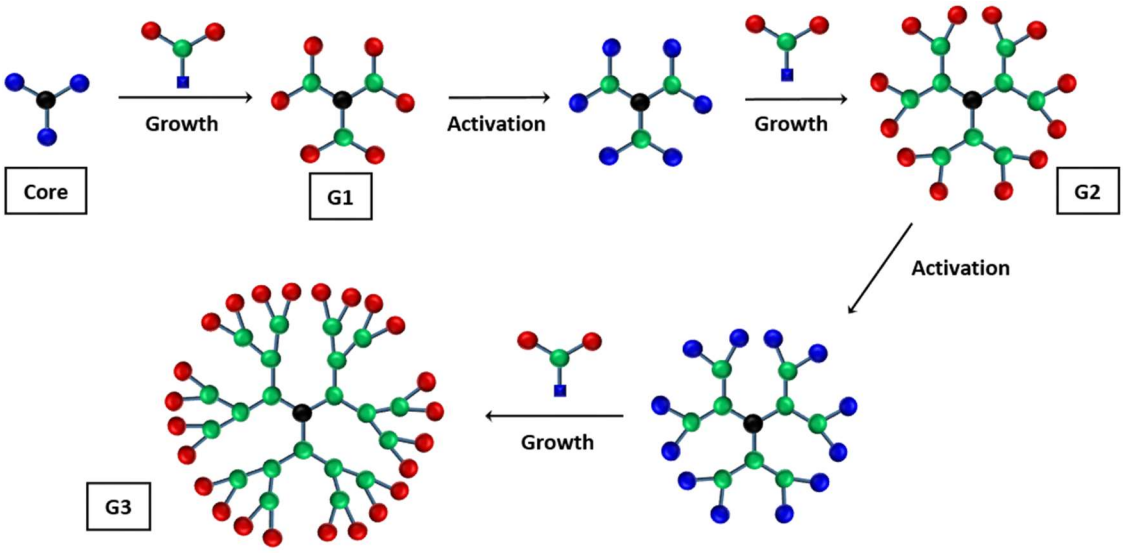

Figure 1.5. Graphical representation of dendrimer synthesis by divergent growth (adapted from ref. 82).

reacted with an excess (greater than two molar equivalents per amine) of acrylonitrile by Michael addition.[79] The nitrile groups were then reduced using sodium borohydride to yield the activated primary amine functionality. This two-step reaction was repeated in an iterative fashion to yield the cascade molecules which can essentially be regarded as low generation dendritic polyamines.

The large-scale divergent synthesis of the poly(propylene imine) (PPI) dendrimers was reported by Meijer and coworkers in 1993;[82,83] this synthetic procedure was adapted from the cascade molecule synthesis described by Vögtle and coworkers in which the low yields in the reduction step hindered the synthesis of higher generations. In this case, diaminobutane was chosen as the core molecule which was then reacted with an excess (greater than 4 molar equivalents) of acrylonitrile by an exhaustive Michael addition. The subsequent nitrile functionalities were hydrogenated by heterogeneous catalysis to yield amine functionality once more. Repeating this two-step synthesis in an iterative fashion on scales ranging from several grams up to several kilograms yielded dendrimers up to generation 4.5 with 64 terminal nitrile groups and a molecular weight of 6912 g mol^{-1}. DSM commercialised these materials under the trademark Astramol™.

However, the best-known example of divergent growth is the synthesis of the commercially available poly(amidoamine) (PAMAM) dendrimers, first reported by Tomalia and coworkers in 1985 (Scheme 1.2).[81,84] Initially, an amine functionalised core molecule (e.g. ammonia, ethylene diamine) was reacted with an excess of methyl

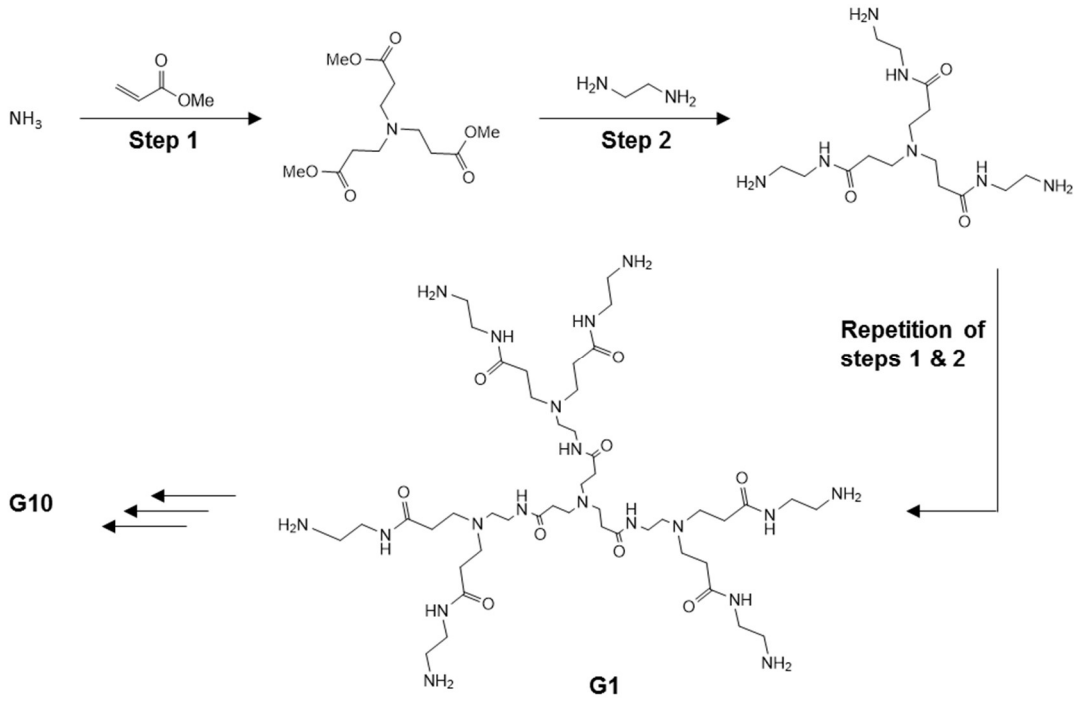

Scheme 1.2. Tomalia's synthesis of PAMAM dendrimers. The iterative reaction sequence involved: (i) exhaustive Michael additions between amines and an excess of methyl acrylate, and (ii) complete amidations using a vast excess of ethylene diamine.

acrylate by an exhaustive Michael addition. Following this, complete amidation of the methyl esters was achieved using a vast excess of ethylene diamine to yield the activated primary amine functionality. This enabled the two-step reaction to be repeated in an iterative fashion, producing high molecular weight dendrimers up to generation 10 (MW = 934,720 g mol^{-1}; 4096 peripheral amine groups). Other noteworthy examples of dendrimers obtained by divergent synthesis include the polyamide arborol systems from Newkome's group[85] and phosphorus-based dendrimers from Majoral and coworkers.[86]

High generation dendrimers can be obtained when adopting a divergent synthetic strategy; however, the purity of divergently synthesised materials remains a significant problem. Each increase in generation number results in an increase in steric hindrance at the periphery of the dendrimer, therefore, ensuring complete reaction to yield defect-free dendrimers at each generation of growth becomes increasingly difficult. This effect is known as the "De Gennes dense packing" or "starburst limit effect", based on the work of De Gennes and Hervet.[87] As a consequence, vast excesses of reagents are required at each synthetic stage to achieve structural perfection; however, even this cannot avoid the inevitable formation of defects at higher generations as the separation of imperfect dendrimers from a mixture of perfectly branched structures is very difficult. The high costs incurred and the lengthy purification procedures required therefore often lead to issues with commercialisation.

1.3.1.2. Convergent Synthesis

The convergent synthetic approach, first proposed by Hawker and Fréchet in 1990,[88] is in direct contrast to the divergent approach in that growth begins with what will eventually constitute the periphery of the dendrimer, and progresses to the core coupling step (Figure 1.6). This strategy initially involves the formation of wedge-like structures called dendrons and generation growth is obtained by activation of the focal point of the dendrons, followed by a coupling reaction to an AB_2 monomer (whereby the A group is unreactive, and the B groups are reactive). Each repetition of this two-step synthetic procedure increases the generation number of the dendrons, whose focal points can be activated and finally coupled to a multifunctional core molecule to yield the desired dendrimer.

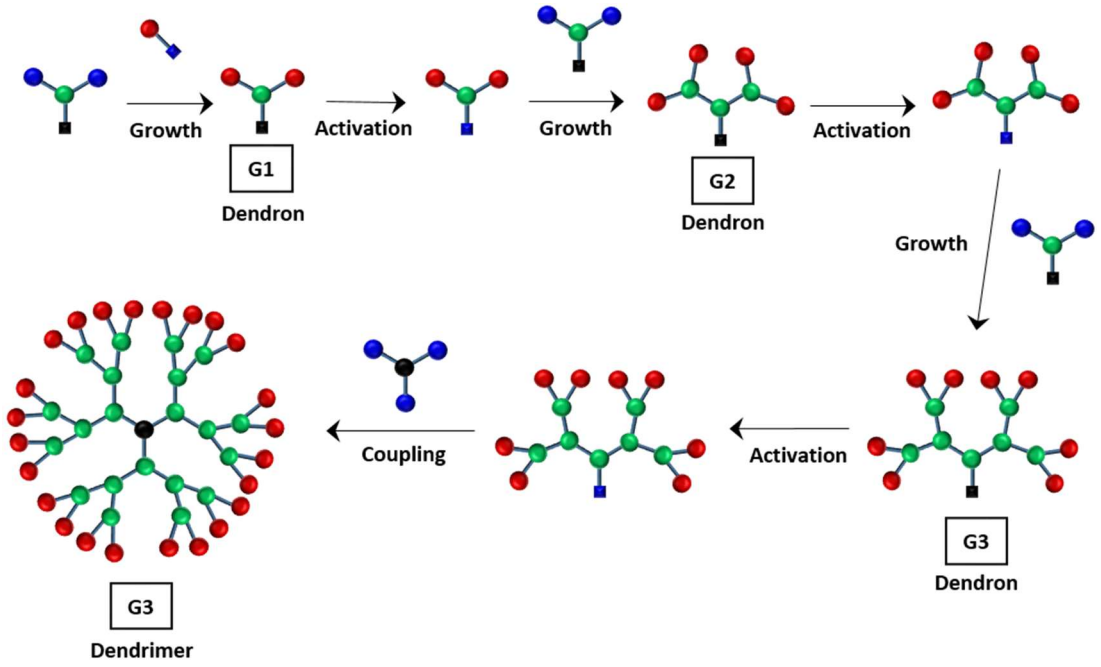

Figure 1.6. Graphical representation of dendrimer synthesis by convergent growth (adapted from ref. 82).

The poly(benzyl ether) dendrimers were the first to be synthesised by the convergent synthetic route (Scheme 1.3).[88,89] Synthesis began by reacting two equivalents of benzyl bromide with the monomer 3,5-dihydroxybenzyl alcohol *via* a Williamson ether coupling to yield the first generation hydroxyl functional benzyl ether dendron. Further reaction with carbon tetrabromide and triphenylphosphine restored the reactive benzyl bromide functionality at the focal point, and enabled the two-step reaction sequence to be repeated iteratively to yield higher generation dendrons. The final step involved coupling the benzyl ether dendrons to a multifunctional core - in this case 1,1,1-tris(4'-hydroxyphenyl)ethane - utilising the Williamson ether reaction once more to yield dendrimers up to generation six (G6).

Due to the small number of coupling reactions per generation growth step, this convergent approach minimises the possible introduction of structural defects, avoids large excesses of reagents, simplifies purification, and ultimately presents greater synthetic control compared to the divergent method. However, this route also has its limitations: as the dendron increases in size with each iterative reaction sequence, the

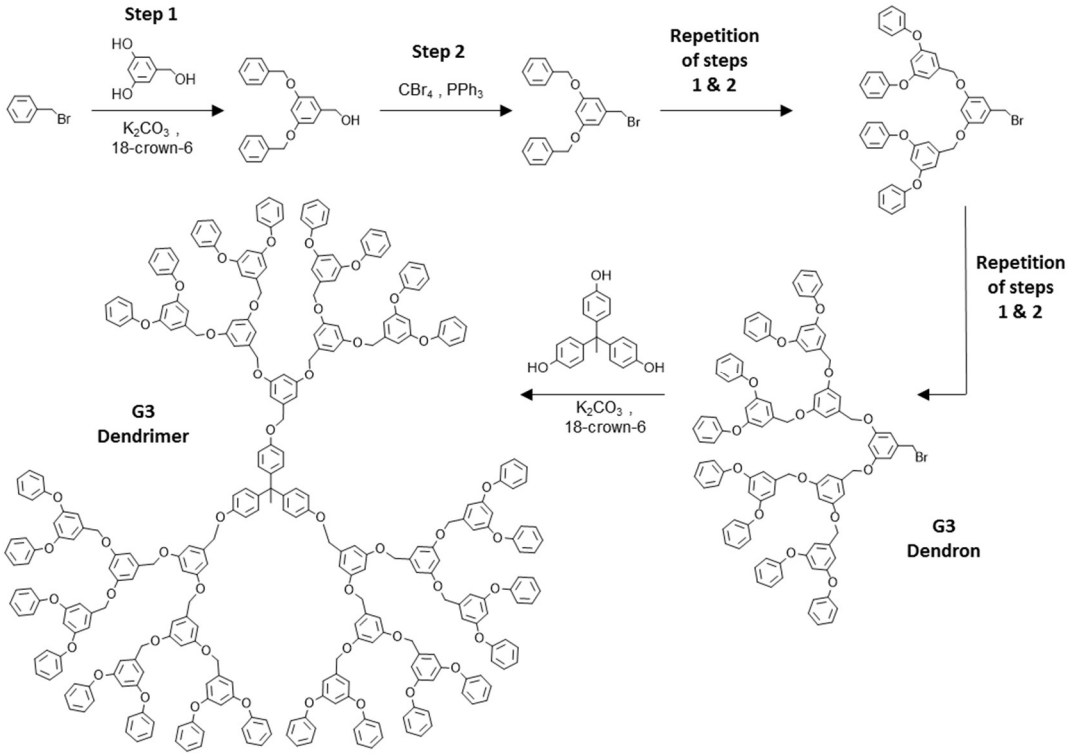

Scheme 1.3. Synthesis of poly(benzyl ether) dendrimers by the convergent approach. The iterative synthesis involved: (i) a Williamson ether coupling between 3,5-dihydroxybenzyl alcohol and 2 eq. of benzylic bromide, and (ii) reaction of the 2° alcohol functionality at the focal point of the dendron with carbon tetrabromide and triphenylphosphine.

accessibility and reactivity of the focal point is reduced as a result of steric inhibition, meaning that the synthesis of high generation dendrimers is difficult to achieve.

1.3.2. Therapeutic Applications of Dendrimers

Dendrimers have generated considerable interest in nanomedicine owing to their nano-metric size and monodispersity. More recently, however, a great deal of research has focussed on exploiting their extensive, multivalent surface functionality to yield nanomedicines with a high density of specific ligands capable of active targeting. Once again, the vast majority of this research is focused on applications in anticancer therapy.[90–98]

Kesharwani *et al* investigated the active targeting potential of PPI dendrimers against various cancer-cell lines after functionalisation with folic acid, dextran, and galactose moieties; the MTT assay results using HeLa and SiHa cells found that the folate-PPI dendrimers exhibited the strongest anticancer activity.[90] The synthesis of PEGylated PPI dendrimers bearing folate acid surface functionality has been described by

Sideratou *et al*; these materials showed low cytotoxicity and folate-receptor specificity.[91] While Iyer and co-workers recently reported the functionalisation of fourth generation PAMAM dendrimers with hyaluronic acid (HA); a ligand capable of actively targeting CD44 receptors overexpressed on pancreatic tumours. Fluorescence studies showed a higher cellular uptake of HA-PAMAM dendrimers in MiaPaCa-2 cancer cells compared to the non-functionalised PAMAM dendrimers.[92]

The ability of dendrimers to entrap guest molecules, either by physical encapsulation[90–94,97,99–101] or chemical conjugation,[96,102,103] has also made these materials promising drug-delivery vehicles.[104] The physical encapsulation of guest molecules was first reported in 1994 by Meijer and coworkers, who described this concept as encapsulation within a '*dendritic box'*.[105] This study involved the synthesis of generation 5 PPI dendrimers whose peripheral amine functionality was further functionalised with a dense shell consisting of tBOC-protected amino acids. Analysis of the encapsulation studies using various dye molecules confirmed their ability to host such guest molecules within the internal cavities, and also found that diffusion out of the box was immeasurably slow due to the close packing of the shell. Further development of this concept has led to the encapsulation of: (i) anticancer drugs (e.g. camptothecin, dimethoxycurcumin, doxorubicin, etoposide, 5-fluorouracil, methotrexate, and paclitaxel), (ii) anti-inflammatory drugs (e.g. diclofenac, diflunisal, ibuprofen, indomethacin, ketoprofen, mefenamic acid, methylprednisolone, naproxen, and nifedipine), and (iii) antimicrobial drugs (e.g. sulfamethoxazole, quinolones, artemether, niclosamide, and anti-chagasics). However, major issues remain regarding the potential of dendrimers as drug-delivery agents utilising such physical encapsulation methods. Firstly, high generation dendrimers are required to form globular structures with internal cavities capable of encapsulation; this involves expensive and difficult syntheses and purification procedures. Secondly, in order to prevent premature drug-leakage, the dendrimers must have a dense shell; this requires multiple reaction steps using small building blocks which consequently increases the risk of defect formation.

The multivalent surface functionality associated with dendrimers theoretically provides the ideal platform for the chemical conjugation of guest molecules; however,

conjugation of hydrophobic drug molecules to the periphery of the dendrimer can significantly alter their physical behaviour (e.g. *in vivo* solubility), enhance opsonisation and recognition by the MPS, and limit their active targeting capabilities. As a consequence, there are currently no dendrimer-based nanomedicines that have been approved for drug-delivery applications.

1.4. Hyperbranched Polymers

Hyperbranched polymers (HBPs) are highly branched, polydisperse materials that share many properties with dendrimers; however, their defining feature is that they are dendritic materials that are structurally imperfect due to statistical branching of AB_2 monomers (Figure 1.7). Despite this, they are regarded as attractive, commercially viable alternatives to dendrimers primarily because they can be synthesised on a large scale through one-pot reactions without the need for laborious purification procedures.[106–108]

This has led to the commercialisation of HBPs that include Boltorn® (hyperbranched aliphatic polyester), Hybrane® (hyperbranched polyesteramide), polyethyleneimine (hyperbranched polyamine) and polyglycerol (hyperbranched polyether).

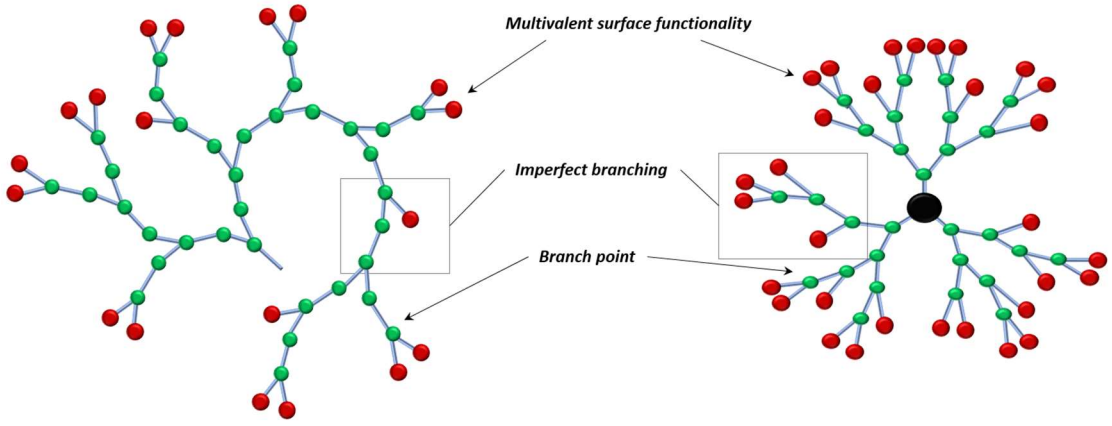

Figure 1.7. Graphical representation of a hyperbranched polymer, highlighting their imperfect branching and multivalent surface functionality.

Highly branched polymers were initially described by Flory in 1952 through the step-growth polycondensation of AB_x monomers,[109] however, the term 'hyperbranched polymers' was later introduced by Kim and Webster who reported the synthesis of hyperbranched polyphenylene.[110,111] Since then, the significant development of these materials, with particular emphasis on biocompatibility and biodegradability, has led to the synthesis of hyperbranched polyethers, hyperbranched polyesters, hyperbranched polyphosphates, hyperbranched polysaccharides, hyperbranched polypeptides, and hyperbranched polyamides; all have potential therapeutic applications in nanomedicine. The incorporation of targeting ligands onto the multivalent periphery of HBPs has highlighted the potential of these materials for the active targeting of disease. For example, the conjugation of folic acid onto the periphery of various amphiphilic HBPs has enabled the active targeting of folate receptors over-expressed on the surface of cancer cells.[112–114]

1.5. Dendritic-Linear Polymer Hybrids

Dendritic-linear polymer hybrids are complex macromolecules that combine key attributes of both individual structures: the extensive surface functionality associated with dendrimers, and the synthetic ease and versatility of linear polymers. Their architectures consist of linear polymers conjugated to at least one dendritic element, which can be combined in a number of ways to yield a range of functional structures. These can be grouped into three categories: (i) dendritic-linear block copolymers, (ii) dendronised polymer-hybrids, and (iii) star-like dendritic-linear polymer hybrids, (Figure 1.8).

1.5.1. Dendritic-Linear Block Copolymers

Dendritic-linear block copolymers are typically linear polymers with dendrons conjugated at one or both chain-ends, synthesis of which can be achieved using one of three general strategies: (i) coupling of a linear polymer with a preformed dendron, (ii) polymerisation of the linear block from the focal point of the dendron, and (iii) divergent growth of the dendron from the terminus of a linear polymer.

These hybrids were first developed by Fréchet and coworkers in the early 1990s using a coupling route, which involved terminating the living anionic polymerisations of

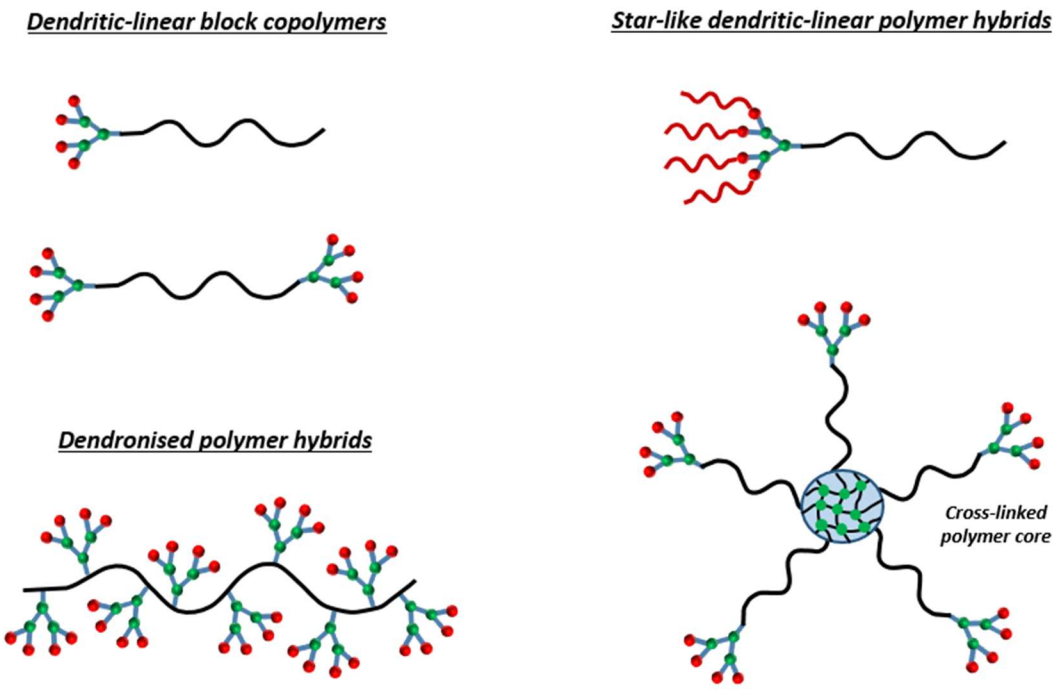

Figure 1.8. Graphical representation of dendritic-linear polymer hybrids categorised into: (i) dendritic-linear block copolymers, (ii) dendronised polymer hybrids, and (iii) star-like dendritic-linear polymer hybrids.

both polystyrene (PS) and PEG with Fréchet-type poly(benzyl ether) (PBE) dendrons bearing benzyl bromide focal functionality, yielding PBE-PS hybrids and amphiphilic PBE-PEG hybrids respectively.[115,116] Investigations into the self-assembly of the PBE-PEG hybrids in methanol/water mixtures enabled the formation of mono- and multi-molecular micelles that were dependent on both the concentration and the dendron generation.[117] Fréchet and coworkers later reported the synthesis of dendritic linear block copolymers using an alternative synthetic strategy that involved the anionic polymerisation of caprolactone from the focal point of a PBE dendron initiator.[118]

Further syntheses of amphiphilic dendritic-linear block copolymers involved the divergent synthesis of poly(L-lysine) dendrons from a linear PEG chain,[119] and the divergent synthesis of poly(propylene imine) dendrons (G1-G5) from amine-terminated PS,[120] reported by Shaffer and coworkers, and Meijer and coworkers respectively.

Significant progress in the development of these hybrid materials, with particular emphasis on synthesis and their aqueous self-assemblies into micelles and vesicles, means they have potential application in drug-delivery and gene-therapy.[121] Research has highlighted their ability to encapsulate and release hydrophobic payloads in a sustained [122–124] or stimuli-responsive manner,[125–128] and to actively target specific tissues through the incorporation of targeting ligands, such as carbohydrates (e.g. galactose,[129] mannose,[129,130] and glucose[131]) and various peptide sequences.[132,133] With regards to the active targeting of these materials, one interesting study, carried out by Gillies and co-workers, compared the ability of dendritic-linear polymer vesicles bearing dendritic mannose functionality, with that of polymeric vesicles bearing non-dendritic mannose functionality, to bind to the mannose-binding lectin Concanavalin A (Con A) using a haemaglutination assay. Using the same overall mannose content on both vesicles, it was found that the dendritic vesicles exhibited a binding affinity over ten orders of magnitude higher than that of the non-dendritic vesicles. This was attributed to the density of the targeting ligands on the multivalent dendritic surface functionality. As a result, dendritic-linear polymer block copolymers and their self-assembled nanostructures present themselves as interesting candidates in the field of nanomedicine.

1.5.2. Dendronised-Polymer Hybrids

Dendronised-polymer hybrids consist of a linear polymer backbone with dendron moieties conjugated to a fraction of the repeat units (up to 100 %), therefore conveying architectures that closely resemble that of comb-polymers. These hybrids can be synthesised using one of two general approaches: the grafting-to approach, or the macromonomer approach. The former involves either the coupling (grafting-to) of a preformed dendron onto the repeat units of the polymer chain, or the divergent growth of a dendron from the polymer chain; whereas the latter approach involves the polymerisation of dendronised-monomers (macromonomers) using techniques such as controlled radical polymerisation, ring-opening metathesis polymerisation (ROMP), and Suzuki polycondensations.

Although the synthesis of these hybrid materials remains challenging due to the high-chain density of the sterically-demanding dendrons, they have recently generated great interest owing to their molecular rigidity, morphological features, phase-

transition properties, solvent-induced hierarchical self-assembly, and thermoresponsive behaviour, that has led to potential applications in photonics,[134] catalysis,[135] biosensing,[136] and photoresponsive drug-delivery.[137]

1.5.3. Star-like dendritic-linear polymer hybrids

Functionalisation at the periphery of dendritic compounds with linear polymers yields dendritic-linear polymer hybrids of a star-like nature. These hybrid materials can be synthesised by: (i) coupling of linear polymers to the periphery of a preformed dendron, or (ii) using the dendron as a macroinitiator to polymerise linear chains from its periphery. In either case, reactive functional groups at the periphery of the dendron are essential, and as such bis(methylol)propionic acid (bis-MPA) dendrons with multivalent hydroxyl functionality are a widely reported platform.[138]

The synthesis of star-like dendritic-linear polymer hybrids *via* the coupling approach has been reported using various reactions. Nyström and coworkers reported the esterification of high molecular weight monofunctional PEG bearing carboxylic acid functionality with hyperbranched bis-MPA dendritic polymers (Boltorn H30 and H40).[139] Studies involving the encapsulation of the anticancer drug doxorubicin were conducted and encapsulation efficiency, *in vitro* release, cellular uptake, cytotoxicity, and apoptosis induction were evaluated. In related studies, Grayson and coworkers utilised copper-catalysed azide-alkyne click (CuAAC) reactions to functionalise the periphery of first and second generation bis-MPA dendrimers with PEG and polystyrene (PS).[140]

Synthesis of these hybrid materials *via* the macro-initiator approach can be achieved by either directly using hydroxyl functionalities for the ring-opening polymerisation (ROP) of monomers such as ε-caprolactone,[141,142] or by decorating the periphery of the dendrons with functional groups capable of initiating controlled radical polymerisations such as atom transfer radical polymerisation (ATRP)[143,144] and reversible addition-fragmentation chain-transfer (RAFT).[145,146]

Qiao and coworkers reported an interesting approach to the synthesis of star-like dendritic-linear polymer hybrids, utilising bis-MPA dendrons (G1-G5) as macroinitiators for the ATRP of styrene: the polymerisation was initiated from the focal point of the dendrons, not the periphery, initially yielding hybrid materials whose architectures resemble that of dendritic-linear block copolymers. However, at high

vinyl conversion, divinylbenzene (DVB) was added to the polymerisation to form a cross-linked core. This yielded star-like hybrids whose final architecture differed from those obtained by conventional synthesis.[147,148]

1.6. Hyperbranched Polydendrons

Hyperbranched-polydendrons (*hyp*-polydendrons) are a new macromolecular architecture designed to combine aspects of reversible-deactivation radical polymerisation, branched vinyl polymerisation, and linear-dendritic hybrids, to yield high molecular weight macromolecules with ideally branched dendritic chain ends with the minimal number of reaction steps (Figure 1.9).[149,150]

Synthesis involves a one-pot polymerisation of a mixture of monofunctional monomer and a low concentration of bifunctional branching monomer, initiated by a dendritic compound; less than one equivalent of branching monomer per primary chain is utilised to avoid gelation, as described by the Flory-Stockmayer theory.[151–155]

Initially, dendritic initiators bearing benzyl ether functionality were utilised in the copper-catalysed ATRP of 2-hydroxypropyl methacrylate (HPMA) in the presence of the branching monomer ethylene glycol dimethacrylate (EGDMA); a degree of polymerisation (DP_n) of 50 monomer units was targeted, and 0.8 equivalents of EGDMA per primary chain maintained.[149] This yielded high molecular weight materials with M_w values as high as 1700 kg/mol, that were self-assembled *via* nanoprecipitation to form monodisperse, stable nanoparticles in aqueous media (D_z = 64 – 134 nm; PDI = 0.064 – 0.160).

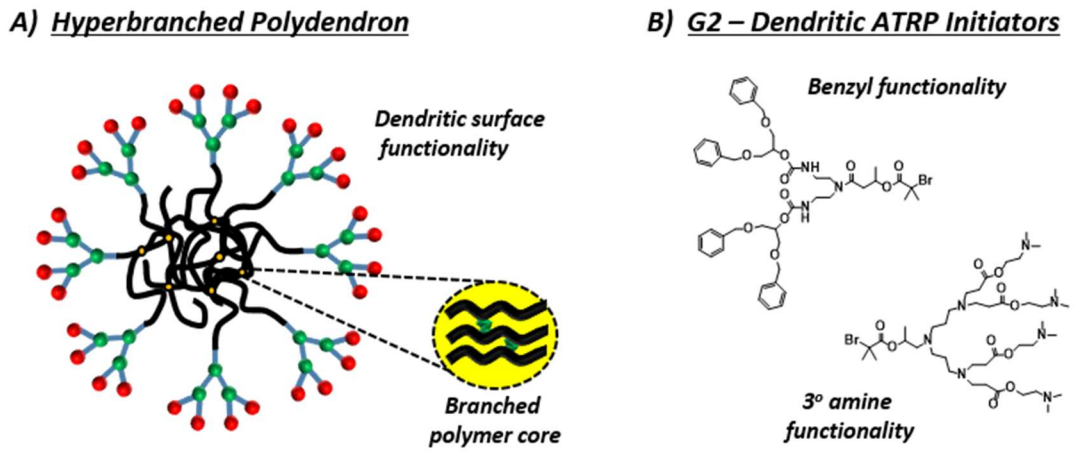

Figure 1.9. A) Schematic representation of a hyperbranched polydendron, showing the dendritic surface functionality and the branched polymer core. B) Examples of G2 dendritic ATRP initiators reported in the synthesis of the hyperbranched polydendrons.

Nanoparticle sizes could be controlled by varying the starting polymer concentration in THF, the final polymer concentration in water, and through manipulation of end-group dendron generation.

The complexity of these *hyp*-polydendrons was developed further by utilising mixed initiator systems to systematically control surface functionality.[150] Here, a series of branched polymerisations were conducted *via* ATRP using varying ratios of a G2 benzyl ether -functional dendritic initiator and a PEG-derived initiator (G2:PEG ratios; 100:0, 90:10, 75:25, 50:50, 25:75, 10:90, 0:100). Nanoprecipitation of these materials into water yielded stable nanoparticles that were able to encapsulate hydrophobic molecules, such as Nile red and pyrene. This enabled preliminary *in vitro* pharmacological evaluation to assess the viability of these materials for drug-delivery applications. Low cytotoxicity was observed for each of the seven *hyp*-polydendron nanoprecipitates when assessed against the human epithelial colorectal adenocarcinoma (Caco-2) cell line. The transcellular permeation of the *hyp*-polydendron nanoprecipitates (encapsulating Nile red) was studied across differentiated Caco-2 monolayers as a model of absorption through the intestinal epithelium. Results show that: (i) all of the nanoprecipitates were able to permeate through the epithelium to a much greater extent than the aqueous Nile red solution, highlighting the potential of these materials as orally administered nanocarrier therapeutics, and (ii) a strong correlation was observed amongst the *hyp*-polydendron nanoprecipitates, where less transcellular permeability was achieved with decreasing dendron content.

More recently, amphiphilicity has been introduced into the *hyp*-polydendron architecture through the use of tertiary-amine functional dendritic ATRP initiators in the branched copolymerisation of HPMA and EGDMA.[156] Nanoprecipitation of these materials into water gave stable aqueous dispersions: the influence of polymer architecture, dendritic chain-end chemistry, and the pH of the precipitation medium, on the formation of nanoparticles was discussed.

Essentially, *hyp*-polydendrons are regarded as an attractive, versatile alternative to dendrimers, particularly for therapeutic applications in nanomedicine. The reasons are, firstly, that *hyp*-polydendrons exhibit extensive surface functionality, yet can be easily obtained by combined dendron synthesis and one-pot branched polymerisation – this

is in stark contrast to the laborious, iterative synthesis widely associated with dendrimers. Secondly, the ability to tune the size of the *hyp*-polydendrons by either varying the degree of polymerisation, and/or modifying nanoprecipitation conditions means that these materials can easily be tailored for desired therapeutic application. Thirdly, mixed surface functionalities can be obtained by simply incorporating mixed initiating systems into a one-pot branched polymerisation. And finally, the branched core functionalities of *hyp*-polydendrons can be tailored for a variety of desired applications through the polymerisation of a wide range of vinyl monomers: the choice of monomer can enable the optimum encapsulation of a particular payload, and/or enable the materials to act in a stimuli-responsive manner (e.g. amine functionalised polymers in acidic environments).

1.7. Research Objectives

Ultimately, this research aims to synthesise amphiphilic *hyp*-polydendrons for potential drug-delivery applications, with a particular emphasis on developing the chemistry of both the hydrophilic surface functionalities and hydrophobic core functionalities to enable the active targeting of disease sites and the encapsulation of hydrophobic drugs (Figure 1.10).

This will involve the convergent synthesis of dendritic ATRP initiators varying in generation number that will then be utilised in a branched vinyl copolymerisation following the Strathclyde approach to give the branched polymer core. Synthetic strategies will be developed to introduce saccharide functionalities to the multivalent periphery, whose hydrophilicity would enable nanoparticle formation in aqueous media, but more importantly facilitate potential interactions with specific lectin receptors. Various reports within the literature have demonstrated the ability of galactose and mannose bearing nanoparticles to target specific lectins that could potentially improve anticancer therapy[157] and antiretroviral therapy,[158] respectively; therefore, this research will aim to incorporate these monosaccharides onto the periphery of the *hyp*-polydendrons. Furthermore, the synthesis will aim to incorporate PEG functionalities - whose stealth properties that have been critical to the success of the majority of clinically-approved nanomedicines are described within this Chapter.

The development of the hydrophobic branched polymer core will initially involve the optimisation of reaction conditions for the ATRP of hydrophobic monomers, *n*-butyl

methacrylate (*n*BuMA), methyl methacrylate (MMA) and *t*-butyl methacrylate (*t*BuMA) (Figure 1.11); it is hypothesised that these core functionalities will provide greater hydrophobicity than the *p*(HPMA) core functionalities previously reported, and thus enable a greater encapsulation efficiency of hydrophobic drug molecules.

Finally, aqueous rapid nanoprecipitations of the *hyp*-polydendrons will be performed to study the effect of (i) the dendritic chain end functionality, (ii) the primary polymer chain length, and (iii) the molecular weight of the branched materials, on the formation of nanoparticles.

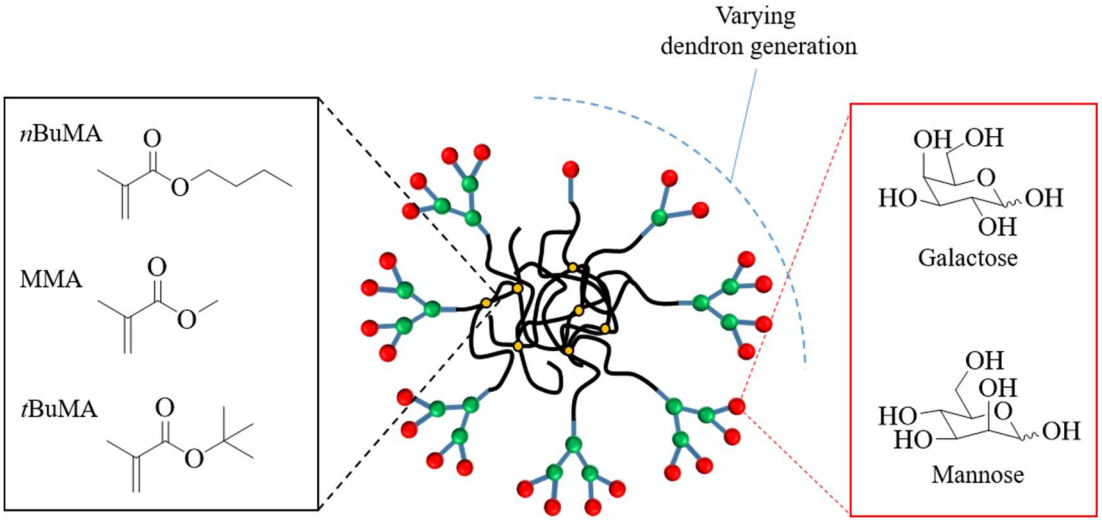

Figure 1.10. Graphical representation of the aims of the project, showing varying dendron generation, hydrophilic surface functionalities and hydrophobic branched core functionalities.

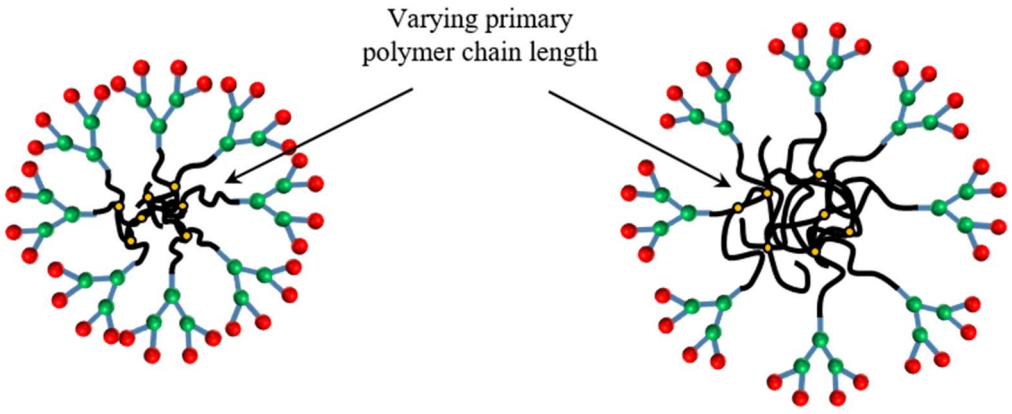

Figure 1.11. Graphical representation of the aims of the project, showing the varying primary polymer chain length of the hydrophobic branched polymer core.

1.8. References

1 Cancer Research UK, *http//www.cancerresearchuk.org/health-professional/cancer-statistics, Accessed Sept. 2015*.

2 Bupa, *http//www.bupa.com/media-centre/news/uk/cost-of-cancer-to-rise-by-almost-two-thirds-over-next-decade, Accessed Sept. 2015*.

3 The World Health Organisation, *http//www.who.int/hiv/en/, Accessed Sept. 2015*.

4 UNAIDS, *http//www.unaids.org/sites/default/files/media_asset/MDG6Report_en.pdf, Accessed Sept. 2015*.

5 Avert, *http//www.avert.org/antiretroviral-drug-prices.htm, Accessed Septmeber 2015*.

6 T. L. Doane and C. Burda, *Chem. Soc. Rev.*, 2012, **41**, 2885–2911.

7 L. Zhang, F. X. Gu, J. M. Chan, A. Z. Wang, R. S. Langer and O. C. Farokhzad, *Clin. Pharmacol. Ther.*, 2008, **83**, 761–769.

8 T. Lammers, S. Aime, W. E. Hennink, G. Storm and F. Kiessling, *Acc. Chem. Res.*, 2011, **44**, 1029–1038.

9 L. Y. Rizzo, B. Theek, G. Storm, F. Kiessling and T. Lammers, *Curr. Opin. Biotechnol.*, 2013, **24**, 1159–1166.

10 British Society for Nanomedicine, *http//www.britishsocietynanomedicine.org/existing-nanomedicines.html, Accessed Sept. 2015*.

11 Y. Barenholz, *J. Control. Release*, 2012, **160**, 117–134.

12 R. Pazdur, a P. Kudelka, J. J. Kavanagh, P. R. Cohen and M. N. Raber, *Cancer Treat. Rev.*, 1993, **19**, 351–386.

13 S. Dhib-Jalbut, *Pharmacol. Ther.*, 2003, **98**, 245–255.

14 R. Duncan, *Nat. Rev. Cancer*, 2006, **6**, 688–701.

15 P. M. Drake and D. Rabuka, *Curr. Opin. Chem. Biol.*, 2015, **28**, 174–180.

16 D. W. Northfelt, B. J. Dezube, J. a. Thommes, R. Levine, J. H. Von Roenn, G. M. Dosik,

A. Rios, S. E. Krown, C. DuMond and R. D. Mamelok, *J. Clin. Oncol.*, 1997, **15**, 653–659.

17 D. W. Northfelt, B. J. Dezube, J. A. Thommes, B. J. Miller, M. A. Fischl, A. Friedman-Kien, L. D. Kaplan, C. Du Mond, R. D. Mamelok and D. H. Henry, *J. Clin. Oncol.*, 1998, **16**, 2445–2451.

18 M. Harrison, D. Tomlinson and S. Stewart, *J. Clin. Oncol.*, 1995, **13**, 914–920.

19 S. T. Duggan and G. M. Keating, *Drugs*, 2011, **71**, 2531–2558.

20 W. Tejada-Berges, T.; Granai C. O.; Gordinier, M.; Gajewski, *Expert Rev. Anticancer Ther.*, 2002, **2**, 143–150.

21 H. Maeda, J. Wu, T. Sawa, Y. Matsumura and K. Hori, *J. Control. Release*, 2000, **65**, 271–284.

22 R. K. Jain and T. Stylianopoulos, *Nat. Rev. Clin. Oncol.*, 2010, **7**, 653–64.

23 J. A. Barreto, W. O'Malley, M. Kubeil, B. Graham, H. Stephan and L. Spiccia, *Adv. Mater.*, 2011, **23**, H18–H40.

24 H. Otsuka, Y. Nagasaki and K. Kataoka, *Adv. Drug Deliv. Rev.*, 2003, **55**, 403–419.

25 K. Knop, R. Hoogenboom, D. Fischer and U. S. Schubert, *Angew. Chemie Int. Ed.*, 2010, **49**, 6288–6308.

26 D. Lorusso, A. Di Stefano, V. Carone, A. Fagotti, S. Pisconti and G. Scambia, *Ann. Oncol.*, 2007, **18**, 1159–1164.

27 R. Duncan and M. J. Vicent, *Adv. Drug Deliv. Rev.*, 2013, **65**, 60–70.

28 M. L. Graham, *Adv. Drug Deliv. Rev.*, 2003, **55**, 1293–1302.

29 P. A. Dinndorf, J. Gootenberg, M. H. Cohen, P. Keegan and R. Pazdur, *Oncologist*, 2007, **12**, 991–998.

30 D. H. Ho, N. S. Brown, A. Yen, R. Holmes, M. Keating, A. Abuchowski, R. A. Newman and I. H. Krakoff, *Drug Metab. Dispos.*, 1986, **14**, 349–52.

31 M. Buchfelder, S. Schlaffer, M. Droste, K. Mann, B. Saller, K. Brübach, G. K. Stalla and C. J. Strasburger, *Eur. J. Endocrinol.*, 2009, **161**, 3–10.

32 G. Y. Melmed, S. R. Targan, U. Yasothan, D. Hanicq and P. Kirkpatrick, *Nat. Rev. Drug*

Discov., 2008, **7**, 641–642.

33 R. Duncan, *J. Control. Release*, 2014, **190**, 371–380.

34 D. M. Piedmonte and M. J. Treuheit, *Adv. Drug Deliv. Rev.*, 2008, **60**, 50–58.

35 A. D. Keefe, S. Pai and A. Ellington, *Nat. Rev. Drug Discov.*, 2010, **9**, 537–550.

36 S. C. Alley, N. M. Okeley and P. D. Senter, *Curr. Opin. Chem. Biol.*, 2010, **14**, 529–537.

37 R. V. J. Chari, M. L. Miller and W. C. Widdison, *Angew. Chemie - Int. Ed.*, 2014, **53**, 3796–3827.

38 G. Casi and D. Neri, *J. Control. Release*, 2012, **161**, 422–428.

39 C. M. Dawidczyk, C. Kim, J. H. Park, L. M. Russell, K. H. Lee, M. G. Pomper and P. C. Searson, *J. Control. Release*, 2014, **187**, 133–144.

40 H. Hatakeyama, H. Akita and H. Harashima, *Adv. Drug Deliv. Rev.*, 2011, **63**, 152–160.

41 H. Hatakeyama, H. Akita and H. Harashima, *Biol. Pharm. Bull.*, 2013, **36**, 892–899.

42 Y. H. Bae, *J. Control. Release*, 2009, **133**, 2–3.

43 H. Maeda, *Adv. Drug Deliv. Rev.*, 2015, **91**, 3–6.

44 U. Prabhakar, H. Maeda, R. K. Jain, E. M. Sevick-Muraca, W. Zamboni, O. C. Farokhzad, S. T. Barry, A. Gabizon, P. Grodzinski and D. C. Blakey, *Cancer Res.*, 2013, **73**, 2412–2417.

45 Q. Yang, C. L. Parker, J. D. McCallen and S. K. Lai, *J. Control. Release*, 2015, **220**, 715–726.

46 F. Danhier, O. Feron and V. Préat, *J. Control. Release*, 2010, **148**, 135–146.

47 Z. M. Qian, H. Li, H. Sun and K. Ho, *Pharmacol. Rev.*, 2002, **54**, 561–587.

48 H. Li and Z. M. Qian, *Med. Res. Rev.*, 2002, **22**, 225–250.

49 J. Sudimack and R. J. Lee, *Adv. Drug Deliv. Rev.*, 2000, **41**, 147–162.

50 Y. Lu, E. Sega, C. P. Leamon and P. S. Low, *Adv. Drug Deliv. Rev.*, 2004, **56**, 1161–1176.

51 P. Low, *Adv. Drug Deliv. Rev.*, 2004, **56**, 1055–1058.

52 C. Bies, C.-M. Lehr and J. F. Woodley, *Adv. Drug Deliv. Rev.*, 2004, **56**, 425–435.

53 R. S. Herbst and D. M. Shin, *Cancer*, 2002, **94**, 1593–1611.

54 C. Mamot, *Cancer Res.*, 2005, **65**, 11631–11638.

55 R. A. Brekken and P. E. Thorpe, *J. Control. Release Off. J. Control. Release Soc.*, 2001, **74**, 173–181.

56 D. Ribatti, *Cancer Treat. Rev.*, 2011, **37**, 344–352.

57 A. Mitra, T. Coleman, M. Borgman, A. Nan, H. Ghandehari and B. R. Line, *J. Control. Release*, 2006, **114**, 175–83.

58 S. Wagner, F. Rothweiler, M. G. Anhorn, D. Sauer, I. Riemann, E. C. Weiss, A. Katsen-Globa, M. Michaelis, J. Cinatl, D. Schwartz, J. Kreuter, H. von Briesen and K. Langer, *Biomaterials*, 2010, **31**, 2388–2398.

59 S. Gosk, T. Moos, C. Gottstein and G. Bendas, *Biochim. Biophys. Acta - Biomembr.*, 2008, **1778**, 854–863.

60 C. Gialeli, A. D. Theocharis and N. K. Karamanos, *FEBS J.*, 2011, **278**, 16–27.

61 A. I. Elegbede, J. Banerjee, A. J. Hanson, S. Tobwala, B. Ganguli, R. Wang, X. Lu, D. K. Srivastava and S. Mallik, *J. Am. Chem. Soc.*, 2008, **130**, 10633–10642.

62 R. Suzuki, T. Takizawa, Y. Kuwata, M. Mutoh, N. Ishiguro, N. Utoguchi, A. Shinohara, M. Eriguchi, H. Yanagie and K. Maruyama, *Int. J. Pharm.*, 2008, **346**, 143–150.

63 R. van der Meel, L. J. C. Vehmeijer, R. J. Kok, G. Storm and E. V. B. van Gaal, *Adv. Drug Deliv. Rev.*, 2013, **65**, 1284–1298.

64 M. Mammen, S.-K. Choi and G. M. Whitesides, *Angew. Chemie Int. Ed.*, 1998, **37**, 2754–2794.

65 H. Ding and Y. Ma, *Biomaterials*, 2012, **33**, 5798–5802.

66 Z. Tang, D. Li, H. Sun, X. Guo, Y. Chen and S. Zhou, *Biomaterials*, 2014, **35**, 8015–8027.

67 J. Wang, S. Tian, R. a. Petros, M. E. Napier and J. M. Desimone, *J. Am. Chem. Soc.*, 2010, **132**, 11306–11313.

68 A.-M. Caminade, A. Ouali, M. Keller and J.-P. Majoral, *Chem. Soc. Rev.*, 2012, **41**,

4113–4125.

69 D. Méry and D. Astruc, *Coord. Chem. Rev.*, 2006, **250**, 1965–1979.

70 D. Astruc and F. Chardac, *Chem. Rev.*, 2001, **101**, 2991–3023.

71 J. Ruiz and S. Mole, *Acc. Chem. Res.*, 2008, **41**, 841–856.

72 D. Astruc and E. Boisselier, *Chem. Rev.*, 2010, **110**, 1857–1959.

73 J. Khandare, M. Calderón, N. M. Dagia and R. Haag, *Chem. Soc. Rev.*, 2012, **41**, 2824–2848.

74 Y. Cheng, L. Zhao, Y. Li and T. Xu, *Chem. Soc. Rev.*, 2011, **40**, 2673–2703.

75 C. Dufès, I. F. Uchegbu and A. G. Schätzlein, *Adv. Drug Deliv. Rev.*, 2005, **57**, 2177–2202.

76 R. M. Kannan, E. Nance, S. Kannan and D. a. Tomalia, *J. Intern. Med.*, 2014, **276**, 579–617.

77 V. Leiro, J. P. Garcia, H. Tomás and A. P. Pêgo, *Bioconjug. Chem.*, 2015, **26**, 1182–1197.

78 J. Satija, V. V. R. Sai and S. Mukherji, *J. Mater. Chem.*, 2011, **21**, 14367–14386.

79 F. Buhleier, E; Wehner, W; Vogtle, *Synthesis (Stuttg).*, 1978, 155–158.

80 G. R. Newkome, Z. Yao, G. R. Baker and V. K. Gupta, *J. Org. Chem.*, 1985, **50**, 2003–2004.

81 P. Tomalia, D, A; Baker, H; Dewald, J; Hall, M; Kallos, G; Martin, S; Roeck, J; Ryder, J; Smith, *Polym. J.*, 1985, **17**, 117–132.

82 E. W. Brabander van den Berg, E.; Meijer, *Angew. Chemie*, 1993, **105**, 1370–1372.

83 E. W. Ellen, M ; de Brabander-van den Berg, M; Meijer, *Angew. Chem. Int. Ed. Engl.*, 1993, **32**, 1308–1311.

84 R. Esfand and D. a. Tomalia, *Drug Discov. Today*, 2001, **6**, 427–436.

85 G. R. Newkome and X. Lin, *Macromolecules*, 1991, **24**, 1443–1444.

86 A.-M. Caminade and J.-P. Majoral, *Prog. Polym. Sci.*, 2005, **30**, 491–505.

87 P. D. G. H. H. G., *J. Phys. lettres*, 1983, **44**, 351–360.

88 C. J. Hawker and J. M. J. Frechet, *J. Chem. Soc. Commun.*, 1990, 1010–1013.

89 M. Hawker, C; Frechet, *J. Am. Chem. Soc.*, 1990, **112**, 7638–7647.

90 P. Kesharwani, R. K. Tekade, V. Gajbhiye, K. Jain and N. K. Jain, *Nanomedicine Nanotechnology, Biol. Med.*, 2011, **7**, 295–304.

91 Z. Sideratou, C. Kontoyianni, G. I. Drossopoulou and C. M. Paleos, *Bioorganic Med. Chem. Lett.*, 2010, **20**, 6513–6517.

92 P. Kesharwani, L. Xie, S. Banerjee, G. Mao, S. Padhye, F. H. Sarkar and A. K. Iyer, *Colloids Surfaces B Biointerfaces*, 2015, **136**, 413–423.

93 M. Saraswathy, G. T. Knight, S. Pilla, R. S. Ashton and S. Gong, *Colloids Surfaces B Biointerfaces*, 2015, **126**, 590–597.

94 P. Singh, U. Gupta, A. Asthana and N. K. Jain, *Bioconjug. Chem.*, 2008, **19**, 2239–2252.

95 S. H. Medina, G. Tiruchinapally, M. V. Chevliakov, Y. Y. Durmaz, R. N. Stender, W. D. Ensminger, D. S. Shewach and M. E. H. Elsayed, *Adv. Healthc. Mater.*, 2013, **2**, 1337–1350.

96 S. Zhu, L. Qian, M. Hong, L. Zhang, Y. Pei and Y. Jiang, *Adv. Mater.*, 2011, **23**, 84–89.

97 C. Han, Liang; Huang, Rongqin; Liu, Shuhuan; Huang, Shixian; Jiang, *Mol. Pharm.*, 2010, **7**, 2156–2165.

98 G. K. Grünwald, A. Vetter, K. Klutz, M. J. Willhauck, N. Schwenk, R. Senekowitsch-Schmidtke, M. Schwaiger, C. Zach, E. Wagner, B. Göke, P. S. Holm, M. Ogris and C. Spitzweg, *Mol. Ther. Nucleic Acids*, 2013, **2**, e131.

99 C. Kojima, K. Kono, K. Maruyama and T. Takagishi, *Bioconjug. Chem.*, 2000, **11**, 910–917.

100 A. K. Patri, J. F. Kukowska-Latallo and J. R. Baker, *Adv. Drug Deliv. Rev.*, 2005, **57**, 2203–2214.

101 D. Bhadra, S. Bhadra, S. Jain and N. K. Jain, *Int. J. Pharm.*, 2003, **257**, 111–124.

102 R. X. Zhuo, B. Du and Z. R. Lu, *J. Control. Release*, 1999, **57**, 249–257.

103 K. Kono, M. Liu and J. M. J. Fréchet, *Bioconjug. Chem.*, 1999, **10**, 1115–1121.

104 P. Kesharwani, K. Jain and N. K. Jain, *Prog. Polym. Sci.*, 2014, **39**, 268–307.

105 J. F. Jansen, E. M. de Brabander-van den Berg and E. W. Meijer, *Science*, 1994, **266**, 1226–1229.

106 Y. Huang, D. Wang, X. Zhu, D. Yan and R. Chen, *Polym. Chem.*, 2015, **6**, 2794–2812.

107 D. Konkolewicz, M. J. Monteiro and S. Perrier, *Macromolecules*, 2011, **44**, 7067–7087.

108 D. Wang, T. Zhao, X. Zhu, D. Yan and W. Wang, *Chem. Soc. Rev.*, 2015, **44**, 4023–4071.

109 P. J. Flory, *J. Am. Chem. Soc.*, 1952, **74**, 2718–2723.

110 O. W. Kim, Y. H.; Webster, *Polym. Prepr.*, 1988, **29**, 310–311.

111 Y. H. Kim and O. W. Webster, *J. Am. Chem. Soc.*, 1990, **112**, 4592–4593.

112 and Z.-W. G. Si Chen,† Xian-Zheng Zhang,† Si-Xue Cheng,*,† Ren-Xi Zhuo, *Biomacromolecules*, 2008, **9**, 2578–2585.

113 M. Prabaharan, J. J. Grailer, S. Pilla, D. a. Steeber and S. Gong, *Biomaterials*, 2009, **30**, 5757–5766.

114 L.-A. Tziveleka, C. Kontoyianni, Z. Sideratou, D. Tsiourvas and C. M. Paleos, *Macromol. Biosci.*, 2006, **6**, 161–169.

115 I. Gitsov, K. L. Wooley, C. J. Hawker, P. T. Ivanova and J. M. J. Fréchet, *Macromolecules*, 1993, **26**, 5621–5627.

116 I. Gitsov and J. M. J. Frechet, *Macromolecules*, 1994, **27**, 7309–7315.

117 I. Gitsov and J. M. J. Frechet, *Macromolecules*, 1993, **26**, 6536–6546.

118 J. M. J. Gitsov, I.; Ivanova P. T.; Frechet, *Macromol. Rapid Commun.*, 1994, **15**, 387–393.

119 T. M. Chapman, G. L. Hillyer, E. J. Mahan and K. a Shaffer, *J. Am. Chem. Soc.*, 1994, **116**, 11195–11196.

120 J. C. van Hest, D. a Delnoye, M. W. Baars, M. H. van Genderen and E. W. Meijer, *Science*, 1995, **268**, 1592–1595.

121 G. Whitton and E. R. Gillies, *J. Polym. Sci. Part A Polym. Chem.*, 2015, **53**, 148–172.

122 I. Gitsov, K. R. Lambrych, V. a. Remnant and R. Pracitto, *J. Polym. Sci. Part A Polym. Chem.*, 2000, **38**, 2711–2727.

123 P. M. Nguyen and P. T. Hammond, *Langmuir*, 2006, **22**, 7825–7832.

124 H. Qiao, J. Li, Y. Wang, Q. Ping, G. Wang and X. Gu, *Int. J. Pharm.*, 2013, **452**, 363–373.

125 J. C. M. van Hest, M. W. P. L. Baars, C. Elissen-Roman, M. H. P. Van Genderen and E. W. Meijer, *Macromolecules*, 1995, **28**, 6689–6691.

126 E. R. Gillies and J. M. J. Fréchet, *Bioconjug. Chem.*, 2005, **16**, 361–368.

127 E. R. Gillies, T. B. Jonsson and J. M. J. Fréchet, *J. Am. Chem. Soc.*, 2004, **126**, 11936–11943.

128 Y. Zhang, C. Xiao, M. Li, J. Chen, J. Ding, C. He, X. Zhuang and X. Chen, *Macromol. Biosci.*, 2013, **13**, 584–94.

129 K. C. Wood, S. R. Little, R. Langer and P. T. Hammond, *Angew. Chemie - Int. Ed.*, 2005, **44**, 6704–6708.

130 A. L. Martin, B. Li and E. R. Gillies, *J. Am. Chem. Soc.*, 2009, **131**, 734–741.

131 J. Kumar, A. Bousquet and M. H. Stenzel, *Macromol. Rapid Commun.*, 2011, **32**, 1620–1626.

132 K. C. Wood, S. M. Azarin, W. Arap, R. Pasqualini, R. Langer and P. T. Hammond, *Bioconjug. Chem.*, 2008, **19**, 403–405.

133 D. K. Bonner, C. Leung, J. Chen-Liang, L. Chingozha, R. Langer and P. T. Hammond, *Bioconjug. Chem.*, 2011, **22**, 1519–1525.

134 W. Wu, J. Qin and Z. Li, *Polymer (Guildf).*, 2013, **54**, 4351–4382.

135 H. Frauenrath, *Prog. Polym. Sci.*, 2005, **30**, 325–384.

136 P. Laurino, R. Kikkeri, N. Azzouz and P. H. Seeberger, *Nano Lett.*, 2011, **11**, 73–78.

137 Z. Wang, M. Gao, J. Sun, D. Liang and X. Jia, *Macromolecules*, 2013, **46**, 1723−1731.

138 A. Carlmark, E. Malmström and M. Malkoch, *Chem. Soc. Rev.*, 2013, **42**, 5858–5879.

139 X. Zeng, Y. Zhang, Z. Wu, P. Lundberg, M. Malkoch and A. M. Nyström, *J. Polym. Sci. Part A Polym. Chem.*, 2012, **50**, 280–288.

140 Y. Li, B. Zhang, J. N. Hoskins and S. M. Grayson, *J. Polym. Sci. Part A Polym. Chem.*, 2012, **50**, 1086–1101.

141 M. Trollsås, J. L. Hedrick, D. Mecerreyes, P. Dubois, H. Ihre and A. Hult, *Macromolecules*, 1997, **30**, 8508–8511.

142 B. Atthoff, M. Trollsås, H. Claesson and J. L. Hedrick, *Macromol. Chem. Phys.*, 1999, **200**, 1333–1339.

143 A. Heise, J. L. Hedrick, C. W. Frank and R. D. Miller, *J. Am. Chem. Soc.*, 1999, **121**, 8647–8648.

144 D. E. Poree, M. D. Giles, L. B. Lawson, J. He and S. M. Grayson, *Biomacromolecules*, 2011, **12**, 898–906.

145 X. Hao, C. Nilsson, M. Jesberger, M. H. Stenzel, E. Malmström, T. P. Davis, E. Östmark and C. Barner-Kowollik, *J. Polym. Sci. Part A Polym. Chem.*, 2004, **42**, 5877–5890.

146 T. P. Davis, M. Jesberger, L. Barner, M. H. Stenzel, E. V. A. Malmstro and C. Barner-kowollik, *J. Polym. Sci. Part A Polym. Chem.*, 2003, **41**, 3847–3861.

147 L. a. Connial, R. Vestberg, C. J. Hawker and G. G. Qiao, *Macromolecules*, 2007, **40**, 7855–7863.

148 L. A. Connal, R. Vestberg, C. J. Hawker and G. G. Qiao, *Adv. Funct. Mater.*, 2008, **18**, 3706–3714.

149 F. L. Hatton, P. Chambon, T. O. Mcdonald and S. P. Rannard, *Chem. Sci.*, 2014, **5**, 1844.

150 F. L. Hatton, L. M. Tatham, L. R. Tidbury, P. Chambon, T. He, A. Owen and S. P. Rannard, *Chem. Sci.*, 2015, **6**, 326–334.

151 J. Flory, *J. Am. Chem. Soc.*, 1941, **63**, 3083–3090.

152 P. J. Flory, *J. Am. Chem. Soc.*, 1941, **63**, 3091–3096.

153 P. J. Flory, *J. Am. Chem. Soc.*, 1941, **63**, 3096–3100.

154 W. H. Stockmayer, *J. Chem. Phys.*, 1943, **11**, 45.

155 W. H. Stockmayer, *J. Chem. Phys.*, 1944, **12**, 125.

156 H. E. Rogers, P. Chambon, S. E. R. Auty, F. Y. Hern, A. Owen and S. P. Rannard, *Soft*

Matter, 2015, **11**, 7005–7015.

157 A. A. D'Souza and P. V. Devarajan, *J. Control. Release*, 2015, **203**, 126–139.

158 C. R. Becer, M. I. Gibson, J. Geng, R. Ilyas, R. Wallis, D. a Mitchell and D. M. Haddleton, *J. Am. Chem. Soc.*, 2010, **132**, 15130–15132.

159 A. Wicki, D. Witzigmann, V. Balasubramanian, J. Huwyler, *J. Control. Release,* 2015, **200**, 138-157.

Chapter 2

Exploring the homogeneous controlled radical polymerisation of hydrophobic monomers in anti-solvents for their polymers

Publications arising from this chapter:

"Is methanol really a bad solvent for poly(*n*-butyl methacrylate)? Low dispersity and high molecular weight polymers of *n*-butyl methacrylate synthesised *via* ATRP in anhydrous methanol"

A. B. Dwyer, P. Chambon, A. Town, T. He, A. Owen, and S. P. Rannard

Polym. Chem., 2014, **5**, 3608

"Exploring the homogeneous controlled radical polymerisation of hydrophobic monomers in anti-solvents for their polymers: RAFT and ATRP of various alkyl methacrylates in anhydrous methanol to high conversion and low dispersity"

A. B. Dwyer, P. Chambon, A. Town, F. L. Hatton, J. Ford and S. P. Rannard

Polym. Chem., 2015, **6**, 7286

2.1. Introduction

2.1.1. Chain growth polymerisation

The polymerisation of vinyl monomers *via* the 'chain-growth' mechanism is thermodynamically driven by the enthalpy change upon reaction of each monomer repeat unit: this overcomes the unfavourable entropy change as the more ordered polymer structure is progressively formed. Generally, these polymerisations consist of four steps that include (i) initiation, (ii) propagation, (iii) termination, and (iv) chain transfer; the rates of which are dependent on the technique that is employed.

Free radical polymerisation is a simple, cost-effective synthetic technique that proceeds with a fast rate of propagation relative to a slow rate of initiation; termination and chain transfer reactions are inevitable due to the highly reactive nature of free radicals.[1] As a consequence, the polymerisations proceed in an uncontrolled manner, yielding high molecular weight polymers with very broad distributions.

The potential to tune polymer composition,[2–4] architecture[5–8] and chain-end[9,10] functionalities was later realised through the development of 'living' ionic polymerisations, whose success relies on a fast initiation relative to a slow propagation, and the omission of termination reactions that may arise through bimolecular coupling;[11–13] the latter are not possible due to the repulsion of like charges. However, ionic polymerisation procedures are very difficult to perform due to the stringent reaction conditions that are required.

Reversible-deactivation radical polymerisation (RDRP) - also known as controlled radical polymerisation - is a technique that aims to combine the synthetic control of a living ionic polymerisation, with the ease of a free radical polymerisation.[14] Chain transfer and termination reactions cannot be avoided due to the highly reactive nature of radicals, but they can be minimised by maintaining a low concentration of the active radical species at any given moment. This concept is based on a dynamic equilibrium between dormant and active species, which can either be achieved by reversible capping of an active radical species or through a degenerative chain transfer mechanism. The most widely used RDRP techniques include atom transfer radical polymerisation (ATRP)[15,16] and reversible addition-fragmentation chain transfer (RAFT).[17,18]

2.1.2. Atom transfer radical polymerisation (ATRP)

During ATRP, the active radical species are generated through a reversible redox process catalysed by a transition metal complex M_t^n/L (Scheme 2.1). The catalytic complex undergoes a one-electron oxidation whilst simultaneously abstracting a halogen atom from the dormant species R-X, forming the oxidised species X-M_t^{n+1}/L, and the active radical species R$^\bullet$; this activation step proceeds with rate constant k_{act}. The active radical R$^\bullet$ can then propagate with vinyl monomer (rate constant k_p) before being capped with the halide (rate constant k_{deact}) to form the dormant species once more. To reiterate, termination reactions can occur with rate constant k_t, however this is minimised when the rate of deactivation is much greater than the rate of activation ($k_{deact} >> k_{act}$): this means that the equilibrium is highly biased towards the dormant species so as to maintain a low concentration of active radicals at any given moment. These reactions are further minimised by the *persistent radical effect*: each termination involving bimolecular coupling results in the irreversible formation of two equivalents of the deactivator X-M_t^{n+1}/L, which consequently increases the rate of deactivation ($k_{deact} >>> k_{act}$) and shifts the equilibrium further towards the dormant species. Given the nature of the mechanism, it is important for the polymerisation to proceed in the absence of oxygen to prevent (i) scavenging of radicals and subsequent termination, and (ii) poisoning of the transition metal catalyst.

The control of the polymerisation is based on two principles: (i) the rate of deactivation is much greater than the rate of activation ($k_{deact} >> k_{act}$), thereby minimising termination reactions and maintaining a constant concentration of active species throughout, and (ii) the equilibrium rate constant ($K_{ATRP} = k_{act}/k_{deact}$) is much greater than the rate of propagation (k_p), enabling the near simultaneous growth of all polymer chains.

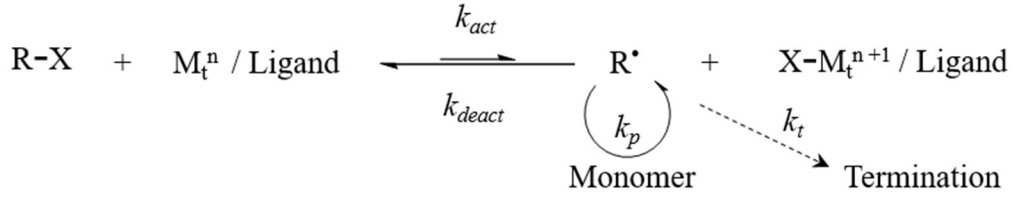

Scheme 2.1. The mechanism of ATRP showing the reversible redox process catalysed by transition metal complex.

2.1.3. Reversible addition-fragmentation chain transfer (RAFT)

In RAFT, the active radical species are generated after decomposition of an initiator, and are maintained through a degenerative chain transfer process involving a range of specialist chain transfer agents (CTA) known as a RAFT agents (Scheme 2.2); suitable RAFT agents include trithiocarbonates and dithioesters. The radicals $I^{\bullet}$, formed after the decomposition of a conventional free radical initiator (rate constant k_d), react with a vinyl monomer (rate constant k_i) to give $P_1^{\bullet}$, which propagates with further monomer (rate constant k_p) to give $P_m^{\bullet}$. This growing polymer chain ($P_m^{\bullet}$) reacts with the thiocarbonyl group of the CTA (rate constant k_{add}) to form the radical intermediate, which subsequently fragments either towards (i) the initial growing chain (rate constant k_{-add}), or (ii) to the free initiating group $R^{\bullet}$ and the macro-CTA (rate constant k_β). However, for well-controlled RAFT, $k_\beta > k_{-add}$ to ensure the pre-equilibrium stage is rapidly completed; therefore fragmentation towards $R^{\bullet}$ is favoured. The new active species can then re-initiate polymerisation (rate constant $k_{re\text{-}i}$) and propagate with vinyl monomer (rate constant k_p), before reacting with the thiocarbonyl of the macro-CTA to form the radical intermediate once more. At this stage, the polymerisation is in its main equilibrium where the original CTA has been fully consumed to leave only the macro-CTA present in the reaction medium. The ensuing rapid exchange between the active and dormant species ensures an equal probability for all polymer chains to grow, yielding polymers with controlled molecular weights and narrow dispersities.

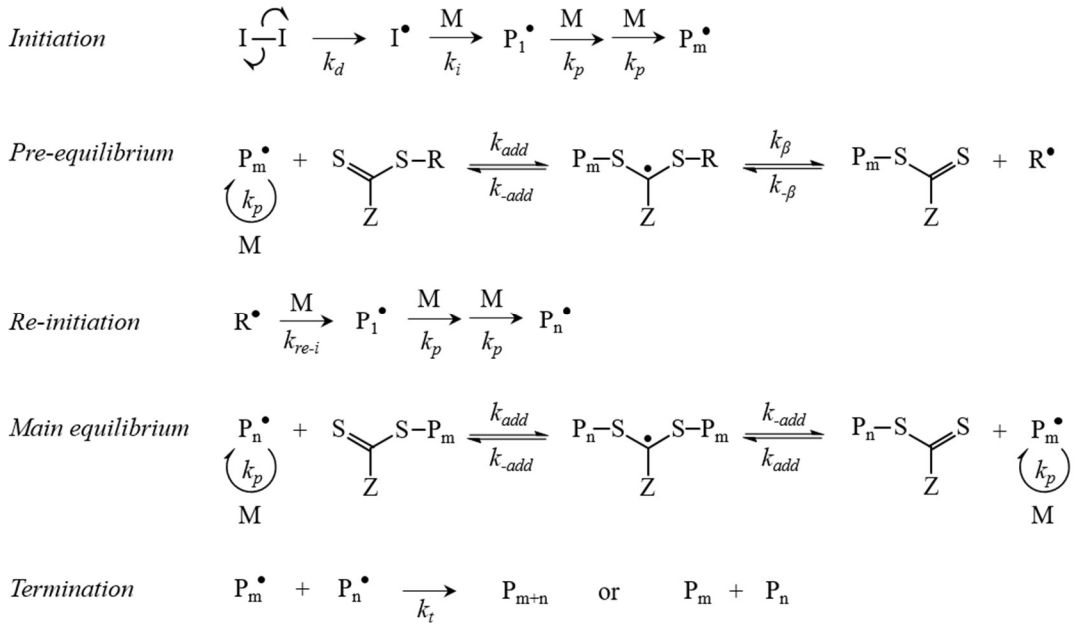

Scheme 2.2. RAFT mechanism showing the degenerative chain transfer process.

RAFT agents are often monomer-specific and correct choice is key to successfully performing RAFT: this requires appropriate selection of both the *Z* and *R* groups. The *Z* group strongly influences the stability of the radical intermediate; therefore, selection should enhance the reactivity of the thiocarbonyl group towards radical addition to enable the formation of the radical intermediate, but it needs to be finely tuned to also enable fragmentation towards the re-initiating group ($R^{\bullet}$). The *R* group also contributes to the stability of the radical intermediate, albeit to a lesser degree. More importantly, its selection requires it to be a good leaving group from the radical intermediate to enable an efficient re-initiation.

2.1.4. Utilising alcohols as the reaction solvent

RDRP techniques - including both ATRP and RAFT - have been instrumental in the design of sophisticated polymeric nanostructures for potential drug-delivery applications.[19] Utilising such techniques has facilitated the synthesis of a diverse array of functional polymers with controlled molecular weights, narrow dispersities, specific compositions, defined architectures, and complex chain-end functionalities.[20] This has required the optimisation of reaction conditions that include initiator chemistry, catalyst selection, design of CTA, ratio of reagents, solvent environment, reaction temperature and concentration; each can vary significantly on a monomer-to-monomer and polymerisation technique basis.[13,20–24] Prior to application, the polymer obtained is usually purified by means of precipitation into an anti-solvent; the use of alcohols for the precipitation of hydrophobic polymers, particularly the use of methanol (MeOH), has been widely reported.[25]

Utilising alcohols as reaction solvents has proven to aid control of some ATRP reactions involving the polymerisation of hydrophilic monomers such as oligo(ethylene glycol) methyl ether methacrylate,[26] 2-hydroxyethyl methacrylate,[27] 2-(dimethylamino)-ethyl methacrylate[28] and glycerol methacrylate;[29] alcohols vary from MeOH to ethanol, propanol and isopropanol (IPA).

The controlled polymerisation of hydrophobic monomers in alcoholic media is more challenging due to the difficulty of maintaining truly homogeneous reaction conditions if the final polymer is insoluble in the protic solvent environment at high monomer conversion. Rannard and coworkers reported the first homogeneous Cu^{I} catalysed ATRP of *n*-butyl methacrylate (*n*BuMA) in IPA and IPA/water mixtures under

ambient reaction conditions;[30] IPA was selected due to its well-known behaviour as a theta solvent for *p*(*n*BuMA), and IPA solutions of the polymer could tolerate up to approximately 10 vol % water before precipitation occurred.[31] Other homogeneous alcoholic polymerisations of hydrophobic monomers include methyl methacrylate (MMA) in ethanol,[32] and 2-hydroxypropyl methacrylate (HPMA) in methanol.[27] In the latter case, *p*(HPMA) is soluble in MeOH, and its polymerisation by Cu^{I} catalysed ATRP has yielded a range of polymers with complex architectures: these include ^{14}C-radiolabelled homopolymers,[33,34] linear and branched copolymers,[35,36] and hyperbranched polydendrons.[37,38] However, polymerisations that undergo phase separation at high monomer conversions, leading to the formation of colloidal structures, is a phenomenon currently gaining significant interest. Through careful selection of the solvent, a polymerisation can be initiated within a solvent environment that is good for the growing polymer chains, but which progressively changes to a poor solvent environment as the chain lengths increase and the monomer is consumed, eventually leading to aggregation; such reactions have been termed *polymerisation induced self-assembly*, often referred to as the PISA approach. Alcoholic solvents, including MeOH, ethanol and IPA, have been widely used for the polymerisation of styrene and benzyl methacrylate following the PISA approach.[39–46]

2.1.5. Chapter aims

The aim of this chapter was to develop a method of obtaining well-defined hydrophobic homopolymers using RDRP techniques that could later be utilised to give the hydrophobic core functionality of amphiphilic polymeric nanoparticles. Given the success of the polymerisations of *n*BuMA and MMA in IPA and ethanol, respectively, one aim of the current research was to investigate their polymerisations in anhydrous MeOH – a well-known anti-solvent for both *p*(*n*BuMA) and *p*(MMA). Comparisons between ATRP and RAFT techniques were to be made, and the behaviour of the polymers in the methanolic environment were to be assessed by studying their cloud-point temperatures (upper critical solution temperature).

2.2. Solubility of *p*(*n*BuMA) in MeOH and cloud point measurements

As previously stated, MeOH is an anti-solvent for *p*(*n*BuMA), often used for purification by means of precipitation to remove residual monomer, initiator and catalytic residues. However, an interesting observation was noted when attempting to

dissolve *p*(*n*BuMA) (M_n = 13 570 g mol^{-1}; 1wt %) in MeOH: complete dissolution was achieved when heated to temperatures approaching the boiling point of the solvent, producing a clear solution which became turbid when cooled to ambient temperature.

Repeating the heating cycle in MeOH-d_4 enabled the study of this behaviour using nuclear magnetic resonance (NMR) spectroscopy: ^{1}H-NMR experiments were performed at 60 °C and 25 °C, and the obtained spectra were analysed and compared (Figure 2.1). The experiment performed at 60 °C produced a well-resolved NMR spectrum that integrated well and provided an excellent assignment of the polymer structure. Whereas, the experiment performed after cooling to 25 °C generated a very weak spectrum; an expansion of the regions between 0.50-2.00 ppm and 3.50-4.25 ppm provided a clear indication of the presence of polymer resonances after cooling, suggesting residual solubility of the sample after the heating cycle (Figure A1, Appendix). As expected, a change in the chemical shift of the water resonance was observed due to the varying degree of hydrogen bonding: this is weaker at the higher temperature, meaning the protons are more shielded and therefore resonate with a lower chemical shift.

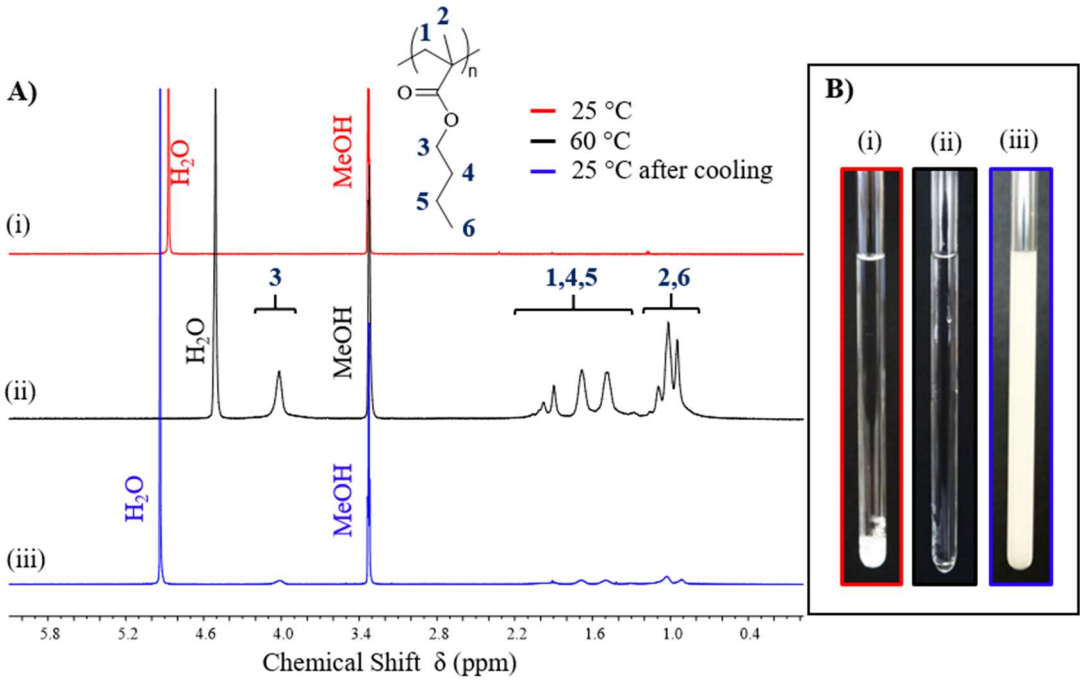

Figure 2.1. Studies of *p*(*n*BuMA) solubility in MeOH-d_4. (A) ^{1}H-NMR spectra of (i) *p*(*n*BuMA) at 25 °C before heating, (ii) *p*(*n*BuMA) heated to 60 °C, (iii) *p*(*n*BuMA) after heating and cooling to 25 °C; (B) photographs of *p*(*n*BuMA) within the NMR tubes – (i) at 25 °C prior to heating, (ii) 60 °C, and (iii) after cooling to 25 °C.

The solubility of the *p*(*n*BuMA) sample without heating cycle was also investigated, which simply involved mixing the polymer with MeOH-d_4 at ambient temperature and performing a ^{1}H-NMR experiment at 25 °C. The spectrum obtained showed no appreciable resonances attributed to the polymer, even after significant expansion.

The behaviour of *p*(*n*BuMA) (M_n = 13 570 g mol^{-1}) within the methanolic environment was also assessed by performing cloud point studies; cloud points were obtained by observing the temperatures at which precipitation occurred for various concentrations of the polymer in MeOH. This involved heating the samples within an oil bath until dissolution occurred below the boiling point of the solvent, after which the heating element was switched off to allow the samples to cool before noting the cloud point temperature as the onset of visible turbidity. Measurements were recorded in triplicate by repeating the heating cycle three times. Initially, anhydrous MeOH was utilised (stated <0.005 % H_2O) and cloud points were observed for polymer solutions up to 5 wt% *p*(*n*BuMA) across a wide range of temperatures (47.5 – 64.7 °C) with excellent reproducibility (Figure 2.2; Table A1, Appendix); a clear trend can be seen whereby cloud point temperatures increased as the concentration of the polymer increased.

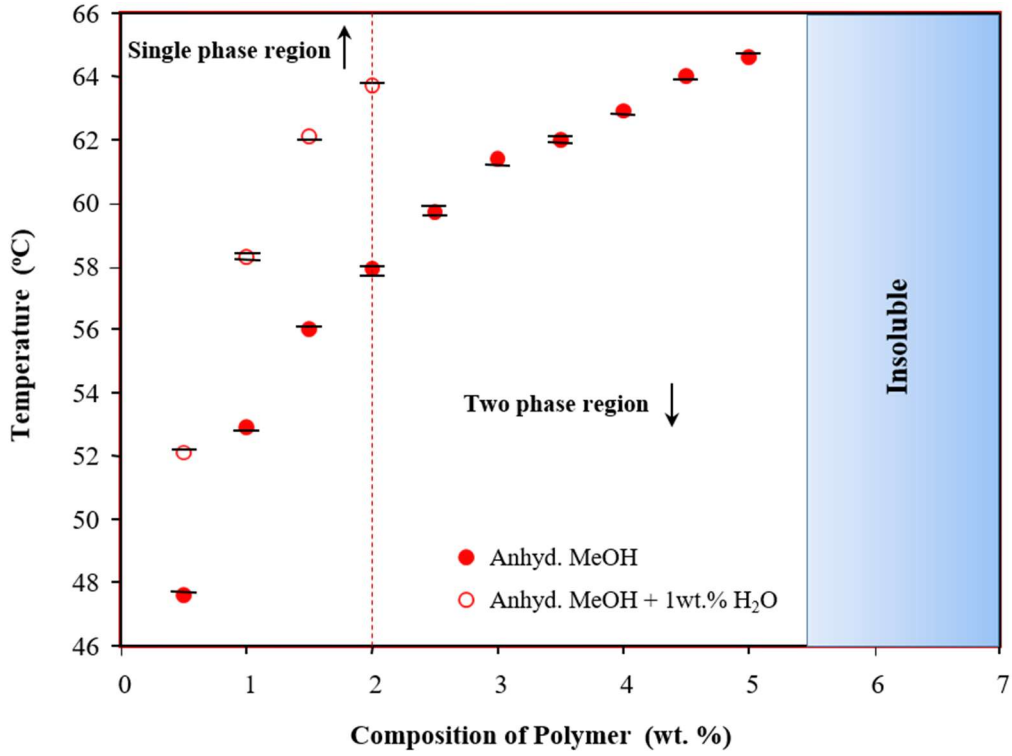

Figure 2.2. Cloud point behaviour for *p*(*n*BuMA) in MeOH with varying water content within the organic solvent. Maximum *p*(*n*BuMA) solubility in MeOH-H_2) (1 wt%) shown by red dashed line. Asymmetric error bars shown.

When analytical grade MeOH (stated <0.05 % H_2O) was utilised, a maximum polymer concentration that achieved complete dissolution decreased to 4.5 wt % (cloud point = 64.1 °C) (Table A1 and Figure A2, Appendix), with a further decrease to 2 wt% (cloud point = 63.7 °C) when the water content was increased to 1 wt% through controlled water addition to anhydrous MeOH (Figure 2.2). Similar trends were observed for both studies, and when comparing data obtained in anhydrous MeOH and MeOH (+ 1 wt% H_2O), an average increase of 5.5 °C was seen for the cloud point temperatures in the aqueous solvent (Figure 2.2).

2.3. ATRP of *n*BuMA in anhydrous MeOH at elevated temperature

Despite the low concentration of *p*(*n*BuMA) that was observed to undergo UCST behaviour in MeOH, the homopolymerisation of *n*BuMA was performed under conventional copper-catalysed (Cu^ICl) ATRP conditions at 50 wt% in anhydrous MeOH at 60 °C, using the bidentate ligand 2,2-bipyridine (bpy), and the commercially available initiator ethyl α-bromoisobutyrate (Scheme 2.3). Initially, number average degrees of polymerisation (DP_n) of 60, 80 and 100 monomer units were targeted (Table 2.1). The polymerisations appeared to progress homogeneously, with the characteristic dark brown opaque colour of the Cu^ICl/bpy catalytic system evident throughout (Figure 2.3.i); no precipitate was observed, even when high monomer conversions were achieved. However, upon cooling the reactions precipitated as the polymer solution passed through the cloud point temperature. Initially, this was difficult to assess because of the strong, opaque colour of the reaction medium, but was more easily observed after deliberate poisoning of the catalytic system with air (Figure 2.3.ii).

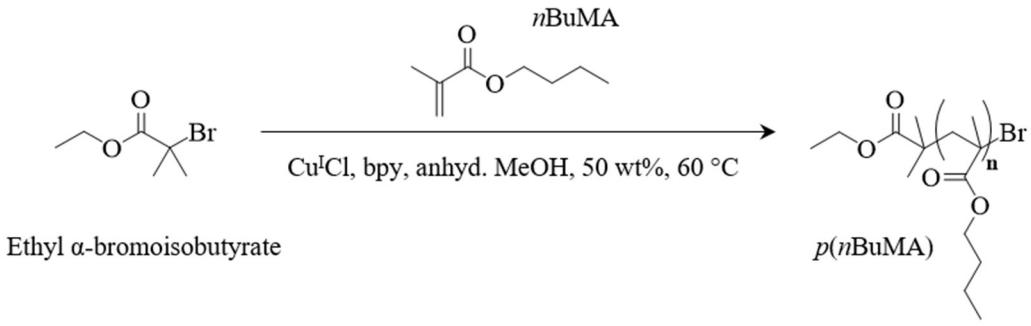

Scheme 2.3. Copper-catalysed ATRP of *n*BuMA in anhydrous MeOH at 60 °C.

Table 2.1. Cu-catalysed methanolic ATRP of *n*BuMA at 60 °C

Target[a] DP_n	Conversion [actual DP_n]	Time (h)	M_n theory[b]	Triple-detection GPC[c] (THF) M_n (g mol^{-1})	M_w (g mol^{-1})	Đ
60	99 % [59]	55	8 640	13 570	13 950	1.03
80	96 % [77]	55	11 120	16 700	17 010	1.02
100[d]	95 % [95]	79	13 700	19 690	21 310	1.03
100[d]	93 % [93]	25	13 420	21 830	22 830	1.05
150	94 % [141]	53	20 250	26 680	27 650	1.04
200	87 % [174]	46	24 940	30 150	33 240	1.10
300	90 % [270]	72	38 590	52 130	57 260	1.10
400	74 % [296]	100	42 290	59 200	64 500	1.09
500	66 % [330]	235	47 120	55 540	61 950	1.12
1000	50 % [500]	648	71 300	75 880	85 500	1.13
p(styrene) Std.[e]	---	---	9 200[e]	9 310	9 620	1.03

[a] Target DP_n calculated as [*n*BuMA]/[initiator]. [b] Theoretical M_n calculated as (target DP_n x actual conversion achieved and includes initiator residue. [c] Triple-detection GPC utilising THF eluent and d*n*/d*c* = 0.0762 mL g^{-1} (averaged across 18 samples; Table A2, Appendix). [d] Repeat syntheses of $p(n\text{BuMA})_{100}$. [e] *p*(styrene) GPC calibration standard (Polymer Laboratories Ltd).

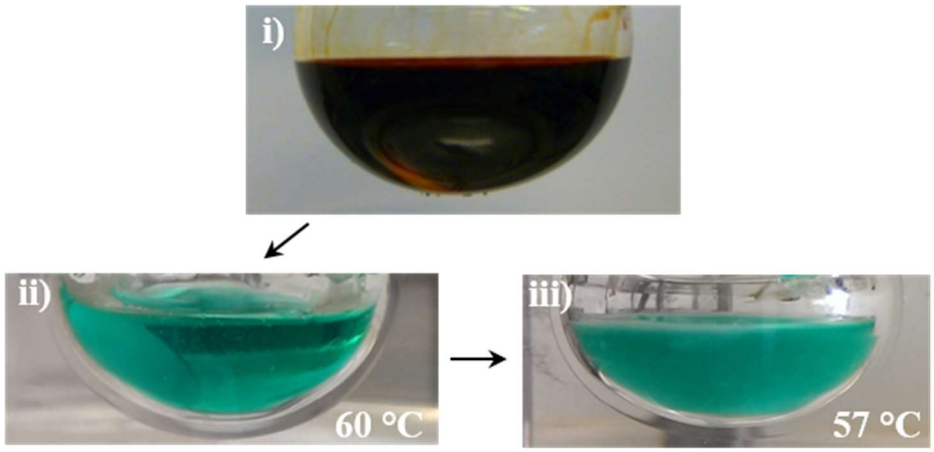

Figure 2.3. Photographs of the methanolic polymerisation of *n*BuMA at 60 °C showing (i) the strong brown catalyst complex during polymerisation, (ii) the homogeneous polymerisation at 60 °C after careful exposure to oxygen, and (iii) precipitation of *p*(*n*BuMA) during cooling (57 °C).

Polymerisations were allowed to reach high conversions before the careful addition of air to the stirred reaction which led to oxidation of the Cu^{I} catalyst and the formation of a transparent green, homogenous solution at 60 °C (Figure 2.3.ii). Precipitation was readily observed upon cooling to 57 °C (Figure 2.3.iii); this is highly surprising given the concentration of the polymer (50 wt %) within the polymerisation and the observed inability to solvate the powdered polymer in anhydrous MeOH at concentrations above 5 wt%. Conveniently, the supernatant formed after the precipitation and sedimentation of the polymers was discarded to remove the vast majority of the catalytic system. After dissolving in THF, the polymers were purified further by passing through a neutral alumina column (using THF as eluent) to remove residual catalyst, and precipitated into cold methanol to give a white solid. In all cases, the polymerisations targeting a DP_n of 60-100 monomer units reached high conversions (>95 %) and analysis by triple detection gel permeation chromatography (GPC) showed low dispersity polymers ($Đ < 1.05$) with number average molecular weight (M_n) values ranging from 13,570 - 21,830 g mol^{-1}; 1.44-1.63 fold higher than theoretical values (Table 2.1., Figure 2.4.).

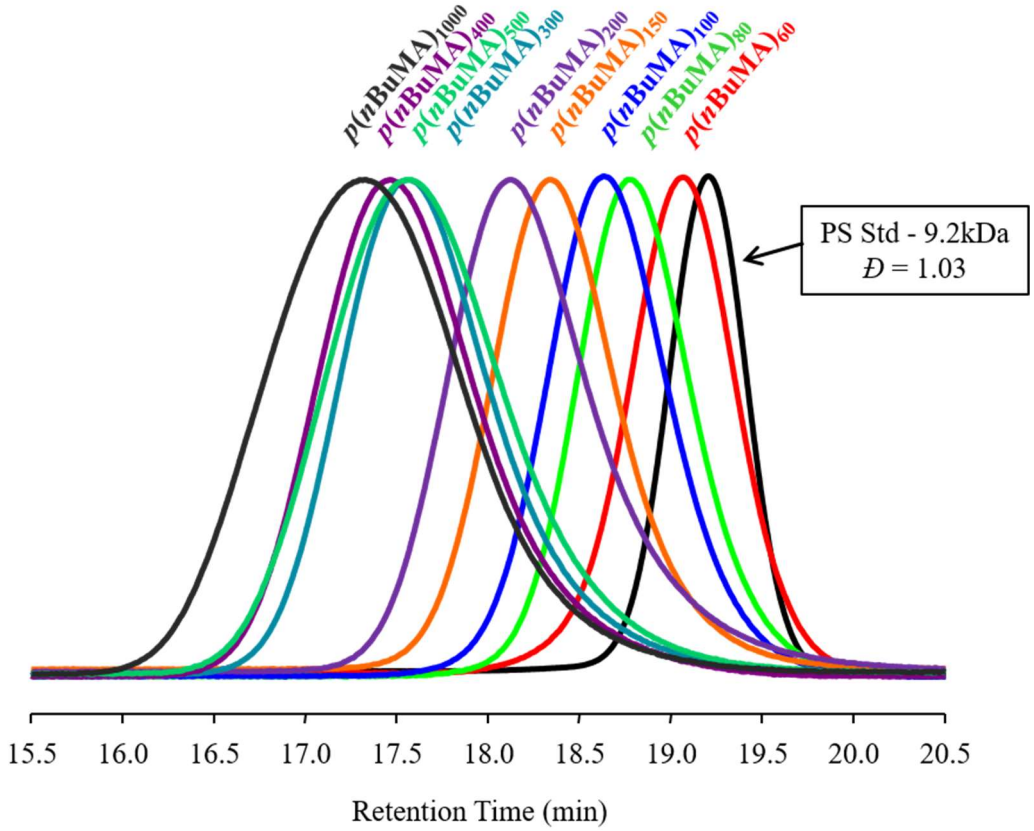

Figure 2.4. GPC chromatograms (RI) showing *p*(*n*BuMA) molecular weight distributions across targeted DP_n = 60-1000 monomer units – *p*(styrene) standard shown for comparison.

Due to the controlled nature of the polymerisations and the very low dispersities obtained, a series of polymerisations with escalating target DP_n values - up to $p(n\text{BuMA})_{1000}$ - were conducted under the same reaction conditions by simply increasing the mass of monomer (Table 2.1). The time required to polymerise the increasingly longer targeted polymer chains increased considerably, with the target $p(n\text{BuMA})_{1000}$ achieving 50 % conversion (effectively a $DP_n = 500$) in 27 days; again, the strong brown colour of the Cu^ICl/bpy catalytic system was evident throughout, and no precipitation was observed. Despite the considerably reduced conversions and very long reaction times, the homogeneous polymerisations remained controlled, yielding polymers with M_n values up to 76,000 g mol^{-1} and low dispersities ($Đ \leq 1.13$). GPC analysis of all recovered polymers gave monomodal and largely symmetrical chromatograms (Figure 2.4), showing no significant loss of propagating chains during the polymerisation. Furthermore, as the targeted polymer chain lengths increased, the deviation from the theoretical M_n values (corrected for actual conversions in Table 2.1.) reduced considerably to a factor of 1.18 for $p(n\text{BuMA})_{500}$ and 1.06 for $p(n\text{BuMA})_{1000}$.

The narrow molecular weight distributions observed for each of the polymerisations strongly indicate that they proceed in a controlled manner, but this was confirmed by performing kinetic studies targeting a $DP_n = 80$ monomer units. The kinetic data was analysed by ^{1}H-NMR spectroscopy and triple detection GPC, and can be seen as a semi-logarithmic plot of $\ln([M]_0/[M])$ *vs.* time (Figure 2.5.A), and as a plot of M_n *vs.* conversion (Figure 2.5.B).

Linear correlations were observed in both plots, meaning that: (i) the rate of the polymerisation follows first order kinetics, where irreversible termination reactions are negligible and the concentration of active species remains constant throughout; and (ii) there is a constant number of chains throughout, all propagating at the same time, where the rate of activation/deactivation ($K_{ATRP} = k_{act}/k_{deact}$) is much greater than the rate of propagation (k_p). Furthermore, the evolution of M_n with conversion was close to the theoretical values, and low dispersities were also observed for each kinetic point ($Đ < 1.10$).

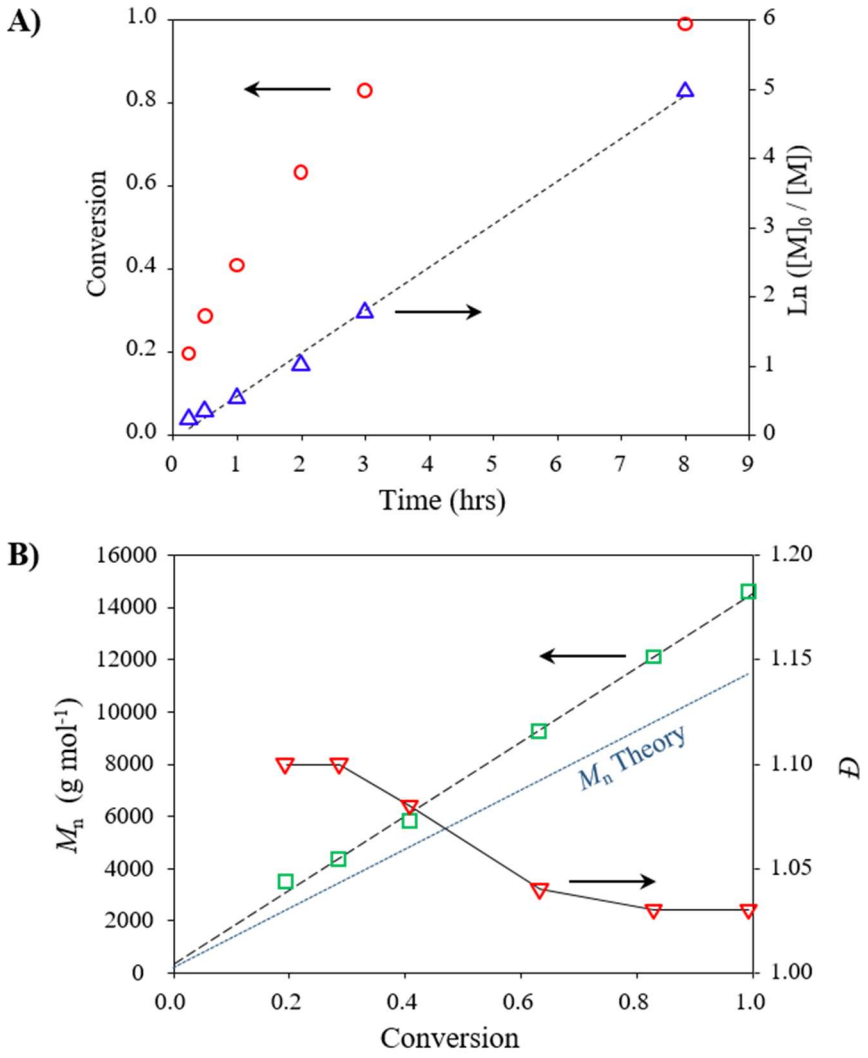

Figure 2.5. Kinetic studies of $p(n\text{BuMA})_{80}$ synthesis: (A) conversion and semi-logarithmic plots *vs.* time; and (B) evolution of M_n and dispersity with conversion.

It is well known that ATRP polymerisations that reach very high conversion are likely to take part in termination reactions either by combination or disproportionation,[47,48] with the latter case more likely when polymerising methacrylate-based monomers. This is because the radicals continue to form by the activation/deactivation process even when the monomer has been fully consumed. Eventually, this will lead to radical-radical coupling (combination) or β-hydrogen abstraction from an active chain (disproportionation); the latter generating a new double bond as well as terminating the radical. Therefore, either case will likely result in broadening of the molecular weight distribution. To determine if such termination reactions occur, a series of four

polymerisations, each with a target DP_n of 60 monomer units, were performed over a period of 14 days in anhydrous MeOH at 60 °C.

^{1}H-NMR analyses of crude samples taken from each reaction flask during the progress of the polymerisations showed that near complete conversion was achieved within the first 24 hours. Each polymerisation was then stopped after different reaction times: the first after 2 days, and the rest after 7 days, 10 days and 14 days. However, GPC analyses showed no appreciable broadening of the molecular weight distribution, or movement of the distribution towards lower retention times (Figure 2.6; Table A3, Appendix); instead, the GPC (RI) traces overlaid almost perfectly. These results rule out termination by combination, but whether disproportionation has taken place without the new vinyl functionality then taking part within a chain growth reaction is difficult to ascertain without any degree of uncertainty.

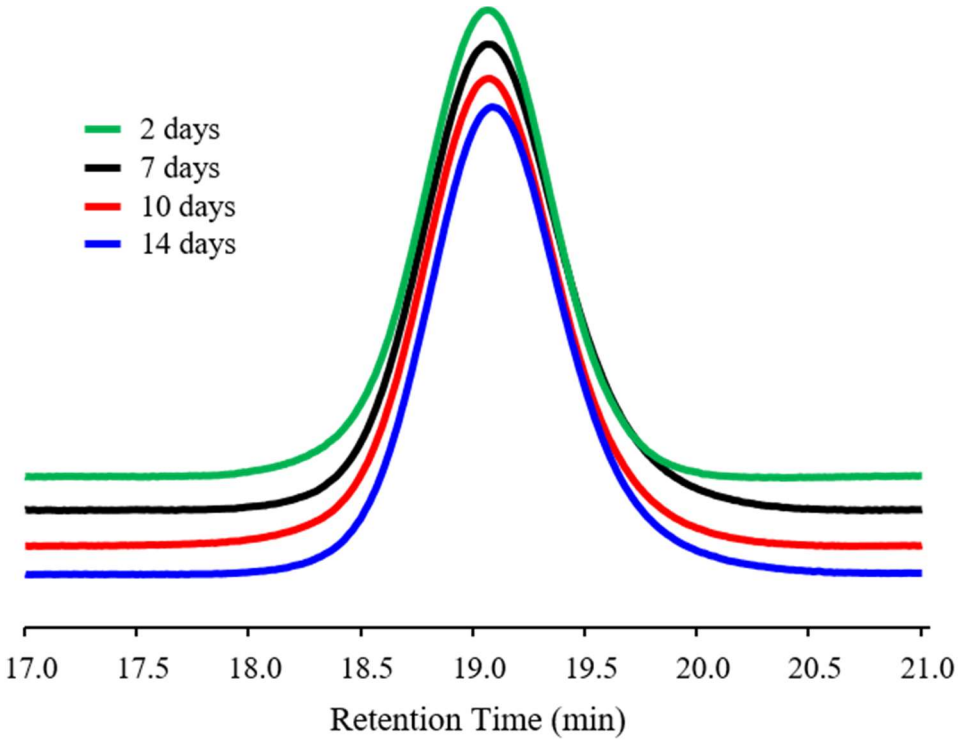

Figure 2.6. GPC (RI) chromatographic overlays of *p*(*n*BuMA)$_{60}$ obtained after methanolic ATRP of *n*BuMA at 60 °C for extended periods of time: after 2 days (green solid line), 7 days (black solid line), 10 days (red solid line), and 14 days (blue solid line).

2.4. Contribution of monomer co-solvency within the methanolic ATRP

The impact of co-solvency from unreacted monomer was studied by determining the cloud points of the purified products of the targeted $p(n\text{BuMA})_{60}$, $p(n\text{BuMA})_{200}$ and $p(n\text{BuMA})_{300}$ polymerisations in MeOH with varying concentrations of *n*BuMA monomer. MeOH-polymer mixtures (50 wt% $p(n\text{BuMA})_x$) were prepared and subjected to a heating cycle prior to the incremental addition of more *n*BuMA monomer and further heat cycling. Once dissolution was achieved below the boiling point of the solvent, the heating element was switched off and the cloud point temperatures were recorded upon cooling. The study can be considered from two perspectives: (i) the concentration of added monomer can be viewed as a single time point within a polymerisation, where the polymer present represents the conversion of the polymerisation within the monomer-methanol environment. As such, each cloud point measurement would represent a polymerisation with a subtly different, and systematically increasing, target DP_n (Figure 2.7; Table A4, Appendix); or (ii) the cloud point data may be assessed as the number of polymer repeat units per monomer (unreacted) co-solvent molecule that generates a particular cloud point temperature (Figure 2.8).

As expected, dissolution of the polymers within the methanolic environment (50 wt % composition) in the absence of monomer was not possible; but when introduced to the MeOH-polymer mixtures, the *n*BuMA monomer eventually solvated the polymers and had a considerable effect on the observed cloud point temperatures. The study was initially performed using the targeted $p(n\text{BuMA})_{60}$ which was subjected to continual heat cycles after the incremental (10μL) addition of monomer. As can be seen from Figure 2.7, 50 μL of monomer was required to solvate the polymer, forming a solution that gave a cloud point temperature of 53.6 °C upon cooling; this represents 11 polymer repeat units per co-solvent monomer molecule or, alternatively a model polymerisation conversion of approximately 92 % for a targeted DP_n = 65 *n*BuMA units (calculated as (1-[(60/11)/((60/11) + 60)] x 100%). A clear trend was observed, with each further addition of monomer reducing the temperature at which precipitation occurred, resulting in cloud points as low as 24.5 °C for the polymer within the monomer-rich environment.

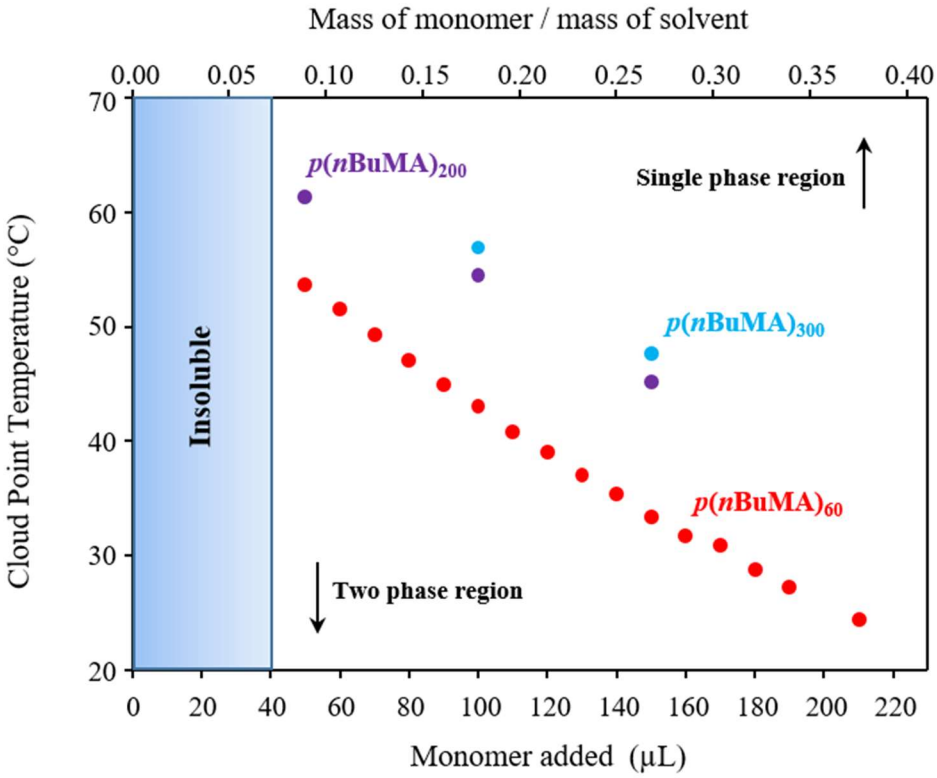

Figure 2.7. Cloud point measurement of $p(n\text{BuMA})_x$ (0.5 g) in anhydrous MeOH (0.5 g) with increasing concentrations of *n*BuMA monomer.

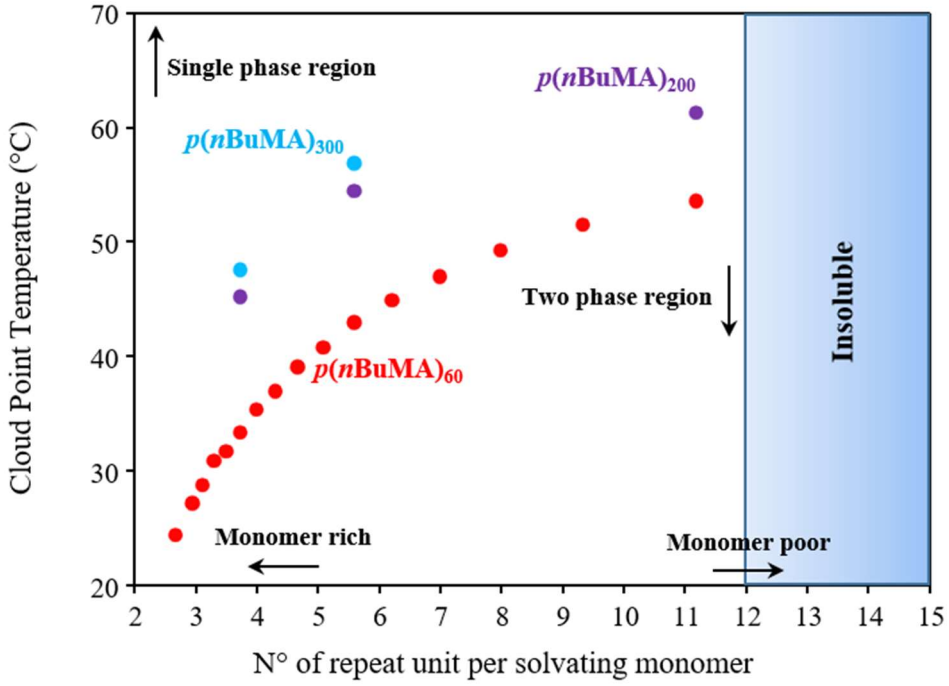

Figure 2.8. Cloud point measurement of $p(n\text{BuMA})_x$ (0.5 g) in anhydrous MeOH (0.5 g) with increasing concentrations of *n*BuMA monomer; presented as a function of the number of repeat unit per solvating monomer.

Interestingly, a noticeable effect was seen when repeating the study using the products of the targeted $p(n\text{BuMA})_{200}$ and $p(n\text{BuMA})_{300}$ polymerisations and comparing the data with that obtained from the targeted $p(n\text{BuMA})_{60}$: the cloud points dramatically increased as the polymer chain lengths increased, even though the mass of $p(n\text{BuMA})_x$ and monomer concentration remained constant. This is highlighted in Figure 2.7, with the total addition of 100μL of monomer resulting in cloud point temperatures of 43.0 °C, 54.5 °C and 56.9 °C, for the solutions of $p(n\text{BuMA})_{60}$, $p(n\text{BuMA})_{200}$ and $p(n\text{BuMA})_{300}$, respectively. This effect is perhaps more clearly observed in Figure 2.8, showing the significant difference in cloud point temperatures even though the number of repeat units per solvating monomer are the same. In addition, $p(n\text{BuMA})_{300}$ could only be induced to show measurable UCST behaviour in monomer rich environments, whilst $p(n\text{BuMA})_{200}$ and $p(n\text{BuMA})_{60}$ both exhibited cloud point behaviour across the range of monomer concentrations studied.

The results of this study highlight the significant co-solvency effect of the *n*BuMA monomer, suggesting that it plays a crucial role in solvating the growing polymer chains in the methanolic environment as the polymerisation progresses; but they also suggest that precipitation will occur at a particular conversion that is dependent on the target DP_n due to the poor solvent environment at high conversions as result of the monomer depletion. This does not explain the high conversions and low dispersities obtained for the homogeneous polymerisations seen in Table 2.1, nor does it explain why the $p(n\text{BuMA})_{60}$ polymerisation was successfully performed for 14 days without precipitation. Clearly, the presence of unreacted *n*BuMA monomer is not the only factor allowing the reaction to proceed with the observed success.

2.5. Cu-catalysed ATRP of *n*BuMA in MeOH at low temperature

The co-solvency studies showed that the *n*BuMA monomer plays a significant role in solvating the polymer within the methanolic environment enabling dissolution at much lower temperatures than our initial reactions, but do not explain how polymerisations progressed to high conversion (*e.g.* targeted $p(n\text{BuMA})_{60}$ conversion = 99%) without observed precipitation. To investigate this further, a series of polymerisations were performed at a temperature of 25 °C, targeting $p(n\text{BuMA})_{60}$, $p(n\text{BuMA})_{100}$ and

$p(n\text{BuMA})_{200}$. It was expected that the polymerisations initiated at low temperature would proceed homogeneously due to the monomer co-solvency effect, but reach a conversion where the monomer-polymer and MeOH-polymer interactions would be overcome by polymer-polymer interactions, leading to precipitation induced phase separation. Surprisingly, this was not the case; all polymerisations proceeded to high conversions (≥ 95%) without observed precipitation, yielding narrow dispersity products ($Đ = 1.03$) (Table 2.2). Furthermore, analysis by triple detection GPC indicated that the targeting of theoretical molecular weights were improved at this lower temperature compared those conducted at 60 °C: $p(n\text{BuMA})_{60}$ deviates from the M_n values by a factor of 1.43; $p(n\text{BuMA})_{100}$ by a factor of 1.19; and $p(n\text{BuMA})_{200}$ by a factor of only 1.08. Also, the GPC chromatograms showed monomodal and symmetrical molecular weight distributions (Figure 2.9).

It is important to note, however, that sampling during a number of the polymerisations at 25 °C did induce precipitation as soon as the hypodermic needle was submerged into the solution; this was easily observed and quickly led to sedimentation of precipitate after stirring was ceased. Consequently, the polymerisations were repeated and left to stir for an extended period of time in order to reach high conversions without precipitation. This also meant that kinetic studies would be very difficult to perform, and were therefore avoided.

Table 2.2. Cu-catalysed methanolic ATRP of *n*BuMA at 25°C

				Triple-detection GPC[c] (THF)		
Target[a] DP_n	Conversion [actual DP_n]	Time (h)	M_n theory[b]	M_n (g mol^{-1})	M_w (g mol^{-1})	Đ
60	95 % [57]	24	8 300	11 810	12 100	1.03
100	97 % [97]	74	13 990	16 660	17 150	1.03
200	97 % [194]	122	27 780	29 960	30 830	1.03

[a] Target DP_n calculated as [*n*BuMA]/[initiator]. [b] Theoretical M_n calculated as (target DP_n x actual conversion achieved and includes initiator residue. [c] Triple-detection GPC utilising THF eluent and d*n*/d*c* = 0.0762 mL g^{-1} (averaged across 18 samples; Table A2, Appendix).

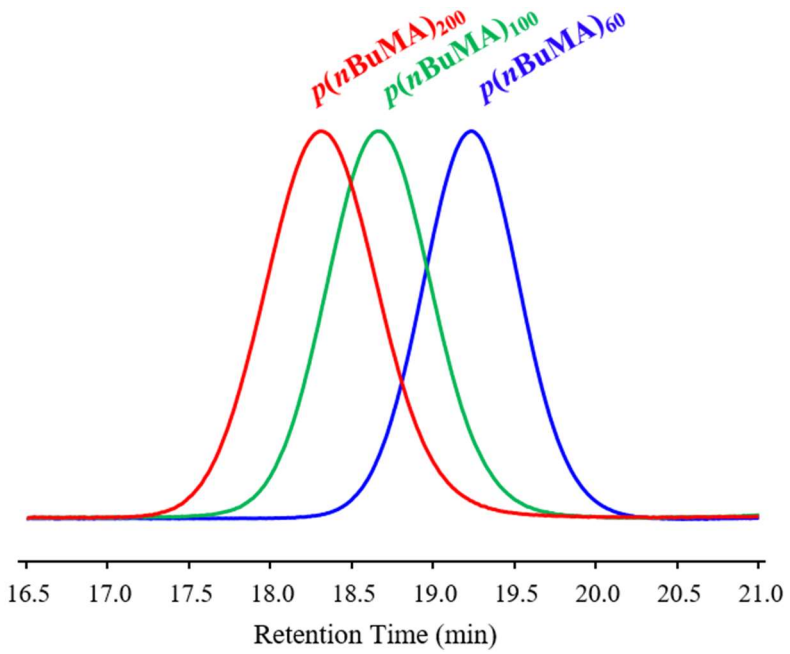

Figure 2.9. GPC chromatograms (RI) showing *p*(*n*BuMA) molecular weight distributions across targeted DP_n = 60 – 200 monomer units; polymerised in anhydrous MeOH at 25 °C.

2.6. Comparative Cu-catalysed ATRP of *n*BuMA in IPA

As already stated, Rannard and coworkers reported the ambient temperature ATRP of *n*BuMA in IPA and IPA/water mixtures, where IPA was selected because it is a theta solvent for the polymer. To compare against the methanolic syntheses described above, a series of polymerisations were, therefore, performed by Cu-catalysed ATRP in IPA at both 60 °C and 25 °C: $p(n\text{BuMA})_{60}$, $p(n\text{BuMA})_{100}$ and $p(n\text{BuMA})_{200}$ were targeted in IPA at 60 °C; and $p(n\text{BuMA})_{60}$ and $p(n\text{BuMA})_{200}$ were targeted in IPA at 25°C (Table 2.3; Figures A3 and A4, Appendix).

The polymerisations at both temperatures proceeded without precipitation, as expected, and achieved high conversions (≥ 97 %) to give low dispersity polymers ($1.14 < Đ < 1.16$). Dispersities were significantly higher than those seen for the products of the methanolic polymerisations (Tables 2.1 and 2.2), but still representative of a well-controlled ATRP. A direct comparison of *p*(*n*BuMA) synthesised at 60 °C within either IPA or MeOH can be seen by overlaying the GPC refractive index (RI) chromatograms (Figure 2.10); the samples of $p(n\text{BuMA})_{60}$, $p(n\text{BuMA})_{100}$ and $p(n\text{BuMA})_{200}$ synthesised in MeOH all displayed molecular weight distributions that were entirely encapsulated within the distributions of the equivalent samples synthesised in IPA, demonstrating the enhanced control in MeOH.

Table 2.3. Cu-catalysed ATRP of *n*BuMA in IPA

Target[a] DP_n	Conversion [actual DP_n]	Time (h)	M_n theory[b]	Triple-detection GPC[c] (THF) M_n (g mol^{-1})	M_w (g mol^{-1})	Đ
60 °C						
60	99 % [59]	47	8 640	11 850	13 500	1.14
100	99 % [99]	68	14 270	17 900	20 740	1.16
200	99 % [198]	68	28 350	33 770	38 900	1.15
25 °C						
60	99 % [59]	68	8 640	14 190	16 400	1.16
200	97 % [194]	100	27 780	32 830	37 980	1.16

[a] Target DP_n calculated as [*n*BuMA]/[initiator]. [b] Theoretical M_n calculated as (target DP_n x actual conversion achieved and includes initiator residue. [c] Triple-detection GPC utilising THF eluent and d*n*/d*c* = 0.0762 mL g^{-1} (averaged across 18 samples; Table A2, Appendix).

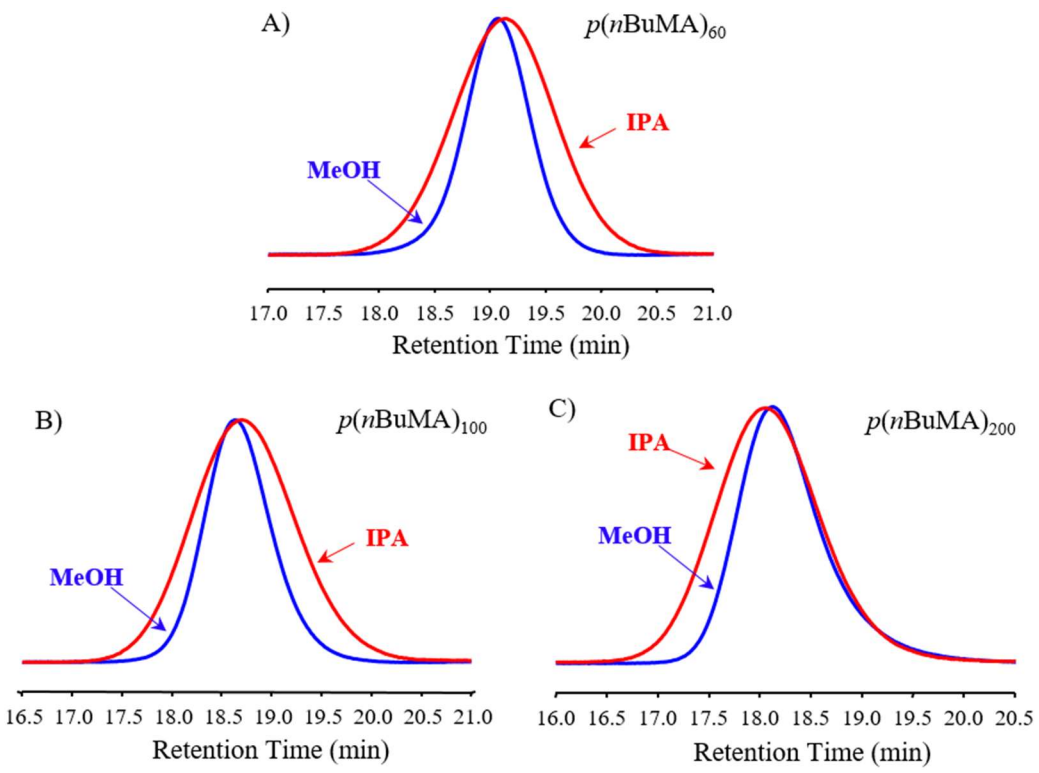

Figure 2.10. GPC (RI) chromatographic overlay comparing the syntheses in MeOH (blue solid line) and IPA (red solid line) for: (A) $p(n\text{BuMA})_{60}$, (B) $p(n\text{BuMA})_{100}$, and (C) $p(n\text{BuMA})_{200}$.

To determine if termination – either by combination or disproportionation – occurs towards the latter stages of the reaction in IPA, a polymerisation targeting a $DP_n = 60$ *n*BuMA monomer units was performed at 60 °C and left to stir for 7 days. Comparisons between the GPC data for $p(n\text{BuMA})_{60}$ obtained after 2 days (99 % conversion) and 7 days (> 99 % conversion) were made (Table A5; Appendix); analysis of the 7 day reaction showed a broadening of the molecular weight distribution towards lower retention times, revealing the presence of higher molecular weight materials (Figure 2.11). This is in direct contrast to the study performed in MeOH (Figure 2.6), where no change in the molecular weight distribution was observed. These results suggest that in comparison to the latter stages of the methanolic polymerisation, the active chain-end functionalities within IPA are more available to take part in termination reactions that lead to an increase in molecular weight. Considering that IPA is a theta solvent for the polymer and MeOH is regarded as an anti-solvent, this is not surprising, and it is reasonable to envisage more densely coiled polymer chains within the methanolic environment that sterically protect the active chain-end functionality as a consequence (Figure 2.12).

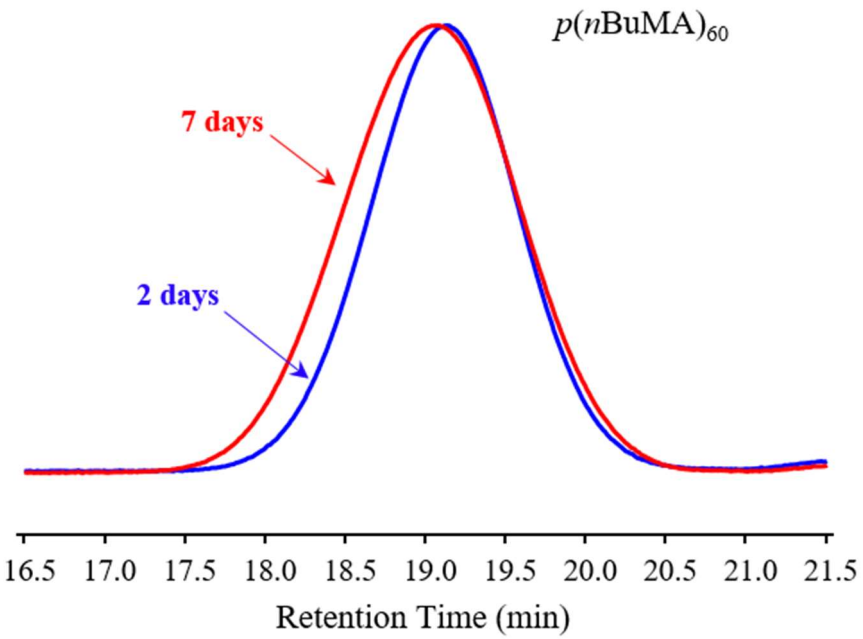

Figure 2.11. GPC (RI) chromatographic overlay of $p(n\text{BuMA})_{60}$ polymerised by ATRP in IPA at 60 °C, over 2 days (blue solid line) and 7 days (red solid line). The extended heating in IPA at 60 °C led to a broadening of molecular weight distribution towards lower retention times.

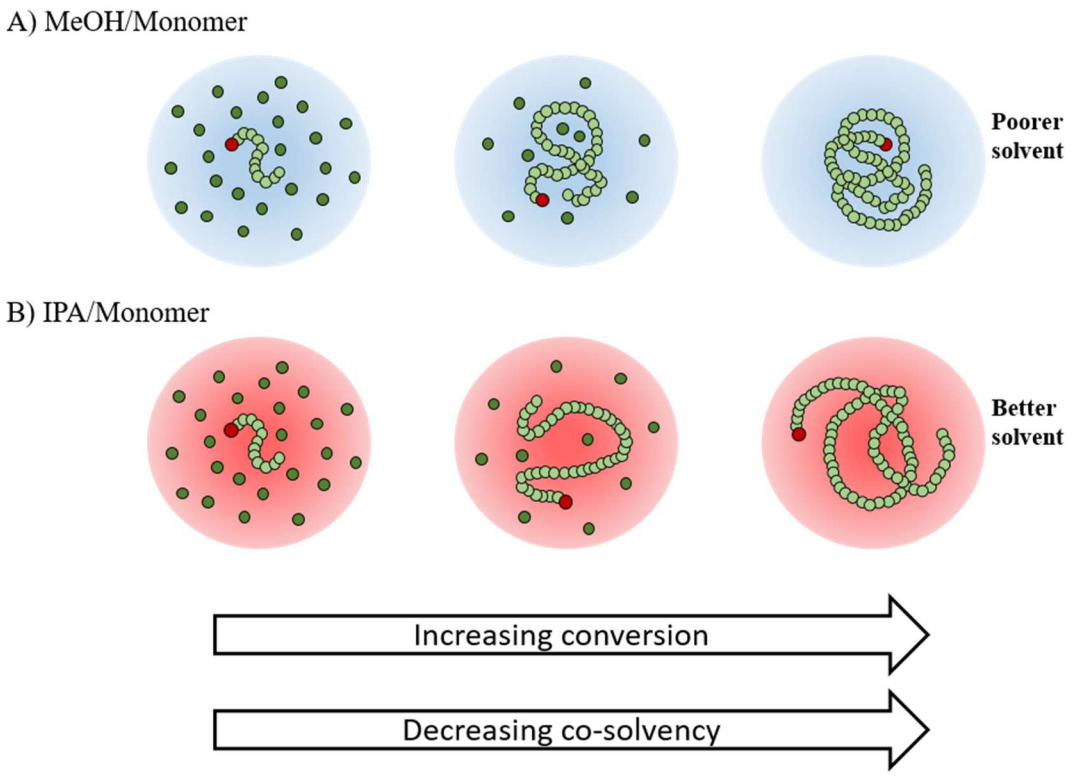

Figure 2.12. Schematic representation of proposed *n*BuMA polymerisation in MeOH and IPA: (A) monomer-MeOH acts as a good solvent for growing oligomers, but larger polymer chains in monomer depleted environments adopt collapsed coils with hidden chain ends; (B) monomer-IPA mixtures act as a good solvent environment and monomer depletion does not generate a poor solvent system at high conversion, leading to more expanded coils and available chain-ends. Key: blue background = MeOH solvent, red background = IPA solvent, dark green spheres represent unreacted *n*BuMA, light green spheres represent reacted *n*BuMA, and red spheres represent active chain-ends.

2.7. Comparative Cu-catalysed ATRP in MeOH using different ligands

As previously described, ATRP is performed *via* a reversible redox process catalysed by a transition metal complex, with those consisting of copper being the most successful. The selection of the ligand, however, is very important as it dictates the kinetics of the polymerisation and the dynamics of exchange between the dormant and active species, both of which are fundamental to its success; for Cu-mediated ATRP, nitrogen-based ligands are often utilised.[49] To investigate the effect of the ligand on the success of the methanolic polymerisation of *n*BuMA, three syntheses of $p(n\text{BuMA})_{60}$ were conducted in MeOH at 60 °C using $Cu^{I}Cl$; selection of the ligand varied from two equivalents of bpy, to one equivalent of

tris[2-(dimethylamino)ethyl]amine (Me6TREN) and N,N,N',N',N''-pentamethyldiethylenetriamine (PMDETA).

All polymerisations proceeded to relatively high conversions, but those utilising Me_6TREN and PMDETA produced polymers with asymmetric molecular weight distributions (Figure 2.13) and much higher M_n and M_w values when compared to the polymerisation utilising bpy ($M_{nPMDETA}$ = 20 360 g mol^{-1}; $M_{nME6TREN}$ = 38 550 g mol^{-1}) (Table A6, Appendix). This suggests an increased initiating efficiency for the Cu-bpy catalytic system under these reaction conditions.

As a qualitative measure, a small study was performed to assess the solubility of each of the catalytic systems within bulk *n*BuMA an *n*BuMA-MeOH mixtures. Upon visual observation, the Cu-bpy complex was insoluble in the bulk monomer at ambient temperature, whereas the Cu-Me_6TREN and Cu-PMDETA complexes existed in a swollen state and were thus sparingly soluble (Figure 2.14). The addition of MeOH enhanced the solubility of the bpy and PMDETA complexes, but decreased the solubility of the Me_6TREN complex (Figure 2.15). Whether this difference in solubility plays a role in the monomer-depleted or monomer-rich stages of the polymerisation is unclear.

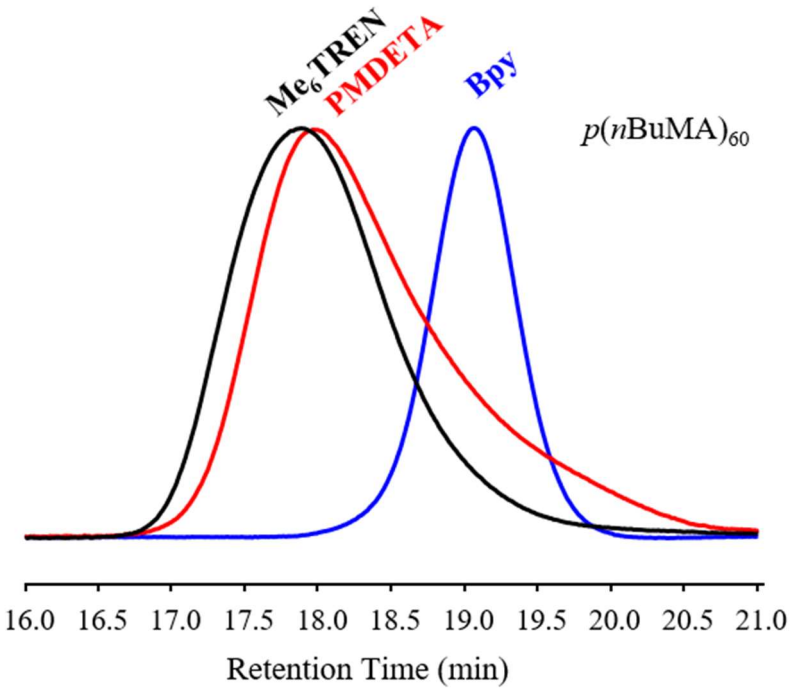

Figure 2.13. Syntheses of $p(n\text{BuMA})_{60}$ in MeOH using different catalytic systems: bpy (blue solid line), PMDETA (red solid line) and Me_6TREN (black solid line).

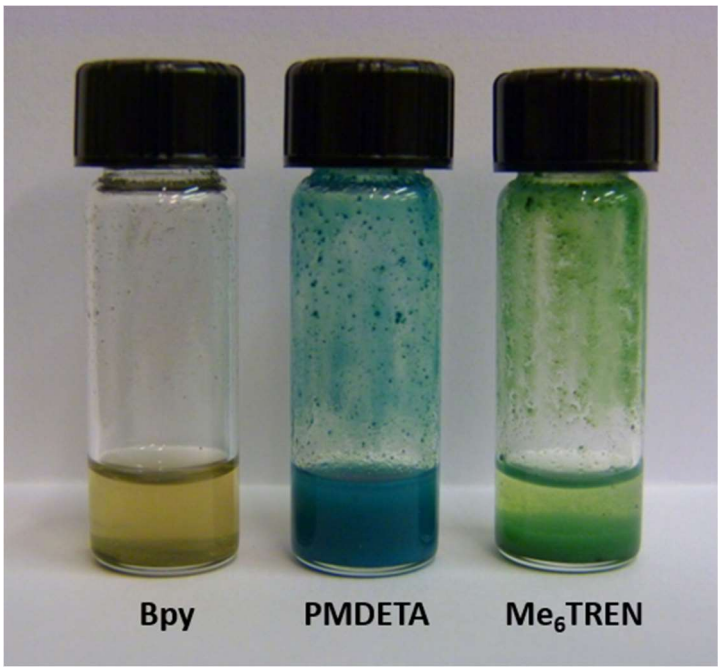

Figure 2.14. Photograph showing the solubility of the ligated $Cu^{I}Cl$ catalytic systems in bulk *n*BuMA.

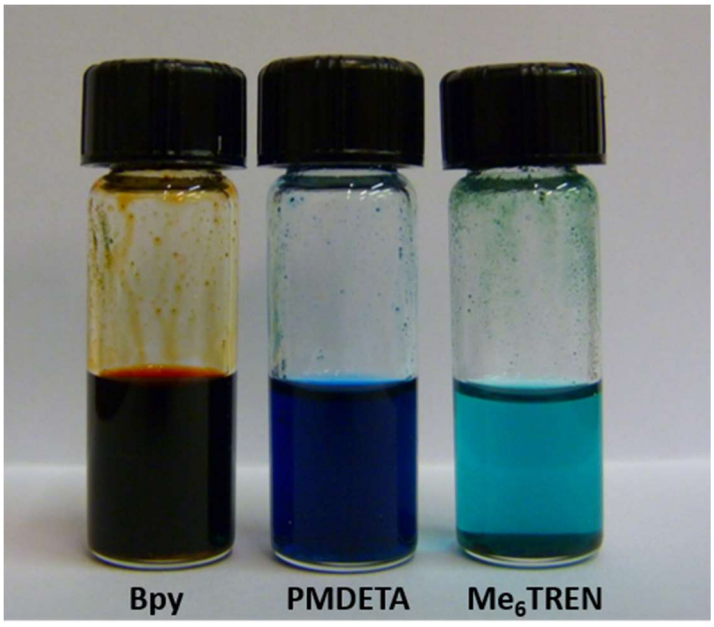

Figure 2.15. Photograph showing the solubility of the ligated $Cu^{I}Cl$ catalytic systems within the monomer-MeOH environment.

There have been many conflicting reports detailing the exact mechanism of ATRP in polar and protic solvents, where the choice of ligand is highly relevant; this ultimately dictates the rate of disproportionation and comproportionation between Cu^0, Cu^I and Cu^{II}, which forms the basis of the debate over whether such polymerisations proceed by supplemental activator and reducing agent ATRP (SARA ATRP) or single-electron transfer living radical polymerisation (SET-LRP). In SARA ATRP, disproportionation of the Cu^I catalytic complex is negligible, thus Cu^I is the major activator and Cu^{II} the deactivator; Cu^0 primarily acts as a supplemental activator and a reducing agent of excess Cu^{II} through comproportionation.[50,51] Whereas in SET-LRP, Cu^0 is the exclusive activator and Cu^{II} is the major deactivator; Cu^I is unable to activate the polymerisation because it undergoes instant disproportionation to Cu^0 and Cu^{II}, and comproportionation is negligible.[52] The use of Me_6TREN as a ligand has been widely reported for SET-LRP because it rapidly induces disproportionation of copper complexes in a variety of solvents,[53–55] including MeOH.[56–59] The studies of disproportionation of Cu^I halides under varying ligand and solvent conditions were recently published by Percec and coworkers, which included the formation of insoluble *nascent* Cu^0 nanoparticles after disproportionation of Cu^IBr-bpy complexes in MeOH;[60] however, it is important to note that this was observed using a 1:1 molar ratio of Cu^IBr:bpy, whereas classical ATRP utilises a 1:2 molar ratio.

To address this, another study was performed to investigate the potential for Cu^0 formation within the successful Cu^ICl:bpy conditions reported here; this involved a qualitative comparison of observed Cu^0 formation between Cu^ICl:bpy mixtures in MeOH at ambient temperature using either 1:1 or 1:2 molar ratios. The samples were prepared in anhydrous MeOH and compared after 90 minutes (Figure 2.16). Significantly less solid material was evident when utilising the 1:2 catalyst ratio, meaning that less disproportionation had taken place. This suggests that under the reaction conditions reported herein using a 1:2 catalyst ratio, the polymerisation proceeds by a mechanism that is analogous to SARA ATRP. Furthermore, the formation of solid material after the addition of MeOH to the Cu^ICl:Me_6TREN complex (Figure 2.15) may suggest the polymerisation conducted using this catalytic system proceeds by SET-LRP. However, no characterisation studies have been performed to confirm either mechanism, therefore the nature of the polymerisations reported throughout this thesis are referred to as conventional ATRP.

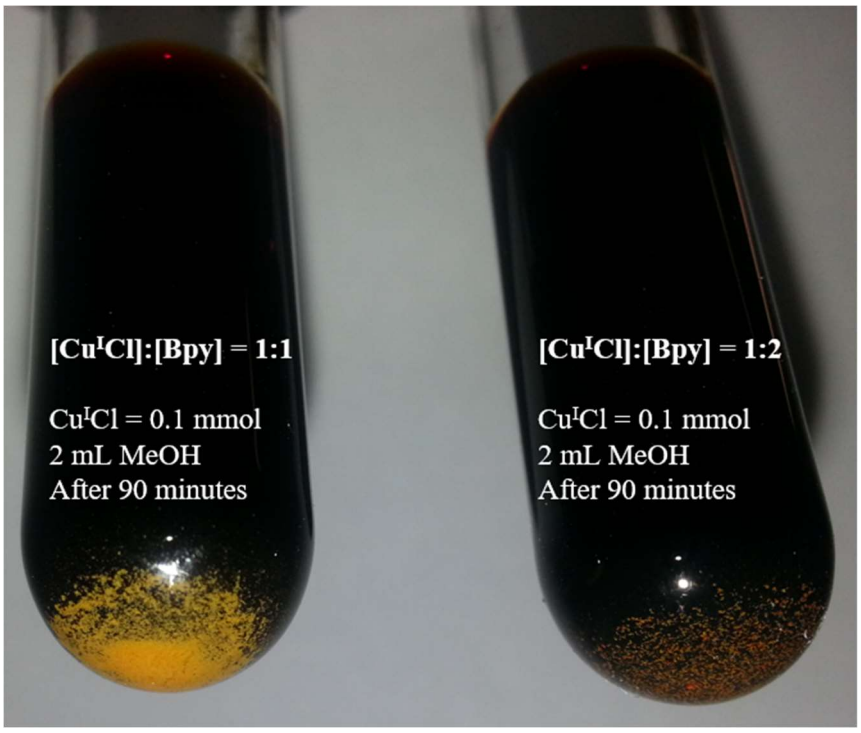

Figure 2.16. Photographic qualitative evaluation of $Cu^{I}Cl$:bpy catalytic systems in MeOH showing variation in Cu^{0} formation by disproportionation at a 1:1 ratio (left) and 1:2 ratio (right) after 90 minutes at ambient temperature.

2.8. Comparative RAFT polymerisation of *n*BuMA in MeOH at 60 °C

The successful polymerisation of *n*BuMA in MeOH by ATRP seems to be significantly enhanced by the co-solvency effect of the unreacted monomer, allowing reactions to proceed to high conversion without observable precipitation to yield low dispersity polymers. However, it also seems that its success is heavily dependent on the ligand chemistry utilised to complex the $Cu^{I}Cl$; those ligated with bpy exhibited enhanced initiating efficiencies and control over the polymerisation.

To investigate further, RAFT was utilised to polymerise *n*BuMA in anhydrous MeOH at 60 °C to provide comparative data to that obtained by ATRP. Polymerisations were conducted at 50 wt% with respect to monomer, utilising 4,4'-azobis(4-cyanopentanoic acid) (ACVA) as the free radical initiator, and 2-cyano-2-propyl benzodithioate (CPBD) as the chain transfer agent (CTA) (Scheme 2.4); both ACVA and CPBD were chosen based on their reported use in aqueous and alcoholic solvents to polymerise methacrylate-based monomers.[61,62]

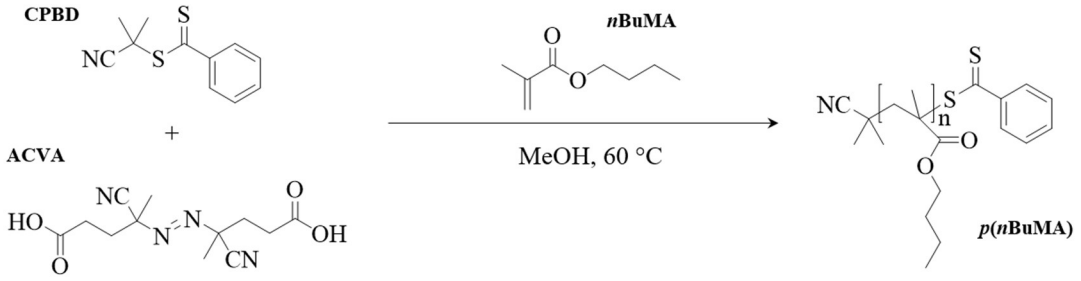

Scheme 2.4. Reaction scheme for the RAFT polymerisation of *n*BuMA in anhydrous MeOH at 60 °C, utilising 4,4'-azobis(4-cyanopentanoic acid) (ACVA) and 2-cyano-2-propyl benzodithioate (CPBD).

It's important to note that due to the high temperature required to thermally decompose the ACVA initiator, polymerisations by RAFT at 25 °C were not possible.

Surprisingly, the polymerisations by RAFT targeting a DP_n = 60-1000 monomer units achieved high conversions (as high as 95 %) and yielded low dispersity polymers ($Đ < 1.12$). Analysis by triple detection GPC showed monomodal and symmetrical molecular weight distributions (Figure 2.17) with M_n values ranging between 9,300 - 107,950 g mol^{-1}, and also highlighted improved M_n control by RAFT compared to ATRP (Table 2.4).

In all cases, the RAFT polymerisations proceeded to high conversions over much shorter reaction times than 'equivalent' ATRP conditions. This is most significant for the targeted $p(n\text{BuMA})_{1000}$, achieving 80 % conversion (*i.e.* $p(n\text{BuMA})_{800}$) in 44 hours; in contrast, the equivalent polymerisation by ATRP achieved 50 % conversion (*i.e.* $p(n\text{BuMA})_{500}$) in 27 days. These results suggest that the ATRP mechanism is not critical to the methanolic polymerisation and, indeed, leads to a slower rate of propagation.

The homogeneity of the RAFT polymerisations could be easily monitored due to the transparent pink solution that is characteristic of this technique. In doing so, this revealed that homogeneous conditions were maintained through to high conversion when targeting $p(n\text{BuMA})_{60}$.

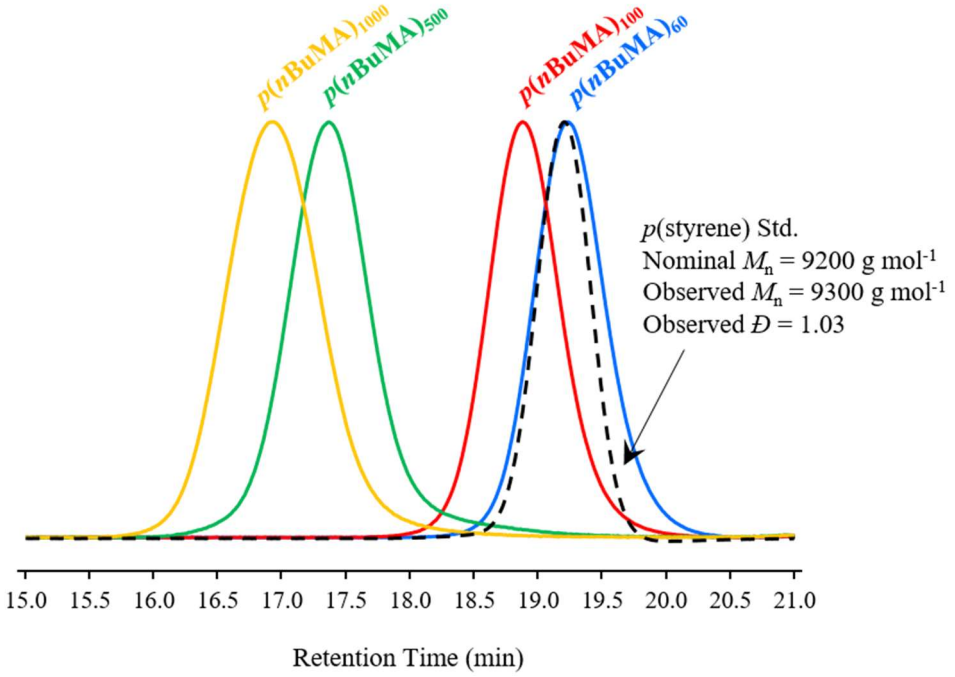

Figure 2.17. GPC (RI) chromatographic overlay of *p*(*n*BuMA) syntheses in MeOH by RAFT.

Table 2.4. Methanolic RAFT and Cu-catalysed ATRP of *n*BuMA at 60 °C

Target[a] DP_n	Conv. [actual DP_n]	Time (h)	M_n theory[b]	Triple-detection GPC[c] (THF) M_n (g mol^{-1})	M_w (g mol^{-1})	Đ
RAFT						
60	95 % [57]	24	8 100	9 300	10 350	1.12
100	91 % [91]	24	12 950	14 550	15 650	1.08
500	93 % [465]	44	66 150	64 750	70 550	1.09
1000	80 % [800]	44	113 750	107 950	113 950	1.06
ATRP						
60	99 % [59]	55	8 650	13 600	13 950	1.03
100	95 % [95]	79	13 700	19 700	20 300	1.03
500	66 % [330]	235	47 100	55 550	61 950	1.12
1000	50 % [500]	648	71 300	75 900	85 500	1.13
p(styrene) Std.[d]	---	---	9 200	9 300	9 600	1.03

[a] Target DP_n calculated as [*n*BuMA]/[initiator or CTA]. [b] Theoretical M_n includes initiator/CTA residues and was calculated as [(target DP_n x 142.2 g mol^{-1}) x experimental monomer conversion]. [c] Triple-detection GPC utilising THF eluent and d*n*/d*c* = 0.0762 mL g^{-1} (averaged across 18 samples; Table A2, Appendix). [d] *p*(styrene) GPC calibration standard (Malvern instruments Ltd.)

However, when targeting a $DP_n \geq 100$ monomer units, polymerisations proceeded homogeneously up to monomer conversions < 90 % (Figure 2.18.i), after which the reaction medium became turbid (Figure 2.18.ii). If stirring was ceased whilst maintaining reaction temperature at 60 °C, phase separation occurred resulting in a clear polymer-rich phase beneath a MeOH-rich turbid phase (Figure 2.18.iii): determined by ^{1}H-NMR (Figure 2.19). Allowing the reaction medium to cool below its cloud point temperature resulted in the precipitation of the polymer from the polymer-rich phase (Figure 2.18.iv). And finally, complete phase separation was achieved after leaving the reaction medium to stand at ambient temperature overnight; evident by the clear MeOH phase (Figure 2.18.v).

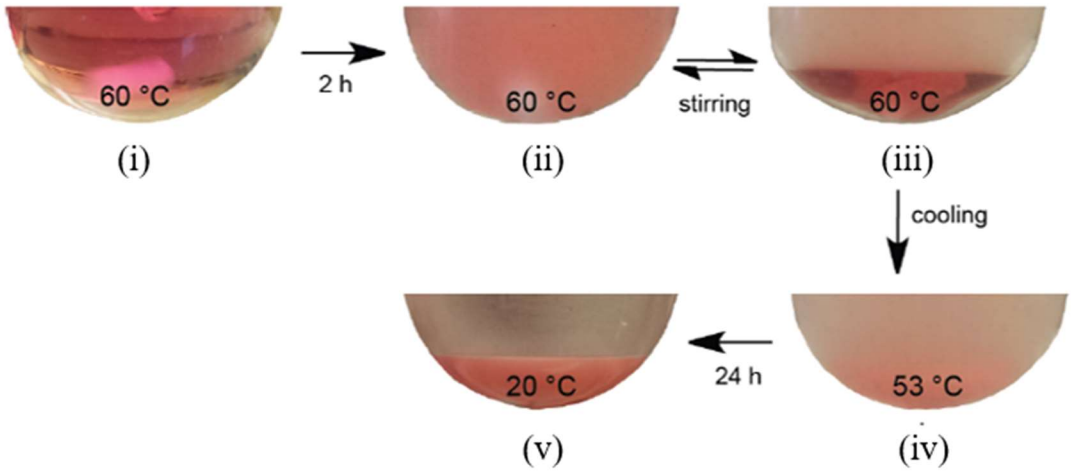

Figure 2.18. Photographs of a RAFT polymerisations showing: (i) homogeneous polymerisation at 60 °C at low conversion; (ii) onset of turbidity as high conversions; (iii) formation of layered phases when stirring is ceased, leaving a MeOH-rich phase (top) and a polymer-rich phase (bottom) above the cloud point temperature; (iv) precipitation of the polymer upon cooling below the cloud point temperature (image taken at 53 °C); and (v) complete phase separation and sedimentation at ambient temperature.

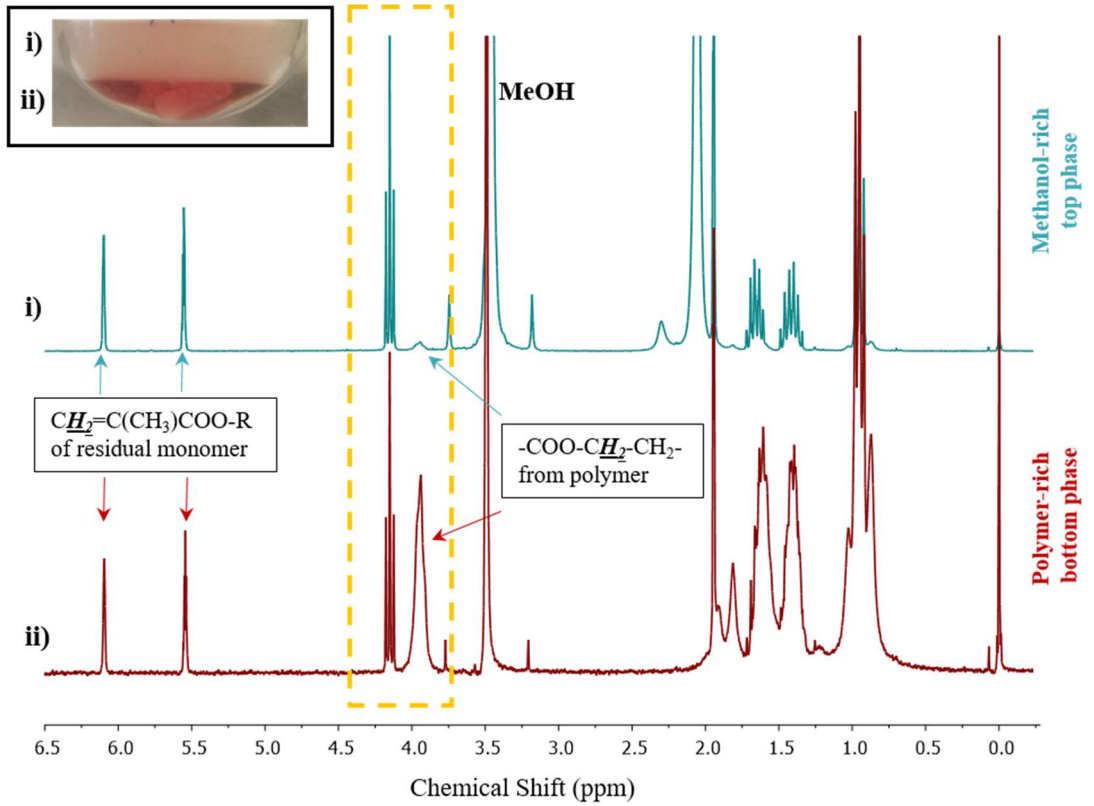

Figure 2.19. ^{1}H-NMR ($CDCl_3$) spectra of the biphasic system (normalised w.r.t. monomer residues) observed during the RAFT polymerisation of *n*BuMA in anhydrous MeOH at 60 °C: (i) MeOH-rich phase (top) showing resonances attributed to residual *n*BuMA monomer and weak signals attributed to *p*(*n*BuMA) (yellow dotted box); and (ii) polymer-rich phase (bottom) showing resonances attributed to residual *n*BuMA monomer, and strong signals attributed to *p*(*n*BuMA) (yellow dotted box). Inset: photograph of the biphasic system when stirring had ceased, from which samples were taken for analysis.

A significant increase in the rate of polymerisation was expected with the onset of turbidity within the RAFT polymerisation, which would indicate that the reaction was proceeding under pseudo-dispersion conditions, as seen in polymerisation-induced self-assembly studies: this is attributed to compartmentalisation leading to a relatively high local concentration of monomer and thus rate enhancement. To determine this, kinetic studies were performed - targeting $p(n\text{BuMA})_{100}$ and $p(n\text{BuMA})_{1000}$ (Figures 2.20 and 2.21 respectively) - through the simultaneous reaction of multiple vials containing monomer/CTA/initiator/MeOH stock solutions; this avoided perturbation of the reaction media when sampling that could potentially induce precipitation. Instead, each vial was used to represent a separate time-point within the overall polymerisation.

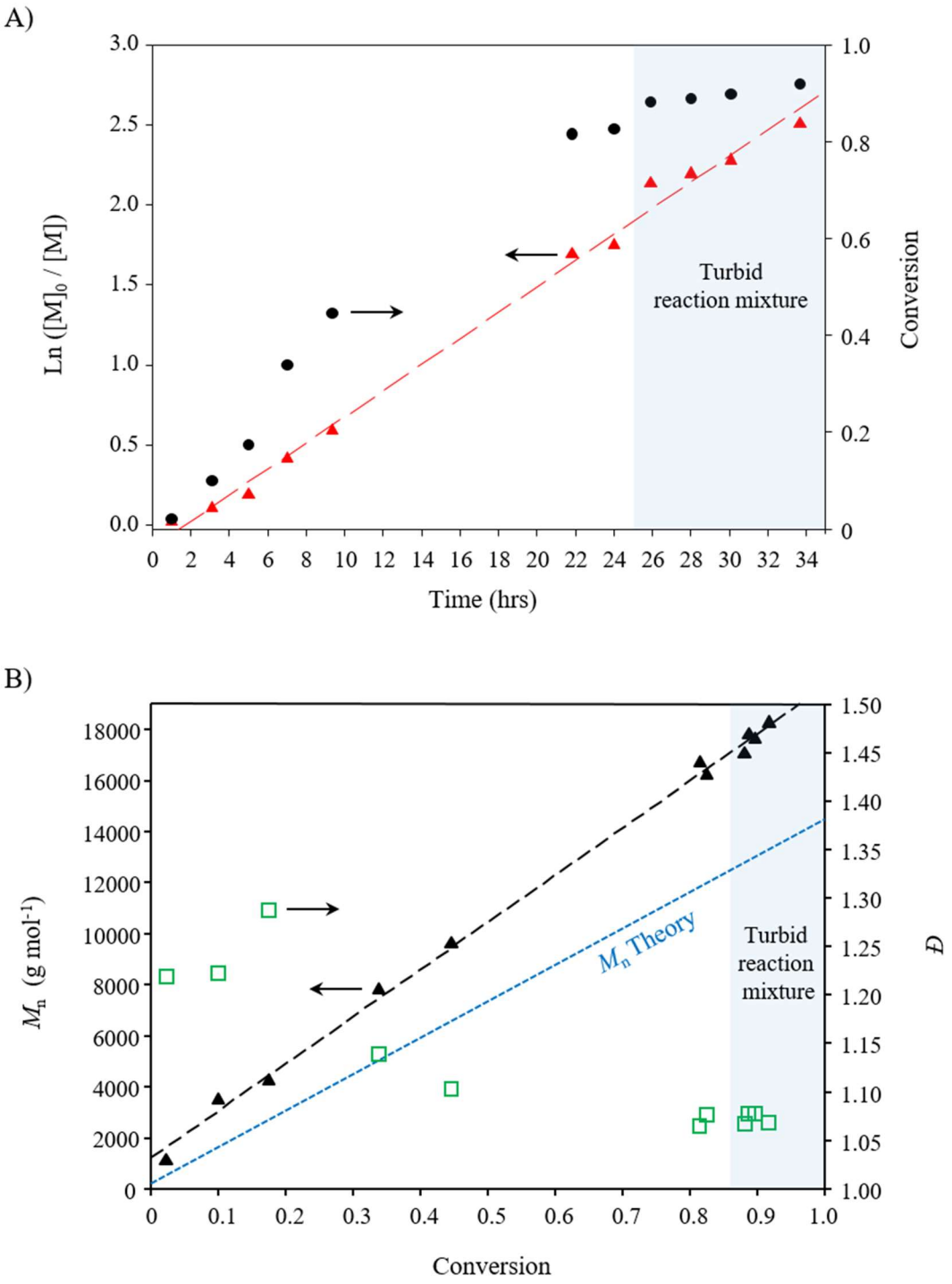

Figure 2.20. Kinetic studies of targeted $p(n\text{BuMA})_{100}$ by RAFT in anhydrous MeOH at 60 °C: (A) conversion and semi-logarithmic plots *vs.* time, and (B) evolution of M_n and dispersity ($Đ$) with conversion.

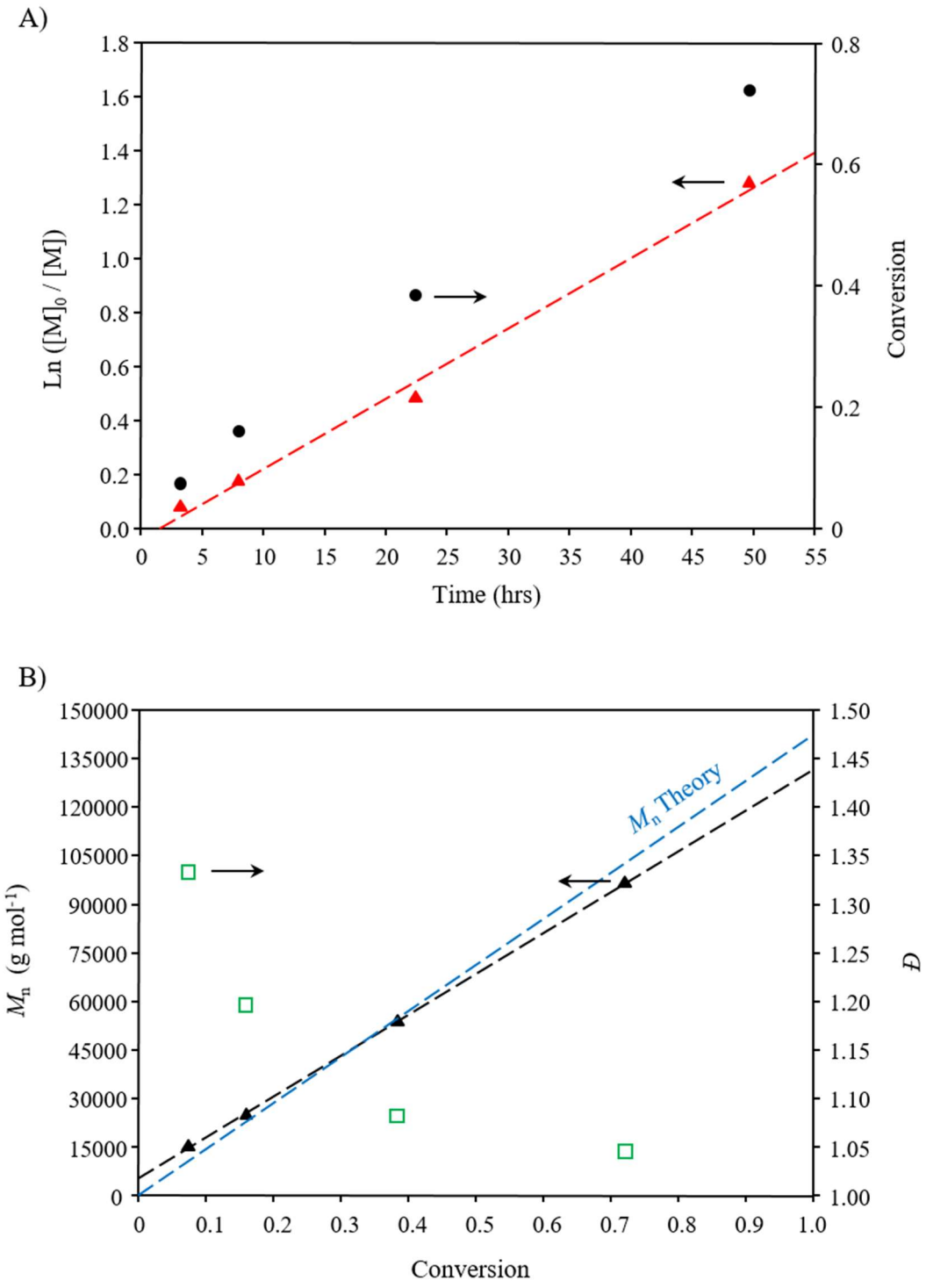

Figure 2.21. Kinetic studies of targeted $p(n\text{BuMA})_{1000}$ by RAFT in anhydrous MeOH at 60 °C: (A) conversion and semi-logarithmic plots *vs.* time, and (B) evolution of M_n and dispersity ($Đ$) with conversion.

When targeting $p(n\text{BuMA})_{100}$, ^{1}H-NMR and GPC analyses of the homogeneous samples terminated within 24 hours of initiation gave linear plots of both $\ln([M]_0/[M])$ *vs.* time, and M_n *vs.* conversion (Figure 2.20), indicating the polymerisation rate followed first order kinetics and termination reactions were negligible. However, after 24 hours – equating to 88 % monomer conversion – the remaining 4 samples became turbid; analysis of these samples showed no deviation in the linear correlations already observed, indicating no change in the polymerisation rate. This suggests that even though the monomer co-solvency effect helps retain the polymer in solution, it is not critical to the controlled polymerisation by RAFT.

The kinetic study targeting $p(n\text{BuMA})_{1000}$ maintained homogeneity up to the last data point, terminated at 72 % conversion, presumably due to the co-solvency effect of the unreacted monomer. Once more, linear correlations were observed when plotting $\ln([M]_0/[M])$ *vs.* time, and M_n *vs.* conversion (Figure 2.21), indicating the rate of polymerisation proceeded with first order kinetics, with minimal termination reactions having taken place. This is particularly surprising given the observed DP_n = 720 monomer units.

2.9. ATRP and RAFT polymerisations of MMA and *t*BuMA in MeOH

Given the success of the methanolic *n*BuMA reactions, the monomer chemistry was extended to include other hydrophobic monomers to verify whether the respective polymerisations proceed with similar controlled behaviour: methyl methacrylate (MMA) and *tert*-butyl methacrylate (*t*BuMA) were selected. Therefore, Cu-catalysed ATRP and RAFT were performed in anhydrous MeOH under identical reaction conditions to the *n*BuMA polymerisations, and the resulting data were compared.

The methanolic MMA polymerisations at 60 °C proceeded in a controlled manner that was analogous to the *n*BuMA reactions, achieving high conversions and yielding low dispersity homopolymers ($1.07 < Đ < 1.19$) by both RAFT (Figure A7, Appendix) and ATRP (Figure A8, Appendix) (Table 2.5). In addition, the onset of turbidity was once again observed towards the latter stages of the RAFT polymerisations when targeting a $DP_n \geq 100$ monomer units.

The Cu-catalysed ATRP of *t*BuMA in MeOH at 60 °C proceeded homogeneously, but a significantly lower rate of polymerisation was observed, achieving only 41 % conversion within 25 hours of initiation (Table 2.5). Analysis by triple-detection GPC

showed much broader molecular weight distributions ($Đ$ = 1.32) compared to the equivalent *n*BuMA polymerisation ($Đ$ = 1.02; Table 2.1), highlighted in Figure 2.22.

Table 2.5. RAFT and Cu-catalysed ATRP of MMA and *t*BuMA in MeOH at 60 °C

Target[a] DP_n	Conv. [actual DP_n]	Time (h)	M_n theory[b]	Triple-detection GPC[c] (THF) M_n (g mol^{-1})	M_w (g mol^{-1})	Đ
MMA						
RAFT						
60	95 % [57]	25	5 950	7 700	8 400	1.10
100	93 % [93]	27	9 550	11 150	11 900	1.07
200	89 % [178]	25	18 850	21 050	22 550	1.07
ATRP						
60	99 % [59]	26	6 150	8 350	9 950	1.19
100	98 % [98]	23	10 000	12 050	13 400	1.11
***t*BuMA**						
ATRP						
80	41 % [33]	25	4 800	5 900	7 800	1.32

[a] Target DP_n calculated as [monomer]/[initiator or CTA]. [b] Theoretical M_n includes initiator/CTA residues and was calculated as [(target DP_n x 100.12 or 142.2 g mol^{-1}) x experimental monomer conversion]. [c] Triple-detection GPC utilising THF eluent and d*n*/d*c* = 0.084 mL g^{-1} for *p*(MMA) (averaged across 6 samples; Table A7, Appendix).

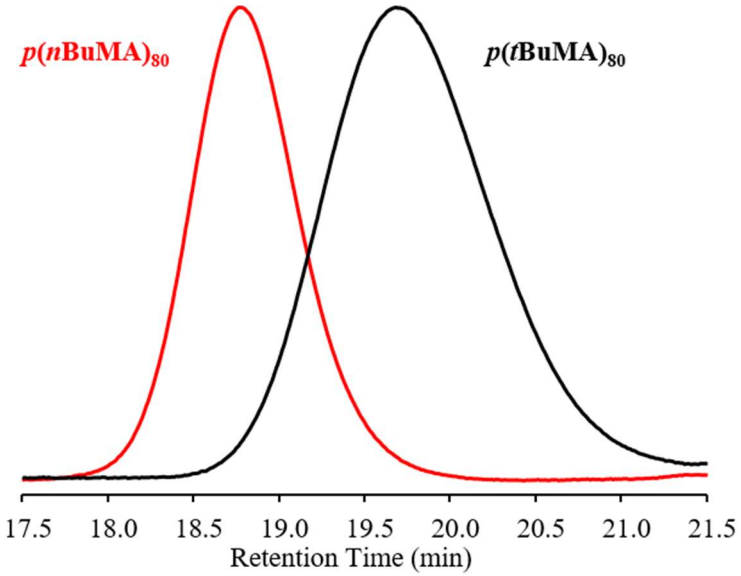

Figure 2.22. GPC (RI) chromatographic overlay of targeted $p(t\text{BuMA})_{80}$ and targeted $p(n\text{BuMA})_{80}$, synthesised by Cu-catalysed ATRP in anhydrous MeOH at 60 °C.

2.10. Conclusions

In conclusion, well-defined *p*(*n*BuMA) homopolymers have been synthesised in anhydrous MeOH – a solvent widely regarded as an anti-solvent for the polymer, often used in purification procedures for precipitation purposes. Polymerisations performed by Cu-catalysed ATRP at 60 °C proceeded homogeneously to high monomer conversions, yielding polymers with narrow molecular weight distributions (*Đ* as low as 1.02); the observed dispersity values are comparable to those typically associated with 'living' ionic polymerisations, and the lack of broadening in the distribution at high monomer conversions offers a relatively easy route to the production of uniform linear polymers. However, the rates of the polymerisation were slow, particularly when targeting a DP_n = 1000 monomer units which achieved 50 % conversion (*i.e.* $p(n\text{BuMA})_{500}$) in 27 days. Initially, it was assumed that the high reaction temperature was critical to the success of the homogeneous polymerisations, but cloud point studies revealed a significant co-solvency effect from the unreacted monomer which helps retain the polymer in solution as the reaction progresses. This enabled the successful methanolic polymerisation of *n*BuMA at 25 °C, achieving high conversions and yielding low dispersity polymers; the lower reaction temperature improved the M_n control compared to the polymerisations at 60 °C. The choice of ligand for the catalytic complex in Cu-catalysed ATRP had a significant effect on the success of the polymerisation, with those ligated with bpy exerting greater control and better M_n targeting. Comparative polymerisations by RAFT at 60 °C were also successful, yielding low dispersity polymers that were analogous to those obtained by ATRP, but more importantly, achieving high conversions in much shorter reaction times; a targeted $p(n\text{BuMA})_{1000}$ by RAFT achieved 80 % conversions in 2 days. The RAFT polymerisations enabled the monitoring of the reactions as they progressed and revealed the onset of turbidity at high conversions under these conditions, indicating a possible pseudo-dispersion towards the latter stages of the polymerisation; however, kinetic analysis revealed no change in the polymerisation rate, suggesting that the monomer co-solvency is not critical to its success. And finally, the monomer chemistry was extended to include the hydrophobic monomers MMA and *t*BuMA, with both polymerisations proceeding homogeneously; however, in the latter case, much broader dispersities were observed and the polymerisation rate was significantly lower when compared to the *n*BuMA polymerisations.

A potential rationale for the success of the methanolic polymerisations is that they are initiated within a good solvent environment, enhanced by the unreacted monomer, which progressively changes to a poor solvent environment as the monomer is depleted. As the monomer concentration decreases, the polymer chains are likely to adopt more densely coiled structures than an equivalent polymerisation within a good solvent, thereby avoiding bimolecular termination of the active chain-end functionalities. The fact that the polymers remain solvated after full consumption of the monomer means that the polymer-MeOH interactions are sufficient enough to prevent the polymer-polymer interactions inducing aggregation and subsequent precipitation.

2.11. References

1 R. A. Hutchinson and A. Penlidis, *Polym. React. Eng.*, 2008, 118–178.

2 J. Li and J. He, *ACS Macro Lett.*, 2015, **4**, 372–376.

3 X. Wang, J. L. Davis, J. P. Hinestrosa, J. W. Mays and S. M. Kilbey, *Macromolecules*, 2014, **47**, 7138–7150.

4 Y. Matsuo, R. Konno, T. Ishizone, R. Goseki and A. Hirao, *Polymers (Basel).*, 2013, **5**, 1012–1040.

5 N. Hadjichristidis, M. Pitsikalis, S. Pispas and H. Iatrou, *Chem. Rev.*, 2001, **101**, 3747–3792.

6 A. Hirao, R. Inushima, T. Nakayama, T. Watanabe, H. Yoo, T. Ishizone, K. Sugiyama, T. Kakuchi, S. Carlotti and A. Deffieux, *Eur. Polym. J.*, 2011, **47**, 713–722.

7 S. Ito, R. Goseki, T. Ishizone and A. Hirao, *Eur. Polym. J.*, 2013, **49**, 2545–2566.

8 H. Ma, Q. Wang, W. Sang, L. Han, P. Liu, H. Sheng, Y. Wang and Y. Li, *Macromol. Rapid Commun.*, 2015, DOI: 10.1002/marc.201500561.

9 L. R. Hutchings, N. M. Sarih and R. L. Thompson, *Polym. Chem.*, 2011, **2**, 851–861.

10 A. Ávila-Ortega, M. Aguilar-Vega, M. I. Loría Bastarrachea, C. Carrera-

Figueiras and M. Campos-Covarrubias, *J. Polym. Res.*, 2015, **22**, 1–8.

11 O. W. Webster, *Science (80-.).*, 1991, **251**, 887–893.

12 J. Smid, M. Van Beylen and T. E. Hogen-Esch, *Prog. Polym. Sci.*, 2006, **31**, 1041–1067.

13 A. Hirao, R. Goseki and T. Ishizone, *Macromolecules*, 2014, **47**, 1883–1905.

14 W. A. Braunecker and K. M. Ã, *Prog. Polym. Sci.*, 2007, **32**, 93–146.

15 K. Matyjaszewski and J. Xia, *Chem. Rev.*, 2001, **101**, 2921–2990.

16 K. Matyjaszewski and N. V Tsarevsky, *Nat. Chem.*, 2009, **1**, 276–288.

17 S. Perrier and P. Takolpuckdee, *J. Polym. Sci. Part A Polym. Chem.*, 2005, **43**, 5347–5393.

18 D. J. Keddie, *Chem. Soc. Rev.*, 2014, **43**, 496–505.

19 C. E. Wang, P. S. Stayton, S. H. Pun and A. J. Convertine, *J. Control. Release*, 2015, **219**, 345–354.

20 K. Matyjaszewski and N. V. Tsarevsky, *J. Am. Chem. Soc.*, 2014, **136**, 6513–6533.

21 H. Bergenudd, G. Coullerez, M. Jonsson and E. Malmstro, *Macromolecules*, 2009, **42**, 3302–3308.

22 A. Sandeau, S. Mazières and M. Destarac, *Polymer (Guildf).*, 2012, **53**, 5601–5618.

23 R. Mincheva, D. Paneva, L. Mespouille, N. Manolova, I. Rashkov and P. Bubois, *J. Polym. Sci. Part a-Polymer Chem.*, 2009, **47**, 1108–1119.

24 N. M. L. Hansen, K. Jankova and S. Hvilsted, *Eur. Polym. J.*, 2007, **43**, 255–293.

25 T. G. Fox, J. B. Kinsinger, H. F. Mason and E. M. Schuele, *Polymer (Guildf).*, 1962, **3**, 71–95.

26 K. L. Robinson, M. V de Paz-Báñez, X. S. Wang and S. P. Armes, *Macromolecules*, 2001, **34**, 5799–5805.

27 K. L. Robinson, M. a. Khan, M. V. De Paz Báñez, X. S. Wang and S. P. Armes, *Macromolecules*, 2001, **34**, 3155–3158.

28 S. Jana, S. P. Rannard and A. I. Cooper, *Chem. Commun.*, 2007, 2962–4.

29 M. Save, J. V. M. Weaver, S. P. Armes and P. McKenna, *Macromolecules*, 2002, **35**, 1152–1159.

30 S. McDonald and S. P. Rannard, *Macromolecules*, 2001, **34**, 8600–8602.

31 R. Horst, R. Mertsch and B. A. Wolf, *Makromol. Chemie*, 1993, **194**, 1387–1395.

32 S. K. Jewrajka, U. Chatterjee and B. M. Mandal, *Macromolecules*, 2004, **37**, 4325–4328.

33 M. Long, D. W. Thornthwaite, S. H. Rogers, F. R. Livens and S. P. Rannard, *Polym. Chem.*, 2012, **3**, 154–161.

34 M. Long, D. W. Thornthwaite, S. H. Rogers, G. Bonzi, F. R. Livens and S. P. Rannard, *Chem. Commun.*, 2009, 6406–6408.

35 Y. Li and S. P. Armes, *Macromolecules*, 2005, **38**, 8155–8162.

36 J. Ford, P. Chambon, J. North, F. L. Hatton, M. Giardiello, A. Owen and S. P. Rannard, *Macromolecules*, 2015, **48**, 1883–1893.

37 F. L. Hatton, P. Chambon, T. O. Mcdonald and S. P. Rannard, *Chem. Sci.*, 2014, **5**, 1844–1853.

38 F. L. Hatton, L. M. Tatham, L. R. Tidbury, P. Chambon, T. He, A. Owen and S. P. Rannard, *Chem. Sci.*, 2015, **6**, 326–334.

39 M. Semsarilar, E. R. Jones, A. Blanazs and S. P. Armes, *Adv. Mater.*, 2012, **24**, 3378–3382.

40 E. R. Jones, M. Semsarilar, A. Blanazs and S. P. Armes, *Macromolecules*, 2012, **45**, 5091–5098.

41 X. Zhang, J. Rieger and B. Charleux, *Polym. Chem.*, 2012, **3**, 1502–1509.

42 D. Zehm, L. P. D. Ratcliffe and S. P. Armes, *Macromolecules*, 2013, **46**, 128–139.

43 W. Cai, W. Wan, C. Hong, C. Huang and C. Pan, *Soft Matter*, 2010, **6**, 5554–5561.

44 W. D. He, X. L. Sun, W. M. Wan and C. Y. Pan, *Macromolecules*, 2011, **44**, 3358–3365.

45 C. Q. Huang and C. Y. Pan, *Polymer (Guildf).*, 2010, **51**, 5115–5121.

46 W.-M. Wan and C.-Y. Pan, *Polym. Chem.*, 2010, **1**, 1475–1484.

47 L. Xue, U. S. Agarwal and P. J. Lemstra, *Macromolecules*, 2002, **35**, 8650–8652.

48 Z. Szablan, T. M. Lovestead, T. P. Davis, M. H. Stenzel and C. Barner-Kowollik, *Macromolecules*, 2007, **40**, 26–39.

49 T. Pintauer and K. Matyjaszewski, *Coord. Chem. Rev.*, 2005, **249**, 1155–1184.

50 D. Konkolewicz, Y. Wang, P. Krys, M. Zhong, A. a. Isse, A. Gennaro and K. Matyjaszewski, *Polym. Chem.*, 2014, **5**, 4409–4430.

51 D. Konkolewicz, Y. Wang, M. Zhong, P. Krys, A. A. Isse, A. Gennaro and K. Matyjaszewski, *Macromolecules*, 2013, **46**, 8749–8772.

52 A. Anastasaki, V. Nikolaou, G. Nurumbetov, P. Wilson, K. Kempe, J. F. Quinn, T. P. Davis, M. R. Whittaker and D. M. Haddleton, *Chem. Rev.*, 2015, 10.1021/acs.chemrev.5b00191.

53 F. Alsubaie, A. Anastasaki, V. Nikolaou, A. Simula and G. Nurumbetov, *Macromolecules*, 2015, **48**, 6421–6432.

54 S. R. Samanta, R. Cai and V. Percec, *J. Polym. Sci. Part A Polym. Chem.*, 2015, **53**, 294–303.

55 S. R. Samanta, A. Anastasaki, C. Waldron, D. M. Haddleton and V. Percec, *Polym. Chem.*, 2013, **4**, 5555–5562.

56 X. Leng, N. H. Nguyen, B. van Beusekom, D. a. Wilson and V. Percec, *Polym. Chem.*, 2013, **4**, 2995–3004.

57 V. Kapishon, R. A. Whitney, P. Champagne, M. F. Cunningham and R. J.

Neufeld, *Biomacromolecules*, 2015, **16**, 2040–2048.

58 Q. Zhang, J. Collins, A. Anastasaki, R. Wallis, D. a. Mitchell, C. R. Becer and D. M. Haddleton, *Angew. Chemie - Int. Ed.*, 2013, **52**, 4435–4439.

59 N. H. Nguyen and V. Percec, *J. Polym. Sci., Part A Polym. Chem.*, 2011, **49**, 4227–4240.

60 M. E. Levere, N. H. Nguyen, X. Leng and V. Percec, *Polym. Chem.*, 2013, **4**, 1635–1647.

61 P. Chambon, a. Blanazs, G. Battaglia and S. P. Armes, *Langmuir*, 2012, **28**, 1196–1205.

62 A. Blanazs, J. Madsen, G. Battaglia, A. J. Ryan and S. P. Armes, *J. Am. Chem. Soc.*, 2011, **133**, 16581–16587.

Chapter 3

Methanolic ATRP of *n*BuMA using PEG macro-initiators: synthesis of amphiphilic copolymers with varying architecture

Publications arising from this chapter:

"Exploring the homogeneous controlled radical polymerisation of hydrophobic monomers in anti-solvents for their polymers: RAFT and ATRP of various alkyl methacrylates in anhydrous methanol to high conversion and low dispersity"

A. B. Dwyer, P. Chambon, A. Town, F. L. Hatton, J. Ford and S. P. Rannard

Polym. Chem., 2015, **6**, 7286

3.1. Introduction

3.1.1. Poly(ethylene glycol) (PEG) functionalisation

Liposomes and polymer-protein conjugates utilising the EPR effect have significantly improved the treatment of various forms of cancer, as described in Chapter 1. Functionalisation with PEG has been pivotal to their clinical success, helping to evade the RES and MPS by reducing adsorption of opsonins (a process known as opsonisation); thus, systemic circulation is prolonged and biodistribution enhanced.[1,2] PEG functionalisation continues to be heavily studied in the design of new drug delivery systems as a result of the *stealth* properties that are imparted to the nanoparticles and the success already achieved.

An interesting study, reported by Borsali and coworkers, involved the synthesis of double hydrophilic PEG-*b*-poly(glycerol monomethacrylate) (PEG-*b*-*p*(GMA)) block copolymers ($Đ < 1.2$) by methanolic ATRP using PEG macro-initiators. The pendant hydroxyl groups present in the *p*(GMA) block enabled post-polymerisation conjugation of the hydrophobic nonsteroidal anti-inflammatory drug, indomethacin (IND), yielding PEG-*b*-(*p*(GMA)-IND) drug conjugates.[3] Self-assembly studies revealed the formation of micelles and vesicles within aqueous media, whose morphology was dependent on the *p*(GMA) block length and the degree of IND-conjugation; encapsulation of free IND drug molecules within the hydrophobic internal phases was also achieved. Similar studies performed by Yang and coworkers involved the synthesis of amphiphilic PEG-*b*-poly(*tert*-butyl acrylate)-*b*-poly(2-hydroxyethyl methacylate) (PEG-*b*-*p*(*t*BA)-*b*-*p*(HEMA)) triblock copolymers by ATRP - also using PEG macro-initiators - whose *p*(HEMA) block was further functionalised through conjugation of doxorubicin (DOX) *via* an acid-sensitive cis-aconityl linkage to yield the corresponding polymer-drug conjugate; self-assembly into micelles in aqueous media enabled the encapsulation of free DOX drug molecules.[4] Additionally, Davis and coworkers used PEG macro-initiators to polymerise N-isopropylacrylamide (NIPAM) by ATRP, yielding thermoresponsive, double hydrophilic PEG-*b*-*p*(NIPAM) block copolymers that were sensitive to the biological messenger molecule, nitric oxide (NO); the amide functionalised *o*-phenylenediamine moieties present at the chain junction point between the two blocks react with NO, resulting in scission of the diblock copolymer into the

corresponding homopolymers.[5] It was concluded that these materials may have the potential for NO-mediated drug release.

3.1.2. Synthesis of branched polymers *via* the chain-growth mechanism

Branched polymerisations *via* the chain-growth mechanism were first reported by Fréchet and coworkers in 1995,[6] who described the self-condensing vinyl polymerisation (SCVP) of inimers (vinyl monomers that also bear an initiating group) (Figure 3.1.A); this involved the polymerisation of 3-(1-chloroethyl)ethenyl benzene in the presence of tin tetrachloride to yield hyperbranched poly(styrene). Since this initial report, the SCVP method was developed to utilise RDRP techniques that include ATRP[7–9] and RAFT.[10–12]

An alternative approach to branched polymer synthesis involves the statistical copolymerisation of vinyl and divinyl monomers, with the incorporation of the latter essentially joining two or more primary polymer chains together to give the branched architecture. It is important to note that less than one equivalent of divinyl monomer per primary polymer chain must be maintained to avoid gelation, as described by the Flory-Stockmayer theory;[13–17] however, this is dependent on the polymerisation technique, monomer concentration, initiator efficiency and the selection of divinyl monomer.[18–20]

Free radical polymerisation in the presence of divinyl monomers rapidly leads to gelation at low conversions - even when maintaining very low concentrations of the bifunctional monomer - due to the uncontrolled nature of the technique and the constant initiation of new polymer chains throughout the polymerisation. To overcome this, Sherrington and coworkers introduced chain transfer agents (typically thiols) into the branched polymerisations to suppress gelation by limiting the primary polymer chain length and thus the average number of branch points per chain, yielding soluble, branched polymers at high conversions (Figure 3.1.B); this is often referred to as the *Strathclyde* route as a result of its development at the University of Strathclyde.[21,22]

Branched polymerisations following the Strathclyde approach can also be achieved using ATRP[23–26] and RAFT[27,28] (Figure 3.1.C). An interesting study performed by Li and Armes describes the methanolic ATRP of 2-hydroxypropyl methacrylate (HPMA) in the presence of a dimethacrylate branching monomer containing a disulfide bond, yielding branched *p*(HPMA) copolymers.[29] Cleavage of the disulphide bonds using

dithiothreitol or benzoyl peroxide gave the corresponding linear polymers; this confirms that the branched architecture is obtained through the statistical linking of primary chains rather than chain transfer reactions associated with free radical polymerisations. Similar studies were performed by Bannister *et al*, describing the synthesis of branched *p*(HPMA) using either ethylene glycol dimethacrylate (EGDMA) or bisphenol A dimethacrylate (BPDMA); the results highlight that branching is negligible at low conversion, occurring only towards that later stages of the polymerisation, and that the observed branching behaviour concurs almost perfectly with the classic Flory-Stockmayer theory.[30] Another interesting example, recently published by Rannard and coworkers, involved the branched polymerisation of HPMA by ATRP using EGDMA as the branching monomer and mixed initiating systems consisting of PEG macroinitiators and generation 2 (G2) benzyl ether-functional dendritic initiators.[31] The branched polymers obtained enabled encapsulation of hydrophobic guest molecules and showed promise as nanocarriers in drug delivery systems.

The advantages of utilising RDRP techniques for branched polymerisations following the Strathclyde approach include: (i) the primary polymer chain length can be controlled by simply adjusting the monomer/initiator molar ratio without the need for chain transfer agents; (ii) the primary polymer chains that are synthesised have narrow dispersities, thereby minimising the probability of chains containing on average greater than one equivalent of branching monomer; and (iii) the greater control of chain end functionalities.

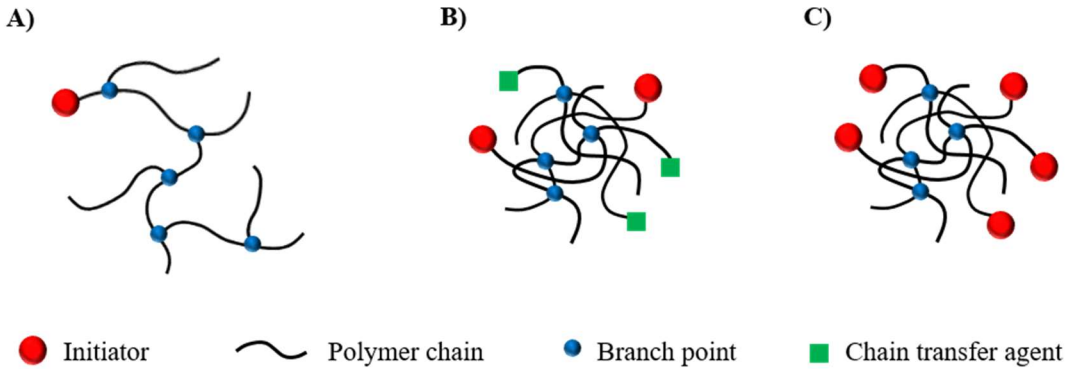

Figure 3.1. Illustration of branched polymers prepared by: (A) self-condensing vinyl polymerisation (SCVP) of inimers, (B) free radical polymerisation in the presence of divinyl monomer following the Strathclyde route, and (C) reversible-deactivation radical polymerisation (RDRP) in the presence of divinyl monomer following the Strathclyde route.

3.1.3. Nanoprecipitation of polymers

Nanoprecipitation is a solvent displacement method that forms nanoparticles via a proposed nucleation/growth mechanism - the rates of which dictate the final particle size and the size distribution.[32,33] It is a technique that can be performed using small organic molecules, inorganic molecules and polymeric materials; in the context of this thesis, only the nanoprecipitation of polymers will be discussed herein. Initially a polymer is solvated within a good, volatile organic solvent (usually acetone, THF or ethanol) which is then added to a miscible anti-solvent (usually water) (Figure 3.2). Upon addition, the mixed binary solvent solution becomes an anti-solvent for the polymer, causing the collapse and subsequent association/aggregation of the solvated chains. Evaporation of the organic solvent can lead to further aggregation of the polymers, forming colloidally stable nanoparticles within the anti-solvent.

An interesting study, performed by Priestley and coworkers, involved the *flash* nanoprecipitation of high molecular weight poly(styrene) (PS), described so because of the rapid solvent displacement achieved as a result of high intensity mixing regimes of THF solutions and water.[34] Nanoparticle size could be controlled by varying the polymer and electrolyte (NaCl) concentrations, with an increase in either case leading to an increase in particle size. The rationale behind the mechanism of particle formation and stabilisation was described through the competitive London Van Der Waals attraction and electrostatic repulsion interactions, highlighting that the size-dependent electrostatic repulsions between nanoparticles and unimers control the aggregation behaviour. A similar study performed by Rannard and coworkers,

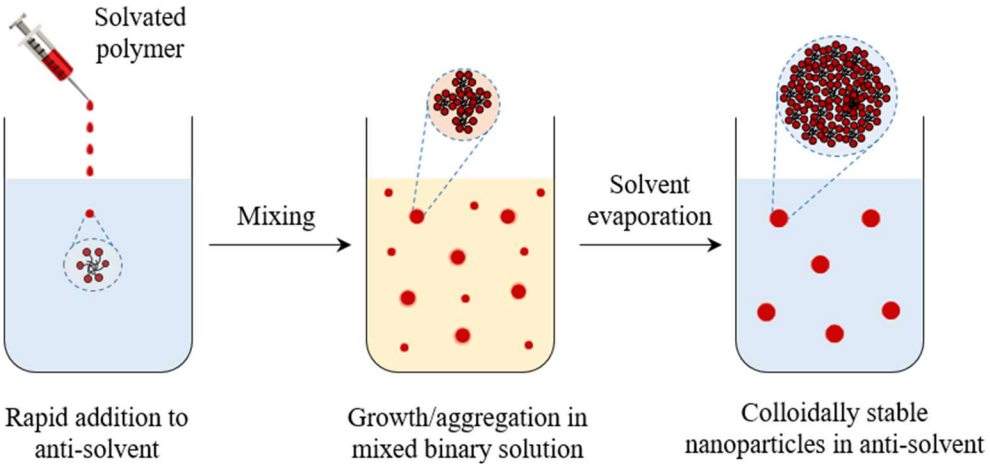

Figure 3.2. Illustration of rapid nanoprecipitation, following the nucleation/growth mechanism to form colloidally stable nanoparticles within the anti-solvent.

involved the rapid nanoprecipitation of acetone solutions of both linear and branched *p*(HPMA) (prepared by methanolic ATRP in the absence/presence of divinyl monomer EGDMA) into water.[35] Particle sizes (ranging from 60-800 nm) could be controlled by varying the primary polymer chain length and the precipitation parameters (*e.g.* polymer concentration, temperature, rate of addition); however, only the branched polymers remained stable within the aqueous environment, revealing that the polymer architecture has a significant effect on the stabilisation of the nanoparticles. Further studies revealed that the aqueous dispersions were stable to dilution, solvent addition, sonication and temperature, with destabilisation occurring only upon addition of NaCl – indicating the presence of charge stabilisation. This study was developed further to include the nanoprecipitation of branched amphiphilic copolymers,[31,36] with one particular study showing the co-nanoprecipitation of branched hydrophobic copolymers with amphiphilic AB block copolymers leading to aggregation behaviour that was different to the individually nanoprecipitated copolymers (branched or diblock).[37]

3.1.4. Chapter aims

The aim of this chapter was to synthesise hydrophilic PEG macro-initiators of various molecular weight, for use in the methanolic ATRP of *n*BuMA to yield amphiphilic materials. Linear PEG-*b*-*p*(*n*BuMA) diblock copolymers were to be synthesised, targeting various degrees of polymerisation, which would then be analysed by ^{1}H-NMR and triple detection GPC; the control of the polymerisations were to be assessed by performing kinetic studies. Various concentrations of the divinyl monomer EGDMA were to be introduced to the polymerisations to obtain amphiphilic branched architectures in a one-pot reaction; their ability to form stable nanoparticle dispersions in aqueous media were to be assessed by performing rapid nanoprecipitation studies.

3.2. Synthesis of PEG macro-initiators

The monofunctional PEG macro-initiators (DP_n = 17, 45, 112 ethylene oxide repeat units) were synthesised *via* an esterification that has been well-reported within the literature;[38–40] this involved reacting PEG monomethyl ether with α-bromo isobutyryl bromide in anhydrous toluene under an inert nitrogen atmosphere (Scheme 3.1).

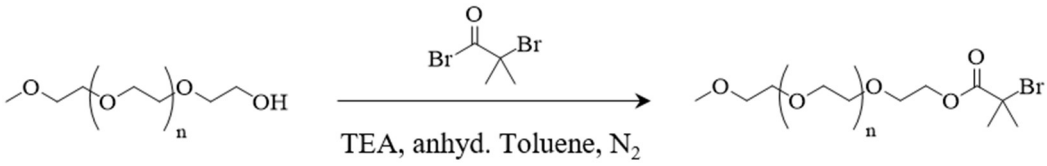

Scheme 3.1. Reaction scheme detailing the PEG macro-initiator syntheses *via* esterifications.

An excess of triethylamine (TEA) was used to scavenge the hydrogen bromide (HBr) side product, forming a triethylammonium bromide salt that precipitated from solution as the reaction progressed. After reaction completion, the salt was filtered off, the solvent removed on the rotary evaporator, and the crude products dissolved in acetone prior to multiple precipitations into petroleum ether (40-60). The purified products were then characterised by ^{1}H-NMR, ^{13}C-NMR and triple detection GPC (Figures 3.3-3.5; Figures A9-A12, Appendix).

^{1}H-NMR analysis of the macro-initiators enabled the full assignment of their structure, with the integrations of each environment in relative agreement with the theoretical values (Figure 3.3; Figures A9 and A11, Appendix); this was determined by normalising the integration of the methoxy group (δ = 3.38 ppm) to three protons. The assignment of the isobutyryl group at 1.94 ppm confirmed the structure of the desired compounds. Furthermore, ^{13}C-NMR analyses for each of the macro-initiators enabled the full assignment of their structure, with the peak at 172 ppm attributed to the ester group of the desired compound (Figure 3.4; Figures A10 and A12, Appendix). Analyses by triple detection GPC revealed narrow molecular weight distributions with M_n and M_w values that closely matched theoretical values (Figure 3.5, Table 3.1).

An α,ω-bifunctional macro-initiator with DP_n = 91 ethylene oxide units was also synthesised under the same reaction conditions (Scheme 3.2), and characterised by ^{1}H-NMR, ^{13}C-NMR and triple detection GPC (Figure A13 and A14, Appendix).

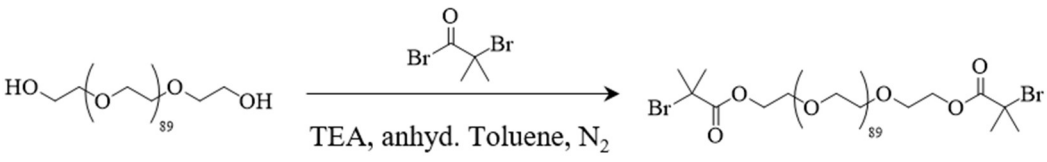

Scheme 3.2. Reaction scheme detailing the PEG macro-initiator syntheses *via* esterifications.

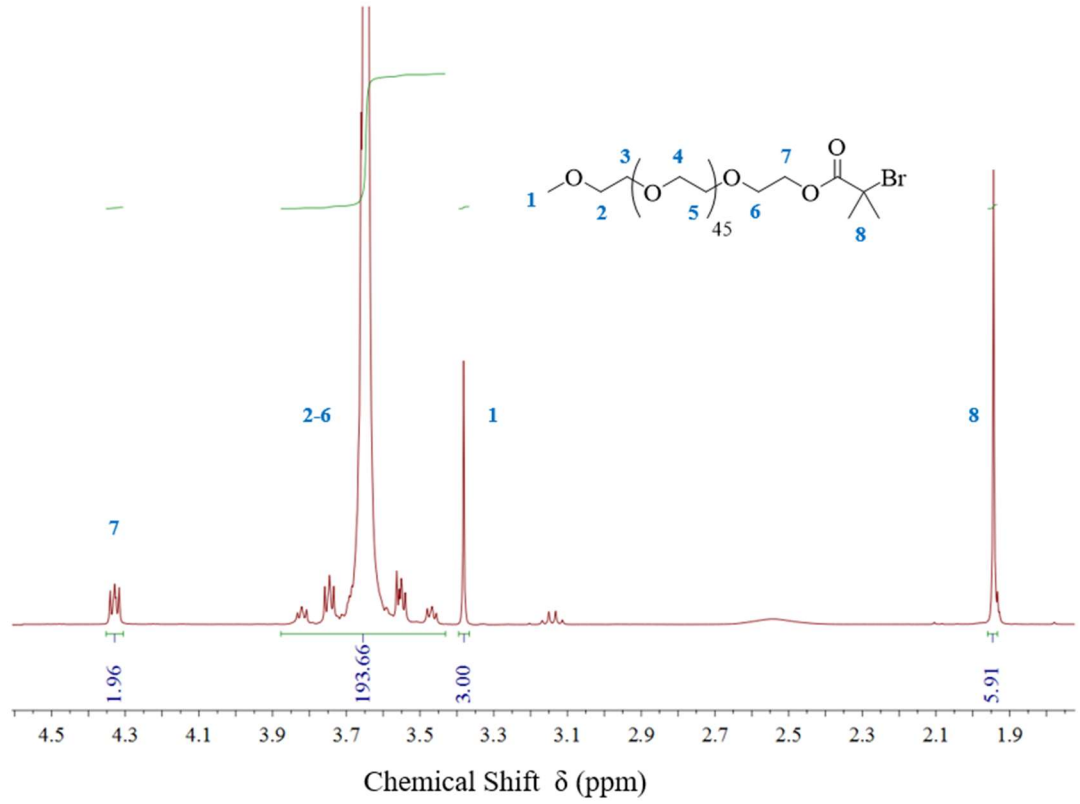

Figure 3.3. ^{1}H-NMR ($CDCl_3$) spectrum of PEG_{45}-Br macro-initiator.

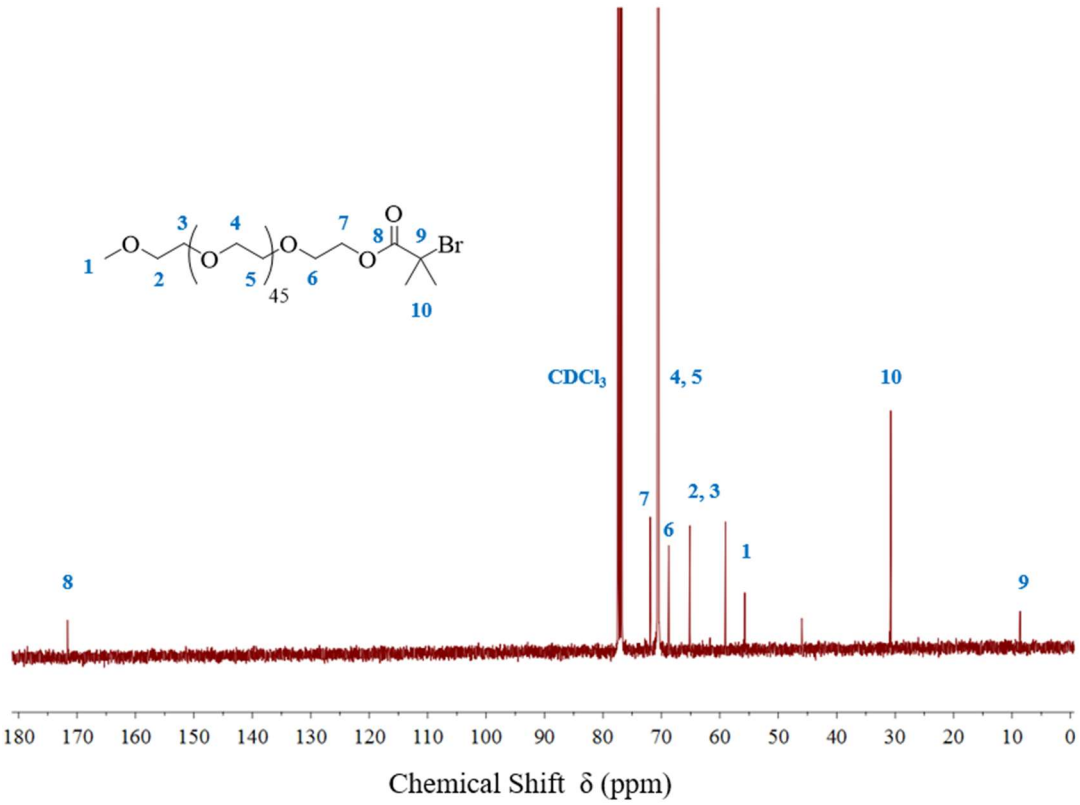

Figure 3.4. ^{13}C-NMR ($CDCl_3$) spectrum of PEG_{45}-Br macro-initiator

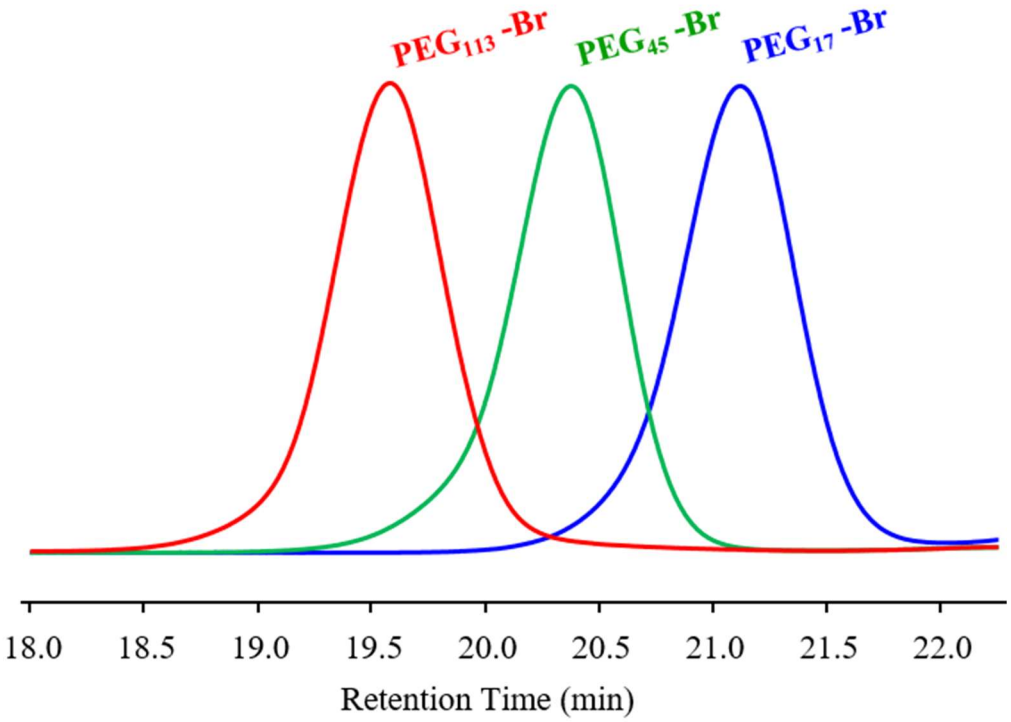

Figure 3.5. GPC chromatograms (RI) showing the molecular weight distributions for each of the PEG macro-initiators.

3.3. Synthesis of PEG-*b*-*p*(*n*BuMA) diblock and triblock copolymers

Initially, methanolic ATRP of *n*BuMA at 60 °C was performed using the monofunctional PEG macro-initiators, targeting a DP_n = 60, 80, 100 monomer units (Scheme 3.3). As expected, the PEG macro-initiators were readily solvated within the MeOH after gentle heating, with the addition of *n*BuMA monomer having no effect on their solubility. The polymerisations proceeded homogeneously to high conversion (≥ 92 %) to yield low dispersity ($Đ \leq 1.05$) amphiphilic AB block copolymers across the different block lengths; determined by ^{1}H-NMR and triple detection GPC (DMF) respectively (Table 3.1). Furthermore, the GPC (RI) chromatograms for each of the AB block copolymers showed monomodal and symmetrical molecular weight distributions (Figure 3.6). Although the low dispersities obtained were characteristic of well-controlled ATRP, the experimental M_n values observed after GPC analysis were significantly higher than theoretical values, indicating poor initiator efficiencies for PEG_x-Br. Estimations for the initiator efficiencies were calculated as

((Theoretical M_n)/(Observed M_n (GPC)) x 100 %), which gave consistent values across the polymer series: PEG_{17}-Br = 55 %, PEG_{45}-Br = 60 %, PEG_{113}-Br = 73 %, with a maximum standard deviation (σ) = 3 % observed for PEG_{113}-Br.

Amphiphilic ABA triblock copolymers were obtained using the bifunctional Br-PEG_{91}-Br macro-initiator, targeting a DP_n = 40 and 80 monomer units on either side (*i.e.* total target DP_n = 80, 160) of the PEG central block. Once again, polymerisations proceeded homogeneously to high conversions (≥ 98 %) to yield narrow dispersity polymers; however, the observed dispersities were significantly higher than those seen for the AB diblock copolymers (Table 3.1; Figure A15, Appendix).

This can be explained by the following two reasons: (i) poor initiation efficiencies will have double the impact on the final molecular weight distributions due to the propagation of monomer on either side of the polymer chain; and (ii) early termination reactions on one side of the bifunctional initiator would essentially lead to a mono-initiated polymer with a considerably lower molecular weight. Either case would lead to a significant impact on the molecular weight distribution.

The methanolic syntheses of PEG_{113}-*b*-*p*$(MMA)_{60\text{-}100}$ diblock copolymers were also attempted, but will not be discussed within the context of this thesis; the results are, however, presented in the Appendix (Table A9, Figures A16 and A17).

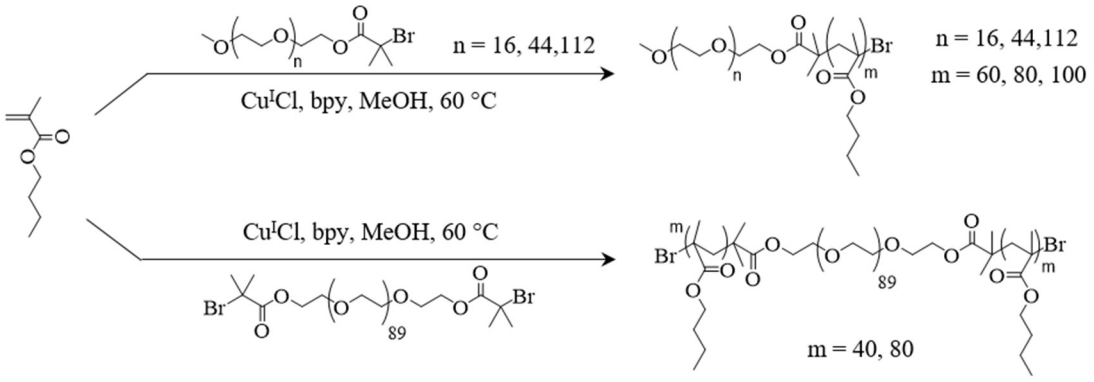

Scheme 3.3. Reaction scheme detailing the AB diblock and ABA triblock copolymer syntheses *via* methanolic ATRP of *n*BuMA using PEG macro-initiators.

Table 3.1. Methanolic Cu-catalysed ATRP of *n*BuMA at 60 °C using PEG-derived macro-initiators

Target[a] DP_n	Conversion [actual DP_n]	Time (h)	M_n theory[b]	M_n ^{1}H-NMR	Triple-detection GPC (DMF)		
					M_n (g mol^{-1})	M_w (g mol^{-1})	Đ
PEG macro-initiators							
PEG_{17}	---	---	900	950	---	---	---
PEG_{45}	---	---	2 150	2 300	2 300	2 500	1.09
PEG_{91}	---	---	4 300	4 650	5 150	5 400	1.05
PEG_{113}	---	---	5 150	5 800	6 000	6 150	1.02
PEG_{17}-Br							
60	99 % [59]	24	9 350	15 550	17 850	18 250	1.02
80	96 % [77]	24	11 850	19 100	21 300	21 700	1.02
100	92 % [92]	24	14 000	23 200	24 900	25 400	1.02
PEG_{45}-Br							
60	99 % [59]	24	10 600	15 950	17 250	17 900	1.04
80	98 % [78]	25	13 250	18 800	23 000	24 050	1.05
100	97 % [97]	27	15 900	29 600	26 800	27 800	1.04
PEG_{113}-Br							
60	97 % [58]	5	13 420	12 400	17 650	18 050	1.02
80	93 % [74]	17	15 800	12 400	21 850	22 500	1.03
100	94 % [94]	17	18 600	16 100	26 600	27 700	1.04
Br-PEG_{91}-Br							
40 (x 2)	99 % [79]	26	15 600	---	22 050	26 000	1.18
80 (x 2)	98 % [157]	26	26 600	---	38 300	38 300	1.13

[a] Target DP_n calculated as [*n*BuMA]/[initiator]. [b] Theoretical M_n includes initiator residue and was calculated as [(Target DP_n x 142.2 g mol^{-1}) x monomer conversion].

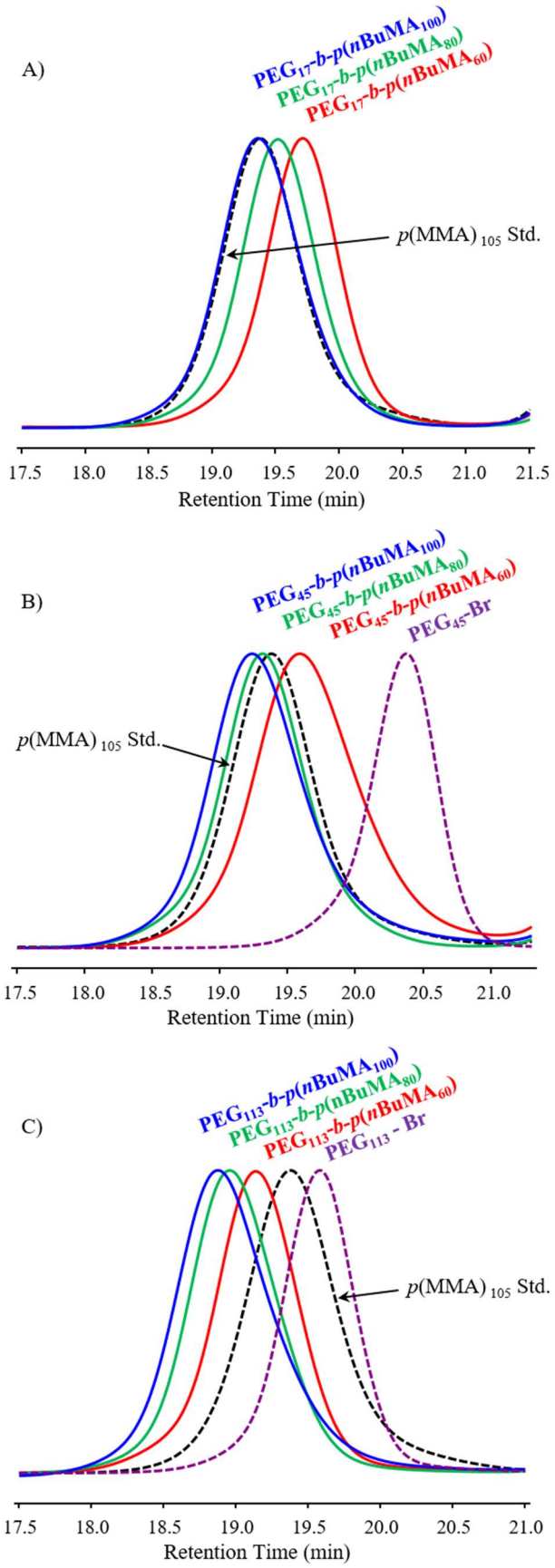

Figure 3.6. GPC (RI) chromatograms showing the molecular weight distributions of PEG-*b*-*p*(*n*BuMA) diblock copolymers using: (A) PEG_{17}-Br, (B) PEG_{45}-Br, (C) PEG_{113}-Br.

3.4. Kinetic studies for the PEG-*b*-*p*(*n*BuMA) diblock copolymer syntheses

The narrow molecular weight distributions observed for each of the polymerisations strongly indicate that they proceed in a controlled manner, but this was confirmed by performing kinetic studies targeting a DP_n = 80 monomer units, using each of the monofunctional PEG macro-initiators. The kinetic data - obtained after analysis by ^{1}H NMR and triple detection GPC - is presented as semi-logarithmic plots of $\ln([M]_0/[M])$ *vs.* time, and as M_n *vs.* conversion (Figure 3.7).

With regards to the plots of M_n *vs.* conversion, it is important to note that the value of the refractive index increment (d*n*/d*c*) of the individual copolymer samples (taken during the kinetic studies) are expected to vary systematically due to the progressively increasing *p*(*n*BuMA) chain length at the end of each PEG block. Therefore, two plots of M_n *vs.* conversion were analysed and compared for each experiment using: (i) M_n values for each kinetic point determined by employing the calculated d*n*/d*c* value from the final recovered polymer, and (ii) M_n values for each kinetic point determined by employing theoretical copolymer d*n*/d*c* values calculated using Eqn. 3.1, as discussed by Hadjichristidis *et al*,[41]

$$(dn/dc)_{\text{Copolymer}} = (W_{\text{PEG}} \times (dn/dc)_{\text{PEG}}) + \left((1 - W_{\text{PEG}}) \times (dn/dc)_{p(n\text{BuMA})}\right) \quad \textbf{(3.1)}$$

where W_{PEG} is the weight fraction of the PEG_x block, and $(dn/dc)_{\text{PEG}}$ and $(dn/dc)_{p(n\text{BuMA})}$ are average values determined by triple detection GPC(DMF) analysis for three linear homopolymer samples of each polymer: $(dn/dc)_{\text{PEG}}$ = 0.0566 mL g^{-1} (σ = 0.0010); $(dn/dc)_{p(n\text{BuMA})}$ = 0.0624 mL g^{-1} (σ = 0.0007), (Table A8, Appendix).

Linear correlations were observed in all plots, meaning that: (i) the rate of the polymerisations follow first order kinetics, where irreversible termination reactions are negligible and the concentration of active species remains constant throughout; and (ii) there is a constant number of chains throughout, all propagating at the same rate, where the rate of activation/deactivation ($K_{ATRP} = k_{act}/k_{deact}$) is much greater than the rate of propagation (k_p). And finally, the comparative M_n *vs.* conversion graphs for the targeted copolymers showed a decreasing discrepancy with increasing PEG macro-initiator chain length, as may be expected due to the increasing weight fraction dominance of the PEG blocks.

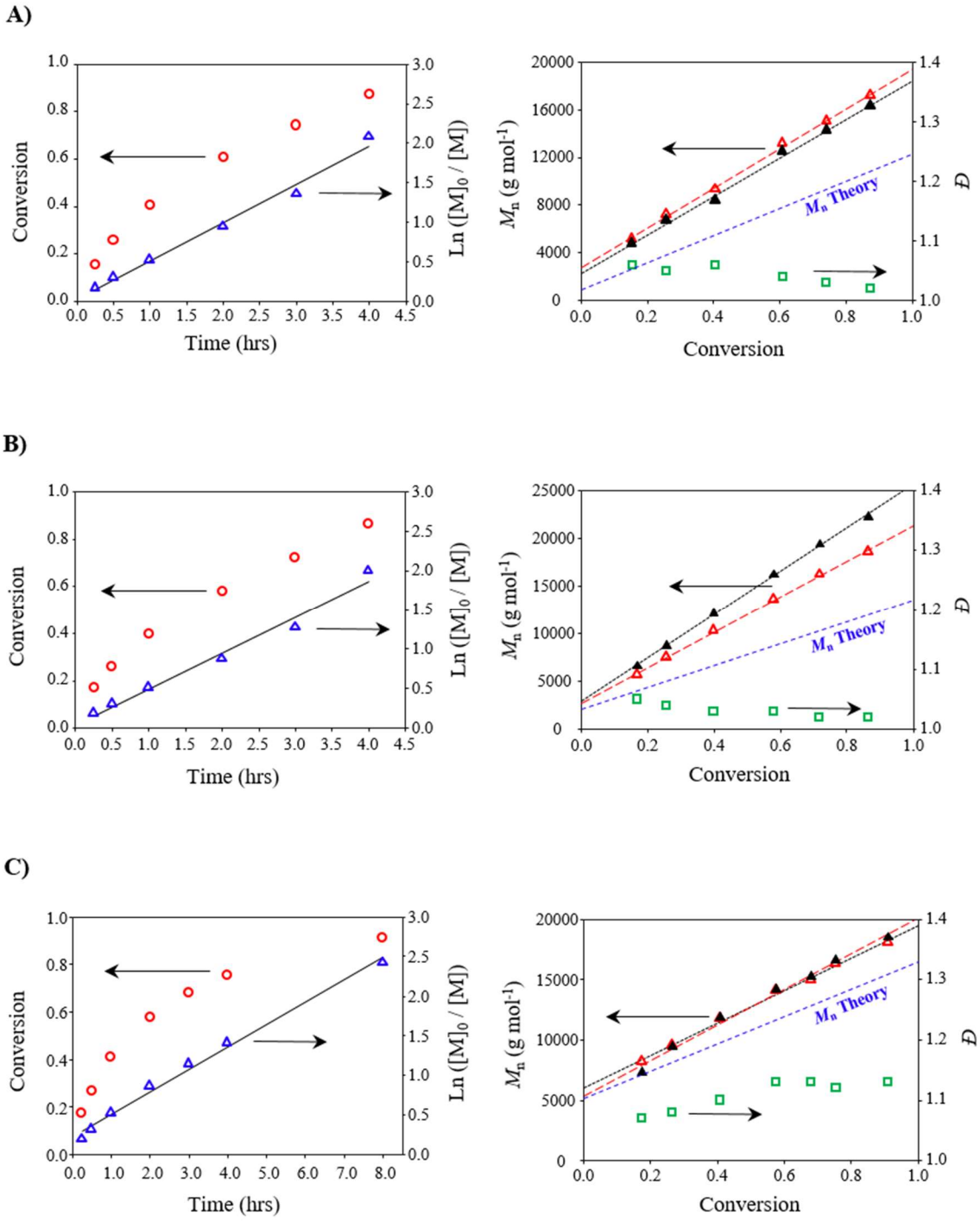

Figure 3.7. Kinetic studies of anhydrous methanolic ATRP at 60 °C showing the conversion and semi-logarithmic plots *vs* time, and the evolution of M_n and dispersity with conversion for PEG$_x$-*p*(*n*BuMA)$_{80}$ block copolymers. (A) Polymerisation initiated with PEG$_{17}$-Br macro-initiator, (B) polymerisation initiated with PEG$_{45}$-Br macro-initiator, and (C) polymerisation initiated with PEG$_{113}$-Br macro-initiator. M_n *vs.* conversion plotted using both the d*n*/d*c* value of the final purified polymer (solid black triangles), and the calculated d*n*/d*c* values using Eqn. 3.1. (open red triangles); dispersities shown as open green squares.

3.5. Synthesis of PEG-*b*-*p*(*n*BuMA) diblock copolymers *via* ATRP at 25 °C

The successful homopolymerisation of *n*BuMA *via* methanolic ATRP at 25 °C was demonstrated in Chapter 2; therefore, a study to establish the potential for AB block copolymer synthesis using ATRP at reduced temperature was conducted using the three monofunctional PEG macro-initiators, targeting a DP_n of 80 *n*BuMA units.

Each of the polymerisations were allowed to react for approximately 25 hours to enable direct comparisons of the data (Figure 3.8, Table 3.2); it was evident that higher monomer conversions and better M_n targeting were achieved when using the larger macro-initiators, with initiator efficiencies estimated as PEG_{17}-Br = 64 %, PEG_{45}-Br = 86 %, and PEG_{113}-Br = 92 %. In comparison to the equivalent polymerisations conducted at the higher temperature (Table 3.1), the initiation efficiencies of all macro-initiators were greater within the polymerisations conducted at 25 °C, which may indicate fewer termination reactions having taken place; however, the dispersities

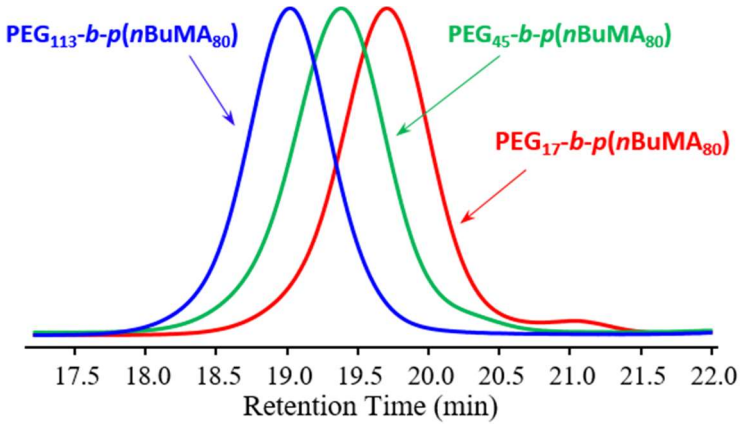

Figure 3.8. GPC (RI) chromatograms for PEG_x-*b*-*p*(nBuMA$_{80}$) obtained *via* ATRP at 25 °C.

Table 3.2. Synthesis of PEG-*b*-*p*(*n*BuMA) block copolymers *via* methanolic ATRP at 25 °C: hydrophobic block target DP_n = 80 *n*BuMA units

Initiator	Conversion [actual DP_n]	Time (h)	M_n theory[a]	M_n ^{1}H-NMR	Triple-detection GPC (DMF)		
					M_n (g mol^{-1})	M_w (g mol^{-1})	Đ
PEG_{17}-Br	68	25	8 600	7 900	13 550	16 300	1.20
PEG_{45}-Br	89	25	12 300	13 100	14 250	18 800	1.32
PEG_{113}-Br	85	26	14 850	14 950	16 200	19 500	1.21

[a] Theoretical M_n includes initiator residue and was calculated as [(Target DP_n x 142.2 g mol^{-1}) x experimental monomer conversion].

observed for all block copolymer samples were significantly higher ($Đ \geq 1.2$).

3.6. Synthesis of branched PEG-*b*-*p*(*n*BuMA-*co*-EGDMA) *via* ATRP

Amphiphilic copolymers consisting of a branched architecture were obtained by polymerisation following the Strathclyde approach. This involved the methanolic ATRP of *n*BuMA in the presence of the divinyl monomer EGDMA, whose statistical incorporation enabled the inter-chain branching of the primary polymer chains; a low concentration of the branching monomer was maintained (less than one equivalent per initiator) so as to avoid gelation, and initiator selection was confined to PEG_{113}-Br (Scheme 3.4).

It is important to note that a reaction temperature of 60 °C was selected for the following reasons: (i) greater control was demonstrated when polymerising at the elevated temperature during the AB diblock copolymer syntheses, which would help to limit the average number of branch points per chain during the branched polymerisations and thus avoid gelation, and (ii) the *n*BuMA homopolymerisation study (Chapter 2) was concluded by hypothesising that the methanolic polymerisations are initiated within a good solvent environment, enhanced by the unreacted monomer, which progressively changes to a poor solvent environment as the monomer is depleted, resulting in densely coiled polymer structures. Therefore, branched polymerisations performed at elevated temperatures will provide a greater entropic effect that will be more likely to promote inter-chain – rather than intra-chain – branching.

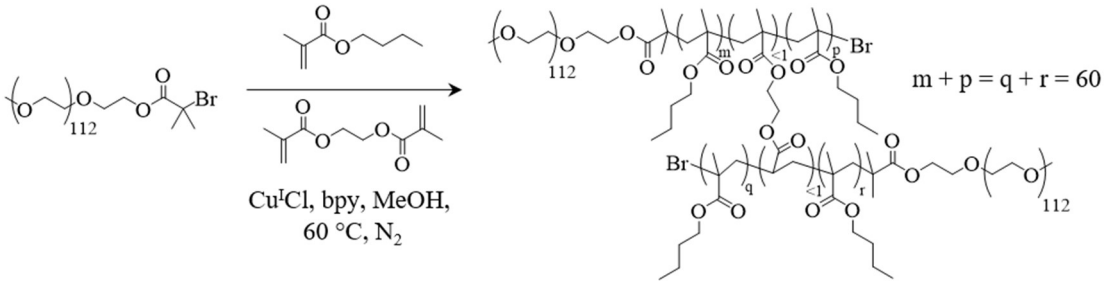

Scheme 3.4. Reaction scheme detailing the methanolic ATRP of *n*BuMA in the presence of EGDMA using a monofunctional PEG_{113}-Br macro-initiator to yield amphiphilic branched AB block copolymers; targeting a $DP_n = 60$ monomer units per primary chain and using less than one equivalent of the divinyl monomer with respect to the initiator.

A series of branched polymerisations were performed using the PEG_{113}-Br macro-initiator, each targeting a DP_n = 60 monomer units, with only the concentration of EGDMA varying from 0.75 to 0.95 equivalents with respect to the initiator. All polymerisations were allowed to progress to 99 % conversion over approximately 2 days to achieve maximum branching and to enable direct comparisons between the data (Table 3.3).

GPC (DMF) analysis of each of the branched copolymers calculated M_n and M_w values that were greater than those calculated for the linear analogue. Generally, an increase in EGDMA concentration resulted in an increase in the observed M_n and M_w values, with the polymerisation proceeding with 0.9 equivalents of the divinyl monomer yielding branched polymers with M_n = 1.62 x 10^5 g mol^{-1} and M_w = 2.33 x 10^6 g mol^{-1} (Figure A18, Appendix); these values correspond to number average structures with approximately 9 conjoined primary amphiphilic AB block copolymer chains and weight average structures containing approximately 129 chains. Anomalously, however, the polymerisation proceeding with 0.95 equivalents of EGDMA yielded branched polymers with lower M_n and M_w values than those obtained after polymerisation with 0.9 equivalents, suggesting the formation of microgel and its subsequent removal during either the filtration step of the GPC sample preparation or when removing the catalytic system from the crude polymer sample; the d*n*/d*c* values obtained for each polymer were consistent, indicating that the GPC sample concentration was not affected during sample preparation.

Table 3.3. Methanolic ATRP of *n*BuMA and EGDMA at 60 °C using PEG_{113}-Br

Target[a] DP_n	Conversion [actual DP_n]	Time (h)	EGDMA: PEG_{113}-Br	Triple-detection GPC (DMF)		
				M_n (g mol^{-1})	M_w (g mol^{-1})	Đ
PEG_{113}-Br						
60	99 % [59]	53	0.95 : 1	36 400	439 550	12.08
60	99 % [59]	51	0.9 : 1	161 500	2 327 000	14.41
60	99 % [59]	51	0.85 : 1	36 600	419 500	11.46
60	99 % [59]	51	0.8 : 1	27 800	184 750	6.62
60	99 % [59]	48	0.75 : 1	34 100	186 200	5.46

[a] Target DP_n calculated as [*n*BuMA]/[initiator].

This, therefore, implies removal of the microgel during purification (alumina column) of the crude polymer.

Furthermore, the observed dispersities for each of the branched copolymer samples were significantly higher than those seen in the linear polymerisations ($Đ$ = 1.02; Table 3.1), due to the statistical nature of the branching; an increase in EGDMA concentration from 0.75 to 0.9 equivalents resulted in an increase in dispersity ($Đ$ = 5.46 - 14.41). This is also reflected in the GPC chromatograms, displaying an increasingly complex molecular weight distribution as the EGDMA concentration increased (Figure 3.9). Overlaying these chromatograms with the linear PEG-*b*-*p*(*n*BuMA$_{60}$) showed the expected presence of linear chains that have not been incorporated into the branched architecture; this also confirmed the formation of primary AB block copolymer chains equivalent in dispersity and molecular weight to the linear polymer analogues.

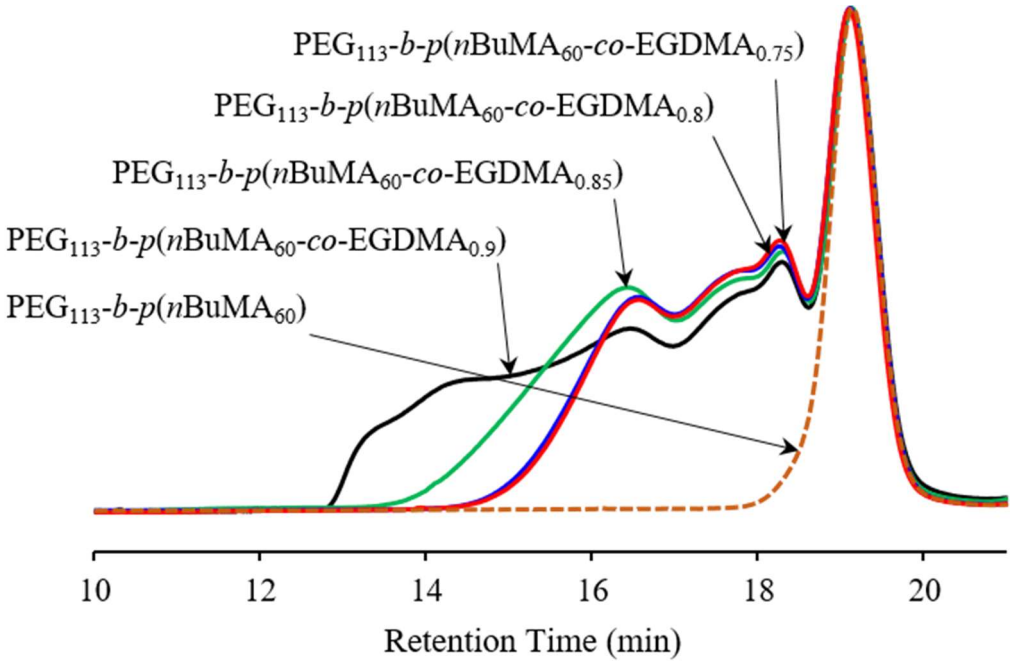

Figure 3.9. Overlaid GPC (RI) chromatograms of linear and branched AB block copolymers produced using methanolic ATRP of *n*BuMA at 60 °C (targeting DP$_n$ = 60 monomer units within the hydrophobic block) using PEG$_{113}$-Br macro-initiator and varying equivalents of (0.75-0.9 wrt. Initiator) of divinyl monomer, EGDMA.

3.7. Nanoprecipitation of PEG-*b*-*p*(*n*BuMA$_{60}$-*co*-EGDMA$_{0.75\text{-}0.95}$)

As previously described, nanoprecipitation is a solvent displacement method that involves the addition of a polymer solution – with the polymer usually solvated within acetone, THF or ethanol - into a miscible antisolvent (*e.g.* H_2O). However, solvating the PEG-*b*-*p*(*n*BuMA$_{60}$-*co*-EGDMA$_{0.75\text{-}0.95}$) branched copolymers within volatile organic solvents that were also miscible with water, such as those listed above, proved to be difficult; rather than clear transparent solutions, those obtained were turbid, suggesting assembly/aggregation had already taken place before its addition to the anti-solvent.

Clear, transparent polymer solutions were achieved, however, when using binary mixtures of THF and H_2O (1:1 ratio by volume). Therefore, nanoprecipitations of the amphiphilic branched copolymers were performed through the rapid addition of 1 mL of these polymer solutions (5 mg mL^{-1}) into 4.5 mL of H_2O, after which the volatile organic solvent was allowed to evaporate under ambient conditions to yield nanoparticles within the antisolvent (Figure 3.10). These aqueous dispersions were analysed by dynamic light scattering (DLS) (Table 3.4, Figure 3.11).

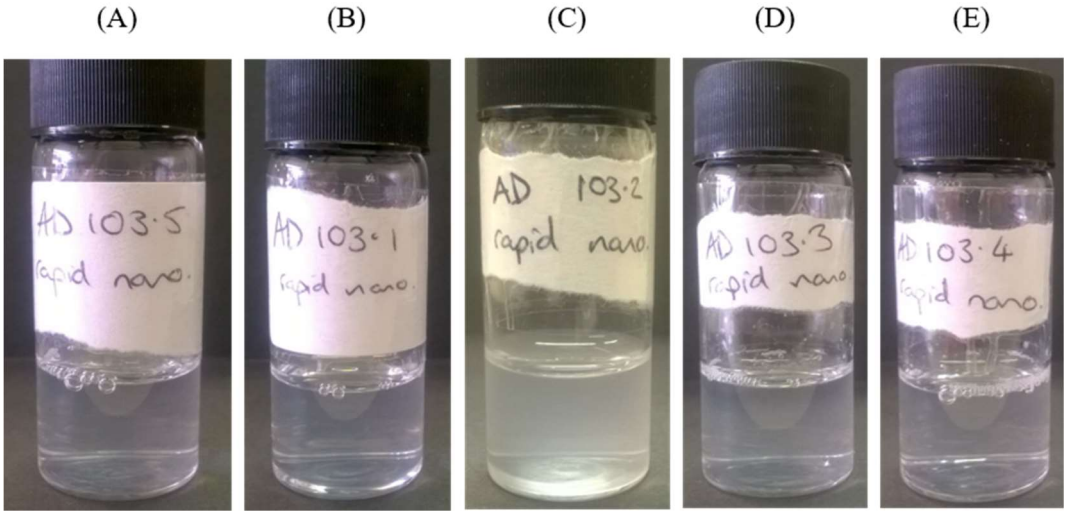

Figure 3.10. Pictures displaying the aqueous dispersions of the amphiphilic branched copolymers after rapid nanoprecipitation and subsequent evaporation of the organic solvent: (A) PEG-*b*-*p*(*n*BuMA$_{60}$-*co*-EGDMA$_{0.95}$), (B) PEG-*b*-*p*(*n*BuMA$_{60}$-*co*-EGDMA$_{0.9}$), (C) PEG-*b*-*p*(*n*BuMA$_{60}$-*co*-EGDMA$_{0.85}$), (D) PEG-*b*-*p*(*n*BuMA$_{60}$-*co*-EGDMA$_{0.80}$), and (E) PEG-*b*-*p*(*n*BuMA$_{60}$-*co*-EGDMA$_{0.75}$).

Table 3.4. DLS data of nanoprecipitations using binary THF-H_2O solutions of PEG-*b*-*p*(*n*BuMA$_{60}$-*co*-EGDMA$_x$) (1 mL) into H_2O (4.5 mL)

Sample	Initial Conc. in THF/H_2O	Final Conc. in H_2O	DLS [a]							
			Unfiltered				Filtered [b]			
			D_z [c] (d.nm)	PdI [d]	D_{Nn} [e] (d.nm)	Derived count rate (kcps) [attenuator]	D_z [c] (d.nm)	PdI [d]	D_n [e] (d.nm)	Derived count rate (kcps) [attenuator]
PEG-*b*-*p*(*n*BuMA$_{60}$-*co*-EGDMA$_{0.95}$)	5 mg mL^{-1}	1 mg mL^{-1}	54	0.330	26	12 000 [7]	66	0.403	25	15 000 [7]
PEG-*b*-*p*(*n*BuMA$_{60}$-*co*-EGDMA$_{0.9}$)	5 mg mL^{-1}	1 mg mL^{-1}	80	0.275	17	19 000 [7]	78	0.296	23	17 000 [7]
PEG-*b*-*p*(*n*BuMA$_{60}$-*co*-EGDMA$_{0.85}$)	5 mg mL^{-1}	1 mg mL^{-1}	98	0.508	27	23 000 [7]	105	0.266	24	31 000 [7]
PEG-*b*-*p*(*n*BuMA$_{60}$-*co*-EGDMA$_{0.8}$)	5 mg mL^{-1}	1 mg mL^{-1}	67	0.376	24	12 000 [7]	52	0.325	24	11 000 [7]
PEG-*b*-*p*(*n*BuMA$_{60}$-*co*-EGDMA$_{0.75}$)	5 mg mL^{-1}	1 mg mL^{-1}	65	0.495	25	11 000 [7]	59	0.392	24	11 000 [8]

[a] DLS measurements recorded at 25 °C after an equilibration period of 2 minutes. [b] Samples filtered using a 1 μm PTFE filter. [c] Size distribution using *z*-average values. [d] Polydispersity index. [e] Size distribution using number average values.

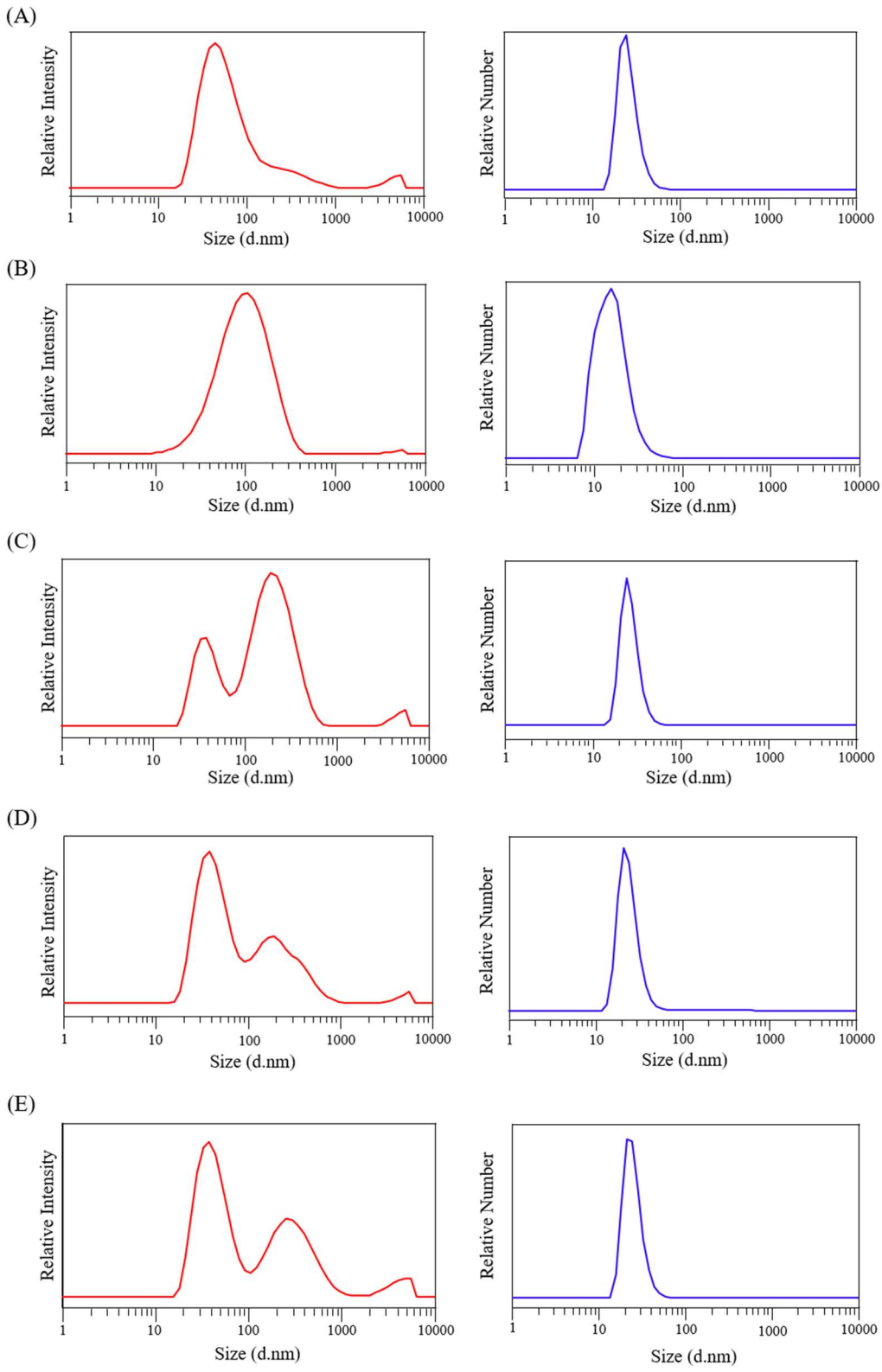

Figure 3.11. DLS traces showing the rapid nanoprecipitations (unfiltered) of: (A) PEG_{113}-*b*-*p*(*n*$BuMA_{60}$-*co*-$EGDMA_{0.95}$), (B) PEG_{113}-*b*-*p*(*n*$BuMA_{60}$-*co*-$EGDMA_{0.9}$), (C) PEG_{113}-*b*-*p*(*n*$BuMA_{60}$-*co*-$EGDMA_{0.85}$), (D) PEG_{113}-*b*-*p*(*n*$BuMA_{60}$-*co*-$EGDMA_{0.8}$), (E) PEG_{113}-*b*-*p*(*n*$BuMA_{60}$-*co*-$EGDMA_{0.75}$). Intensity weighted distribution displayed on the left (red traces); Number weighted distributions displayed on the right (blue traces).

DLS analysis of the unfiltered samples revealed that the amphiphilic branched copolymer nanoparticles had *z*-average diameter values (D_z) ranging from 54 to 98 nm with high polydispersity index (PdI) values ranging from 0.275 to 0.508; however, the intensity weighted distributions were multimodal (Figure 3.11), which consequently discredits these values as they do not truly reflect the particle size of the majority of the sample.

Although an indirect measurement, number weighted particle size distributions (D_n) can be derived from the intensity distributions using Mie theory[42] to give results that are more representative of the whole sample (Table 3.4). Analysis of these distributions for each of the branched copolymers gave monomodal traces (Figure 3.11) with similar D_n values ranging from 17 to 27 nm; the small particle sizes observed suggest the nanoparticles are formed by a solvent-switch rather than conventional nanoprecipitation, leading to very small structures without subsequent aggregation.

In all cases, a small peak at approximately 5000 nm was observed in the intensity weighted distributions which may be due to multiple scattering, aggregates or dust. Attempts were made to remove this small population by passing the samples through 1 µm PTFE filters; however, DLS measurements of the filtered samples retained this small population. To investigate further, the samples were passed through 0.22 µm PTFE filters, fully aware that the filtration may also remove the population at approximately 200-300 nm. Once again, this small population at 5000 nm was observed (Figure 3.12), suggesting a loosely self-assembled structure that is broken during filtration, but quickly re-assembles afterwards. These populations at 200 nm and 5000 nm could potentially be attributed to the linear polymers present within the sample that did not form part of the branched architecture (Figure 3.9), which self-assemble into large structures upon rapid addition to the aqueous media.

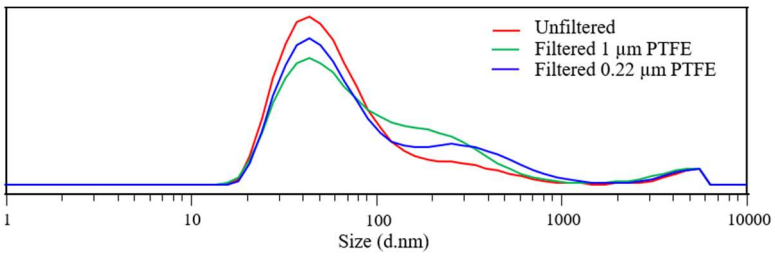

Figure 3.12. DLS traces of the aqueous dispersion of PEG-*b*-*p*(*n*BuMA$_{60}$-*co*-EGDMA$_{0.95}$), before and after filtration.

It was believed that these small populations were loose associations rather than aggregations, which would break upon dilution to give a monomodal, intensity weighted particle size distribution. Therefore, a small study was performed to determine if this was the case; this involved taking aliquots of the unfiltered PEG-*b*-*p*(*n*BuMA$_{60}$-*co*-EGDMA$_{0.95}$) sample, and diluting with H_2O to give various concentrations of the nanoparticles within the aqueous media, which were then left to roll overnight. DLS measurements were recorded at 25 °C after having set the attenuator and measurement position constant: attenuator = 7, and measurement position = 4.65 mm.

Analysis of the results show no change in either the D_z or the D_n values upon dilution, with only the derived count rate decreasing approximately by a factor of 2 with each dilution (Table 3.5). Furthermore, very little change can be observed in both the intensity weighted and number weighted particle size distributions (Figure 3.13).

Table 3.5. Dynamic light scattering data of the PEG-*b*-*p*(*n*BuMA$_{60}$-*co*-EGDMA$_{0.95}$) branched copolymer after various dilutions in H_2O

Concentration	DLS [a]		
	D_z (d. nm) [b]	D_n (d. nm) [c]	Derived count rate (kcps)
1 mg mL^{-1}	54	26	12 000
0.5 mg mL^{-1}	54	26	6 500
0.25 mg mL^{-1}	54	27	3 250
0.125 mg mL^{-1}	53	28	1750

[a] DLS measurements recorded at 25 °C after an equilibration period of 2 minutes, with the attenuator set equal to 7 and the measurement position set at 4.65 mm. [b] Size distribution using *z*-average values. [c] Size distribution using number average values.

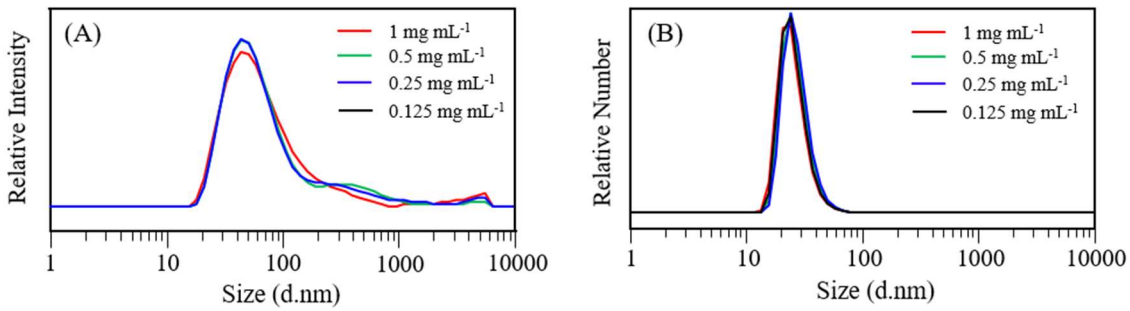

Figure 3.13. DLS traces of PEG-*b*-*p*(*n*BuMA$_{60}$-*co*-EGDMA$_{0.95}$) after dilution to various concentrations in H_2O: (A) intensity weighted particle size distribution, and (B) number weighted particle size distribution.

3.8. Conclusion

In conclusion, monofunctional and bifunctional PEG macroinitiators - synthesised *via* esterifications with *α*-bromo isobutyryl bromide - were used to initiate the methanolic ATRP of *n*BuMA at 60 °C, targeting various degrees of polymerisation, yielding well-defined AB diblock ($Đ$ = 1.02-1.05) and ABA triblock ($Đ$ = 1.13, 1.18) amphiphilic copolymers; however, analysis by triple detection GPC calculated M_n values greater than the theoretical values, indicating poor initiation efficiencies.

Kinetic studies were performed under the same reaction conditions using each of the monofunctional PEG-Br macroinitiators, targeting a DP_n = 80 monomer units; linear correlations were observed in semi-logarithmic plots of $\ln([M]_0/[M])$ *vs.* time, and in plots of M_n *vs.* conversion, indicating a well-controlled ATRP where the consumption of monomer follows first order kinetics and termination reactions are negligible.

The synthesis of PEG_x-*b*-*p*(*n*BuMA) diblock copolymers were also achieved at a lower temperature of 25 °C, with GPC analysis indicating higher initiation efficiencies but showing broader molecular weight distributions ($Đ$ = 1.20-1.32) compared to those obtained at 60 °C.

Branched polymerisations were performed at 60 °C using the PEG_{113}-Br macro-initiator and EGDMA as the branching monomer, yielding amphiphilic branched copolymers with M_w values as high as 2.33 x 10^6 g mol^{-1}.

Nanoprecipitations of these branched copolymers into H_2O gave stable nanoparticles in aqueous media, sterically stabilised by the PEG functionalities; although DLS studies showed multimodal intensity weighted particle size distributions, the number weighted distributions showed monomodal traces with D_n = 17-27 nm.

Although encapsulation and pharmacological studies were not performed, it is thought that the synthesised amphiphilic branched copolymers bearing PEG surface functionalities are interesting materials with potential drug-delivery applications that have high relevance to nanomedicine with regards to passively targeting tumours. Furthermore, the establishment of reaction conditions to form amphiphilic materials can be regarded as a key tool that will enable the future development of more complex branched structures.

3.9. References

1 A. Kolate, D. Baradia, S. Patil, I. Vhora, G. Kore and A. Misra, *J. Control. Release*, 2014, **192**, 67–81.

2 J. S. Suk, Q. Xu, N. Kim, J. Hanes and L. M. Ensign, *Adv. Drug Deliv. Rev.*, 2015, DOI: 10.1016/j.addr.2015.09.012.

3 C. Giacomelli, V. Schmidt and R. Borsali, *Macromolecules*, 2007, **40**, 2148–2157.

4 L. Yuan, W. Chen, J. Li, J. Hu, J. Yan and D. Yang, *J. Polym. Sci. Part A Polym. Chem.*, 2012, **50**, 4579–4588.

5 J. Hu, M. R. Whittaker, S. H. Yu, J. F. Quinn and T. P. Davis, *Macromolecules*, 2015, **48**, 3817–3824.

6 J. M. J. Frechet, M. Henmi, I. Gitsov, S. Aoshima, M. R. Leduc and R. B. Grubbs, *Science (80-.).*, 1995, **269**, 1080–1083.

7 S. G. Gaynor, S. Edelman and K. Matyjaszewski, *Macromolecules*, 1996, **29**, 1079–1081.

8 C. Porsch, Y. Zhang, C. Ducani, F. Vilaplana, L. Nordstierna, A. M. Nyström and E. Malmström, *Biomacromolecules*, 2014, **15**, 2235–2245.

9 R. W. Graff, X. Wang and H. Gao, *Macromolecules*, 2015, **48**, 2118–2126.

10 M. Rikkou-Kalourkoti, M. Elladiou and C. S. Patrickios, *J. Polym. Sci. Part A Polym. Chem.*, 2015, **53**, 1310–1319.

11 S. Ghosh Roy and P. De, *Polym. Chem.*, 2014, **5**, 6365–6378.

12 K. Wang, H. Peng, K. J. Thurecht, S. Puttick and A. K. Whittaker, *Biomacromolecules*, 2015, **16**, 2827–2839.

13 J. Flory, *J. Am. Chem. Soc.*, 1941, **63**, 3083–3090.

14 P. J. Flory, *J. Am. Chem. Soc.*, 1941, **63**, 3091–3096.

15 P. J. Flory, *J. Am. Chem. Soc.*, 1941, **63**, 3096–3100.

16 W. H. Stockmayer, *J. Chem. Phys.*, 1943, **11**, 45.

17 W. H. Stockmayer, *J. Chem. Phys.*, 1944, **12**, 125.

18 J. Rosselgong, S. P. Armes, W. R. S. Barton and D. Price, *Macromolecules*, 2010, **43**, 2145–2156.

19 H. Gao, A. Miasnikova and K. Matyjaszewski, *Macromolecules*, 2008, **41**, 7843–7849.

20 W. Li, J. A. Yoon, M. Zhong and K. Matyjaszewski, *Macromolecules*, 2011, **44**, 3270–3275.

21 N. O'Brien, A. McKee, D. C. Sherrington, A. T. Slark and A. Titterton, *Polymer (Guildf).*, 2000, **41**, 6027–6031.

22 P. . Costello, I. . Martin, A. . Slark, D. . Sherrington and A. Titterton, *Polymer (Guildf).*, 2002, **43**, 245–254.

23 F. Isaure, P. a G. Cormack, S. Graham, D. C. Sherrington, S. P. Armes and V. Bütun, *Chem. Commun.*, 2004, 1138–1139.

24 H.-J. Yang, B.-B. Jiang, W.-Y. Huang, D.-L. Zhang, L.-Z. Kong, J.-H. Chen, C.-L. Liu, F.-H. Gong, Q. Yu and Y. Yang, *Macromolecules*, 2009, **42**, 5976–5982.

25 D. C. Bouhier, Marc-henri; Cormack, Peter A. G.; Graham, Susan; Sherrington, *J. Polym. Sci. Part a-Polymer Chem.*, 2007, **45**, 2375–2386.

26 X. Xue, Y. Wang, W. Huang, H. Yang, J. Chen, J. Fang, Y. Yang, L. Kong and B. Jiang, *Macromol. Chem. Phys.*, 2015, **216**, 1555–1561.

27 B. Liu, A. Kazlauciunas, J. T. Guthrie and S. Perrier, *Macromolecules*, 2005, **38**, 2131–2136.

28 C.-D. Vo, J. Rosselgong, S. P. Armes and N. C. Billingham, *Macromolecules*, 2007, **40**, 7119–7125.

29 Y. Li and S. P. Armes, *Macromolecules*, 2005, **38**, 8155–8162.

30 I. Bannister, N. C. Billingham, S. P. Armes, S. P. Rannard and P. Findlay, *Macromolecules*, 2006, **39**, 7483–7492.

31 F. L. Hatton, L. M. Tatham, L. R. Tidbury, P. Chambon, T. He, A. Owen and

S. P. Rannard, *Chem. Sci.*, 2015, **6**, 326–334.

32 S. M. D'Addio and R. K. Prud'homme, *Adv. Drug Deliv. Rev.*, 2011, **63**, 417–426.

33 E. Lepeltier, C. Bourgaux and P. Couvreur, *Adv. Drug Deliv. Rev.*, 2014, **71**, 86–97.

34 C. Zhang, V. J. Pansare, R. K. Prud'homme and R. D. Priestley, *Soft Matter*, 2012, **8**, 86–93.

35 R. A. Slater, T. O. McDonald, D. J. Adams, E. R. Draper, J. V. M. Weaver and S. P. Rannard, *Soft Matter*, 2012, **8**, 9816–9827.

36 H. E. Rogers, P. Chambon, S. E. R. Auty, F. Y. Hern, A. Owen and S. P. Rannard, *Soft Matter*, 2015, **11**, 7005–7015.

37 J. Ford, P. Chambon, J. North, F. L. Hatton, M. Giardiello, A. Owen and S. P. Rannard, *Macromolecules*, 2015, **48**, 1883–1893.

38 M. Long, D. W. Thornthwaite, S. H. Rogers, G. Bonzi, F. R. Livens and S. P. Rannard, *Chem. Commun.*, 2009, 6406–6408.

39 D. Lu, M. D. Hossain, Z. Jia and M. J. Monteiro, *Macromolecules*, 2015, **48**, 1688–1702.

40 J. Rolland, E. Poggi, A. Vlad and J.-F. Gohy, *Polymer (Guildf).*, 2015, **68**, 344–352.

41 N. Hadjichristidis, S. Pispas and G. Floudas, *Block Copolymers: Synthetic Strategies, Physical Properties, and Applications*, John Wiley & Sons, Inc., Hoboken, New Jersey, 2002.

42 Malvern, *http://www.malvern.com/en/support/resource-center/Whitepapers/WP100108MieTheoryHundred.aspx*, Accessed October 2015.

Chapter 4

Synthesis of Hyperbranched Glycopolydendrons Bearing Galactose Surface Functionalities

4.1. Introduction

4.1.1. Hepatocellular carcinoma and the asialoglycoprotein receptor

Hepatocellular carcinoma accounts for approximately 85-90 % of primary liver cancers – one of the most common causes of cancer mortality worldwide despite its early diagnosis, with an estimated 745,000 deaths in 2012 alone.[1,2,3] It can be treated by anti-cancer therapy, but serious issues remain; in most cases, a strong resistance to anti-cancer drugs are shown, and patients generally have a poor tolerance to chemotherapy due to liver dysfunction.[4] To address these issues, research is directed towards developing drug delivery systems that actively target hepatocytes to improve the efficacy of the treatment and avoid undesirable side-effects.

An interesting target is the asialoglycoprotein receptor (ASGPR) - a C-type lectin abundantly expressed on hepatocytes that has a high affinity for D-galactose (Gal) and N-acetylgalactosamine (GalNAc) residues.[5] Cellular internalisation by clathrin enabled receptor-mediated endocytosis is rapidly induced through polyvalent and calcium-dependent interactions between these residues and the carbohydrate recognition domains present on ASGPR.

4.1.2. Galactose-functionalised polymers targeting ASGPR on hepatocytes

Biessen and coworkers reported the synthesis of a series of amphiphilic glycolipids containing a multivalent dendritic galactosylated head-group, whose incorporation into liposomes (5 wt% loading) resulted in efficient recognition and cellular uptake by the liver.[6] A small study was performed that involved monitoring the rate of internalisation of the galactosylated liposomes in the presence of free asialofetuin – an established competitor for ASGPR-mediated uptake;[7,8] the results showed almost complete inhibition by the asialofetuin, thereby confirming that cellular internalisation of the liposomes proceeded *via* interactions between the galactose moieties and the hepatic ASGPR receptors.

Zhuo and coworkers reported the synthesis of galactosylated and fluorescein isothiocyanate labelled polycaprolactone-*g*-dextran graft copolymers that could self-assemble into spherical micelles (approx. 120 nm) in aqueous media and in serum. Both *in vivo* and *in vitro* studies showed that the galactosylated micelles could be

selectively internalised into HepG2 cells - a human hepatocellular liver carcinoma cell line – through interactions with ASGPR receptors.[9]

More recently, Narain and coworkers reported the synthesis of galactosylated block and statistical cationic copolymers of varying compositions and molecular weights *via* RAFT polymerisation of 2-lactobionamidoethyl methacrylamide (LAEMA) and 2-aminoethyl methacrylamide hydrochloride (AEMA).[10] Evaluation of their transfection efficiencies in HepG2 and Huh7.5 cells found that the block copolymer with composition *p*($AEMA_{58}$-*b*-$LAEMA_{56}$) showed the highest transfection efficiency, driven by the interactions of the galactose functionalities with the overexpressed ASGPR of hepatocytes. In a similar study to that performed by Biessen and coworkers described above, a competitive assay of transfection and cellular uptake of the copolymers in the presence of free asialofetuin was performed on HepG2 cells; this resulted in significant reduction in transfection efficiency of the copolymers. Additionally, transfection efficiencies of the copolymers in ASGPR deficient cells (HeLa and SK hep1 cells) was negligible, emphasising the specificity of these polymers towards ASGPR receptors.

Other interesting studies detailing the syntheses of galactosylated polymers that have the potential to target ASGPR receptors on hepatocytes have been reported by Pan[11] and coworkers, Gillies[12] and coworkers, Huang[13] and coworkers, and Akaike[14] and coworkers.

4.1.3. The Michael addition reaction

The Michael addition (named after the organic chemist, Arthur Michael) is an example of a conjugate addition that involves the reaction between nucleophiles (Michael donors) and olefins/alkynes (Michael acceptors), where the nucleophile adds across a carbon-carbon multiple bond.[15] Generally, the Michael addition is considered as the base-catalysed addition of an enolate nucleophile to an *activated* olefin; described so due to the requirement of an electron-withdrawing and resonance-stabilising *activating* group that can stabilise the anionic intermediate. However, amines,[16–18] thiols[19,20] and phosphines[21,22] have also shown the ability to act as efficient nucleophiles, meaning that nucleophile selection is not limited to enolates; these reactions are typically referred to as Michael-*type* additions.

The reactions using nitrogen-based nucleophiles (often described as aza-Michael-type additions) do not require additional base due to the nucleophilicity and basicity of the amine functionality. In fact, primary amines are nucleophilic enough to react with two equivalents of a Michael acceptor to form tertiary amines; this is, however, highly dependent on the electronic and steric environment of the intermediate secondary amine formed after reaction with one equivalent of the acceptor. A well-known example of this type of reaction is the synthesis of PAMAM dendrimers, described in Chapter 1 (Section 1.3.1.1).[23]

4.1.4. Chapter aims

The aims of this Chapter were to synthesise galactose functionalised dendritic initiators (G0, G1 and G2) using exhaustive aza-Michael-type additions and esterification reactions, which would be utilised in the methanolic Cu-catalysed ATRP of *n*BuMA (Figure 4.1B). Linear polymerisations, targeting chain lengths of various chain DP_n values, were selected to assess the control of the polymerisations. Progression to branched copolymerisation in the presence of a low concentration of divinyl monomer, EGDMA, would yield galactosylated *hyp*-glycopolydendrons (Figure 4.1A). Deprotection strategies will be developed to yield amphiphilic materials that are capable of targeting hepatic ASGPR receptors; their ability to form stable nanoparticle dispersions in aqueous media will be assessed by performing rapid nanoprecipitation studies.

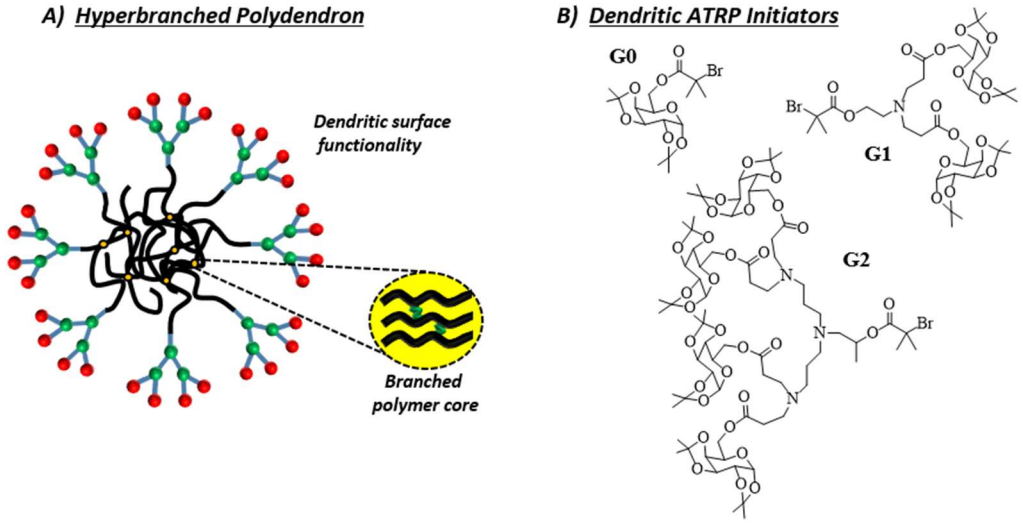

Figure 4.1. Schematic representation of: (A) a hyperbranched polydendron, showing the dendritic surface functionality and the branched polymer core, and (B) galactose functionalised dendritic initiators (G0, G1 and G2) prepared by a sequence of exhaustive aza-Michael-type additions and bromo-esterifications.

4.2. Synthesis of galactose functionalised dendritic initiators

Synthesis of the dendritic initiators (G0, G1 and G2) began using the commercially available 1,2:3,4-Di-*O*-isopropylidene-α-D-galactopyranose (proGal-OH [1]).

4.2.1 Synthesis of G0 galactose initiator

Synthesis of the G0 galactose initiator (G0-proGal-Br [2]) began by reacting proGal-OH [1] with α-bromo isobutyryl bromide in anhydrous dichloromethane (DCM) under an inert nitrogen atmosphere (Scheme 4.1). The reaction was catalysed by 4-dimethylaminopyridine (DMAP), and an excess of triethylamine (TEA) was used to scavenge the hydrogen bromide (HBr) side product. After reaction completion, the DCM was removed on the rotary evaporator to give a viscous brown coloured oily residue; the product was extracted from this residue using diethyl ether, with each extract passed through filter paper to remove the triethylammonium bromide ($Et_3N^+Br^-$) salt. After removal of the solvent on the rotary evaporator, the product was purified further by normal phase flash chromatography to give the G0-proGal-Br [2] initiator in 60 % yield. In comparison to the proGal-OH starting material, ^{1}H-NMR analysis of the purified product showed the disappearance of the broad resonance at 2.72 ppm attributed to the hydroxyl group, and the appearance of a resonance at 1.95 ppm attributed to the isobutyryl group introduced as a result of the bromo-esterification (Figures 4.2 and 4.3). Furthermore, ^{13}C-NMR analysis revealed resonances at 31 ppm, 57 ppm and 173 ppm that are attributed to the C(=O)C(**C**H_3)$_2$Br, C(=O)**C**$(CH_3)_2$Br and **C**(=O)C$(CH_3)_2$Br carbon environments, respectively (Figure 4.4), and electrospray ionisation (ESI) mass spectrometry showed a molecular ion $[M+Na]^+$ peak at 433 Da (Figure 4.5). Further NMR studies were also performed that included one-dimensional APT experiments and two-dimensional COSY and HSQC experiments, all of which enabled the assignment of each proton and carbon environment within the compound; the spectra are presented in the Appendix (Figures A19-A21).

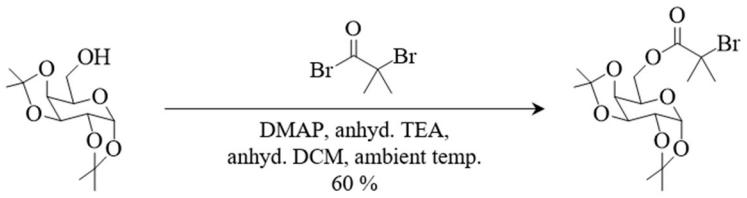

proGal-OH; [1] **G0-proGal-Br; [2]**

Scheme 4.1. Reaction scheme detailing the synthesis of the G0-proGal-Br ATRP initiator.

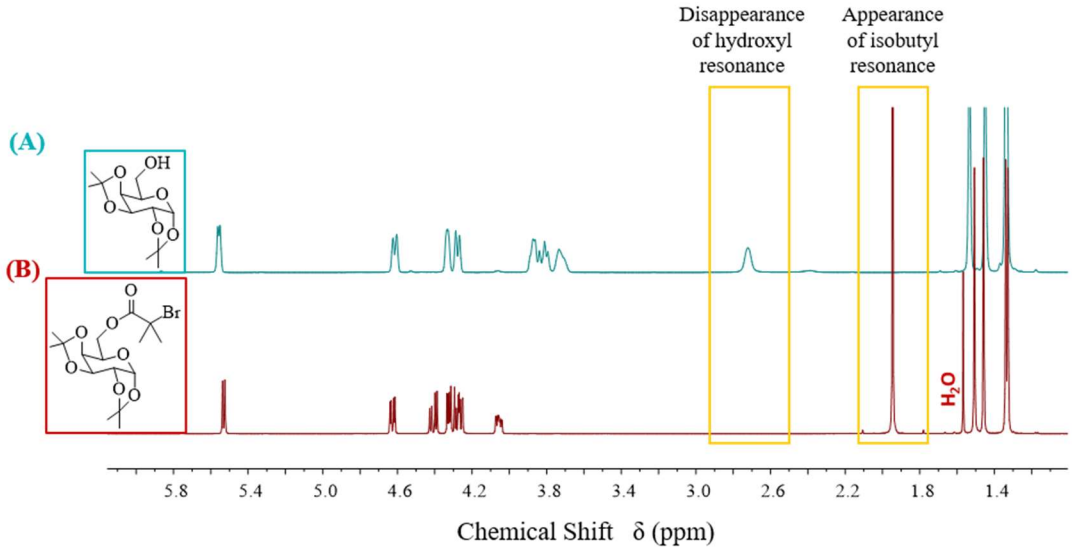

Figure 4.2. ^{1}H-NMR ($CDCl_3$) of: (A) proGal-OH [1], and (B) G0-proGal-Br [2]. The observed disappearance of the resonance attributed to the hydroxyl group and the appearance of a resonance attributed to the isobutyryl group are highlighted by the yellow boxes.

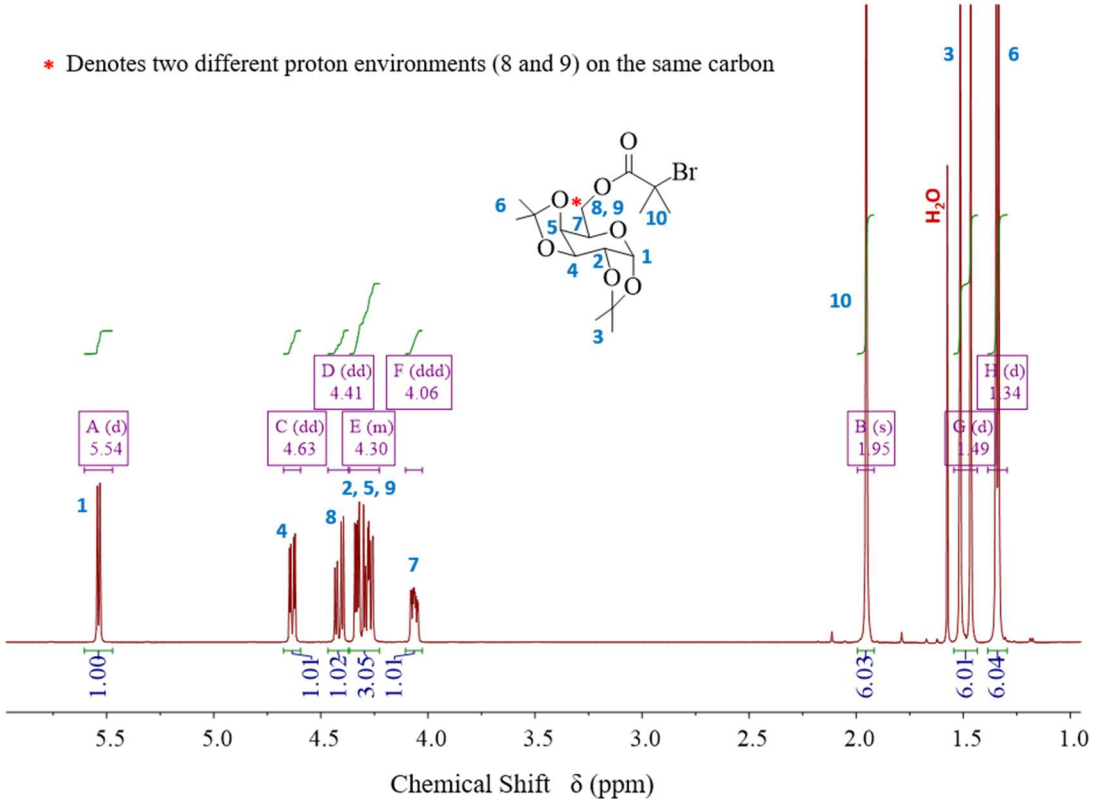

Figure 4.3. ^{1}H-NMR ($CDCl_3$) of G0-proGal-Br [2], showing the multiplicity and integrations of each environment after normalising the integration of the anomeric proton (1) at 5.54 ppm to 1H.

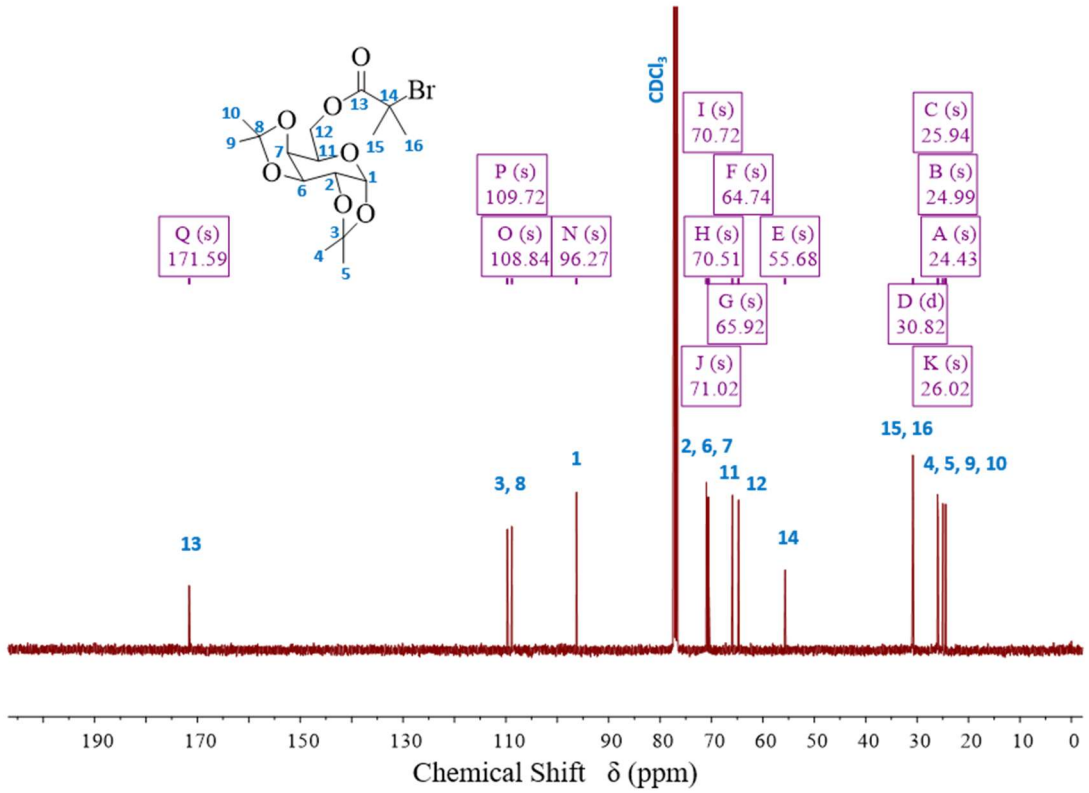

Figure 4.4. ^{13}C-NMR ($CDCl_3$) of G0-proGal-Br [2], showing a total of 16 carbon environments that matches the theoretical number.

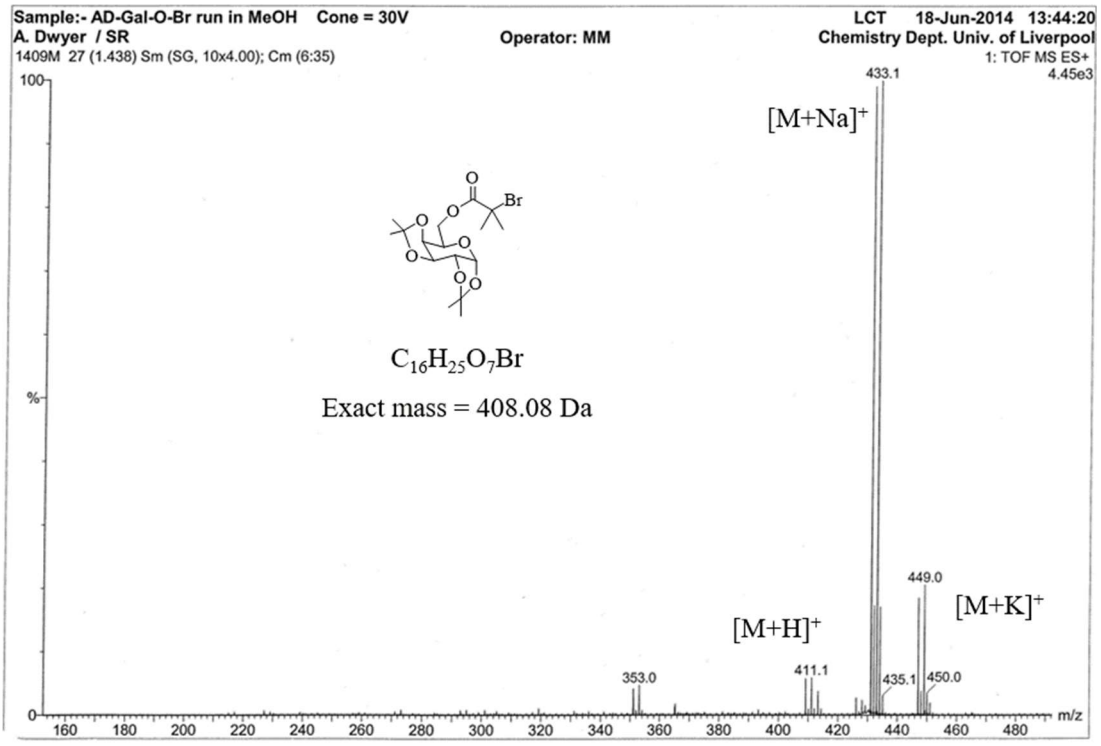

Figure 4.5. ESI mass spectrometry of G0-proGal-Br [2] showing the $[M+H]^+$, $[M+Na]^+$ and $[M+K]^+$ molecular ion peaks.

4.2.2 Synthesis of G1 galactose initiator

4.2.2.1. Synthesis of proGal-acrylate

Synthesis began by reacting proGal-OH [1] with acryloyl chloride in anhydrous DCM under an inert nitrogen atmosphere (Scheme 4.2); the reaction was catalysed by DMAP, and an excess of TEA was used to scavenge the HCl by-product, forming a $Et_3N^+Cl^-$ salt that precipitated from solution as the reaction progressed. After reaction completion, the salt was filtered off and washed with cold DCM before removing the solvent on the rotary evaporator (at 35 °C to avoid self-polymerisation) to give a brown coloured residue. The product was extracted from this residue using diethyl ether, with each extract filtered to remove residual $Et_3N^+Cl^-$ salt, before being concentrated and purified further by normal phase flash chromatography to give the proGal-acrylate [3] as a yellow coloured oil in 81 % yield. In comparison to the proGal-OH starting material, ^{1}H-NMR analysis of the purified product showed the disappearance of the broad resonance at 2.72 ppm attributed to the hydroxyl group, and the appearance of a further three resonances between 5.80-6.50 ppm attributed to the vinyl protons introduced as a result of the esterification (Figure 4.6; Figure A22, Appendix).

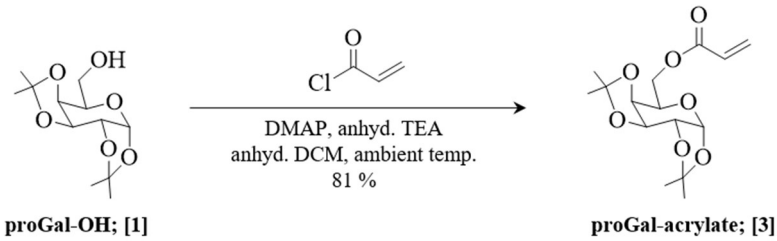

Scheme 4.2. Reaction scheme detailing the synthesis of proGal-acrylate.

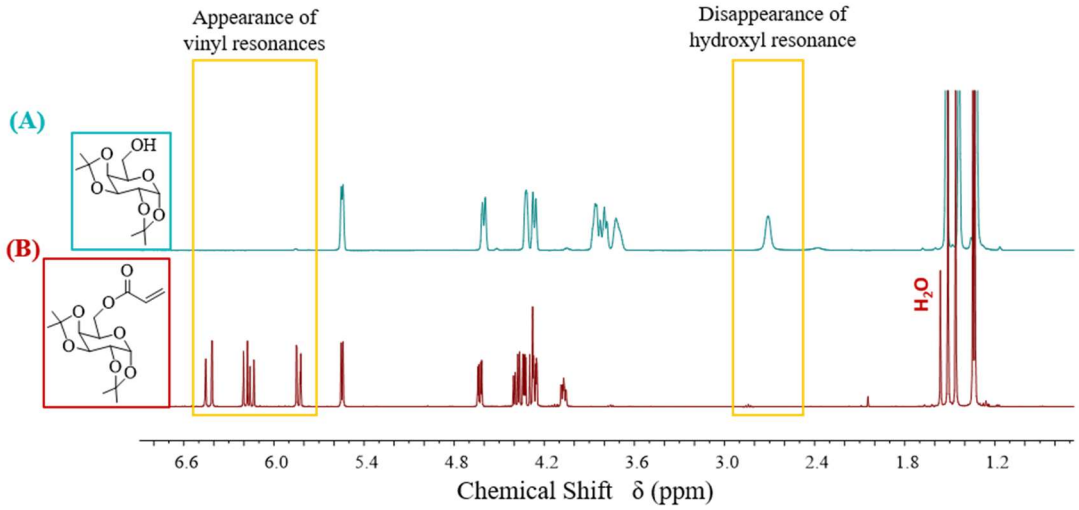

Figure 4.6. ^{1}H-NMR ($CDCl_3$) of: (A) proGal-OH, and (B) proGal-acrylate. The observed disappearance of the resonance attributed to the hydroxyl group and the appearance of resonances attributed to the vinyl group are highlighted by the yellow boxes.

Analysis by ^{13}C-NMR revealed the appearance of a peak at 166 ppm attributed to the ester carbonyl functionality, and a further two peaks between 127-132 ppm that can be assigned to each carbon of the vinyl functionality introduced by the esterification (Figure A23, Appendix).

4.2.2.2. Synthesis of G1-proGal-OH

The next step in the synthesis involved the reaction of ethanolamine with a 4-fold excess of proGal-acrylate [3] *via* aza-Michael-type additions; initially, a 35 % yield of the purified product was obtained when performing the reaction in DCM over 4 days, but this was increased to 74 % yield after repeating the reaction in IPA (Scheme 4.3); clearly, the protic solvent has a catalytic effect on the reaction. In comparison to the proGal-acrylate starting material, ^{1}H-NMR analysis showed the disappearance of the vinyl resonances between 5.80-6.50 ppm, and the appearance of two resonances at 2.58 ppm and 3.57 ppm - each integrating to 2H - that are attributed to the CH_2 environments of the ethanolamine moiety (Figure 4.7; Figure A24, Appendix). The appearance of a further two resonances at 2.51 ppm and 2.82 ppm - each integrating to 4H - can be assigned to the CH_2 environments introduced as a result of the aza-Michael-type addition. Additionally, ^{13}C-NMR ($CDCl_3$) analysis showed the disappearance of two peaks between 127-132 ppm attributed to each carbon of the vinyl functionality of proGal-acrylate [3], and the appearance of peaks at 49 ppm and 63 ppm attributed to the CH_2 environments introduced as a result of the aza-Michael-type addition (Figure A25, Appendix); ESI mass spectrometry analysis showed a $[M+H]^+$ molecular ion peak at 690 Da (Figure 4.8).

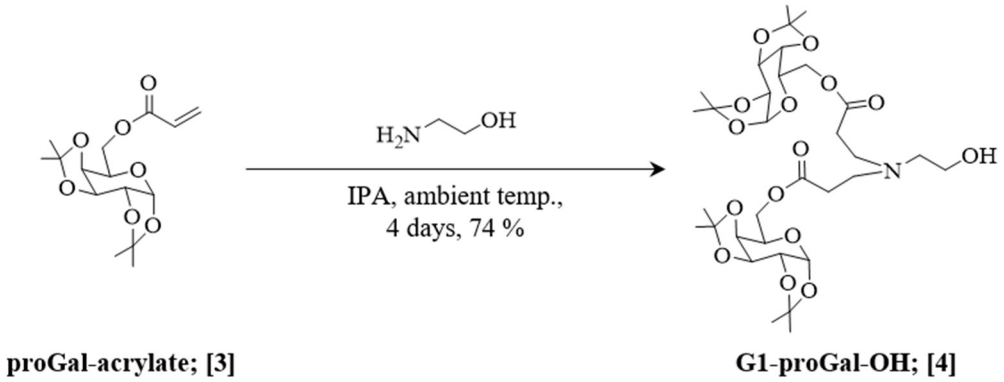

Scheme 4.3. Reaction scheme detailing the synthesis of G1-proGal-OH [4] *via* aza-Michael-type additions between ethanolamine and an excess of proGal-acrylate [3].

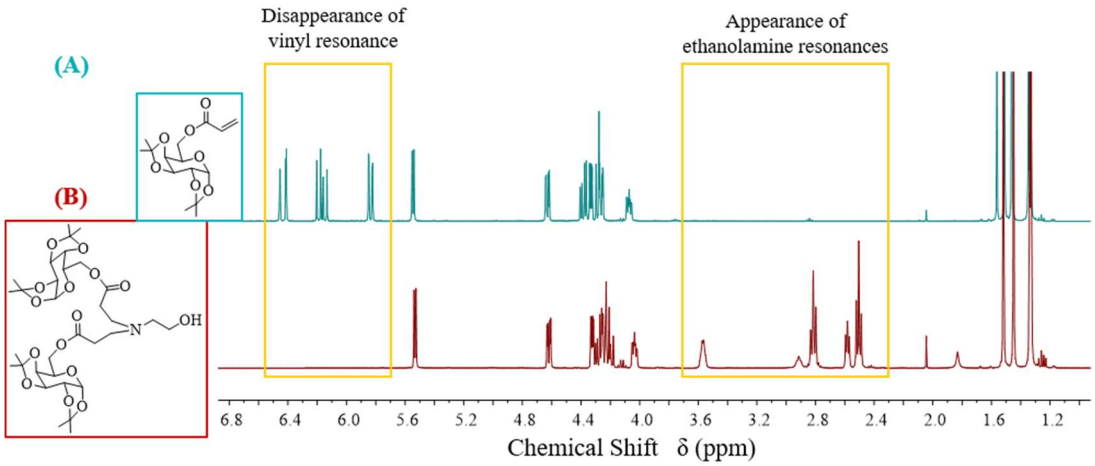

Figure 4.7. ^{1}H-NMR ($CDCl_3$) of: (A) proGal-acrylate [3], and (B) G1-proGal-OH [4]. The observed disappearance of the resonances attributed to the vinyl group and the appearance of resonances attributed to the ethanolamine group are highlighted by the yellow boxes.

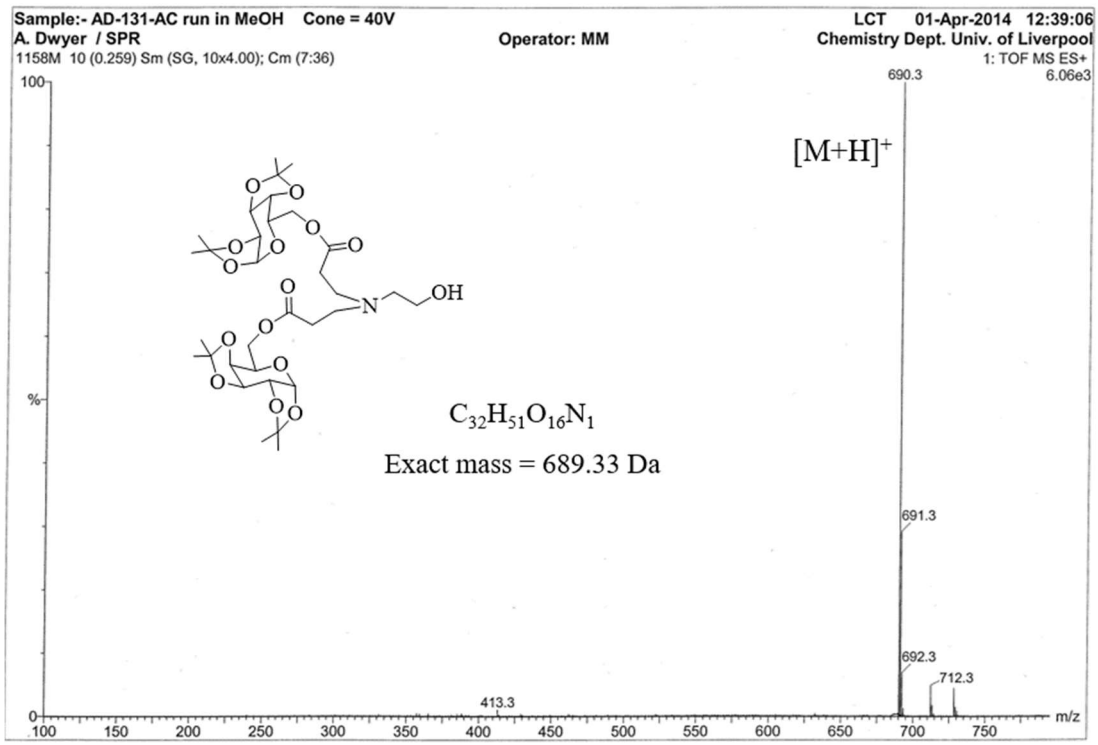

Figure 4.8. ESI mass spectrometry analysis of G1-proGal-OH [4] showing the $[M+H]^+$ molecular ion peak.

4.2.2.3. Synthesis of G1-proGal-Br initiator

The final synthetic step involved the reaction between G1-proGal-OH [4] with α-bromo isobutyryl bromide in anhydrous DCM under an inert nitrogen atmosphere (Scheme 4.4). The reaction was catalysed by DMAP, and an excess of TEA was used to scavenge the HBr side product. After reaction completion, the DCM was removed on the rotary evaporator to give a viscous brown coloured oily residue; the product was extracted from this residue using diethyl ether, with each extract passed through filter paper to remove the triethylammonium bromide ($Et_3N^+Br^-$) salt. After removal of the solvent on the rotary evaporator, the product was purified further by normal phase flash chromatography to give G1-proGal-Br [5] initiator in 82 % yield. In comparison to the G1-proGal-OH [4] starting material, ^{1}H-NMR ($CDCl_3$) analysis of the purified product showed the disappearance of the broad resonance at 2.90 ppm attributed to the hydroxyl group, the appearance of a resonance at 1.95 ppm (integrating to approximately 6H) attributed to the isobutyryl group introduced as a result of the bromo-esterification, and a down-field shift for the resonances attributed to the CH_2 environments of the ethanolamine moiety (Figures 4.9 and 4.10). Furthermore, ^{13}C-NMR analysis revealed resonances at 31 ppm, 57 ppm and 173 ppm that are attributed to the C(=O)C(**C**H_3)$_2$Br, C(=O)**C**(CH_3)$_2$Br and **C**(=O)C(CH_3)$_2$Br carbon environments, respectively (Figure 4.11), and ESI mass spectrometry showed a molecular ion $[M+H]^+$ peak at 838 Da (Figure 4.12).

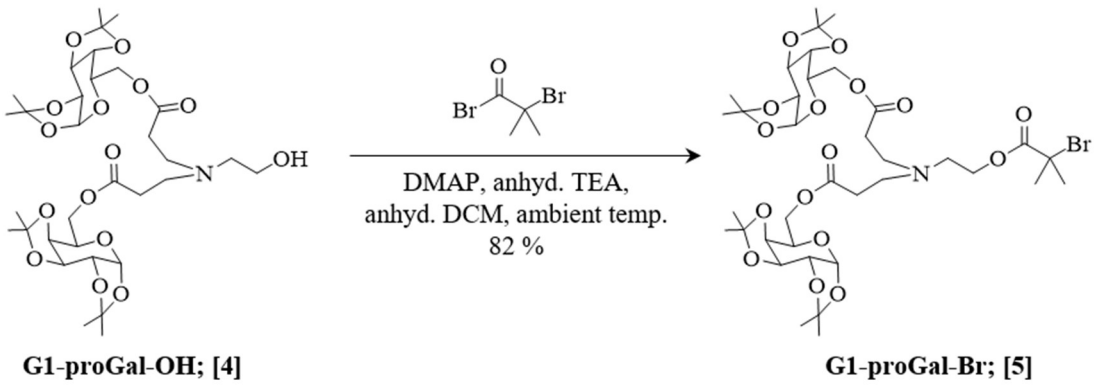

Scheme 4.4. Reaction scheme detailing the synthesis of the G1-proGal-Br [5] initiator.

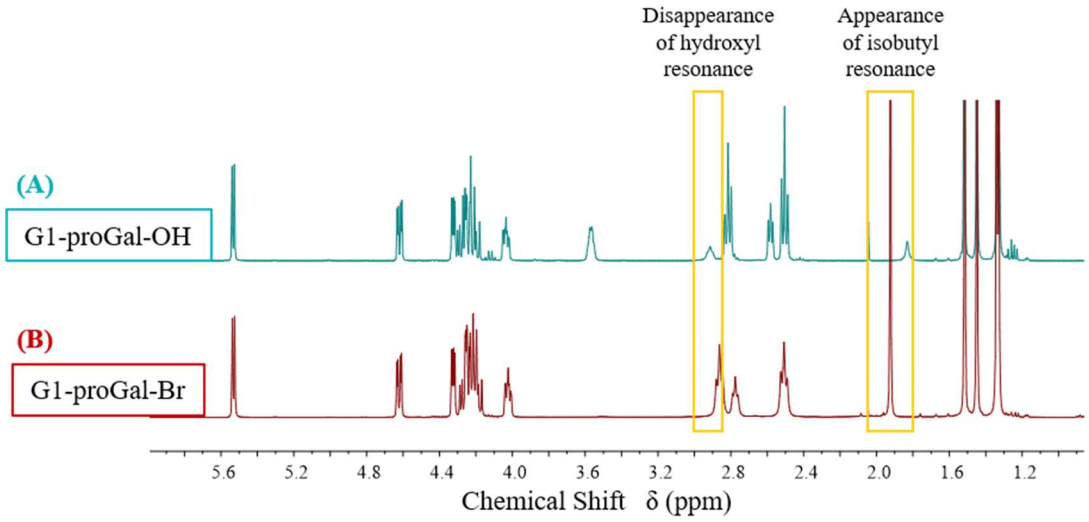

Figure 4.9. ^{1}H-NMR ($CDCl_3$) of: (A) G1-proGal-OH [4], and (B) G1-proGal-Br [5]. The observed disappearance of the resonance attributed to the hydroxyl group and the appearance of the resonance attributed to the isobutyryl group are highlighted by the yellow boxes.

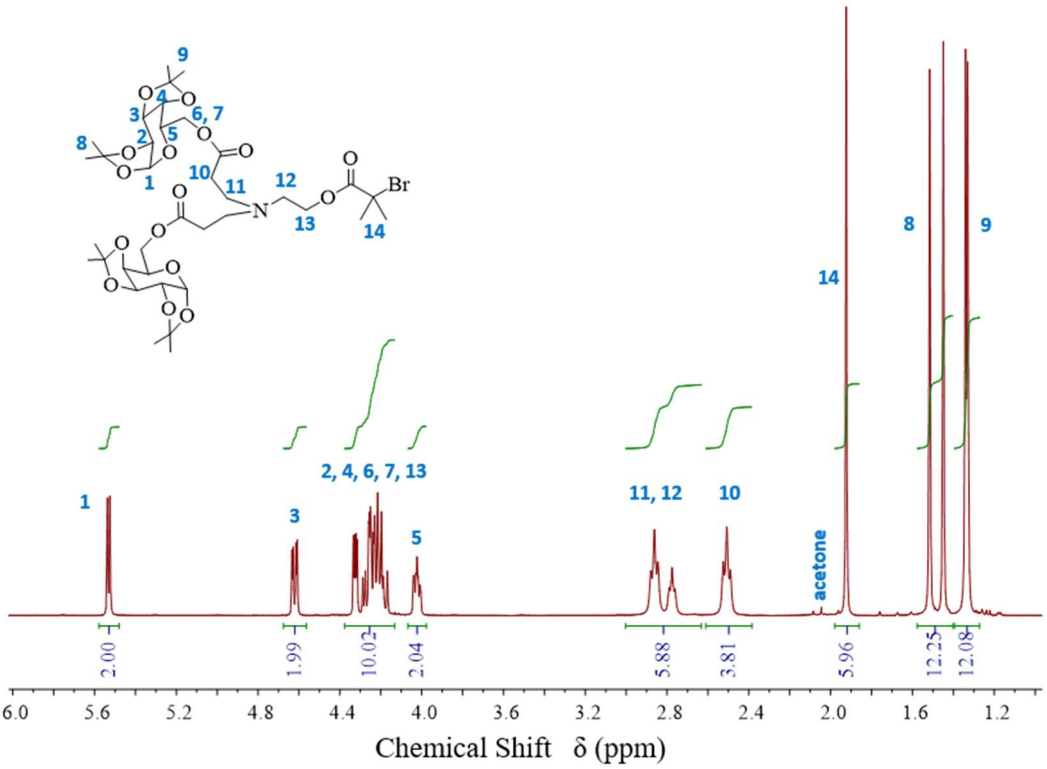

Figure 4.10. ^{1}H-NMR ($CDCl_3$) analysis of the G1-proGal-Br [5] initiator showing the assignment and integration of each proton environment.

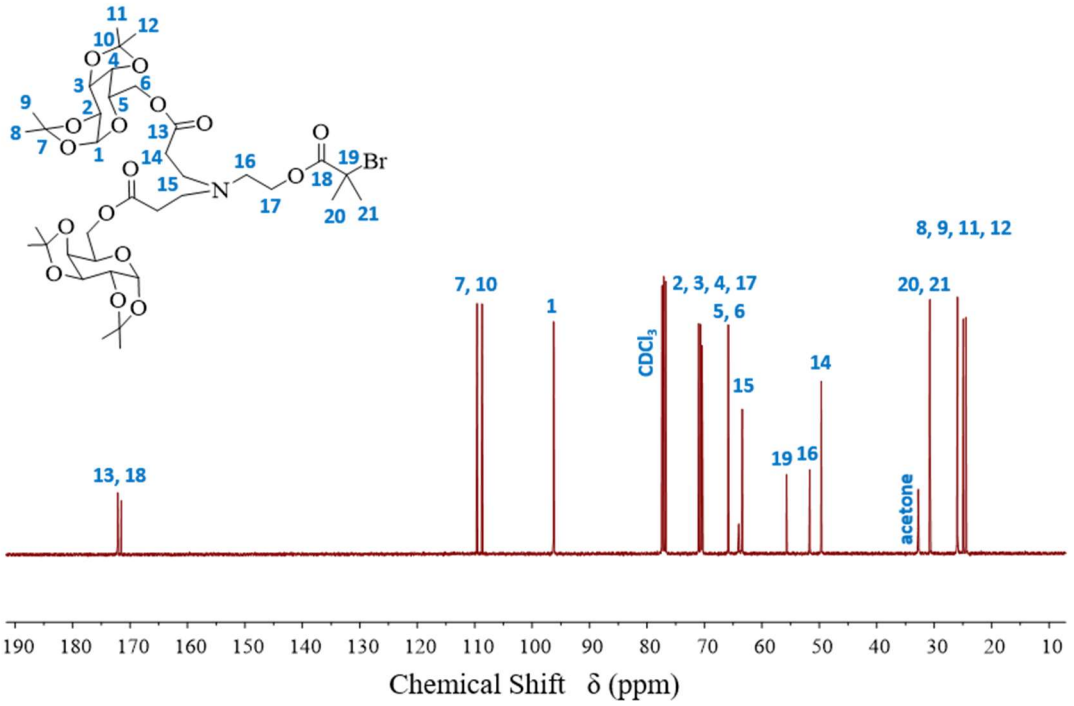

Figure 4.11. ^{13}C-NMR ($CDCl_3$) analysis of the G1-proGal-Br [5] initiator showing the assignment of each carbon environment.

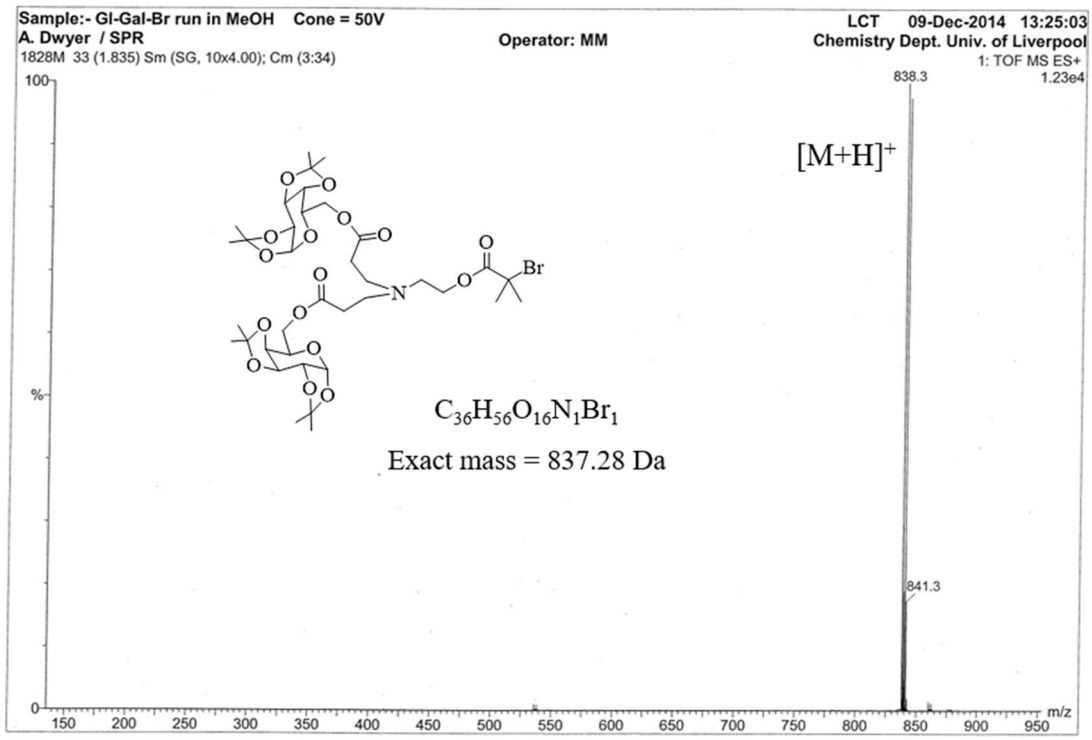

Figure 4.12. ESI mass spectrometry analysis of the G1-proGal-Br [5] initiator showing the $[M+H]^+$ molecular ion peak.

4.2.3. Synthesis of G2 galactose initiator

4.2.3.1. Synthesis of APAP branching unit

The synthesis of higher generation (G2) dendritic initiators bearing galactose functionalities *via* aza-Michael-type additions required an alternative organic compound with a greater degree of amine functionality; thus, the three-step synthesis of 1-[N, N-bis(2-aminopropyl)-amino]-2-propanol (APAP; [8]) was developed and this was used as an AB_2 branching unit.

Synthesis began by reacting a 2-fold excess of tertiary-butanol (*tert*-BuOH) with 1,1'-carbonyldiimidazole (CDI) in anhydrous toluene for 6 hours at 60 °C under an inert nitrogen atmosphere (Scheme 4.5), forming an imidazole carboxylic ester intermediate; an excess of *tert*-BuOH was used to ensure that the CDI coupling agent had been fully consumed, thereby preventing undesirable side-reactions in the next stage of the synthesis. After the dropwise addition of bis(3-aminopropyl)amine (BAPA), the reaction was stirred for a further 18 hours whilst maintaining the temperature at 60 °C; the reaction mixture was then cooled to ambient temperature, causing the imidazole by-product to precipitate from solution. This was subsequently filtered off and washed with toluene. The reaction solvent was removed on the rotary evaporator prior to further purification by repeated solvent-solvent extraction to give the intermediate product [6] as a white solid in 84 % yield. ^{1}H-NMR ($CDCl_3$) analysis showed resonances at 1.63 ppm, 2.65 ppm and 3.22 ppm - each integrating to approximately 4H - that are attributed to the CH_2 environments of the BAPA

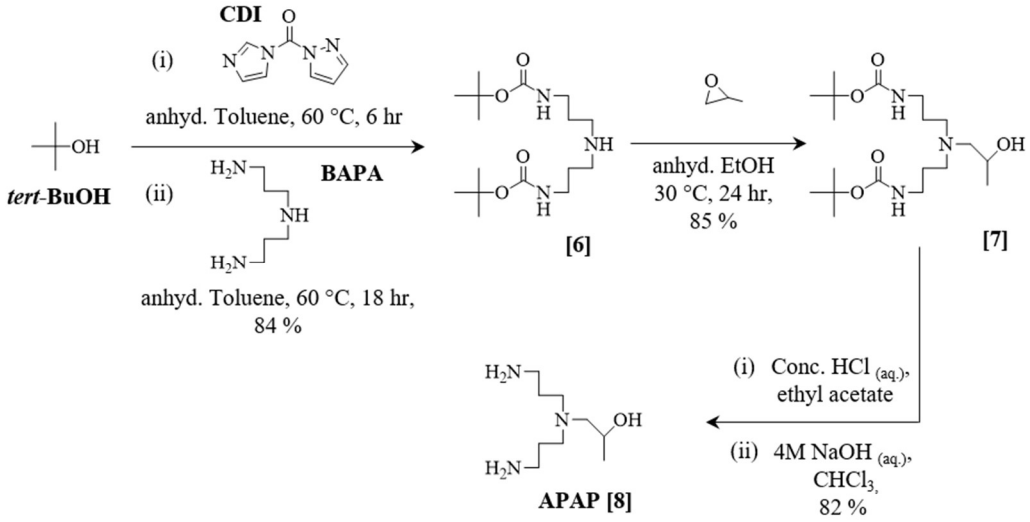

Scheme 4.5. Reaction scheme detailing the 3-step synthesis of the AB_2 branching moiety, APAP.

moiety, and a resonance at 1.44 ppm - integrating to approximately 18H - attributed to the *tert*-butoxycarbonyl functional group (Figure A26, Appendix).

The second synthetic step involved the ring-opening of propylene oxide (PO) after nucleophilic attack from the secondary amine functionality of the intermediate [6]; excess PO was removed under high vacuum, and further purification by normal phase flash chromatography afforded the second intermediate [7] in 85 % yield. ^{1}H-NMR ($CDCl_3$) analysis revealed resonances at 1.13 ppm, 2.32 ppm and 3.79 ppm that are attributed to the CH_3, CH_2 and CH environments introduced as result of the reaction (Figure A27, Appendix); furthermore, chemical ionisation mass spectrometry showed a $[M+H]^+$ molecular ion peak at 390 Da (Figure A28, Appendix).

The third synthetic step involved the cleavage of the *t*BOC protecting groups using concentrated hydrochloric acid (HCl) in ethyl acetate in an open-necked reaction flask, causing a significant evolution of CO_2 gas in the process. ^{1}H-NMR ($CDCl_3$) analysis allowed the reaction to be monitored by observing the disappearance of the resonance at 1.44 ppm attributed to the protecting groups, with complete deprotection achieved after stirring at ambient temperature for 4 hours followed by further stirring at 50 °C for 3 hours. Treatment with 4M sodium hydroxide ($NaOH_{aq}$) followed by solvent-solvent extractions gave the desired product [8] as a yellow coloured oil in 82 % yield. Characterisation by ^{1}H-NMR ($CDCl_3$), ^{13}C-NMR ($CDCl_3$) and ESI mass spectrometry confirmed the structure of the compound (Figures 4.13–4.15).

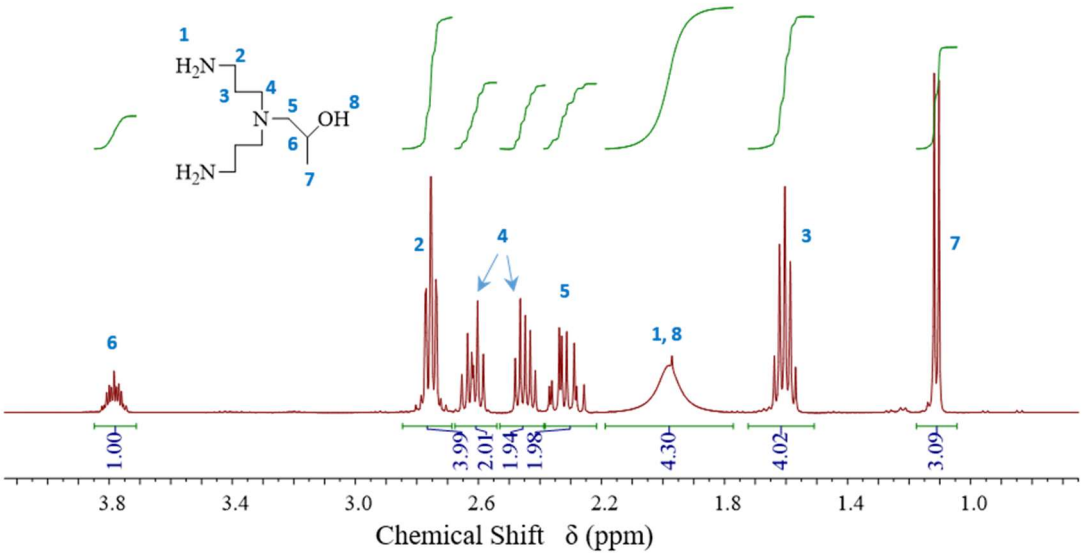

Figure 4.13. ^{1}H-NMR ($CDCl_3$) of APAP [8], showing the integration of each environment after normalising the peak at 3.78 ppm to 1H.

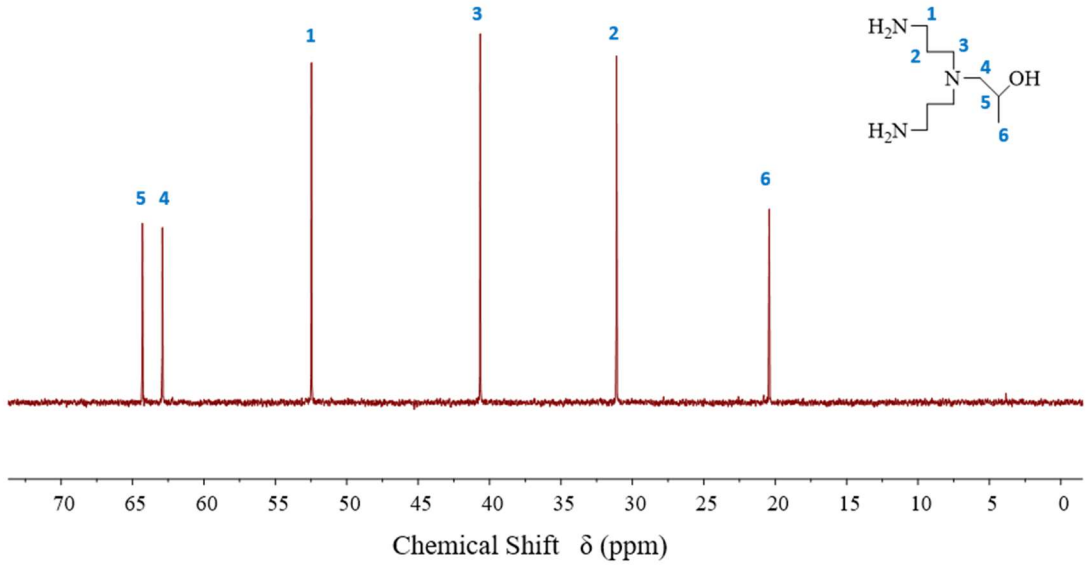

Figure 4.14. ^{13}C-NMR ($CDCl_3$) of APAP [8], showing 6 carbon environments that matches the theoretical number.

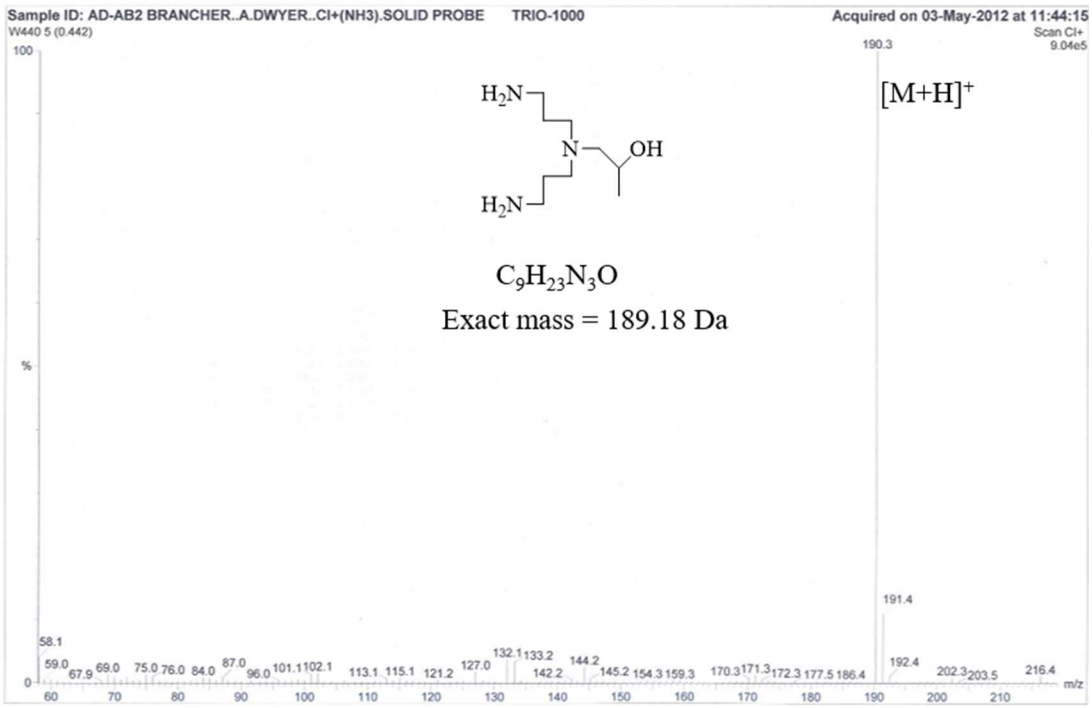

Figure 4.15. Chemical ionisation mass spectrometry analysis of APAP [8], showing the $[M+H]^+$ molecular ion peak.

4.2.3.2. Synthesis of G2-proGal-OH

The next step in the synthesis involved the 7-day reaction of APAP [8] with an 8-fold excess of proGal-acrylate [3] *via* aza-Michael-type additions in IPA at ambient temperature (Scheme 4.6). After reaction completion, the solvent was removed on the rotary evaporator, and the crude product was purified by normal phase flash chromatography to give the G2-proGal-OH [9] dendritic compound as pale-yellow coloured syrup in 76 % yield. In comparison to the proGal-acrylate [3] starting material, ^{1}H-NMR ($CDCl_3$) analysis showed the disappearance of the vinyl resonances between 5.80-6.50 ppm, and the appearance of resonances at approximately 2.20 ppm, 2.40 ppm and 3.70 ppm that are attributed to the CH_3, CH_2 and CH environments of the APAP branching unit, and the appearance of a further two resonances at approximately 2.50 ppm and 2.75 ppm that can be assigned to the CH_2 environments introduced as a result of the exhaustive aza-Michael-type addition (Figure 4.16). The integrations of each environment confirmed that a total of four protected galactose functionalities were present on the periphery of the dendritic compound (Figure A29, Appendix). Additionally, ^{13}C-NMR ($CDCl_3$) analysis showed the disappearance of two peaks between 127-132 ppm attributed to each carbon of the vinyl functionality of proGal-acrylate, and the appearance of peaks at 49 ppm and 63 ppm attributed to the CH_2 environments introduced as a result of the aza-Michael-type addition (Figure A30, Appendix); ESI mass spectrometry analysis showed a $[M+H]^+$ molecular ion peak at 1,447 Da (Figure 4.17).

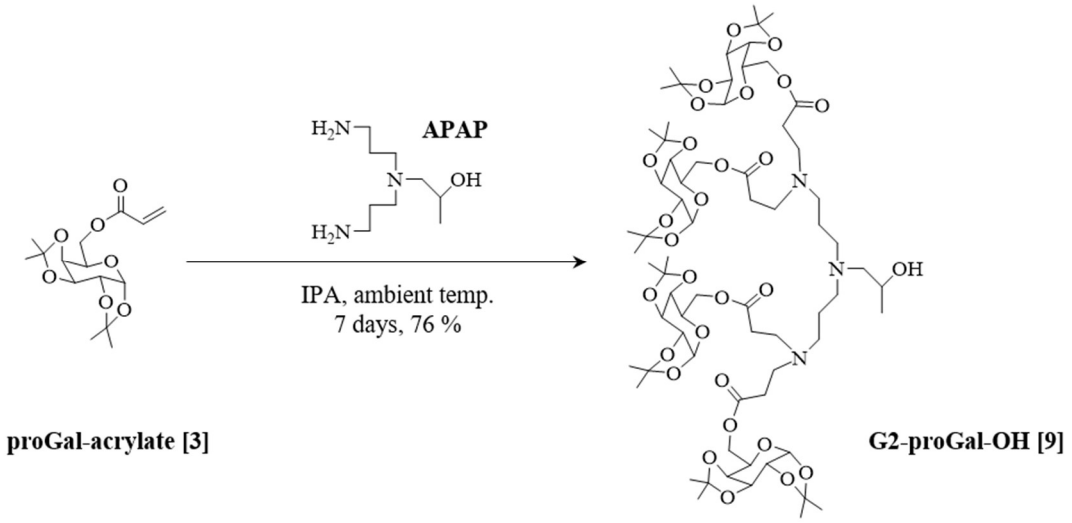

Scheme 4.6. Reaction scheme detailing the synthesis of G2-proGal-OH [9] by aza-Michael-type additions between proGal-acrylate [3] and APAP [8].

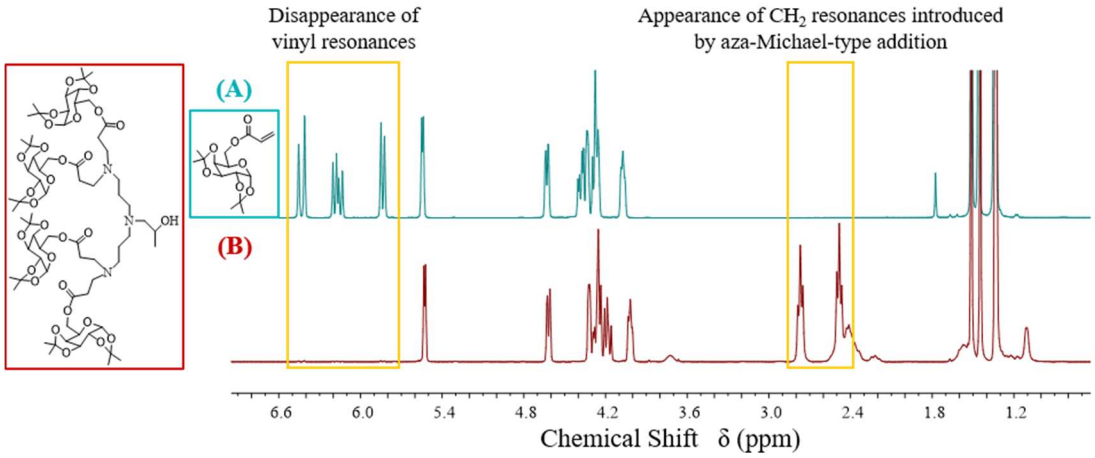

Figure 4.16. ^{1}H-NMR ($CDCl_3$) of: (A) proGal-acrylate [3], and (B) G2-proGal-OH [9]. The observed disappearance of the vinyl resonances and the appearance of resonances attributed to the CH_2 environments introduced as a result of the aza-Michael-type additions are highlighted by the yellow boxes.

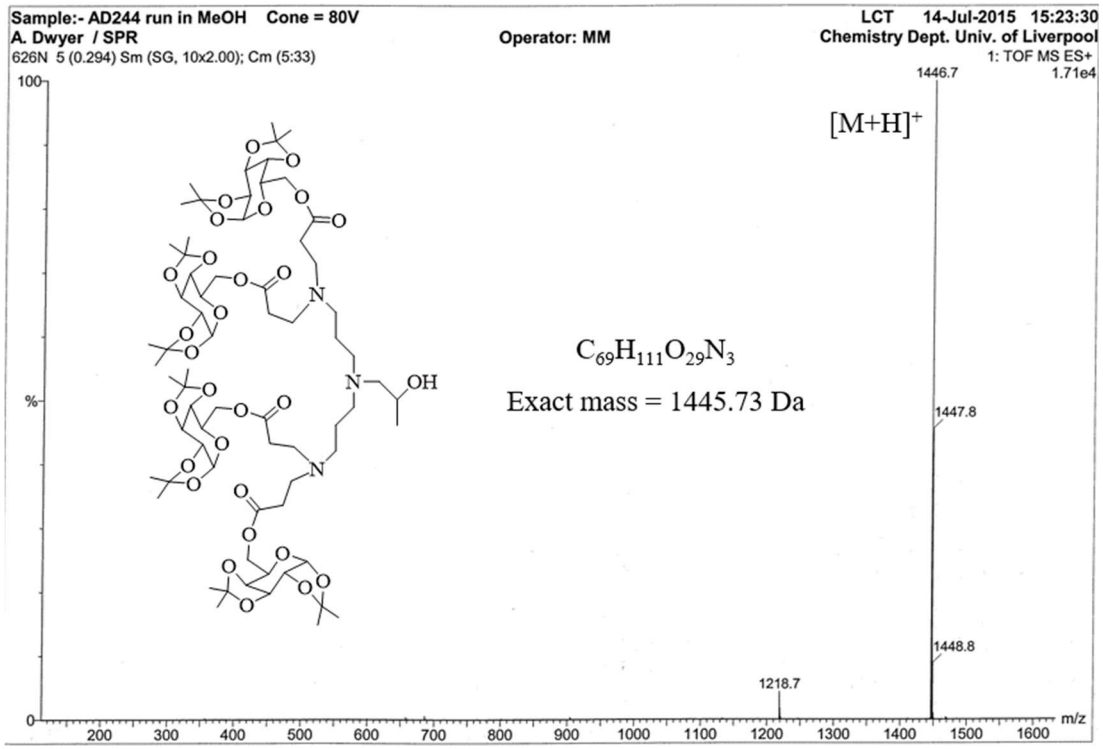

Figure 4.17. ESI mass spectrometry analysis of G2-proGal-OH [9] showing the $[M+H]^+$ molecular ion peak.

4.2.3.3. Synthesis of G2-proGal-Br initiator

The final step in the synthesis involved the reaction between G2-proGal-OH [9] and α-bromo isobutyryl bromide in anhydrous DCM under an inert nitrogen atmosphere (Scheme 4.7). The reaction was catalysed by DMAP, and a three-fold excess of TEA was used to scavenge the HBr side product. After reaction completion, the DCM was removed on the rotary evaporator to give a viscous brown coloured oily residue that was then purified by normal phase flash chromatography to give the G2-proGal-Br [10] initiator in 68 % yield. ^{1}H-NMR ($CDCl_3$) analysis showed a shift in resonance attributed to the CH environment of the APAP moiety from 3.70 ppm to approximately 5.20 ppm, thereby suggesting that the esterification had indeed taken place (Figure 4.18). However, an unusual group of resonances between 1.85-2.00 ppm were observed rather than the expected singlet attributed to the isobutyryl functionality (Figure 4.18(B)). Initially, it was thought that this could potentially be due to different orientations of the isobutyryl functional group over the saccharide ring structure that have different chemical shifts as a consequence of various through-space intramolecular interactions, but it was later realised that the tertiary amines of the dendritic compound were scavenging the HBr by-product rather than the excess TEA, with the resulting protonated amines causing unexpected shifts for various resonances.

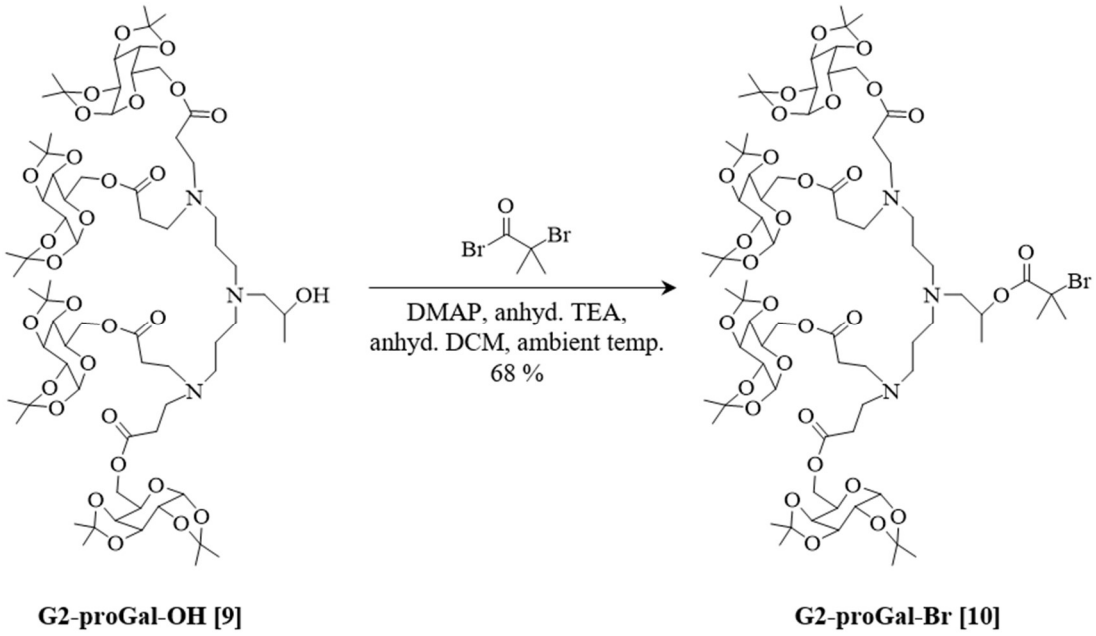

Scheme 4.7. Reaction scheme detailing the synthesis of G2-proGal-Br.

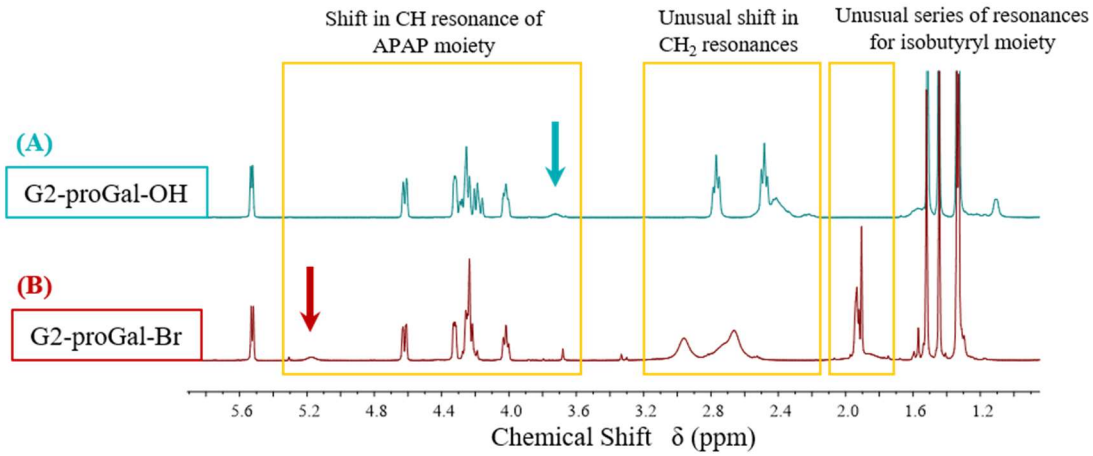

Figure 4.18. ^{1}H-NMR ($CDCl_3$) of: (A) G2-proGal-OH [9], and (B) G2-proGal-Br [10]. The observed shift of the CH resonance of the APAP moiety from 3.70 ppm to 5.20 ppm is highlighted by the yellow box. However, an unexpected shift in CH_2 resonances, and the appearance of a group of unusual resonances attributed to the isobutyryl group were also observed; they, too, are highlighted by yellow boxes.

In an attempt to deprotonate these amines, 4M $NaOH_{aq}$ was added to G2-proGal-Br [10] in THF, and the solution was then stirred for 30 minutes at ambient temperature. After removing the solvent on the rotary evaporator, the crude product was re-purified by normal phase flash chromatography and dried *in vacuo*. ^{1}H-NMR ($CDCl_3$) analysis showed an up-field shift for the CH resonance of the APAP moiety from 5.20 ppm to 5.00 ppm, and an up-field shift for the CH_2 resonances (introduced as a result of the aza-Michael-type additions earlier on in the synthesis) from 2.50-3.10 ppm to 2.30-2.85 ppm, with the resonances also becoming less broad and more defined (Figure 4.19). Additionally, the unexpected group of resonances between 1.85-2.00 ppm had disappeared, and the expected singlet attributed to the isobutyryl group – integrating to approximately 6H – was now observed at 1.91 ppm (Figure 4.20). Each of these changes in the ^{1}H-NMR spectra confirm that the tertiary amines have been deprotonated to the neutral species once more, and consequently exhibit a reduced electron-withdrawing effect on their neighbouring environments. Furthermore, ^{13}C-NMR ($CDCl_3$) analysis revealed resonances at 31 ppm, 56 ppm and 171 ppm that are attributed to the C(=O)C(**C**H_3)$_2$Br, C(=O)**C**$(CH_3)_2$Br and **C**(=O)C$(CH_3)_2$Br carbon environments of the isobutyryl group, respectively (Figure 4.21), and ESI mass spectrometry showed a molecular ion $[M+Na]^+$ peak at 1,597 Da (Figure 4.22).

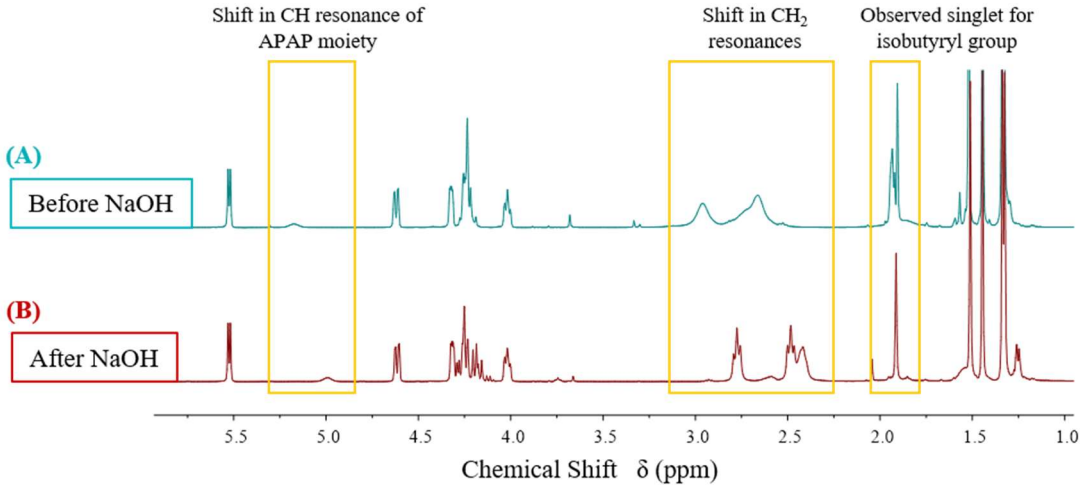

Figure 4.19. ^{1}H-NMR ($CDCl_3$) of G2-proGal-Br [10]: (A) prior to treatment with 4M $NaOH_{aq}$, and (B) after treatment with 4M $NaOH_{aq}$. The observed shift in resonances are highlighted by the yellow boxes.

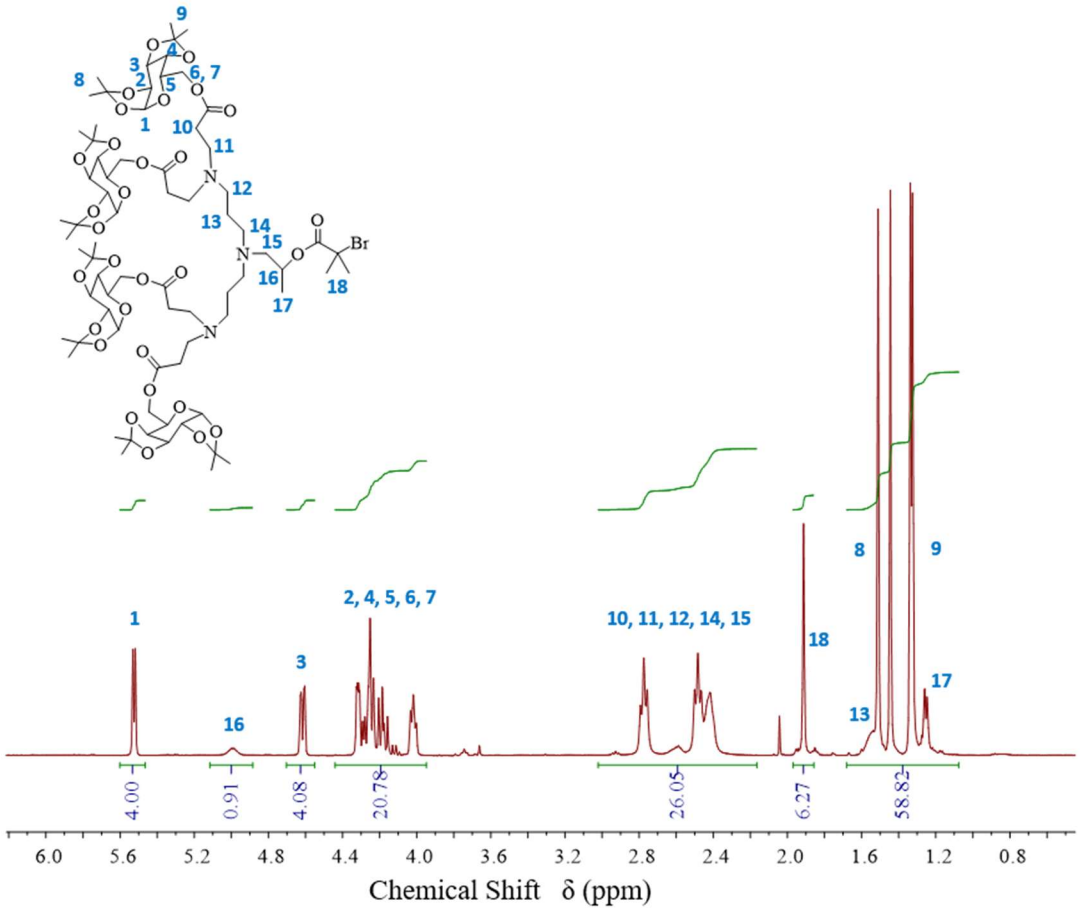

Figure 4.20. ^{1}H-NMR ($CDCl_3$) analysis of G2-proGal-Br [10], showing the integrations of each environment after normalising the integration of the anomeric protons to 4H.

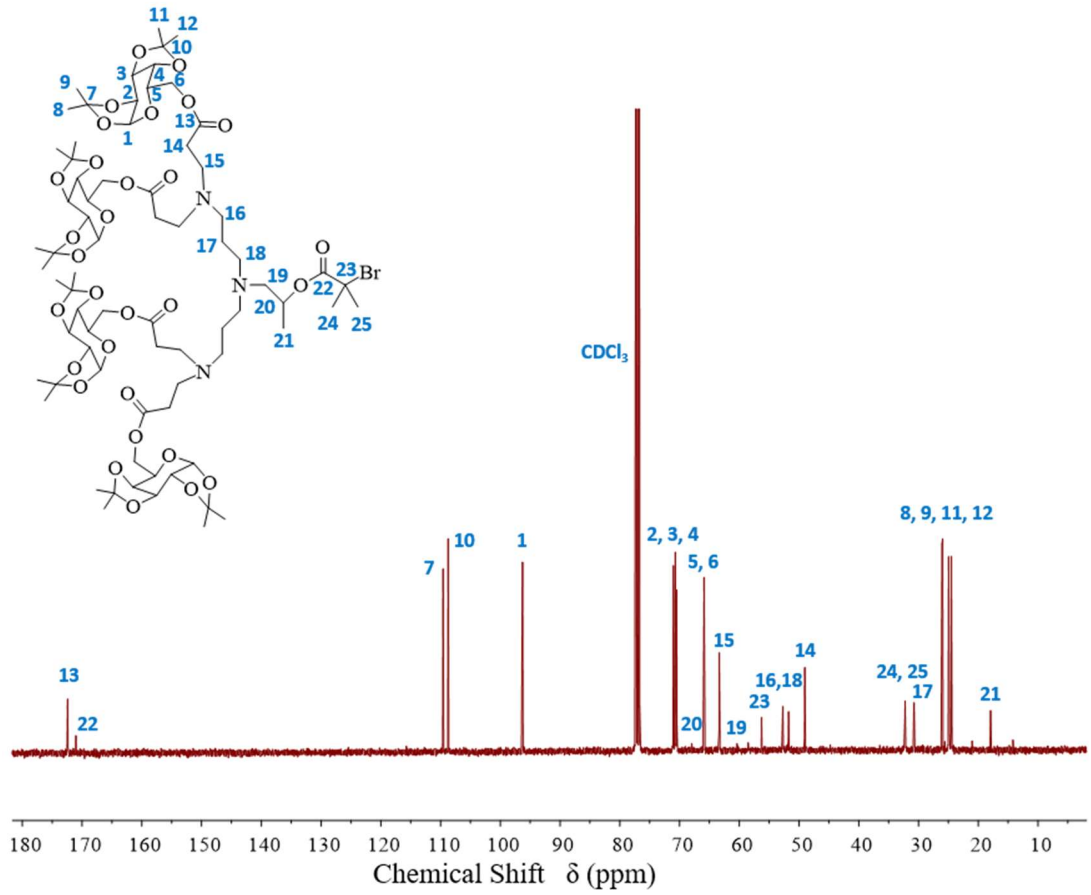

Figure 4.21. ^{13}C-NMR ($CDCl_3$) analysis of G2-proGal-Br [10] showing the assignment of each environment.

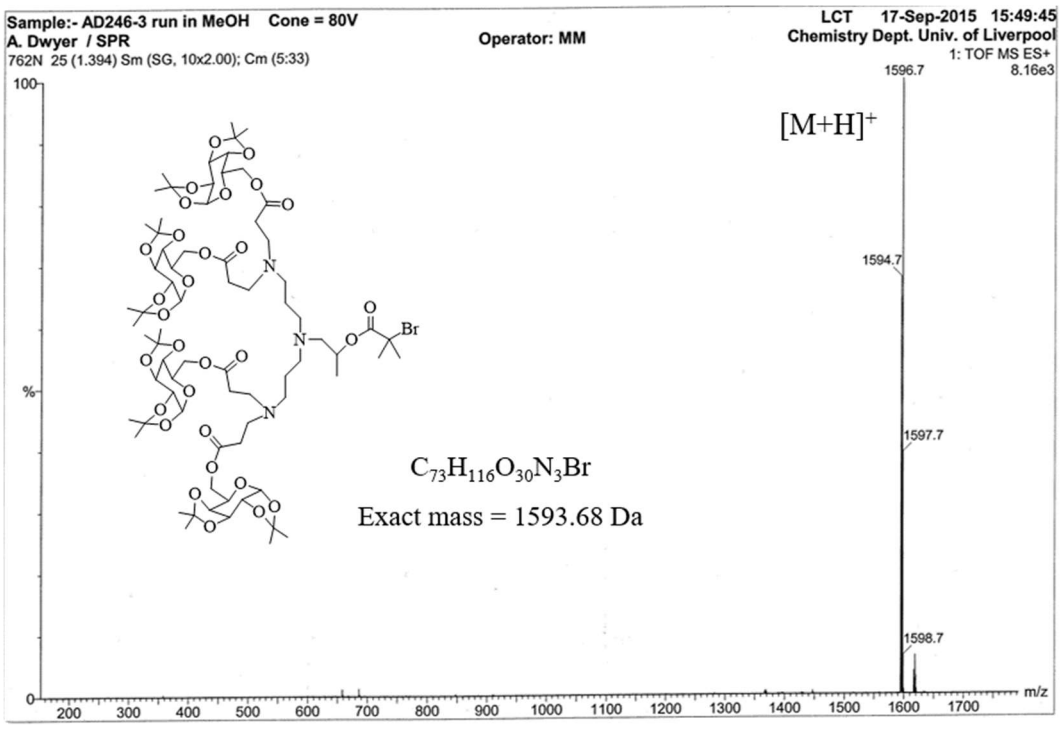

Figure 4.22. ESI mass spectrometry analysis of G2-proGal-Br [10] showing the $[M+H]^+$ molecular ion peak.

4.3. Methanolic ATRP of *n*BuMA using galactosylated dendritic initiators

A series of polymerisations that involved the methanolic Cu-catalysed ATRP of *n*BuMA were performed at 60 °C using each of the galactose-functionalised dendritic initiators (G0, G1 and G2), with each series targeting a DP_n = 60, 80, 100 monomer units; the polymerisations were allowed to progress to high conversion over similar reaction times to enable direct comparisons between the data. After reaction completion, crude samples were taken for ^{1}H-NMR analysis to determine the conversion before exposing the polymerisations to air to poison the catalytic system; the polymers were then diluted with THF and purified by passing through an alumina column to remove the Cu^{II} catalyst before being concentrated and precipitated into cold hexane to give white solids.

All polymerisations proceeded homogeneously to high conversions (≥ 98%), with those initiated by G0-proGal-Br [2] yielding low dispersity polymers ($1.13 \leq Đ \leq 1.17$) with number average molecular weight (M_n) values ranging from 13,950 – 18,500 g mol^{-1}; these values were 1.28-1.58 fold higher than theoretical values, with the deviation decreasing as the targeted DP_n increased (Table 4.1). Whereas, those initiated by G1-proGal-Br [5] yielded low dispersity polymers ($1.12 \leq Đ \leq 1.30$) with M_n values ranging from 14,450 – 18 200 g mol^{-1} (1.22 – 1.57 fold higher than theoretical values), and those initiated by G2-proGal-Br [10] yielded low dispersity polymers ($1.15 \leq Đ \leq 1.19$) with M_n values ranging from 14,450 – 26 000 g mol^{-1} (1.37 – 1.64 fold higher than theoretical values). In comparison to the linear polymerisations described in Chapters 2 and 3 (using ethyl α-bromoisobutyrate and PEG macro-initiators, respectively), triple-detection GPC(DMF) analysis of the polymers initiated by the galactosylated dendritic compounds revealed higher dispersities than was expected; however, these values are still highly indicative of well-controlled ATRP, with the increase likely due to poorer initiation efficiencies. Furthermore, the GPC (RI) chromatograms showed narrow, monomodal and symmetrical molecular weight distributions (Figure 4.23 - 4.25).

Table 4.1. Cu-catalysed methanolic ATRP of *n*BuMA at 60 °C using the galactosylated dendritic initiators (G0, G1 and G2).

Target [a] DP_n	Conversion [actual DP_n]	Time (h)	M_n theory [b]	Triple-detection GPC (DMF) M_n (g mol^{-1})	M_w (g mol^{-1})	Đ
G0-proGal-Br						
60	99 % [59]	25	8 850	13 950	16 100	1.16
80	99 % [79]	48	11 650	17 300	19 600	1.13
100	99 % [99]	72	14 500	18 500	21 600	1.17
G1-proGal-Br						
60	98 % [59]	19	9 200	14 450	16 250	1.12
80	99 % [79]	48	12 100	15 400	18 900	1.23
100	99 % [99]	74	14 900	18 200	23 600	1.30
G2-proGal-Br						
60	99 % [59]	22	10 050	14 450	16 600	1.15
80	99 % [79]	50	12 850	17 650	20 950	1.19
100	99 % [99]	72	15 800	26 000	29 850	1.15

[a] Target DP_n calculated as [*n*BuMA]/[initiator]. [b] Theoretical M_n calculated as (target DP_n x actual conversion achieved and includes initiator residue).

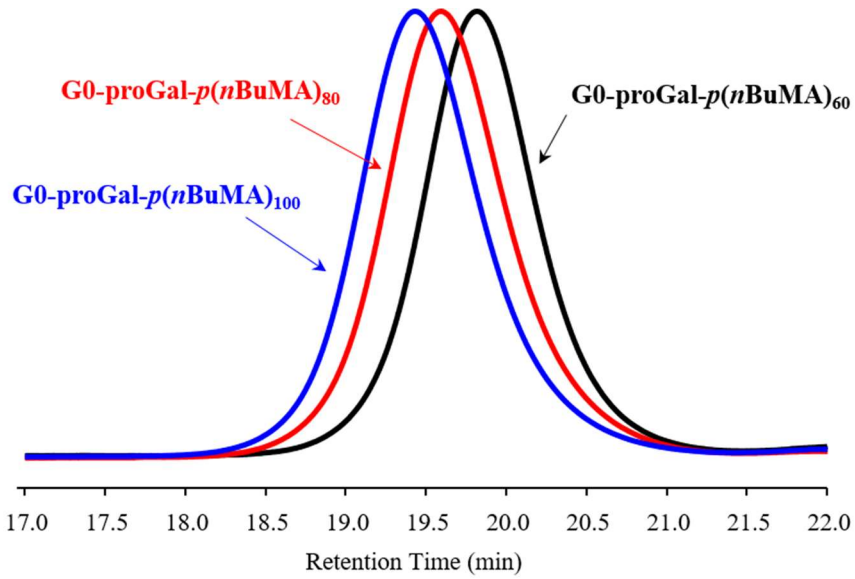

Figure 4.23. GPC chromatograms (RI) showing G0-proGal-*p*(*n*BuMA)$_x$ molecular weight distributions across targeted DP_n = 60-100 monomer units.

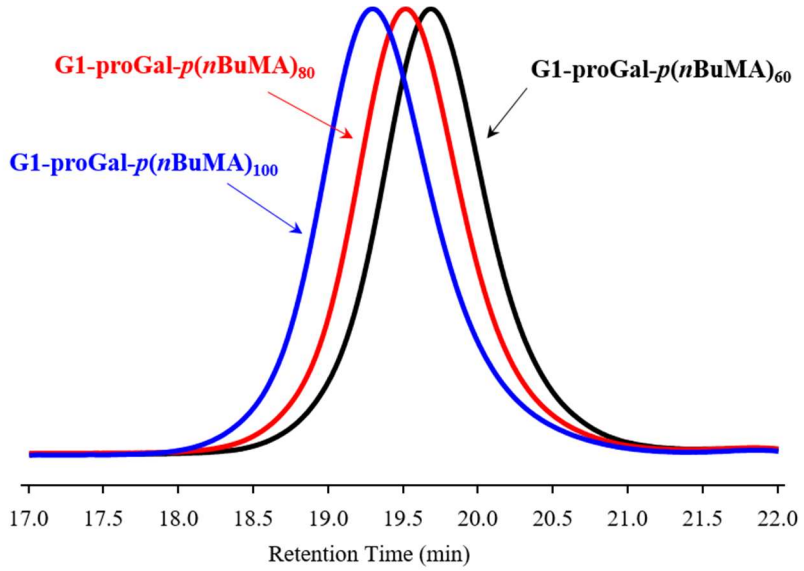

Figure 4.24. GPC chromatograms (RI) showing G1-proGal-*p*(*n*BuMA)$_x$ molecular weight distributions across targeted DP_n = 60-100 monomer units.

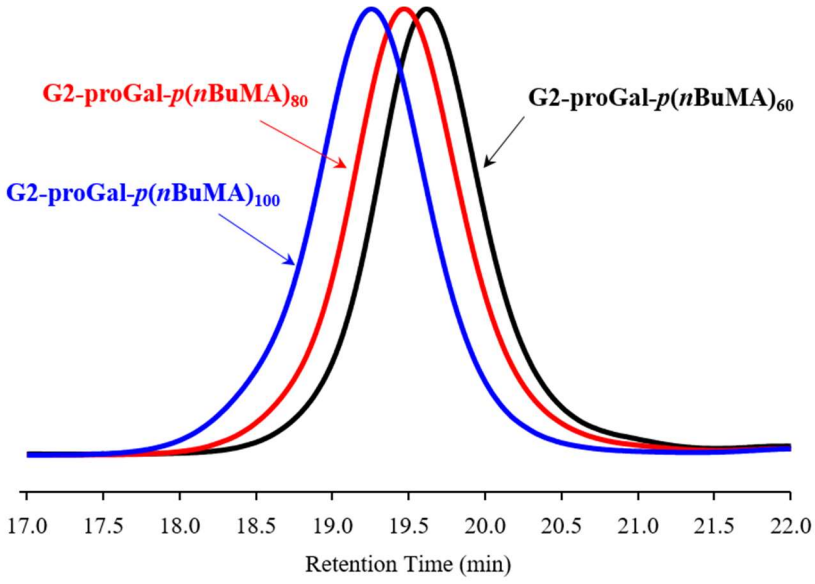

Figure 4.25. GPC chromatograms (RI) showing G2-proGal-*p*(*n*BuMA)$_x$ molecular weight distributions across targeted DP_n = 60-100 monomer units.

It is important to note that Tomalia *et al* highlighted the potential for deleterious *retro*-Michael additions when synthesising PAMAM dendrimers at temperatures greater than 80 °C;[23] these reactions are the reverse reaction of the Michael addition, which caused the dendrimers to fragment. To determine whether such reactions had taken place during the polymerisations conducted at 60 °C, ^{1}H-NMR analysis of the purified G2-proGal-*p*(*n*BuMA)$_{60}$ polymer was performed (Figure 4.26). As can be seen from Figure 4.26, the resonances at 2.45 ppm and 2.75 ppm attributed to the dendritic CH_2 environments (introduced as a result of the Michael-type additions) can be easily observed, and the resonances at 4.10-4.40 ppm, 4.60 ppm and 5.50 ppm confirm that the protected galactose units are still present on the dendritic chain end functionality; this suggests that *retro*-Michael additions have not taken place. However, the integrations of the protons attributed to the protected galactose functionalities were marginally lower than expected, with the resonances at 4.60 ppm and 5.50 ppm integrating to 3.64H and 3.67H, respectively, rather than the theoretical value of 4H; these figures were determined by normalising the integration of the resonance at 2.75 ppm to 8H. Furthermore, the analysis revealed an unexpected resonance at 3.65 ppm, integrating to 4.33H. This analysis suggests that the MeOH solvent may have trans-esterified with the dendritic chain end functionality and/or the repeat units of the polymer backbone; however, this was not conclusive at this stage.

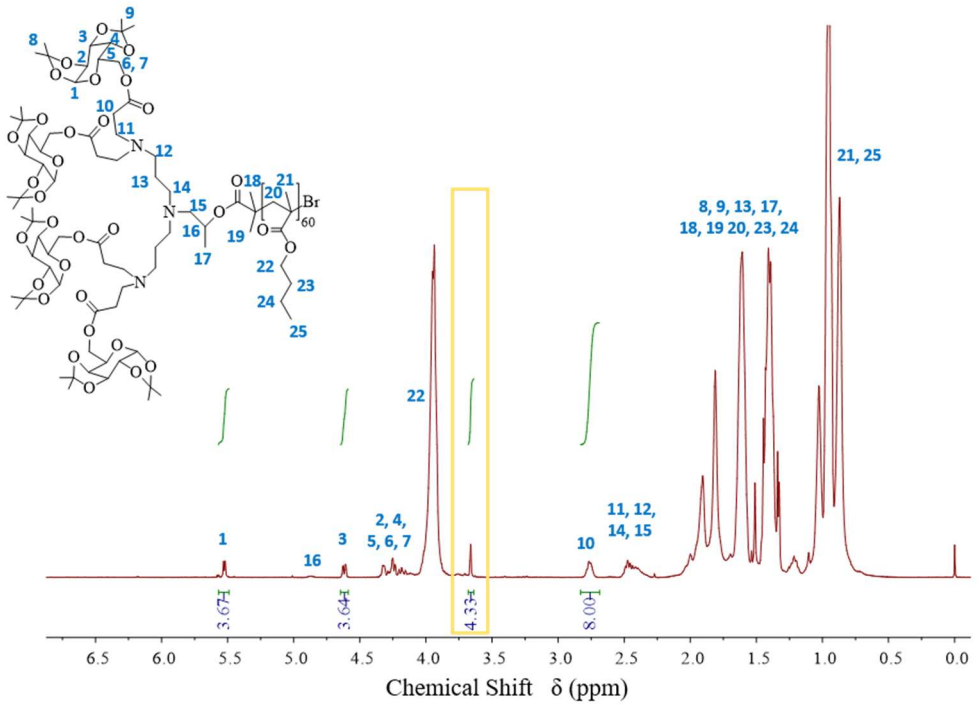

Figure 4.26. ^{1}H-NMR ($CDCl_3$) analysis of G2-proGal-*p*(*n*BuMA)$_{60}$ after purification; the resonance potentially due to transesterification reactions is highlighted by the yellow box.

4.4. Synthesis of galactosylated *hyp*-glycopolydendrons

As described in Chapter 1 (section 1.6), hyperbranched polydendrons (*hyp*-polydendrons) - a new macromolecular architecture designed to combine aspects of RDRP, branched vinyl polymerisation, and linear-dendritic hybrids - can be synthesised using dendritic initiators in a one-pot branched polymerisation following the Strathclyde approach. Therefore, the Cu-catalysed methanolic ATRP of *n*BuMA, targeting a DP_n = 30 monomer units, was performed at 60 °C using the galactosylated dendritic initiators. Once again, a low concentration of EGDMA (0.8 eqv. per initiator) was utilised to promote the statistical inter-chain branching of primary polymer chains, with each polymerisation allowed to progress to high conversion over 12 hours to enable direct comparisons between the data (Table 4.2; Figure 4.27).

All polymerisations proceeded homogeneously to high conversion (99 %) to yield high molecular weight polymers with weight average molecular weight (M_w) values ranging from 102,650 g mol^{-1} to 159,450 g mol^{-1}. Although linear polymerisations targeting a DP_n = 30 *n*BuMA using the galactose functionalised initiators were not performed, M_w values for such linear polymers can be estimated as half those values observed for the linear polymers with targeted DP_n = 60 monomer units (Table 4.1). Therefore, the M_w values can be estimated as: 8,050 g mol^{-1} for G0-proGal-*p*(*n*BuMA)$_{30}$, 8,150 for G1-proGal-*p*(*n*BuMA)$_{30}$, and 8,300 g mol^{-1} for G2-proGal-*p*(*n*BuMA)$_{30}$. Using these values, the number of conjoined primary polymer chains within the weight average structures of the branched polymers can be estimated as: 15 chains for G0-proGal-*p*(*n*BuMA$_{30}$-*co*-EGDMA$_{0.8}$), 13 chains for G1-proGal-*p*(*n*BuMA$_{30}$-*co*-EGDMA$_{0.8}$), and 19 chains for G2-proGal-*p*(*n*BuMA$_{30}$-*co*-EGDMA$_{0.8}$). Furthermore, the observed dispersities for each of the branched polymer samples ($4.09 \leq Đ \leq 6.69$) were significantly higher than those seen in the linear polymerisations (Table 4.1) due to the statistical nature of the branching.

As used for the linear polymerisations performed at 60 °C, ^{1}H-NMR analysis of the purified G2-proGal-*p*(*n*BuMA$_{30}$-*co*-EGDMA$_{0.8}$) showed that the integrations of the protons attributed to the protected galactose functionalities were slightly lower than expected, with the resonances at 4.60 ppm and 5.50 ppm integrating to 3.57H and 3.59H, respectively, rather than the theoretical value of 4H (Figure A31, Appendix). Additionally, the resonance at 3.65 ppm (integrating to 3.27H) was also observed.

Table 4.2. Branched Cu-catalysed methanolic ATRP of *n*BuMA at 60 °C using the galactosylated dendritic initiators (G0, G1 and G2) and EGDMA as branching monomer.

Target[a] DP_n	Conversion [actual DP_n]	Time (h)	EGDMA: Initiator	Triple-detection GPC (DMF)		
				M_n (g mol^{-1})	M_w (g mol^{-1})	Đ
G0-proGal-Br						
30	99 % [30]	12	0.8 : 1	17 900	119 600	6.69
G1-proGal-Br						
30	99 % [30]	12	0.8 : 1	25 100	102 650	4.09
G2-proGal-Br						
30	99 % [30]	12	0.8 : 1	24 350	159 450	6.55

[a] Target DP_n calculated as [*n*BuMA]/[initiator].

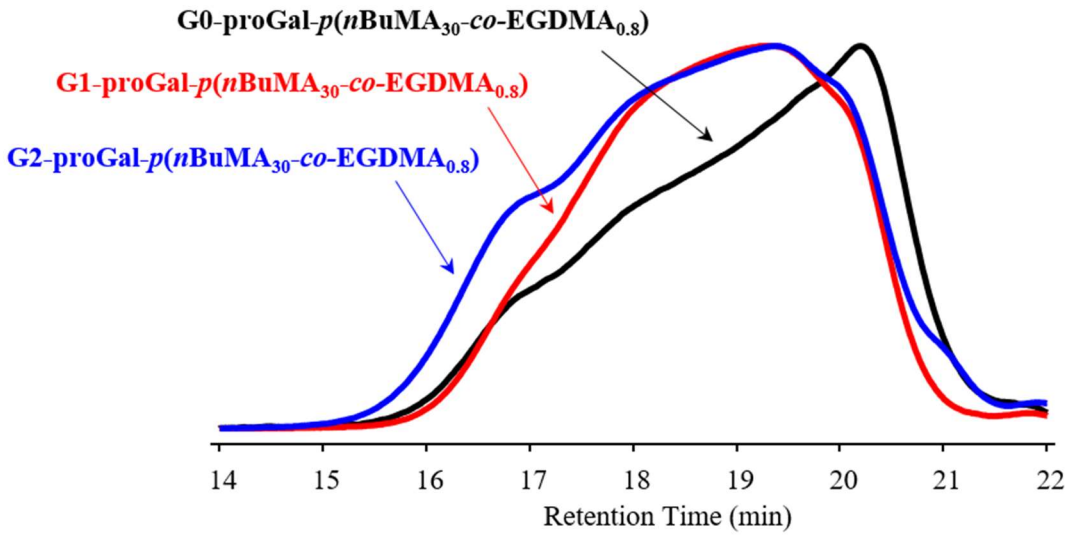

Figure 4.27. GPC chromatograms (RI) showing the molecular weight distributions of G*x*-proGal-*p*(*n*BuMA$_{30}$-*co*-EGDMA$_{0.8}$) obtained *via* Cu-catalysed methanolic ATRP at 60 °C: G0-proGal-*p*(*n*BuMA$_{30}$-*co*-EGDMA$_{0.8}$) shown by the black solid line, G1-proGal-*p*(*n*BuMA$_{30}$-*co*-EGDMA$_{0.8}$) shown by the red solid line, and G2-proGal-*p*(*n*BuMA$_{30}$-*co*-EGDMA$_{0.8}$) shown by the blue solid line.

4.5. Deprotection of the galactosylated *hyp*-glycopolydendrons

The synthesis of *hyp*-glycopolydendrons capable of actively targeting hepatic ASGPR receptors required the removal of the isopropylidene protecting groups from the dendritic chain end functionality. Many reports have demonstrated this deprotection under harsh acidic conditions, often using trifluoroacetic acid (TFA)[24–27] or formic acid[11,28,29] in polar protic solvents. Therefore, numerous attempts were made to deprotect the *hyp*-glycopolydendrons using TFA, DOWEX-H^+ and DOWEX-Na^+ ion exchange resins in THF, THF-H_2O (90/10) binary solutions and IPA reaction solvents, but all proved unsuccessful; one possible explanation for this may be that the chain end functionalities are not easily accessible within the branched architecture. However, successful deprotection was achieved when using *para*-toluene sulfonic acid monohydrate (PTSA).

4.5.1. Deprotection of proGal-OH using PTSA

Initially, the isopropylidene protecting groups of the proGal-OH [1] starting material were deprotected as a proof of concept; this involved the reaction between proGal-OH [1] and a catalytic amount (0.1 eqv.) of PTSA, which was performed in MeOH at 50 °C for 6 hours (Scheme 4.8). ^{1}H-NMR (MeOD) analysis of the crude product showed the near-complete absence of resonances attributed to the isopropylidene protecting groups, and an up-field shift for all resonances attributed to the galactose (Gal [11]) protons (Figure 4.28). Furthermore, IR spectroscopy revealed a significant increase in transmittance at approximately 3,400 cm^{-1} attributed to the hydroxyl (O-H) stretch (Figure 4.29). The results therefore confirm that the isopropylidene protecting groups can be successfully removed using PTSA in the protic solvent MeOH at elevated temperature.

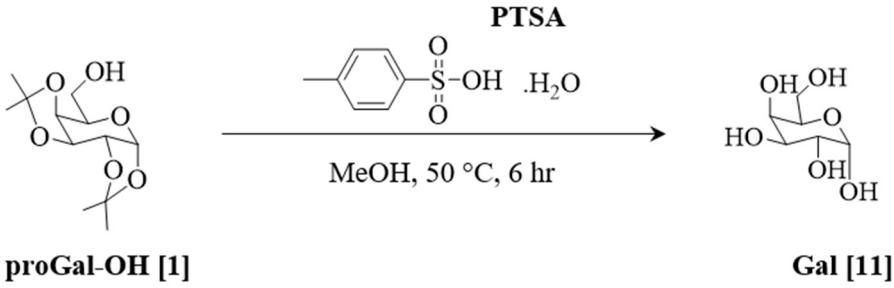

proGal-OH [1] **Gal [11]**

Scheme 4.8. Reaction scheme detailing the deprotection of isopropylidene groups of proGal-OH [1] using *para*-toluene sulfonic acid monohydrate (PTSA) in MeOH at 50 °C.

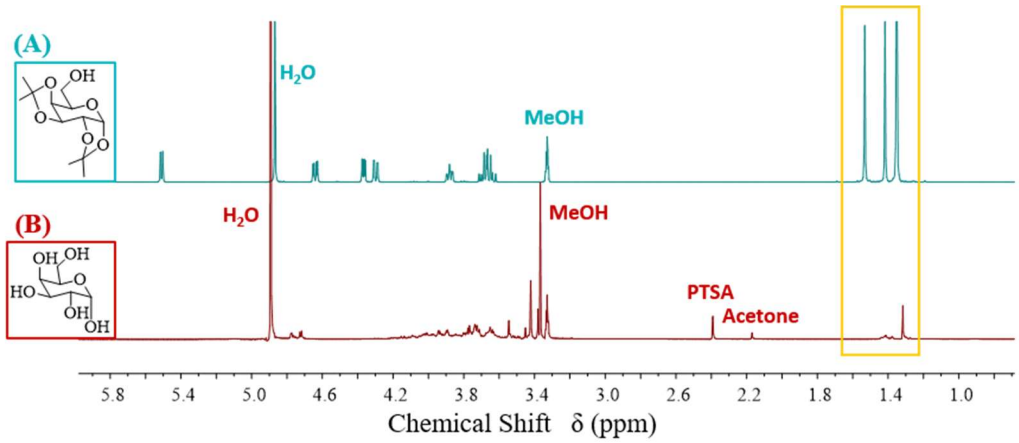

Figure 4.28. ^{1}H-NMR (MeOD) analysis of: (A) proGal-OH [1], and (B) Gal [11]. The disappearance of the isopropylidene resonances is highlighted by the yellow box.

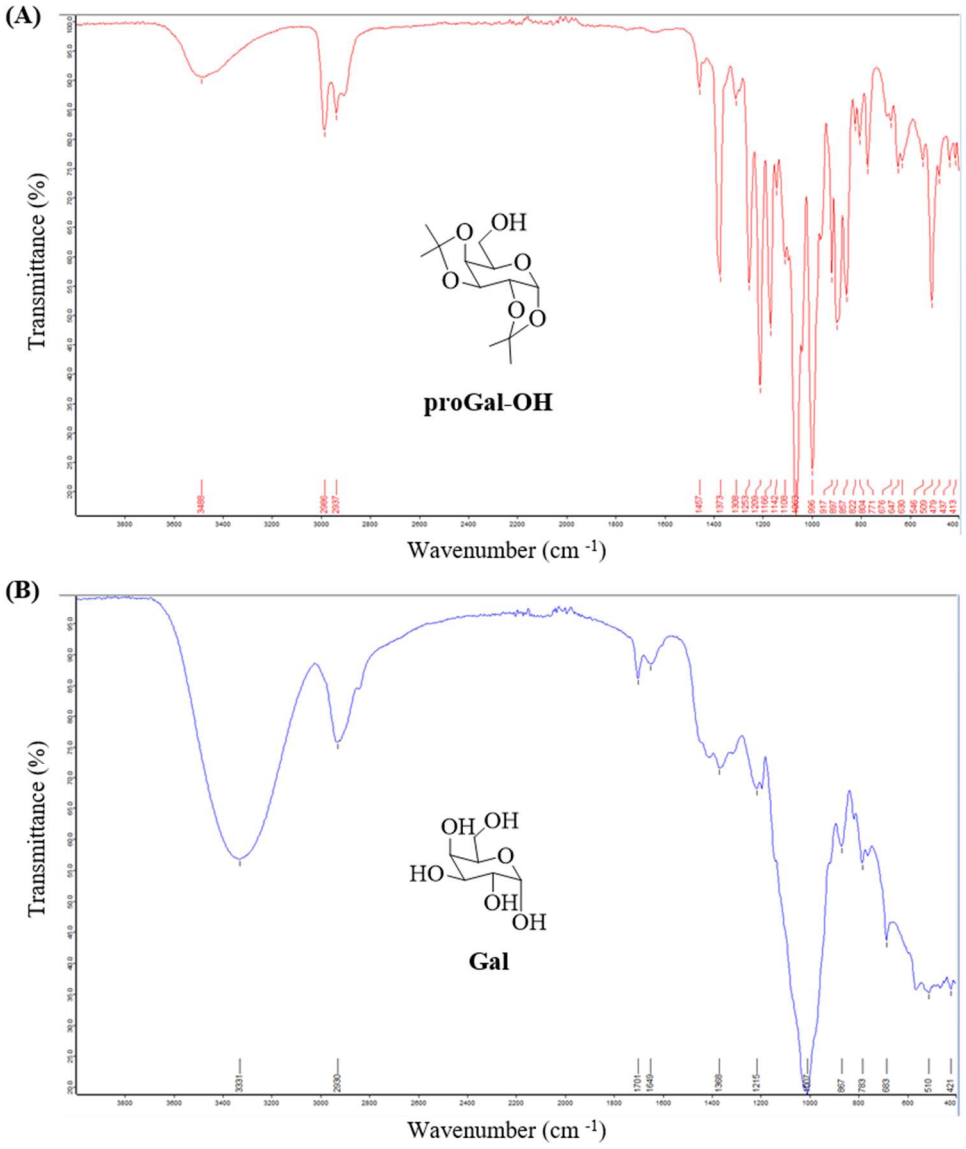

Figure 4.29. IR spectroscopy analysis of: (A) proGal-OH [1], and (B) deprotected Gal [11], showing the greater transmittance at approximately 3,400 cm^{-1} (attributed to the O-H stretch) after deprotection.

4.5.2. Deprotection of *hyp*-glycopolydendrons using PTSA

Deprotection of the *hyp*-glycopolydendrons using PTSA was then performed using similar reaction conditions to that described in section 4.5.1; however, dissolution of the *p*(*n*BuMA-*co*-EGDMA) copolymers within the methanolic environment required the co-solvency effect of *n*BuMA monomer, and the complete removal of the isopropylidene protecting groups required an excess of PTSA with respect to the protected chain end functionality. After stirring at the elevated temperature for 24 hours, the MeOH reaction solvent was removed on the rotary evaporator and the crude product was dissolved in THF before being treated with 4M $NaOH_{aq}$; this formed a $PTSA^{-}Na^{+}$ salt that precipitated from solution. The salt was filtered off, and the polymer-THF solution was dialysed against THF for 48 hours using a regenerated cellulose dialysis tubing with a molecular weight cut-off of 2000 g mol^{-1}. ^{1}H-NMR ($CDCl_3$) analysis of the purified polymers showed the disappearance of resonances at 4.60 ppm and 5.50 ppm attributed to the protons of the protected galactose functionalities, and the disappearance of resonances at approximately 1.35 ppm and 1.50 ppm attributed to the isopropylidene protecting groups, therefore indicating that deprotection had been achieved (Figure 4.30). Furthermore, resonances attributed to the CH_2 environments of the dendritic chain end (introduced as a result of the aza-Michael-type additions during the initiator synthesis) could be easily observed at approximately 2.40 ppm and 2.75 ppm, thereby confirming that the dendritic chain end functionality remains present and has not been cleaved during the reaction, nor has it undergone deleterious retro-Michael additions. However, resonances attributed to the deprotected galactose functionalities were not easily observed. The proof of concept study involving the deprotection of proGal-OH [1] (described in section 4.5.1) showed ^{1}H-NMR (MeOD) resonances attributed to the deprotected compound in the region of 3.40 - 4.20 ppm; unfortunately, this region in the ^{1}H-NMR spectrum of the deprotected *hyp*-glycopolydendrons is masked by the large, broad resonance attributed to the pendant CH_2 environment of the *n*BuMA polymer repeat units. Expansion of this region certainly revealed resonances around the baselines of the polymer CH_2 resonance, but whether these can be attributed to the deprotected galactose chain end functionalities is difficult to say without any degree of uncertainty. To investigate further, IR spectroscopy was performed; the analysis revealed a small transmittance at

approximately 4,500 cm^{-1}, which suggests that the deprotected galactose functionalities are present on the chain ends (Figure A32, Appendix).

Once again, resonance at approximately 3.65 ppm was observed in the ^{1}H-NMR ($CDCl_3$) spectrum, this time resonating with a higher integration (11H) compared to those observed in the ^{1}H-NMR spectra of the protected polymers (sections 4.3 and 4.4). As described earlier, this is likely due to transesterification reactions between the MeOH solvent and either the galactose chain end functionalities or the *p*(*n*BuMA) pendant groups, in this case catalysed under the acidic conditions.

Triple detection GPC analysis of the *hyp*-glycopolydendrons before and after the deprotection experiments were performed once more to determine whether their branched architecture had been affected by the proposed transesterification reactions (Figure 4.31). The G0 and G1 series were both analysed in DMF eluent; however, dissolution of the deprotected G2 *hyp*-glycopolydendron was difficult to achieve in the DMF solvent, and so the G2 series were analysed in THF eluent. The analysis of each series revealed high M_w values for both the protected and deprotected polymers, indicating that the *hyp*-glycopolydendrons retained their branched architecture despite transesterifications having taken place.

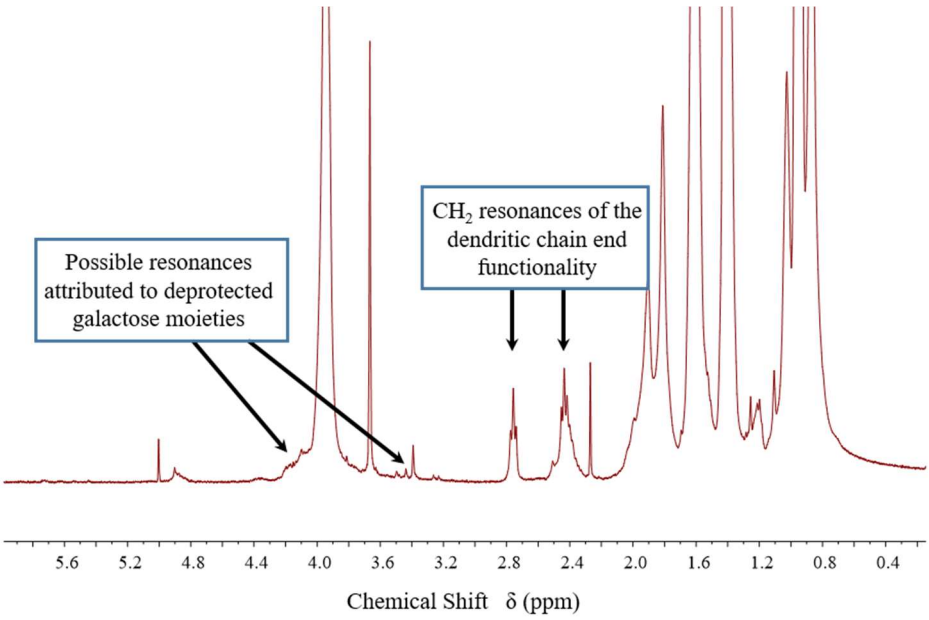

Figure 4.30. ^{1}H-NMR ($CDCl_3$) analysis of the deprotected G2-proGal-*p*(*n*BuMA$_{30}$-*co*-EGDMA$_{0.8}$) *hyp*-glycopolydendron, showing resonances attributed to the CH_2 environments of the dendritic chain end functionality, and possible resonances attributed to the deprotected galactose moieties.

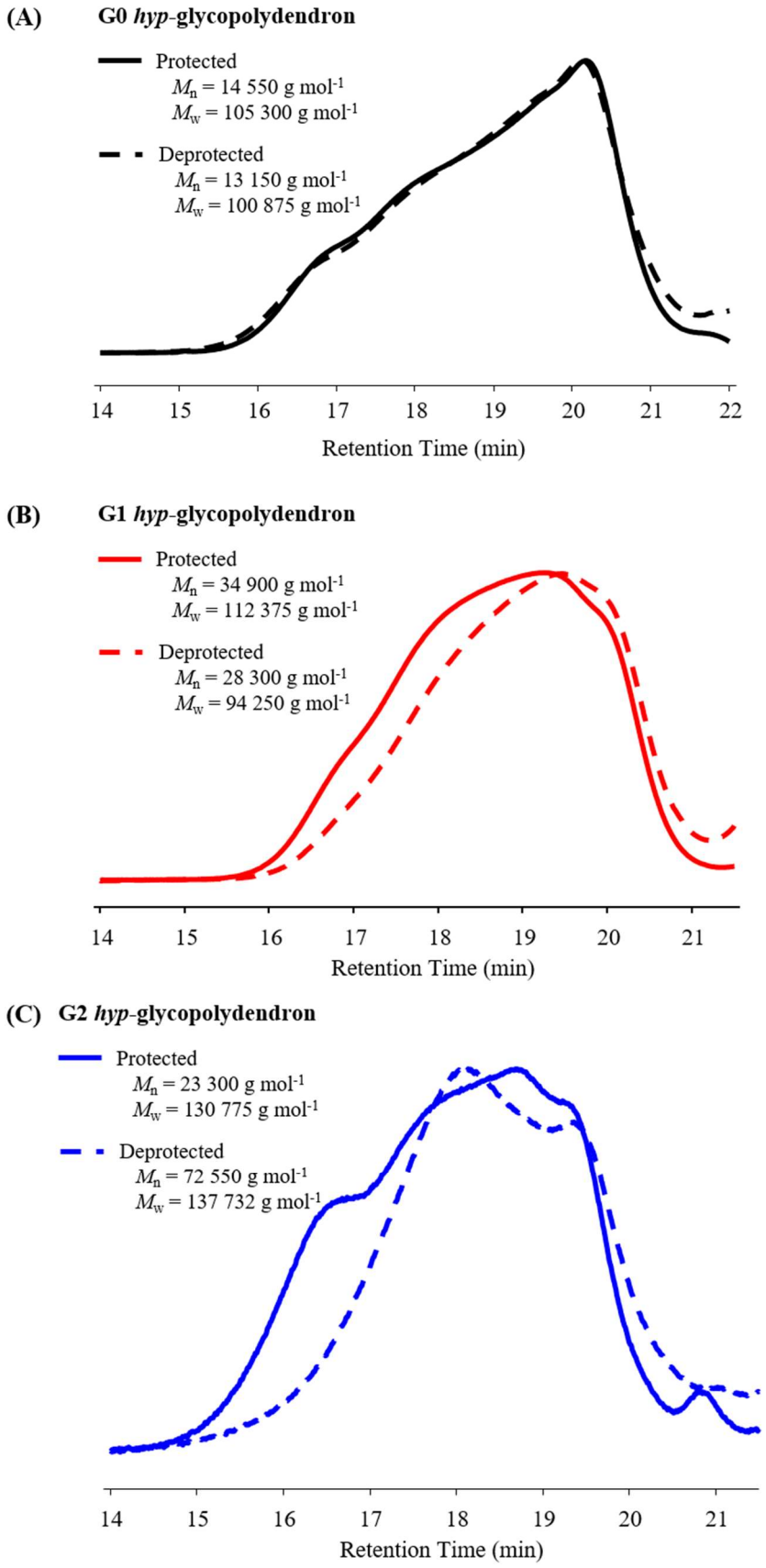

Figure 4.31. Triple-detection GPC (DMF) analysis of the protected and deprotected *hyp*-glycopolydendrons: (A) G0 series, and (B) G1 series. (C) GPC (THF) analysis of the protected and deprotected of the G2 *hyp*-glycopolydendrons.

4.6. Nanoprecipitations of protected and deprotected *hyp*-glycopolydendrons

Nanoprecipitations of each of the *hyp*-glycopolydendrons were performed through the rapid addition of 1 mL of polymer-THF solutions (5 mg mL^{-1}) into 5 mL of H_2O, after which the volatile organic solvent was allowed to evaporate under ambient conditions to yield nanoparticles within the aqueous antisolvent. These aqueous dispersions were analysed by dynamic light scattering (DLS) (Table 4.3, Figure 4.32).

DLS analysis of each of the protected *hyp*-glycopolydendrons revealed monomodal intensity-weighted distributions, with *z*-average values (D_z) ranging from 123 nm to 197 nm and low polydispersity index (PdI) values ranging from 0.015 to 0.109; monomodal number-weighted distributions, with number-average values (D_n) ranging from 93 to 178 nm (Figures 4.32A-C) were also observed. The large sizes observed indicate that the nanoparticles are formed *via* the proposed nucleation/growth mechanism that is described in Chapter 3 (Section 3.1.3). Additionally, negative zeta potentials (ranging from -10.8 to -34.6 mV) were observed for each sample, indicating the presence of charge stabilisation. Analysis of the data shows that an increase in generation number of the dendritic chain end functionality from G0 to G1 results in a decrease in D_z values from 197 to 123 nm, and an increase in negative zeta potential from -26.4 to -34.6 mV; however, the data obtained for the protected G2 *hyp*-glycopolydendron revealed a higher D_z value (143 nm) and zeta potential (-10.8 mV) when compared to its G1 analogue. This out-of-trend result can be explained by the proposed transesterification side-reactions occurring during polymer synthesis, whereby the MeOH solvent has displaced protected galactose functionalities. Scanning electron microscopy (SEM) images taken of the protected G0 and G1 *hyp*-glycopolydendrons showed spherical particles with sizes that correlate well with the data obtained by DLS (Figure 4.33); however, the SEM images taken of the protected G2 *hyp*-glycopolydendron showed spherical particles that seem to have aggregated to form a film-like structure. This is likely due to a drying effect as the water evaporated during sample preparation.

Table 4.3. DLS data of nanoprecipitations of protected and deprotected hyp-glycopolydendron – THF solutions (1 mL) into H_2O (5 mL)

Hyp-glycopolydendron	Initial concentration in THF	Final concentration in H_2O	DLS [a]				Zeta potential (mV)
			D_z (d.nm) [b]	PdI [c]	D_n (d.nm) [d]	DCR [e] (kcps) [attenuator]	
Protected							
G0-proGal-*p*(*n*BuMA$_{30}$-*co*-EGDMA$_{0.8}$)	5 mg mL^{-1}	1 mg mL^{-1}	197	0.015	178	292 481 [5]	-26.4
G1-proGal-*p*(*n*BuMA$_{30}$-*co*-EGDMA$_{0.8}$)	5 mg mL^{-1}	1 mg mL^{-1}	123	0.079	93	54 296 [6]	-34.6
G2-proGal-*p*(*n*BuMA$_{30}$-*co*-EGDMA$_{0.8}$)	5 mg mL^{-1}	1 mg mL^{-1}	143	0.109	111	35 877 [6]	-10.8
Deprotected							
G0-Gal-*p*(*n*BuMA$_{30}$-*co*-EGDMA$_{0.8}$)	5 mg mL^{-1}	1 mg mL^{-1}	46	0.185	25	25 725 [7]	-42.3
G1-Gal-*p*(*n*BuMA$_{30}$-*co*-EGDMA$_{0.8}$)	5 mg mL^{-1}	1 mg mL^{-1}	43	0.140	25	30 784 [7]	-47.6
G2-Gal-*p*(*n*BuMA$_{30}$-*co*-EGDMA$_{0.8}$) [f]	5 mg mL^{-1}	1 mg mL^{-1}	22	0.435	8	2 170 [9]	-34.3

[a] DLS measurements recorded at 25 °C after an equilibration period of 2 minutes. [b] Size distribution using *z*-average values. [c] Polydispersity index. [d] Size distribution using number average values. [e] Derived count rate. [f] Sample filtered using 0.45 μm PTFE filter.

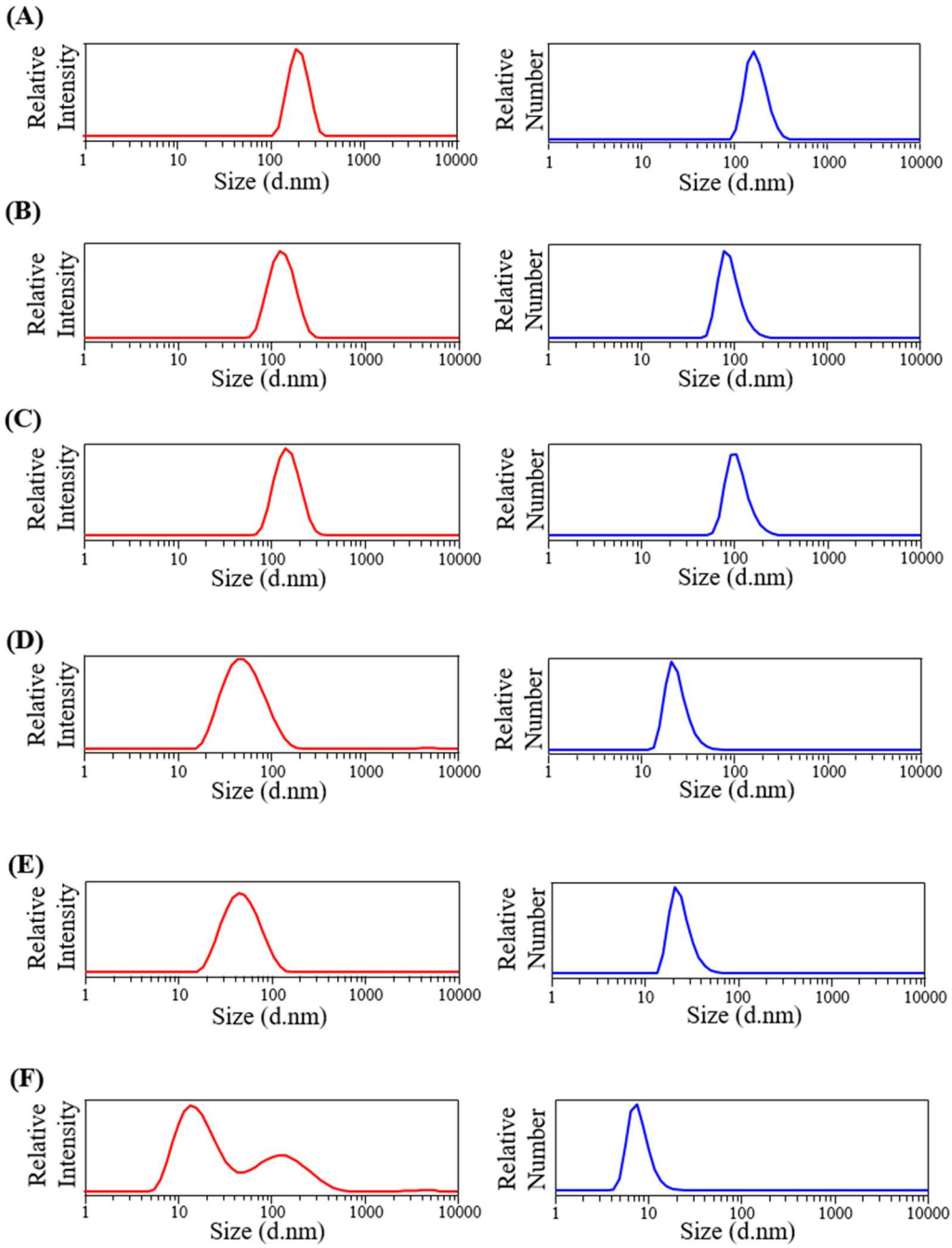

Figure 4.32. DLS traces showing the rapid nanoprecipitations of: (A) protected G0 *hyp*-glycopolydendron, (B) protected G1 *hyp*-glycopolydendron, (C) protected G2 *hyp*-glycopolydendron, (D) deprotected G0 *hyp*-glycopolydendron, (E) deprotected G1 *hyp*-glycopolydendron, and (F) deprotected G2 *hyp*-glycopolydendron.

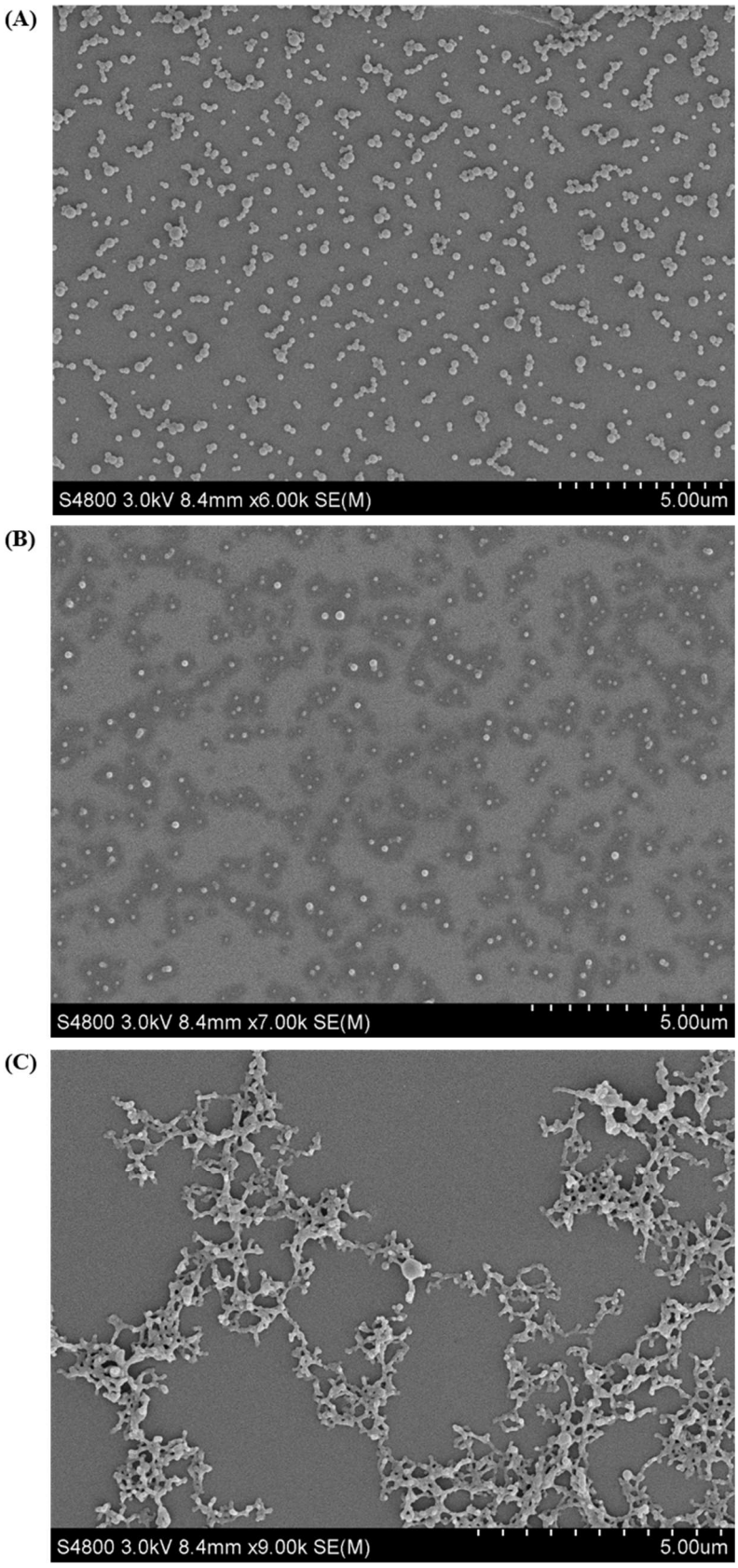

Figure 4.33. Scanning electron microscopy (SEM) images of nanoparticles formed after nanoprecipitation of: (A) protected G0 *hyp*-glycopolydendron, (B) protected G1 *hyp*-glycopolydendron, and (C) protected G2 *hyp*-glycopolydendron. Scale bars of 5 μm are observed in all images.

DLS analysis of the deprotected G0 and G1 *hyp*-glycopolydendrons revealed monomodal intensity-weighted distributions (Figures 4.32D and 4.32E) with significantly smaller D_z values (46 and 43 nm, respectively), and greater zeta potentials (-42.3 mV and -47.6 mV, respectively) compared to their protected equivalents; these results confirm that the deprotected galactose functionalities are present on the surface of the nanoparticle, with the liberated hydroxyl groups providing a greater degree of charge stabilisation that has resulted in colloidally stable nanoparticles with much smaller hydrodynamic diameters. It was also apparent that the deprotection of the hyp-glycopolydendrons yielded nanoparticles with broader PdI values of 0.185 and 0.140 for the G0 and G1 deprotected materials, respectively.

Analysis of the G2 *hyp*-glycopolydendron required filtration of the sample using a 0.45 μm PTFE filter due to the presence of precipitate; it is important to note that nanoprecipitations of branched *p*(*n*BuMA$_{30}$-*co*-EGDMA$_{0.8}$) obtained by the methanolic Cu-catalysed ATRP of *n*BuMA using ethyl α-bromoisobutyrate as the initiator resulted in macro-phase separation and precipitation of the polymer upon addition of the polymer-THF solution to H_2O. Therefore, the precipitate observed after the nanoprecipitation of the deprotected G2 *hyp*-glycopolydendron is likely attributed to the branched material that had taken part in the acid-catalysed transesterification reactions between the dendritic chain ends and the MeOH solvent during the deprotection step. DLS analysis of the filtered sample also showed a significantly smaller D_z value (22 nm) and greater zeta potential (-34.3 mV) compared to its protected equivalent, suggesting that deprotected galactose functionalities are present on the dendritic chain ends of the branched polymer. However, the analysis also revealed a bimodal intensity-weighted distribution (Figure 4.32F), meaning that the D_z values are not reliable and therefore have to be discredited; instead, a D_n value of 8 nm was calculated using Mie theory. This small nanoparticle size is analogous to that observed for dendrimers, but the high attenuator and low derived count rate observed during the measurement indicate that the concentration of the filtered sample is too low to provide a reliable result.

4.7. Conclusions

In conclusion, G0, G1 and G2 dendritic ATRP initiators bearing protected galactose functionalities were successfully synthesised *via* aza-Michael-type additions and esterifications, with each synthesis beginning with the commercially available 1,2:3,4-Di-*O*-isopropylidene-α-D-galactopyranose (proGal-OH [1]); the structure of each compound was confirmed by ^{1}H-NMR, ^{13}C-NMR spectroscopy and ESI mass spectrometry. The synthesis of the G2 dendritic initiator (G2-proGal-Br [10]) initially encountered a small problem, with the tertiary amines scavenging the HBr by-product of the bromo-esterification despite a 3-fold excess of TEA present within the reaction medium. Treatment with 4M $NaOH_{aq}$ followed by normal phase flash chromatography resolved this issue, with ^{1}H-NMR analysis of the purified product showing down-field shifts for resonances attributed to the APAP moiety of the compound; it is believed that this could be avoided in future syntheses by simply increasing the moles of TEA (*e.g.* 12-fold excess) used within the reaction.

Each of the dendritic initiators were utilised in the methanolic Cu-catalysed ATRP of *n*BuMA at 60 °C, targeting DP_n = 60, 80, 100 monomer units, with all polymerisations proceeding homogeneously to high conversion (≥ 98 %) to yield low dispersity polymers ($1.12 \leq Đ \leq 1.30$); the observed dispersities were higher than those seen in Chapters 2 and 3, but still highly indicative of a well-controlled polymerisation. ^{1}H-NMR analysis of the purified G2-proGal-*p*(*n*BuMA)$_{60}$ polymer clearly showed the presence of the dendritic chain end functionality despite conducting the polymerisation at high temperature; this confirmed that the deleterious retro-Michael additions had not taken place during the reaction. However, the analysis did show a small unexpected peak at 3.65 ppm, suggesting that the MeOH solvent may have trans-esterified the dendritic chain end functionality and/or the repeat units of the polymer backbone.

Hyp-glycopolydendrons bearing protected galactose functionalities were synthesised by utilising the galactosylated dendritic initiators in branched polymerisations following the Strathclyde approach, using EGDMA as the divinyl branching monomer; DP_n = 30 monomer units were targeted and the reaction temperature was maintained at 60 °C. Each of the branched polymerisations proceeded homogeneously to high conversion (99 %) to yield high molecular weight polymers with weight

average molecular weight (M_w) values ranging from 102,650 g mol^{-1} to 159,450 g mol^{-1}.

Deprotection of the *hyp*-glycopolydendrons was achieved using *para*-toluene sulfonic acid monohydrate (PTSA) in MeOH, utilising the co-solvency effect of the *n*BuMA monomer to solvate the branched polymers. ^{1}H-NMR analysis of the deprotected polymers showed the absence of resonances attributed to the isopropylidene protecting groups and protected galactose functionalities, and showed resonances attributed to the APAP moiety of the dendritic chain end functionality; however, resonances attributed to the deprotected galactose functionalities were not easily observed, with a proof-of-concept study involving the deprotection of the proGal [1] starting material showing that the resonances are likely to reside beneath the large broad peak attributed to the CH_2 environment of the *p*(*n*BuMA) pendant groups. IR spectrometry analysis did show a small transmittance at 3,400 cm^{-1} attributed to the O-H stretch, indicating that deprotected galactose functionalities are present within the polymer. Unfortunately, the ^{1}H-NMR analysis revealed a significantly greater intensity for the unexpected peak at 3.65 ppm, which suggests a greater degree of transesterification reactions having occurred during the deprotection step, catalysed under the acidic reaction conditions.

Finally, nanoprecipitations of the protected and deprotected hyp-glycopolydendrons were performed by the rapid addition of polymer-THF solutions into H_2O; DLS analysis of the aqueous dispersions revealed smaller D_z values and greater negative zeta potentials for the deprotected G0 and G1 *hyp*-glycopolydendrons when compared to their protected equivalents, therefore suggesting that the isopropylidene protecting groups were successfully removed to leave the deprotected galactose functionalities on the surface of the nanoparticles. However, the analysis of the protected G2 *hyp*-glycopolydendron revealed data that did not follow the trend of decreasing size with increasing generation number of the dendritic chain end functionality, indicating that the galactose functionalities may have been displaced by the MeOH solvent during the deprotection step. The analysis of the deprotected G2 *hyp*-glycopolydendron required sample filtration due to the presence of precipitate; the results did show a greater negative zeta potential than its protected equivalent, but the high attenuator and low derived count rate suggest that the sample concentration is too low to provide a credible result.

Although the analysis suggests that the deprotection of the G0 and G1 *hyp*-glycopolydendrons using PTSA successfully yielded galactosylated nanoparticles capable of actively targeting ASGPR receptors expressed on hepatic cells, it is believed that the deprotection step requires optimisation so that transesterification reactions can be completely avoided; future attempts would involve deprotection using PTSA in THF-H_2O mixtures at low temperature.

4.8. References

1 H. B. El-Serag and K. L. Rudolph, *Gastroenterology*, 2007, **132**, 2557–2576.

2 A. Jemal, F. Bray and J. Ferlay, *CA Cancer J Clin*, 2011, **61**, 69–90.

3 Cancer Research UK and Http://www.cancerresearchuk.org/health-professional/cancer-statistics/statistics-by-cancer-type/liver-cancer#heading-One, Accessed November 2015.

4 H. R. Seo, *Curr. Cancer Ther. Rev.*, 2015, **11**, 82–93.

5 A. A. D'Souza and P. V. Devarajan, *J. Control. Release*, 2015, **203**, 126–139.

6 L. a Sliedregt, P. C. Rensen, E. T. Rump, P. J. van Santbrink, M. K. Bijsterbosch, a R. Valentijn, G. a van der Marel, J. H. van Boom, T. J. van Berkel and E. a Biessen, *J. Med. Chem.*, 1999, **42**, 609–618.

7 Y. Kaneo, T. Tanaka, T. Nakano and Y. Yamaguchi, *J. Control. release*, 2001, **70**, 365–373.

8 J. Wu, P. Liu, J. L. Zhu, S. Maddukuri and M. a. Zern, *Hepatology*, 1998, **27**, 772–778.

9 D. Q. Wu, B. Lu, C. Chang, C. S. Chen, T. Wang, Y. Y. Zhang, S. X. Cheng, X. J. Jiang, X. Z. Zhang and R. X. Zhuo, *Biomaterials*, 2009, **30**, 1363–1371.

10 B. Thapa, P. Kumar, H. Zeng and R. Narain, *Biomacromolecules*, 2015, **16**, 3008–3020.

11 Y. Wang, C. Y. Hong and C. Y. Pan, *Biomacromolecules*, 2013, **14**, 1444–1451.

12 A. Peyret, J. F. Trant, C. V. Bonduelle, K. Ferji, N. Jain, S. Lecommandoux and E. R. Gillies, *Polym. Chem.*, 2015, **6**, 7902–7912.

13 F.-L. Mi, Y.-Y. Wu, Y.-L. Chiu, M.-C. Chen, H.-W. Sung, S.-H. Yu, S.-S. Shyu and M.-F. Huang, *Biomacromolecules*, 2007, **8**, 892–898.

14 T. Hiratsuka, M. Goto, Y. Kondo, C.-S. Cho and T. Akaike, *Macromol. Biosci.*, 2008, **8**, 231–238.

15 B. D. Mather, K. Viswanathan, K. M. Miller and T. E. Long, *Prog. Polym. Sci.*, 2006, **31**, 487–531.

16 M. Retailleau, A. Ibrahim, C. Croutxé-Barghorn, X. Allonas, C. Ley and D. Le Nouen, *ACS Macro Lett.*, 2015, **4**, 1327–1331.

17 P. R. Krishna, A. Sreeshailam and R. Srinivas, *Tetrahedron*, 2009, **65**, 9657–9672.

18 H. E. Rogers, P. Chambon, S. E. R. Auty, F. Y. Hern, A. Owen and S. P. Rannard, *Soft Matter*, 2015, **11**, 7005–7015.

19 S. E. R. Auty, O. C. J. Andrén, F. Y. Hern, M. Malkoch and S. P. Rannard, *Polym. Chem.*, 2014, **6**, 573–582.

20 S. E. R. Auty, O. Andrén, M. Malkoch and S. P. Rannard, *Chem. Commun.*, 2014, **50**, 6574.

21 Y. Xu, Z. Yang, B. Ding, D. Liu, Y. Liu, M. Sugiya, T. Imamoto and W. Zhang, *Tetrahedron*, 2015, **71**, 6832–6839.

22 R. J. Chew, K. Y. Teo, Y. Huang, B.-B. Li, Y. Li, S. A. Pullarkat and P.-H. Leung, *Chem. Commun.*, 2014, **50**, 8768–8770.

23 P. Tomalia, D, A; Baker, H; Dewald, J; Hall, M; Kallos, G; Martin, S; Roeck, J; Ryder, J; Smith, *Polym. J.*, 1985, **17**, 117–132.

24 P. Besenius, S. Slavin, F. Vilela and D. C. Sherrington, *React. Funct. Polym.*, 2008, **68**, 1524–1533.

25 J. Lu, C. Fu, S. Wang, L. Tao, L. Yan, D. M. Haddleton, G. Chen and Y. Wei, *Macromolecules*, 2014, **47**, 4676–4683.

26 Z. Wei, X. Hao, Z. Gan and T. C. Hughes, *J. Polym. Sci. Part A Polym. Chem.*, 2012, **50**, 2378–2388.

27 L. I. Liu, J. Zhang, L. V. Wenhui, Y. a N. Luo and X. Wang, *J. Polym. Sci. Part A Polym. Chem.*, 2010, **48**, 3350–3361.

28 Y. Luo, L. Liu, X. Wang, H. Shi, W. Lv and J. Li, *Soft Matter*, 2012, **8**, 1634–1642.

29 V. U. Shinde, Vaishali S.; Pawar, *J. Appl. Polym. Sci.*, 2009, **111**, 2607–2615.

Chapter 5

Synthesis of Branched Copolymers Bearing Mannose Surface Functionalities

Chapter 5

5.1. Introduction

5.1.1. HIV/AIDS

The human immunodeficiency virus (HIV) is a lentivirus - a sub-group of the retrovirus family - that infects and progressively diminishes vital cells of the immune system;[1,2] its main targets are CD4+ T lymphocytes, with the infection cycle beginning with fusion of the viral envelope to the host cell after interactions between the virion glycoprotein gp120 and the CD4 receptor.[3] This induces a conformational change that enables the interaction of gp120 with the chemokine CCR5 and CXCR4 co-receptors, resulting in the exposure of a fusogenic peptide that then anchors into the host cell membrane.[4,5] After cellular internalisation, the viral RNA is released into the host cell's cytoplasm, transcribed to viral double-stranded DNA by the viral enzyme, reverse transcriptase, and incorporated into the host cell genome by the viral enzyme, integrase.[6] Through transcription and translation processes, viral proteins are formed that then self-assemble to form the replicated virion, encapsulating two copies of single stranded RNA, and the viral enzymes integrase, reverse transcriptase and protease. The final stage involves the enveloping of the virus by a lipid bilayer derived from the membrane of the host cell as it buds out into the extracellular fluid. This viral replication results in the depletion of the CD4+ T lymphocytes, which consequently weakens immune function and eventually leads to acquired immunodeficiency syndrome (AIDS) if untreated.

5.1.2. Antiretroviral therapy (ART)

At present, there is no cure for HIV/AIDS, but antiretroviral therapy (ART) has been hugely successful in suppressing viral replication by significantly reducing the plasma viral load and increasing the CD4+ T cell count; as a result, this has changed the prognosis from that of high mortality to a chronic, yet manageable, disease.[1] Currently, there are 38 antiretroviral drugs that have gained FDA approval for clinical use, each categorised into 1 of 6 mechanistic classes that target different stages of the viral replication cycle; these classes include nucleoside reverse transcriptase inhibitors, non-nucleoside reverse transcriptase inhibitors, protease inhibitors, integrase inhibitors, fusion inhibitors and entry inhibitors.[7] ART involves a strict regimen whereby patients are administered a combination of three or more of these drugs (selected from at least two mechanistic classes) on a daily basis.

As a result, ART improves the quality of life for infected individuals and delays the progression to AIDS, but it is not sufficient enough to eradicate the virus. This is because the virus is able to establish latent cellular reservoirs (*e.g.* CD4+ memory T cells, macrophages and follicular dendritic cells)[8–14] and anatomical reservoirs (*e.g.* central nervous system, lymphatic system, lungs and genital organs)[15], in which the viral genome persists in a DNA form as an integrated pro-virus that is not actively transcribed; for as long as these latently infected reservoirs remain dormant, they will evade recognition by the immune system, enabling the replication cycle to be re-activated at any time. Furthermore, the presence of numerous biological barriers (*e.g.* blood-brain barrier, blood-cerebrospinal fluid barrier, blood-testes barrier) make it very difficult to attain therapeutically relevant antiretroviral drug concentrations within these reservoirs.

To address these problems, research is directed towards actively targeting the viral reservoirs to achieve therapeutically relevant concentrations of the antiretroviral drugs, or alternatively, to force the activation of latently infected cells; in the latter case, activation of the viral replication cycle enables recognition and elimination of the infected cells by the immune system.[16]

5.1.3. Actively targeting DC-SIGN receptors and mannose receptors

Dendritic cell-specific intercellular adhesion-molecule-3-grabbing non-integrin (DC-SIGN) and the mannose receptor are C-type lectins abundantly present on the surface of dendritic cells and macrophages.[17,18] Through multi-valent and calcium-dependent interactions, they are able to bind to highly glycosylated proteins presented on the surface of pathogens, including the gp120 high mannose glycan of HIV, rendering them viable targets for anti-HIV drug delivery systems and vaccines.[19–21]

Two interesting studies, reported by Haddleton and coworkers, involved the synthesis of a library of glycopolymers - consisting of mannose, galactose, glucose and fucose functionalities - *via* a combination of Cu-mediated SET-LRP and Cu-catalysed azide-alkyne click (CuAAC) reactions; the binding behaviour of the glycopolymers to DC-SIGN was assessed, with the results showing a greater affinity for the polymers with higher mannose content.[22,23] Another interesting study, reported by Dutta and Jain, investigated the targeting potential and anti-HIV activity of mannosylated 5th

generation PPI dendrimers encapsulating the antiretroviral drug, lamivudine (43 % entrapment efficiency). The results showed the extent of cellular internalisation of the mannosylated PPI dendrimers was significantly greater than that seen for the free-drug and the non-functionalised PPI dendrimer (by a factor of 21 and 8.3 respectively); consequently, a significantly higher anti-HIV activity was observed for the mannose functionalised dendrimer.[24]

5.1.4. Chapter aims

The aim of this Chapter was to synthesise mannose-functionalised dendritic initiators (G0 and G2) using similar chemistry to that demonstrated in Chapter 4; these initiators will then be utilised in the methanolic Cu-catalysed ATRP of *n*BuMA to yield amphiphilic materials capable of actively targeting DC-SIGN and mannose receptors. Linear polymerisations will be performed, targeting various degrees of polymerisation, to assess the control of the polymerisations before being repeated in the presence of a low concentration of the divinyl monomer, EGDMA, to yield mannosylated *hyp*-glycopolydendrons. Their ability to form stable nanoparticle dispersions in aqueous media will be assessed by performing rapid nanoprecipitation studies.

5.2. Synthesis of G0 mannose initiator

The synthesis of the mannose functionalised G0 ATRP initiator was performed in 3 steps that involved the protection of all hydroxyl groups, followed by the selective deprotection of the anomeric centre and, finally, a bromo-esterification to introduce the tertiary bromide functionality required to initiate the polymerisation (Scheme 5.1).

The hydroxyl groups of D-mannose were protected *via* an acetylation procedure

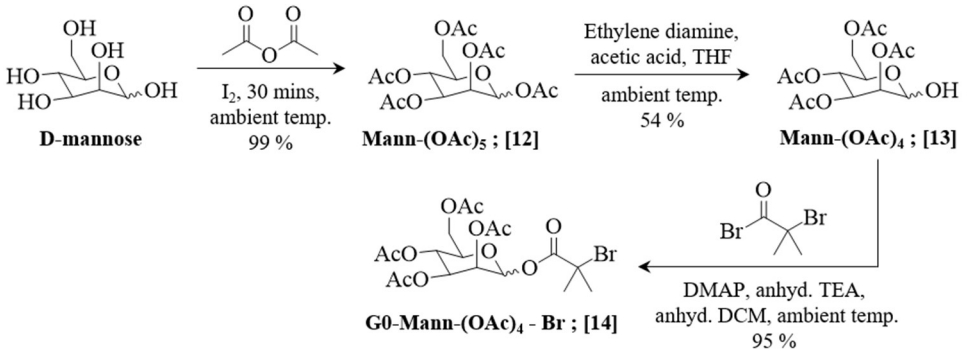

Scheme 5.1. Reaction scheme detailing the 3-step synthesis of the mannose functionalised G0 ATRP initiator.

reported by Kartha and Field, which involved reacting the monosaccharide with acetic anhydride, using iodine as a lewis acid catalyst;[25] the exothermic reaction was complete within 30 minutes. The crude product was purified by solvent-solvent extractions that involved an aqueous sodium thiosulfate wash to remove the iodine, and saturated sodium bicarbonate washes to remove the acetic acid by-product. Further purification by normal phase flash-chromatography afforded the Mann-$(OAc)_5$ [12] acetylated product in a 98 % yield. The structure of the desired compound was confirmed by resonances between 2.0-2.25 ppm in the ^{1}H-NMR spectrum attributed to the COC**H$_3$** acetyl protons (Figure 5.1A; Figure A33, Appendix), and resonances between 168-172 ppm in the ^{13}C-NMR spectrum attributed to the O**C**=OCH_3 ester groups introduced as a result of the acetylation (Figure A24, Appendix). The purified product was also characterised by ESI-mass spectrometry showing a molecular ion peak $[M+Na]^+$ at 413 Da (Figure A35, Appendix).

Deprotection of the anomeric centre was achieved by reacting Mann-$(OAc)_5$ [12] with ethylene diamine and acetic acid in THF under ambient reaction conditions, a method that is widely reported in the literature.[26–28] The crude product was purified by solvent-solvent extraction and normal phase flash chromatography to afford Mann-$(OAc)_4$ [13] (2:98 α:β ratio) in 56 % yield. In comparison to the Mann-$(OAc)_5$ [12] starting material, ^{1}H-NMR analysis of the purified product showed the disappearance of resonances between 6.0-6.3 ppm and the appearance of resonances between 3.25-3.60 ppm; each of these environments are attributed to the anomeric protons, with the observed shift confirming the selective deacetylation at the anomeric centre (Figure 5.1; Figure A36, Appendix).

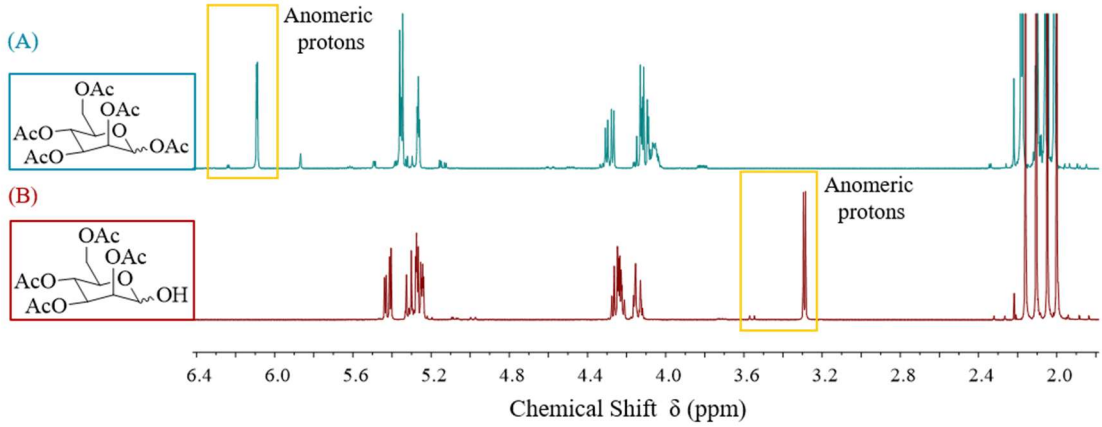

Figure 5.1. ^{1}H-NMR ($CDCl_3$) spectra of: (A) Mann-$(OAc)_5$ [12], and (B) Mann-$(OAc)_4$ [13]. The observed shift in resonance of the anomeric protons after selective deacetylation is highlighted by the yellow boxes.

This is also confirmed by the disappearance of a peak at 2.18 ppm attributed to the COC**H**$_3$ acetyl protons. Furthermore, ^{13}C-NMR analysis showed 4 peaks between 169-171 ppm attributed to the remaining acetyl groups, and ESI-mass spectrometry analysis showed a molecular ion $[M+Na]^+$ peak at 371.1 Da (Figures A37 and A38, Appendix).

Finally, Mann-$(OAc)_4$ [13] was reacted with α-bromo isobutyryl bromide in anhydrous dichloromethane (DCM) under an inert nitrogen atmosphere. The reaction was catalysed by 4-dimethylaminopyridine (DMAP), and an excess of triethylamine (TEA) was used to scavenge the hydrogen bromide (HBr) side product. After reaction completion, the DCM was removed on the rotary evaporator to give a viscous brown coloured oily residue; the product was extracted from this residue using diethyl ether, with each extract passed through filter paper to remove the triethylammonium bromide ($Et_3N^+Br^-$) salt. After removal of the solvent on the rotary evaporator, the product was purified further by normal phase flash chromatography to give G0-Mann-Br [14] initiator in 95 % yield. Although assignment of each resonance was difficult to achieve, the total integration of the peaks within the ^{1}H-NMR spectrum matched theoretical values when normalising the multiple resonances between 1.70-2.40 ppm to 18H (Figure 5.2). Furthermore, ^{13}C-NMR analysis revealed a resonance at 30 ppm attributed to the isobutyl group introduced by the esterification (Figure 5.3), and ESI mass spectrometry showed a molecular ion $[M+Na]^+$ peak at 519 Da (Figure 5.4).

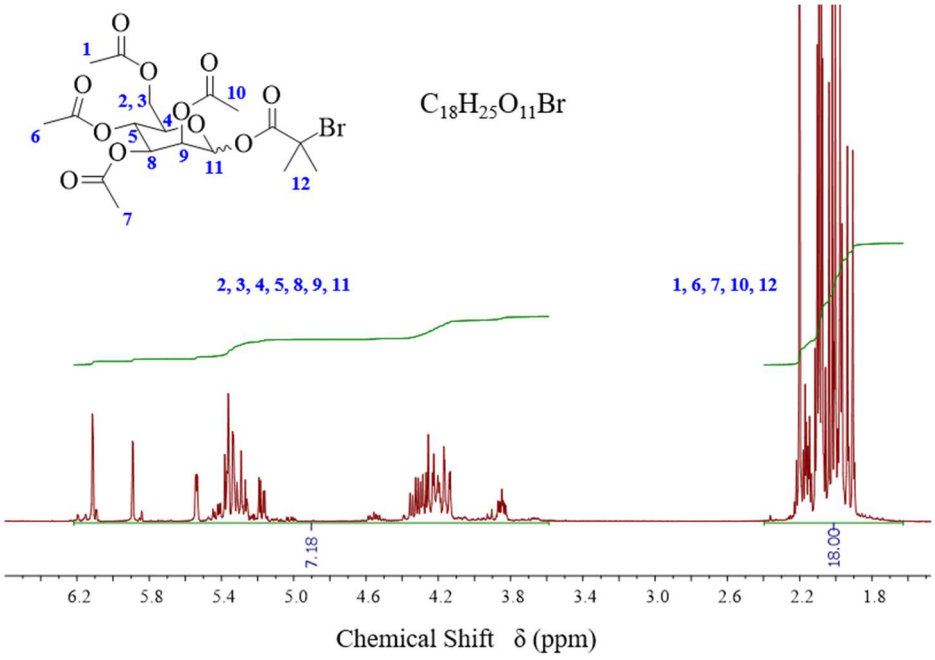

Figure 5.2. ^{1}H-NMR ($CDCl_3$) of G0-Mann-Br [14] initiator.

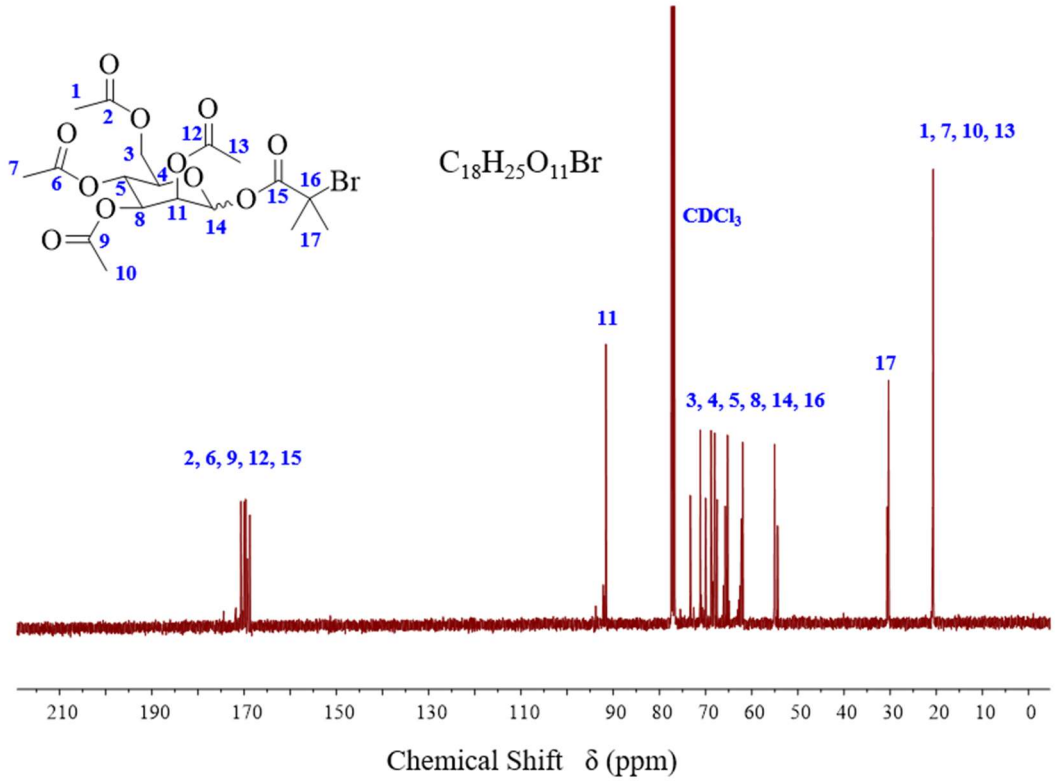

Figure 5.3. ^{13}C-NMR ($CDCl_3$) of G0-Mann-Br [14] initiator.

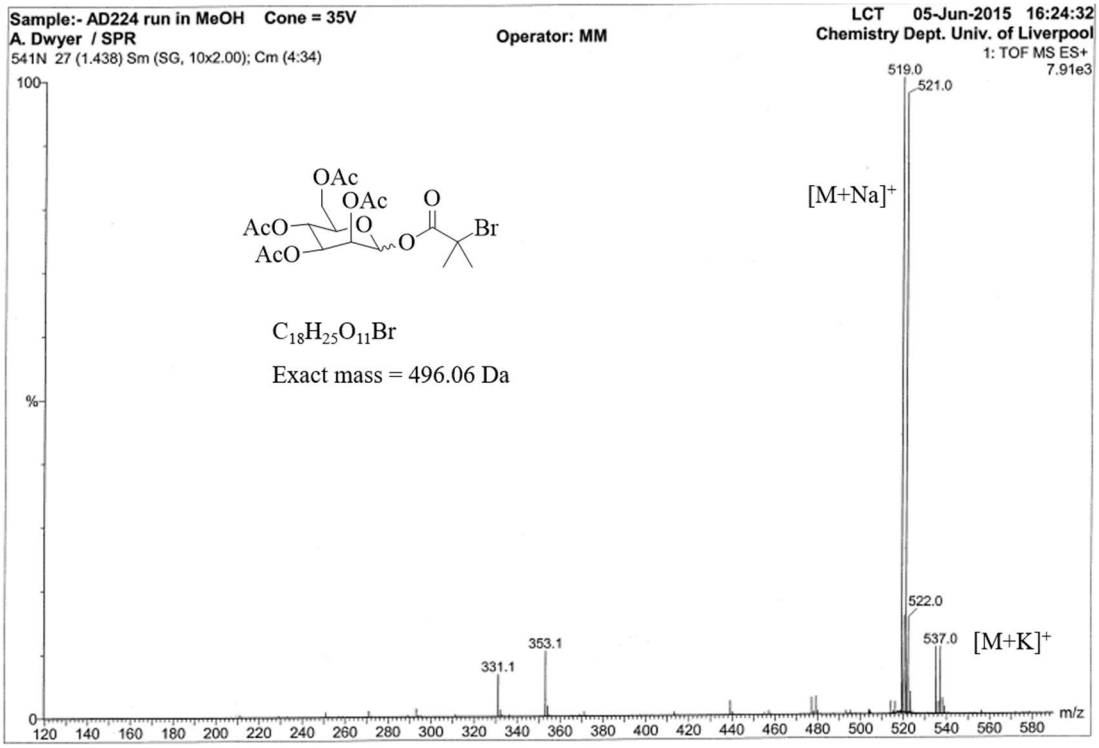

Figure 5.4. ESI mass spectrometry analysis of G0-Mann-Br [14], showing the $[M+Na]^+$ and $[M+K]^+$ molecular ion peaks.

5.3. Synthesis of G2 mannose functionalised dendritic initiator

Synthesis began by reacting Mann-$(OAc)_4$ [13] with acryloyl chloride in anhydrous DCM under an inert nitrogen atmosphere (Scheme 5.2); the reaction was catalysed by DMAP, and an excess of TEA was used to scavenge the HCl by-product, forming a $Et_3N^+Cl^-$ salt that precipitated from solution as the reaction progressed. After reaction completion, the salt was filtered off and washed with cold DCM before removing the solvent on the rotary evaporator (at 35 °C to avoid self-polymerisation) to give a brown coloured residue. The product was extracted from this residue using diethyl ether, with each extract filtered to remove residual $Et_3N^+Cl^-$ salt, before being concentrated and purified further by normal phase flash chromatography to give the Mann-$(OAc)_4$-acrylate [15] as a yellow coloured oil in 66 % yield. In comparison to the Mann-$(OAc)_4$ starting material, ^{1}H-NMR analysis of the purified product showed a shift for anomeric resonances from 3.25-3.60 ppm to approximately 6.20 ppm, and the appearance of a further three resonances attributed to vinyl protons of the acrylate functional group (Figure 5.5; Figure A39, Appendix). Analysis by ^{13}C-NMR revealed the appearance of two peaks between 129-137 ppm that can be assigned to each carbon of the vinyl functionality introduced by the esterification, and ESI-mass spectrometry gave a $[M+Na]^+$ molecular ion peak at 425.1 Da (Figures A40 and A41, Appendix).

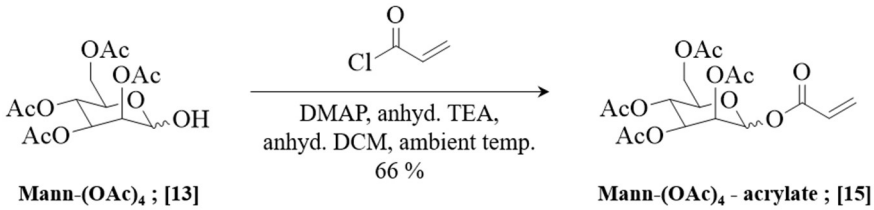

Scheme 5.2. Reaction scheme detailing the synthesis of Mann-$(OAc)_4$-acrylate [15].

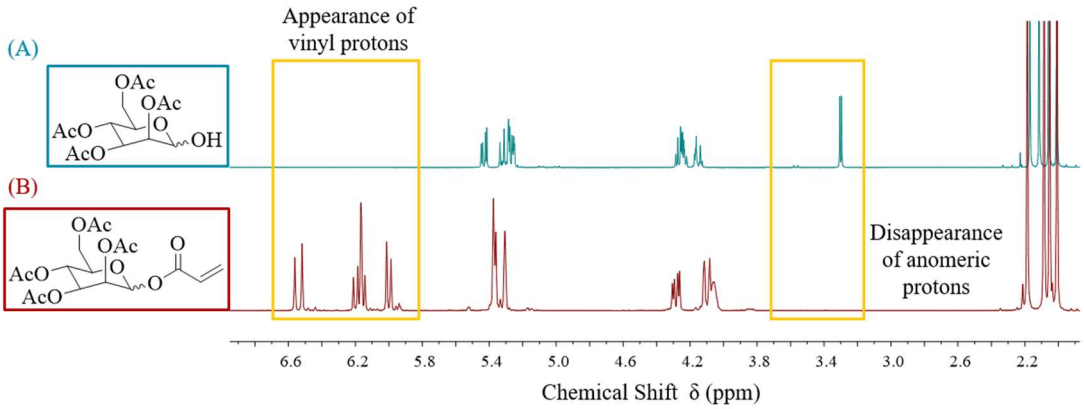

Figure 5.5. ^{1}H-NMR ($CDCl_3$) of: (A) Mann-$(OAc)_4$ [13], and (B) Mann-$(OAc)_4$-acrylate [15]. The observed disappearance of the anomeric protons and the appearance of the vinyl protons are highlighted by the yellow boxes.

The next step in the synthesis involved the reaction of Mann-$(OAc)_4$-acrylate [15] with the AB_2 branching unit, APAP [8], *via* exhaustive aza-Michael-type addition; it was demonstrated in Chapter 4 that aza-Michael-type addition in protic solvents resulted in significantly higher yields, therefore this reaction was performed in IPA at ambient temperature for 7 days, using an 8:1 excess of the acrylate relative to APAP [8] (Scheme 5.3). Analysis of the crude product by thin layer chromatography (TLC) on silica plates revealed 5 spots with R_f values ranging from 0.03 to 0.8. Thus, utilising normal phase flash chromatography, the first four compounds were collected and analysed by ^{1}H-NMR and ^{13}C-NMR spectroscopy (Figures 5.6). The compound attributed to the fifth spot on the TLC plate ($R_f = 0.03$) was retained by the column and could not be analysed; this is likely to be unreacted APAP [8] that did not elute from the column due to the strong acid-base interactions between the silica and the compound.

Analysis of the first eluted compound showed resonances between 5.70-6.50 ppm in the ^{1}H-NMR spectrum (Figure 5.6A(i)) and resonances between 129-137 ppm in the ^{13}C-NMR spectrum (Figure 5.6B(i)), both of which are attributed to the vinyl functionality of Mann-$(OAc)_4$-acrylate [15]; this is to be expected given that it was in excess to drive the reaction to completion. Analysis of the second eluted compound showed an identical ^{13}C-NMR spectrum (Figure 5.6B(ii)) to that observed for the Mann-$(OAc)_4$ [13]; however, the ^{1}H-NMR spectrum showed identical resonances with only one exception - no resonance between 3.20-3.60 ppm that would be attributed to the anomeric proton (Figure 5.6A(ii)). Instead, a small, broad resonance at

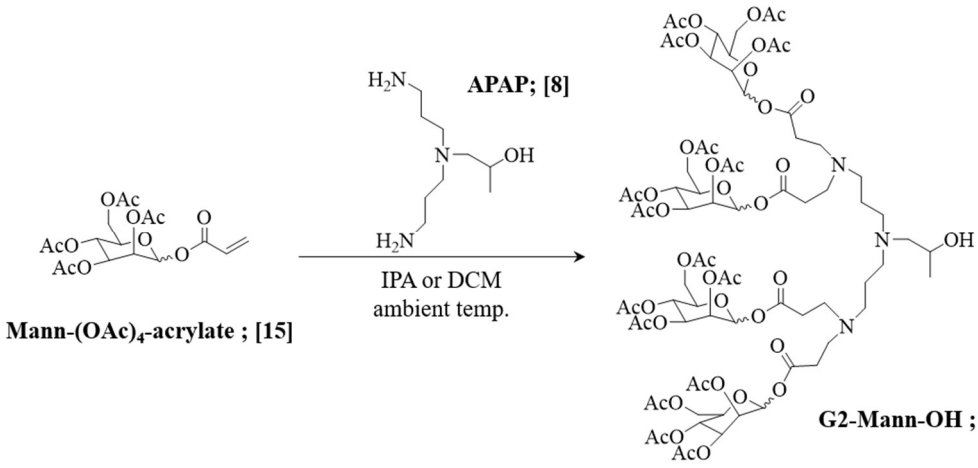

Scheme 5.3. Reaction scheme detailing the attempted synthesis of dendritic G2-Mann-OH [16] *via* aza-Michael-type additions.

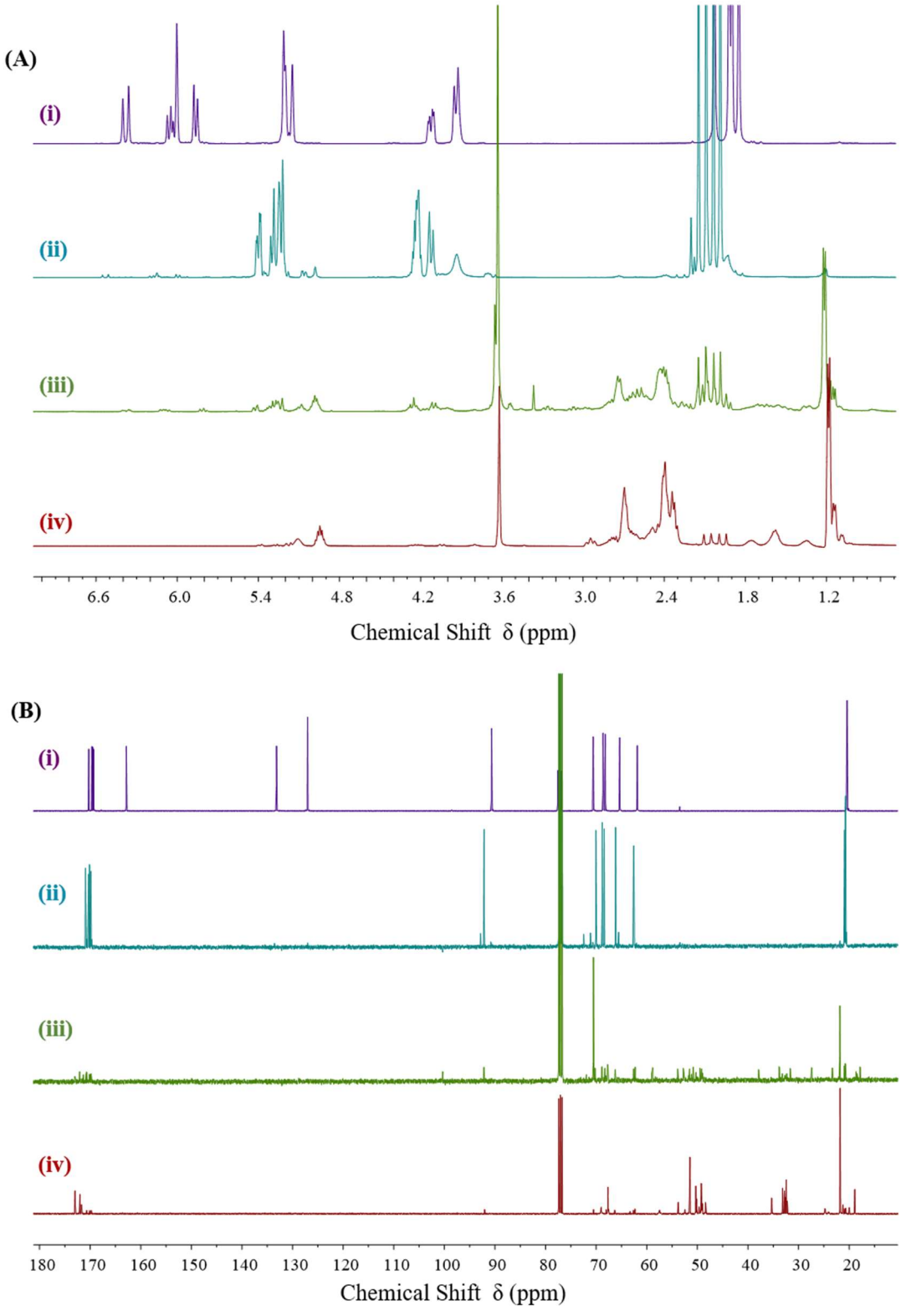

Figure 5.6. ^{1}H-NMR spectra (A), and ^{13}C-NMR spectra (B) of the compounds formed during the attempted synthesis of the G2-Mann-OH [16] dendritic compound; the compounds are shown in order of their elution from the silica column, with (i) being the first compound to elute, and (iv) the last compound to elute.

approximately 3.90 ppm was observed which may be attributed to the anomeric proton that has shifted down-field as a consequence of running the NMR sample at high concentration; a concentrated sample could induce hydrogen-bonding between hydroxyl groups on the anomeric carbons and subsequently reduce electron-density, resulting in a de-shielding effect with respect to the external magnetic field of the spectrometer. Therefore, even though a significant shift in resonance attributed to the anomeric proton was observed, both the ^{1}H-NMR and ^{13}C-NMR spectra strongly suggest that the eluted compound is indeed Mann-$(OAc)_4$ [13], formed as a result of a transesterification side-reaction between Mann-$(OAc)_4$-acrylate [15] and the IPA solvent. ^{1}H-NMR analysis of both the third and fourth eluted compounds showed resonances attributed to APAP [8] (δ = 1.10 ppm, 2.40-3.00 ppm), and weak resonances attributed to the acetyl groups of the protected mannose functionalities (δ = 1.90-2.20 ppm) (Figure 5.6A(iii-iv)). Furthermore, two strong resonances at approximately 2.40 and 2.70 ppm are likely to be attributed to CH_2 environments introduced as a result of aza-Michael-type addition, therefore, suggesting that the desired reaction has indeed taken place to some degree. However, a large doublet at approximately 1.20 ppm was also observed, which could be attributed to methyl environments introduced *via* aza-Michael-type addition between the proposed isopropyl-acrylate side-product and APAP [8]. The high intensity of this peak in both compounds indicates a greater degree of the isopropyl functionality compared to the protected mannose functionality; it's important to note that due to overlapping of resonances and poor baselines observed in each spectrum, it was difficult to determine the exact ratios of each functionality reacted onto the APAP [8] unit.

Therefore, after analysis of each of the compounds formed during the reaction, it is clearly evident that the desired G2-Mann-OH dendritic compound was not formed and that the reaction was unsuccessful. It has been proposed that a series of side-reactions have taken place that were instigated by the protic IPA solvent (Scheme 5.4); such reactions were not observed during the synthesis of the G2-Gal-OH dendritic compound in Chapter 4, suggesting that the position of the acrylate functionality on the ring structure of the saccharide is an important parameter to consider when utilising such chemistry. Additionally, it is not clear if APAP [8] plays a negative role but, its structural similarity to ethylene diamine (used in the selective deprotection step to yield Mann-$(OAc)_4$ [13]) may go some way to explain the observed issues.

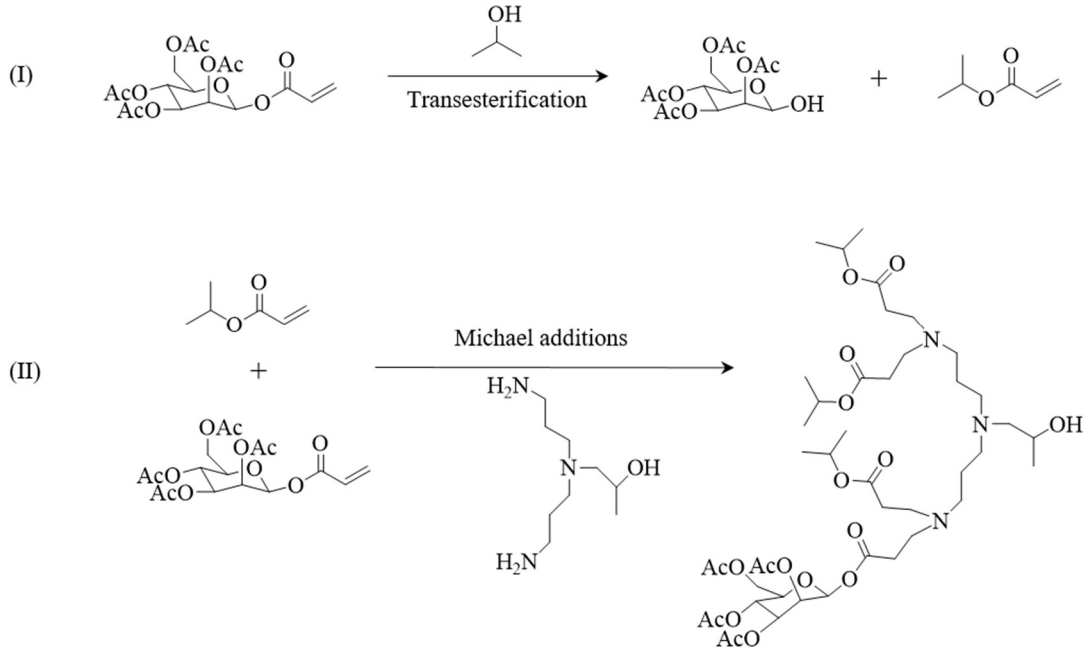

Scheme 5.4. Reaction scheme detailing the proposed side-reactions during the attempted synthesis of G2-Mann-OH [16]: (I) transesterification between Mann-$(OAc)_4$-acrylate [15] and the IPA solvent, and (II) the subsequent aza-Michael-type additions between the isopropyl acrylate/ Mann-$(OAc)_4$-acrylate [15] and APAP [8].

5.4. Methanolic ATRP of *n*BuMA using G0-Mann-Br initiator

The methanolic Cu-catalysed ATRP of *n*BuMA was performed using the G0-Mann-Br [14] initiator, targeting a DP_n = 60, 80, 100 monomer units (Scheme 5.5); the effect of temperature was assessed by performing the series of polymerisations at both 60 °C and 25 °C. Each polymerisation was allowed to progress to high conversion before exposing the reaction flask to air to poison the catalytic system. The polymers were purified by passing through an alumina column to remove the Cu^{II} catalyst before being concentrated in THF and precipitated into cold hexane to give white solids.

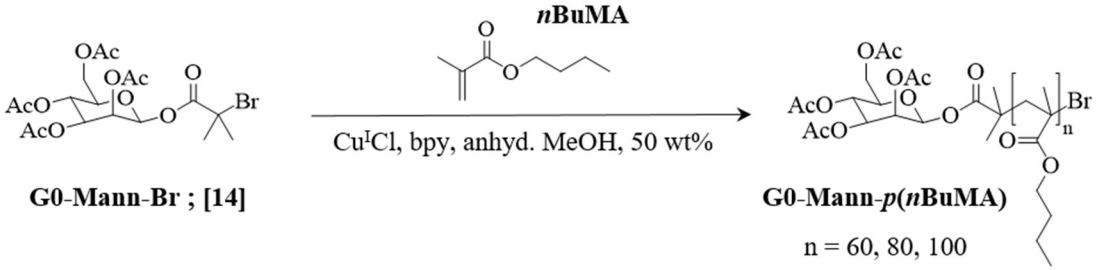

Scheme 5.5. Cu-catalysed ATRP of *n*BuMA in anhydrous MeOH at 50 wt%.

The polymerisations performed at 60 °C progressed homogeneously to high conversion (99 %) to yield low dispersity ($Đ \leq 1.08$) homopolymers with number average molecular weight (M_n) values ranging from 15,530 – 23,000 g mol^{-1}; 1.58-1.72 fold higher than theoretical values, with the deviation decreasing as the targeted DP$_n$ increased (Table 5.1). Furthermore, the GPC (RI) chromatograms for each of the polymers showed monomodal and symmetrical molecular weight distributions, indicating no significant loss of propagating chains during the polymerisation (Figure 5.7).

The polymerisations performed at 25 °C, targeting DP$_n$ = 60, 80 *n*BuMA units, progressed homogeneously to high conversions (91 % and 92 % respectively); however, the polymerisation targeting DP$_n$ = 100 monomer units phase separated at towards the end of the polymerisation to give a viscous, polymer-rich phase clumped around the magnetic stirrer bar. This was not obvious at first, but could be more easily observed when manipulating the stirrer bar with a magnet. This phase separation behaviour could be due to one of two reasons: (i) the anhydrous MeOH solvent had been contaminated with moisture, which would have a significant effect on the cloud point temperature of the polymer in the methanolic environment – as demonstrated in the cloud point studies of Chapter 2, or (ii) the protected mannose chain-end functionality may have a significant effect on the ability of the polymer to remain in

Table 5.1. Cu-catalysed methanolic ATRP of *n*BuMA at 60 °C and 25 °C using G0-Mann-Br

				Triple-detection GPC (DMF)		
Target[a] DP$_n$	Conversion [actual DP$_n$]	Time (h)	M_n theory[b]	M_n (g mol^{-1})	M_w (g mol^{-1})	Đ
60 °C						
60	99 % [59]	24	8 950	15 350	16 600	1.08
80	99 % [79]	48	11 750	19 150	20 300	1.06
100	99 % [99]	72	14 600	23 000	24 950	1.08
25 °C						
60	91 % [55]	24	8 250	12 850	13 500	1.05
80	92 % [74]	48	10 950	16 400	17 400	1.06
100	98 % [98]	72	14 450	21 550	22 500	1.05

[a] Target DP$_n$ calculated as [*n*BuMA]/[initiator]. [b] Theoretical M_n calculated as (target DP$_n$ x actual conversion achieved and includes initiator residue).

solution. Rannard and coworkers have previously demonstrated how the LCST behaviour for *p*(DMAEMA) is affected by very subtle (single methylene group) changes in the structure of the initiating chain-end functionalities;[29] it is, therefore, reasonable to assume that the changes in the structure of the initiating groups presented within this thesis may have a significant effect of the UCST behaviour of *p*(*n*BuMA).

For the targeted DP_n = 100 polymer, it is important to note that before taking a crude sample for ^{1}H-NMR analysis, chloroform was added to the reaction flask to give a single phase that enabled the monomer conversion to be determined accurately as 98 %. In all cases, the polymerisations proceeded to lower monomer conversions when compared to those performed at 60 °C over similar reaction times, indicating a slower rate of polymerisation at this reduced temperature. Additionally, triple detection GPC (DMF) analysis revealed low dispersity polymers ($Đ$ < 1.06) with M_n values ranging from 12,850 – 21,550 g mol^{-1}; 1.49-1.56 fold higher than theoretical values, with the deviation, once again, decreasing as the targeted DP_n increased. In all cases, narrower molecular weight distributions and improved M_n targeting were observed for the polymers obtained at 25 °C compared to those obtained at 60 °C. Interestingly, the best results were observed for the G0-Mann-*p*(*n*BuMA)$_{100}$ polymer despite having phase-separated during the reaction, indicating no negative effect on the control of the polymerisation. Furthermore, the GPC (RI) chromatograms for each of the polymers showed monomodal and symmetrical molecular weight distributions (Figure 5.7).

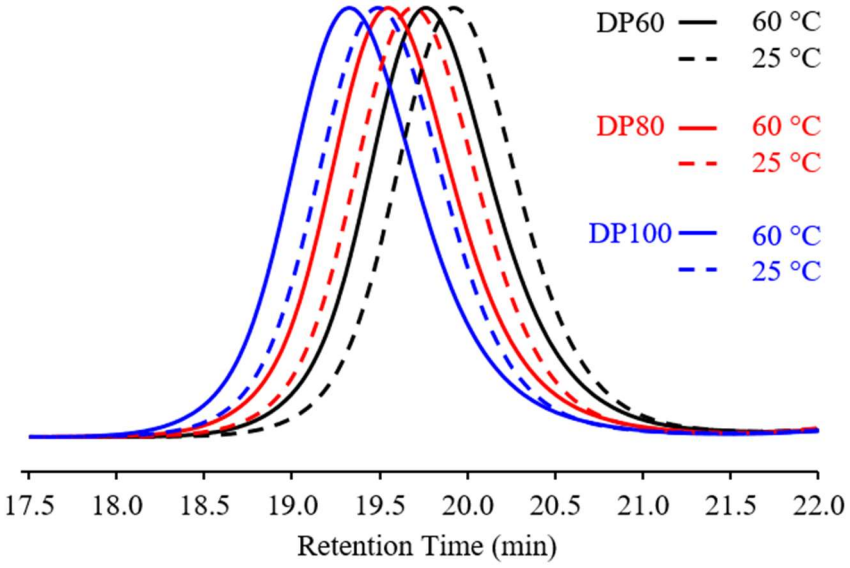

Figure 5.7. GPC (RI) chromatograms showing the molecular weight distributions of *p*(*n*BuMA)$_{60\text{-}100}$, obtained *via* ATRP using the G0-Mann-Br initiator [14] at 60 °C (solid lines) and 25 °C (dashed lines).

5.5. Branched methanolic ATRP of *n*BuMA using G0-Mann-Br initiator

Polymers consisting of a branched architecture with protected mannose surface functionalities were obtained by polymerisation following the Strathclyde approach; this involved the Cu-catalysed methanolic ATRP of *n*BuMA, targeting a DP_n = 30 monomer units, in the presence of the divinyl monomer, EGDMA, to promote the statistical inter-chain branching of primary polymer chains (Scheme 5.6). A low concentration of EGDMA was maintained (0.8 equivalents per initiator) so as to avoid gelation, and the reaction temperature was varied from 60 °C to 25 °C to study its effect on the degree of branching.

Each polymerisation was allowed to progress to high conversion over 21 hours to enable direct comparisons between the data (Table 5.2), after which the reaction flask was exposed to air to poison the catalytic system. The polymers were purified by passing through an alumina column to remove the Cu^{II} catalyst before being concentrated in THF and precipitated into cold hexane to give white solids.

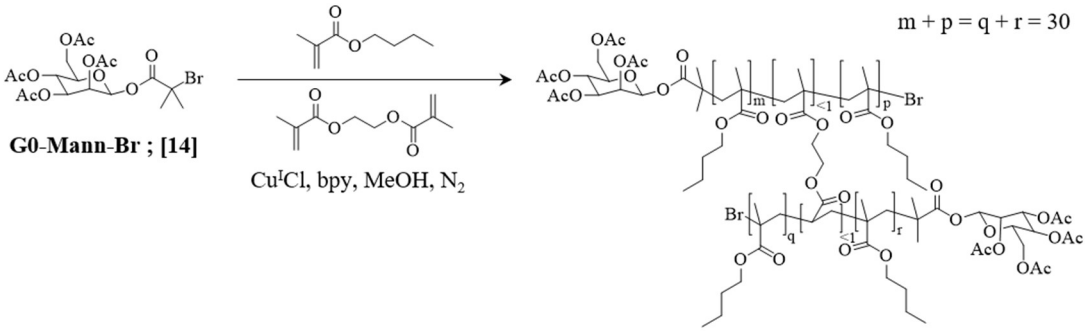

Scheme 5.6. Cu-catalysed methanolic ATRP of *n*BuMA in the presence of a low concentration of EGDMA at both 60 °C and 25 °C.

Table 5.2. Branched Cu-catalysed methanolic ATRP of *n*BuMA at 60 °C and 25 °C using EGDMA as branching monomer and G0-Mann-Br [14] as initiator.

Target[a] DP_n	Conversion [actual DP_n]	Time (h)	EGDMA: G0-Mann-Br	Triple-detection GPC (DMF)		
				M_n (g mol^{-1})	M_w (g mol^{-1})	Đ
60 °C						
30	99 % [30]	21	0.8 : 1	19 750	89 800	4.54
25 °C						
30	94 % [28]	21	0.8 : 1	17 300	66 400	3.84

[a] Target DP_n calculated as [*n*BuMA]/[initiator].

As seen with, linear polymerisations performed in the absence of EGDMA (Section 5.4), the reaction at the elevated temperature proceeded homogeneously to high conversion; however, the reaction at 25 °C phase separated towards the later stages of the polymerisation, which is surprising given that the linear polymers with target DP_n = 60, 80 monomer units remained in solution to high conversion (≥ 91%; Table 5.1). This suggests that the polymer architecture also influences the UCST behaviour of the polymer. In this case, chloroform was added to the reaction flask to give a single phase before sampling for ^{1}H-NMR analysis.

^{1}H-NMR ($CDCl_3$) analysis of crude samples taken at the end of each polymerisation showed that higher monomer conversions were achieved when polymerising at 60 °C, indicating a greater rate of polymerisation at the elevated temperature. Furthermore, GPC (DMF) analysis calculated higher weight average molecular weight values (M_w = 89,800 g mol^{-1}) for the polymers obtained at 60 °C compared to those obtained at 25 °C (M_w = 66,400 g mol^{-1}), which is to be expected given that that the statistical branching mainly occurs towards the latter stages of the polymerisation,[30] and that lower monomer conversions were achieved at the reduced temperature. This is also reflected in the GPC chromatograms, showing the elution of higher molecular weight materials at lower retention times for the polymer obtained at 60 °C (Figure 5.8).

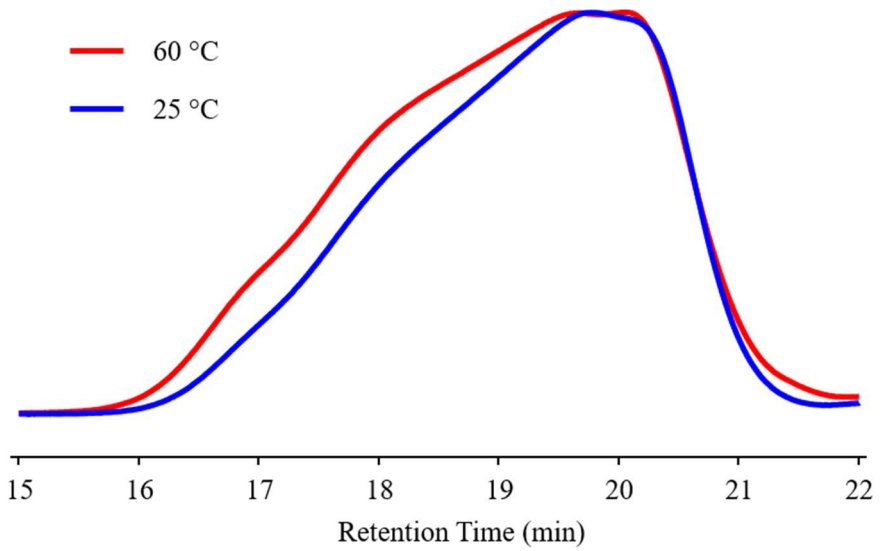

Figure 5.8. GPC (RI) chromatograms showing the molecular weight distributions of G0-Mann-*p*(*n*BuMA$_{30}$-*co*-EGDMA$_{0.8}$) obtained *via* Cu-catalysed methanolic ATRP at both 60 °C (red solid line) and 25 °C (blue solid line).

5.6. Nanoprecipitation of G0-Mann-*p*(*n*BuMA$_{30}$-*co*-EGDMA$_{0.8}$)

Nanoprecipitations of each of the branched copolymers were performed through the rapid addition of 1 mL of polymer-THF solutions (5 mg mL^{-1}) into 5 mL of H_2O, after which the volatile organic solvent was allowed to evaporate under ambient conditions to yield nanoparticles within the aqueous antisolvent (Figure 5.9). These aqueous dispersions were analysed by dynamic light scattering (DLS) (Table 5.3, Figure 5.10).

DLS analysis of the unfiltered samples revealed monomodal intensity-weighted distributions (Figure 5.10A) for each of the branched copolymer nanoparticles, with *z*-average values (D_z) ranging from 120 to 140 nm and low polydispersity index (PdI) values ranging from 0.046 to 0.074. The number-weighted particle size distributions (D_n), derived from the intensity distributions using Mie theory, were also monomodal (Figure 5.10B) and gave D_n values ranging from 96 to 113 nm. Additionally, negative zeta potentials were observed for each sample (≥ -18.4 mV) indicating the presence of charge stabilisation. The large sizes of the nanoparticles observed in both the intensity-weighted and number-weighted distributions indicate that the nanoparticles are formed *via* the proposed nucleation/growth mechanism that is described in Chapter 3 (Section 3.1.3). Scanning electron microscopy (SEM) images were taken of each sample, both of which showed spherical particles with sizes that correlate well with the data obtained by DLS (Figure 5.11); however, fewer nanoparticles were observed for the branched copolymer obtained at 25 °C (Figure 5.11B). This is also reflected in lower derived count rate that was calculated by the DLS instrument.

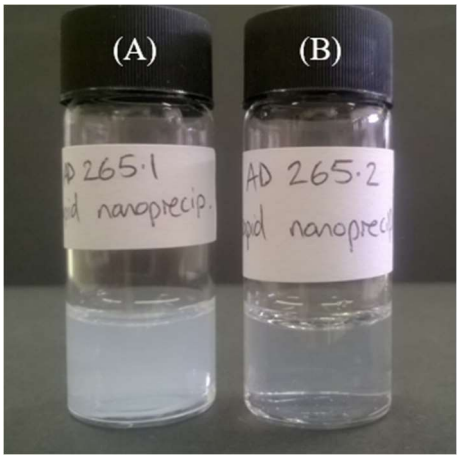

Figure 5.9. Pictures displaying the aqueous dispersions of the amphiphilic branched copolymers after rapid nanoprecipitation and subsequent evaporation of the organic solvent: (A) G0-Mann-*p*(*n*BuMA$_{30}$-*co*-EGDMA$_{0.8}$) obtained at 60 °C, and (B) G0-Mann-*p*(*n*BuMA$_{30}$-*co*-EGDMA$_{0.8}$) obtained at 25 °C.

Table 5.3. Dynamic light scattering data of nanoprecipitations using THF solutions of G0-Mann-*p*(*n*BuMA$_{30}$-*co*-EGDMA$_{0.8}$) (1 mL) into H_2O (5 mL)

Sample	Initial concentration in THF	Final concentration in H_2O	DLS [a]				
			D_z (d.nm) [b]	PdI [c]	D_n (d.nm) [d]	DCR [e] (kcps) [attenuator]	Zeta potential (mV)
G0-Mann-*p*(*n*BuMA$_{30}$-*co*-EGDMA$_{0.8}$) **(60 °C)**	5 mg mL^{-1}	1 mg mL^{-1}	144	0.074	113	301 250 [5]	-26.2
G0-Mann-*p*(*n*BuMA$_{30}$-*co*-EGDMA$_{0.8}$) **(25 °C)**	5 mg mL^{-1}	1 mg mL^{-1}	120	0.046	96	29 700 [7]	-18.4

[a] DLS measurements recorded at 25 °C after an equilibration period of 2 minutes. [b] Size distribution using *z*-average values. [c] Polydispersity index. [d] Size distribution using number average values. [e] Derived count rate.

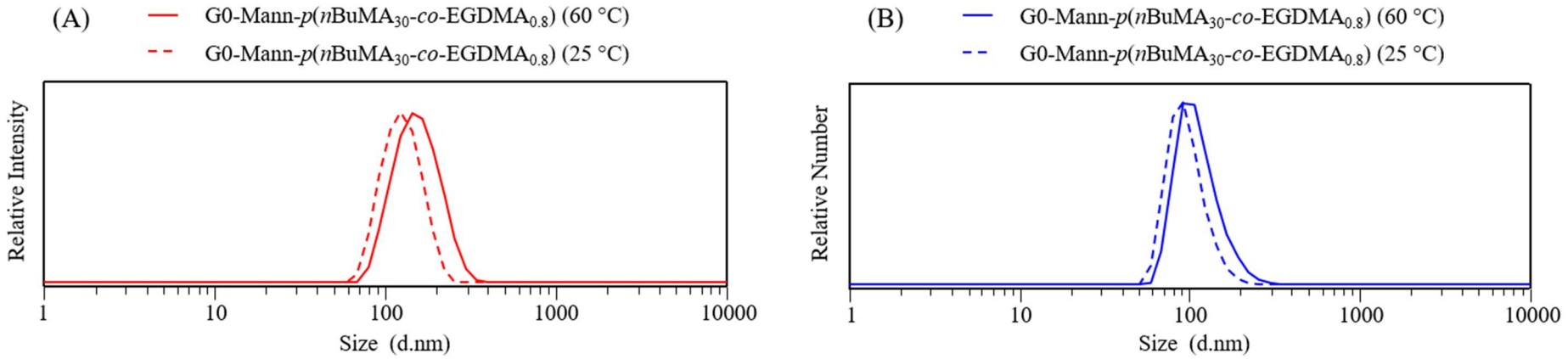

Figure 5.10. DLS traces showing: (A) intensity-weighted distributions, and (B) number-weighted distributions of the G0-Mann-*p*(*n*BuMA$_{30}$-*co*-EGDMA$_{0.8}$) branched copolymers obtained at 60 °C (solid lines) and 25 °C (dashed lines).

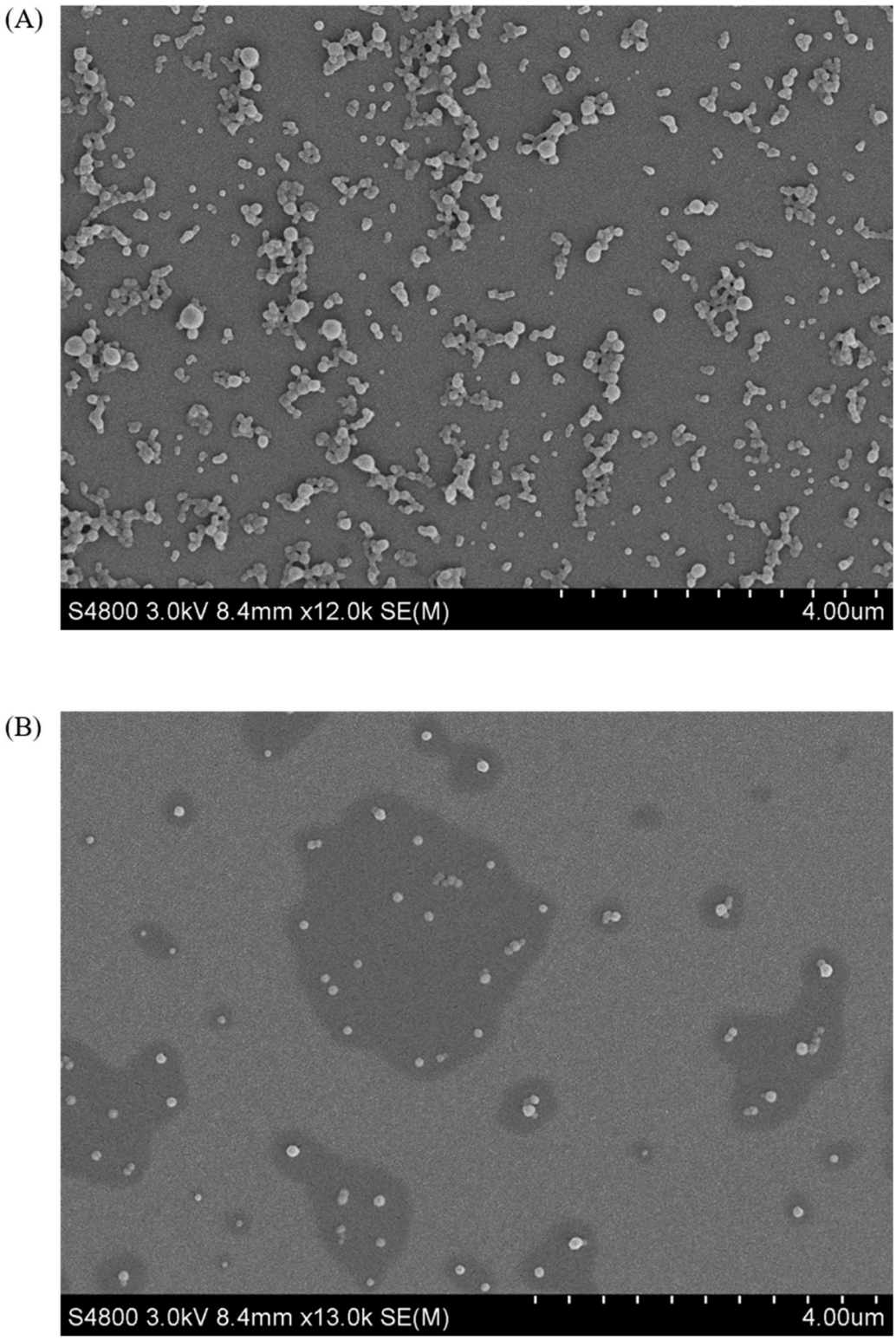

Figure 5.11. Scanning electron microscopy (SEM) images of nanoparticles formed after nanoprecipitation of: (A) G0-Mann-*p*(*n*BuMA$_{30}$-*co*-EGDMA$_{0.8}$) obtained at 60 °C, and (B) G0-Mann-*p*(*n*BuMA$_{30}$-*co*-EGDMA$_{0.8}$) obtained at 25 °C. Scale bars of 4 μm are observed in both images.

5.7. Conclusions

In conclusion, a generation zero (G0), mannose functionalised ATRP initiator was successfully synthesised by a 3 step reaction procedure that involved protection and selective deprotection strategies, followed by a bromo-esterification to introduce the required tertiary bromide functionality at the anomeric centre of the saccharide; the structure of the compound was confirmed by ^{1}H-NMR and ^{13}C-NMR spectroscopy, and ESI mass spectrometry.

The methanolic Cu-catalysed ATRP of *n*BuMA was performed using the G0-Mann-Br [14] initiator, under the same reaction conditions that have been utilised throughout this thesis. Linear G0-Mann-*p*(*n*BuMA) polymers were synthesised at both 60 °C and 25 °C, targeting a DP_n = 60, 80, 100 monomer units, with all polymerisations achieving high conversions (≥ 91 %) to yield low dispersity polymers ($Đ \leq 1.08$); narrower molecular weight distributions and improved M_n targeting were observed when polymerising at the reduced temperature. However, phase separation did occur when polymerising at 25 °C, targeting a DP_n = 100 *n*BuMA units; this could either be due to contamination of the reaction solvent with H_2O, or the presence of the protected mannose chain-end functionalities having a significant effect on the UCST behaviour of the polymer within the methanolic environment. It is important to note that no effect was observed on the molecular weight distribution of the obtained G0-Mann-*p*(*n*BuMA)$_{100}$, despite phase separation having taken place.

Branched polymerisations were performed following the Strathclyde approach, using EGDMA as the divinyl branching monomer; a DP_n = 30 monomer units was targeted, and the reaction temperature was varied to study its effect on the degree of branching. Once again, phase separation occurred when polymerising at 25 °C, suggesting that the polymer architecture also has an effect on the UCST behaviour of the polymer within the methanolic environment. Analysis by ^{1}H-NMR and triple detection GPC (DMF) revealed that higher conversions were achieved and higher M_w values (M_w = 89 800 g mol^{-1}) obtained when polymerising at 60 °C. Nanoprecipitations were performed using each of the branched materials to yield nanoparticles that, once deprotected, have the potential to actively target DC-SIGN and mannose receptors that abundantly present on latent cellular reservoirs of HIV. DLS analysis of the formed nanoparticles showed monomodal and symmetrical distributions with D_z values

ranging from 120-140 nm, very low PdI values (≤ 0.074) and negative zeta potentials (≥ -18.4 mV); the latter indicating the presence of charge stabilisation. Furthermore, SEM images confirmed the presence of spherical nanoparticles with sizes that correlate well with the DLS data. Unfortunately, deprotection of the mannose chain-end functionalities of the branched polymers were not attempted due to lack of time, but future attempts would involve similar deprotection strategies to that described in Chapter 4, employed to remove isopropylidene protecting groups present on the galactose functionalities; this would involve treating the protected G0-Mann-*p*(*n*BuMA$_{30}$-*co*-EGDMA$_{0.8}$) branched copolymers with *para*-toluene sulfonic acid monohydrate within a protic solvent.

Attempts were made to synthesise generation 2 (G2) dendritic initiators that involved protection and selective deprotection strategies, followed by an esterification with acryloyl chloride to introduce an activated acrylate functionality at the anomeric centre of the saccharide. The Mann-(OAc)$_4$-acrylate [15] obtained was then used in the attempted aza-Michael-type addition with APAP [8] within the protic solvent IPA; unfortunately, however, the reaction proved unsuccessful. ^{1}H-NMR and ^{13}C-NMR analysis strongly suggested that a series of side-reactions had taken place that initially involved a transesterification between the Mann-(OAc)$_4$-acrylate [15] and the IPA solvent, yielding an isopropyl-acrylate compound, which then reacted with APAP [8] *via* aza-Michael-type addition. Such reactions were not observed when reacting the galactose equivalent with APAP [8], described in Chapter 4, suggesting that the position of the activated acrylate functionality on the ring structure of the saccharide is critical to the success of the reaction. Therefore, a solution to this problem may involve alternative protection/deprotection strategies to enable the acrylate functionality to be introduced to a different position of the saccharide ring structure.

5.8. References

1 Y. Mehellou and E. De Clercq, *J. Med. Chem.*, 2010, **53**, 521–538.

2 M. Danial and H.-A. Klok, *Macromol. Biosci.*, 2015, **15**, 9–35.

3 P. D. Kwong, R. Wyatt, J. Robinson, R. W. Sweet, J. Sodroski and W. A. Hendrickson, *Nature*, 1998, **393**, 648–659.

4 T. Dragic, *J. Gen. Virol.*, 2001, **82**, 1807–1814.

5 D. M. Eckert and P. S. Kim, *Annu. Rev. Biochem.*, 2001, **70**, 777–810.

6 B. G. Turner and M. F. Summers, *J. Mol. Biol.*, 1999, **285**, 1–32.

7 AIDSinfo, *https//aidsinfo.nih.gov/education-materials/fact-sheets/21/58/fda-approved-hiv- Med.*, Accessed November 2015.

8 T. Igarashi, C. R. Brown, Y. Endo, A. Buckler-White, R. Plishka, N. Bischofberger, V. Hirsch and M. a Martin, *Proc. Natl. Acad. Sci. U. S. A.*, 2001, **98**, 658–663.

9 J. Embretson, M. Zupancic, J. L. Ribas, A. Burke, P. Racz, K. Tenner-Racz and A. T. Haase, *Nature*, 1993, **362**, 359–362.

10 E. Eisele and R. F. Siliciano, *Immunity*, 2012, **37**, 377–388.

11 S. Aquaro, R. Caliò, J. Balzarini, M. C. Bellocchi, E. Garaci and C. F. Perno, *Antiviral Res.*, 2002, **55**, 209–225.

12 J. Zhang and A. S. Perelson, *J. Virol.*, 2013, **87**, 7893–7901.

13 T. W. Chun and a S. Fauci, *Proc. Natl. Acad. Sci. U. S. A.*, 1999, **96**, 10958–10961.

14 J. N. Blankson, D. Persaud, R. F. Siliciano, P. R. In and P. A. R. Ecycling, *Annu. Rev. Med.*, 2002, **53**, 557–593.

15 T. J. Cory, T. W. Schacker, M. Stevenson and C. V Fletcher, *Curr Opin HIV AIDS*, 2013, **8**, 190–195.

16 S. Gunaseelan, K. Gunaseelan, M. Deshmukh, X. Zhang and P. J. Sinko, *Adv. Drug Deliv. Rev.*, 2010, **62**, 518–531.

17 H. Feinberg, D. a Mitchell, K. Drickamer and W. I. Weis, *Science*, 2001, **294**, 2163–2166.

18 M. E. Taylor, K. Bezouska and K. Drickamer, *J. Biol. Chem.*, 1992, **267**, 1719–1726.

19 X. Ji, H. Gewurz and G. T. Spear, *Mol. Immunol.*, 2005, **42**, 145–152.

20 J. J. Reina and J. Rojo, *Brazilian J. Pharm. Sci.*, 2013, **49**, 109–124.

21 D. G. Nguyen and J. E. K. Hildreth, *Eur. J. Immunol.*, 2003, **33**, 483–493.

22 C. R. Becer, M. I. Gibson, J. Geng, R. Ilyas, R. Wallis, D. a Mitchell and D. M. Haddleton, *J. Am. Chem. Soc.*, 2010, **132**, 15130–15132.

23 Q. Zhang, J. Collins, A. Anastasaki, R. Wallis, D. a. Mitchell, C. R. Becer and D. M. Haddleton, *Angew. Chemie - Int. Ed.*, 2013, **52**, 4435–4439.

24 T. Dutta and N. K. Jain, *Biochim. Biophys. Acta*, 2007, **1770**, 681–686.

25 K. P. R. Kartha and R. A. Field, *Tetrahedron*, 1997, **53**, 11753–11766.

26 J. Boutet, T. H. Kim, C. Guerreiro and L. A. Mulard, *Tetrahedron Lett.*, 2008, **49**, 5339–5342.

27 H. Y. Lee, J. T. Kwon, M. Koh, M. H. Cho and S. B. Park, *Bioorg. Med. Chem. Lett.*, 2007, **17**, 6335–6339.

28 M. van Scherpenzeel, R. J. B. H. N. van den Berg, W. E. Donker-Koopman, R. M. J. Liskamp, J. M. F. G. Aerts, H. S. Overkleeft and R. J. Pieters, *Bioorg. Med. Chem.*, 2010, **18**, 267–273.

29 S. Jana, S. P. Rannard and A. I. Cooper, *Chem. Commun.*, 2007, 2962–2964.

30 I. Bannister, N. C. Billingham, S. P. Armes, S. P. Rannard and P. Findlay, *Macromolecules*, 2006, **39**, 7483–7492.

Chapter 6

Conclusions and future work

6.1. Conclusions

The application of nanotechnology to medicine (an emerging field known as nanomedicine) has resulted in more than 40 nanoparticle based therapeutic products in routine clinical use, designed to address the issues of low efficacy and poor economic viability associated with some conventional medicinal treatments.[1] The majority of these products are used in anticancer therapy to transport and deliver hydrophobic, toxic anticancer drugs to solid tumours *via* the enhanced permeability and retention (EPR) effect.[2] However, one key issue remains; the PEG surface functionality required to utilise the EPR effect prevents cellular internalisation after accumulation within the tumour tissue.[3] Therefore, research is now heavily focused on the development of nanoparticle-based therapeutics that will promote entry of the drug-carriers into specific cells (a concept known as active targeting), which can be achieved by functionalising the surface of the nanomaterials with targeting ligands (e.g. carbohydrates, peptides, vitamins, proteins, antibodies, aptamers and oligonucleotides) that have a high affinity for specific cell-receptors.[4] Such research has shown that ligand density has a significant effect on the rate of cellular internalisation, with higher ligand densities generally resulting in greater cellular uptake;[5,6] in this respect, dendrimers are the ideal nanoparticle platform for active targeting in drug-delivery applications. However, the synthesis and purification procedures of dendrimers are often laborious and expensive, which consequently affects their commercial viability.

To address these issues, the synthesis of hyperbranched-polydendrons (*hyp*-polydendrons) has been developed - a new macromolecular architecture designed to combine aspects of reversible-deactivation radical polymerisation, branched vinyl polymerisation, and linear-dendritic hybrids, to yield high molecular weight macromolecules with ideally branched dendritic chain ends; they are essentially regarded as an attractive, versatile alternative to dendrimers, particularly for therapeutic applications in nanomedicine.[7–9] Currently, the reported synthesis of these materials has involved using dendritic ATRP initiators bearing surface functionalities that are not capable of actively targeting specific cellular receptors. Furthermore, reports of the chemistry of the branched polymer core are currently limited to *poly*(2-hydroxypropyl methacrylate) (*p*HPMA) - a hydrophobic polymer that has

demonstrated its ability to encapsulate hydrophobic molecules, such as Nile red and pyrene.

Therefore, the research described within this thesis has aimed to expand the chemistry of both the dendritic surface functionalities and the branched polymer core to yield amphiphilic materials that have the potential to encapsulate hydrophobic drugs and actively target specific cell receptors.

6.1.1. Chapter 2

Chapter 2 demonstrated the synthesis of well-defined hydrophobic *p*(*n*BuMA) homopolymers in anhydrous MeOH - an anti-solvent for the polymer, often used in purification procedures for precipitation purposes.

The polymerisation of *n*BuMA was initially performed at 60 °C by Cu-catalysed ATRP using bpy as the complexing ligand and ethyl 2-bromoisobutyrate as the initiator, with each polymerisation proceeding homogeneously to high conversion, yielding polymers with narrow molecular weight distributions ($Đ$ as low as 1.02); these results were highly surprising, as the observed dispersity values were comparable to those typically associated with living ionic polymerisations. It was assumed that the high reaction temperature was critical to its success, but cloud point studies revealed a significant co-solvency effect from the unreacted monomer which helps retain the polymer in solution as the reaction progresses. This enabled the successful methanolic polymerisation of *n*BuMA at 25 °C, achieving high conversions and yielding low dispersity polymers, with the lower reaction temperature also improving the M_n control compared to the polymerisations at 60 °C. However, the ligand selection for the catalytic complex did prove critical to the reaction, with a change from bpy to PMDETA and Me_6TREN having a dramatic effect on the control of the polymerisation.

Comparative polymerisations by RAFT at 60 °C were also successful, yielding low dispersity polymers that were analogous to those obtained by ATRP but, more importantly, achieving high conversions in much shorter reaction times; this proved that successful polymerisation was not limited to RDRP techniques based on the reversible capping of an active radical species, but could be expanded to include techniques based on a degenerative chain transfer mechanism.

Furthermore, the monomer chemistry utilised within the methanolic polymerisation was extended to include the hydrophobic monomers MMA and *t*BuMA, with the polymerisations of both proceeding homogeneously; however, in the latter case, much broader dispersities were observed and the polymerisation rate was significantly lower when compared to the *n*BuMA polymerisations.

It was hypothesised that the methanolic polymerisations were initiated within a good solvent environment enhanced by the unreacted monomer, which progressively changed to a poor solvent environment as the monomer was depleted. Therefore, as the monomer was consumed, the polymer chains were likely to adopt densely coiled structures. However, the fact that the polymers remain solvated after full consumption of the monomer means that the polymer-MeOH interactions were sufficient enough to prevent the polymer-polymer interactions inducing aggregation and subsequent precipitation.

It is believed that this method of synthesising such well-defined hydrophobic *p*(*n*BuMA) and *p*(MMA) homopolymers may prove valuable to the development of amphiphilic polymeric nanoparticles capable of the encapsulation of hydrophobic drug molecules.

6.1.2. Chapter 3

Chapter 3 demonstrated the synthesis of linear amphiphilic copolymers by the methanolic Cu-catalysed ATRP of *n*BuMA using monofunctional and bifunctional hydrophilic PEG$_x$-Br macro-initiators. Various degrees of polymerisation (DP$_n$ = 60, 80, 100 monomer units) were targeted, with each series performed at 60 °C yielding well-defined AB diblock ($Đ$ = 1.02-1.05) and ABA triblock ($Đ$ = 1.13-1.18) amphiphilic copolymers; the results highlight that the presence of the hydrophilic PEG block as the chain end functionality did not have an adverse effect on the control of the *n*BuMA polymerisation. However, the calculated M_n values were significantly greater than the theoretical values, indicating poor initiation efficiencies.

The synthesis of PEG$_x$-*b*-*p*(*n*BuMA) diblock copolymers were also achieved at a lower temperature of 25 °C, with GPC analysis indicating higher initiation efficiencies but showing broader molecular weight distributions ($Đ$ = 1.20-1.32) compared to those obtained at 60 °C.

Furthermore, the architecture of the amphiphilic copolymers was varied to give branched materials that were obtained by polymerisation following the Strathclyde approach using the PEG_{113}-Br macro-initiator. This involved the methanolic ATRP of *n*BuMA in the presence of the divinyl monomer EGDMA, whose statistical incorporation enabled the inter-chain branching of the primary polymer chains; a reaction temperature of 60 °C was selected due to the greater control that was demonstrated when polymerising at the elevated temperature during the AB diblock copolymer syntheses, but also to provide a greater entropic effect that was more likely to promote inter-chain – rather than intra-chain – branching. Triple detection GPC (DMF) analysis revealed high molecular weight materials with M_w values as high as 2.33×10^6 g mol^{-1}.

Nanoprecipitations of these branched copolymers yielded nanoparticles in aqueous media, sterically stabilised by the PEG surface functionalities; DLS analysis showed multimodal intensity weighted particle size distributions, however, the number weighted distributions showed monomodal traces with D_n = 17-27 nm.

Although encapsulation and pharmacological studies were not performed, it is thought that the synthesised amphiphilic branched copolymers bearing PEG surface functionalities are interesting materials with potential drug-delivery applications that have high relevance to nanomedicine with regards to passively targeting tumours; however, larger particle sizes are required to target tumours *via* the EPR effect, which could be achieved by simply increasing the *p*(*n*BuMA) block length that will consequently affect their aggregation within the aqueous media during nanoprecipitation.

Finally, the establishment of reaction conditions for the *n*BuMA polymerisation to form amphiphilic materials was a key tool that enabled the development of more complex branched structures, described in later chapters.

6.1.3. Chapter 4

Chapter 4 demonstrated the synthesis of G0, G1 and G2 dendritic ATRP initiators bearing protected galactose functionalities by aza-Michael-type additions and esterifications, with the synthesis of each beginning with the commercially available 1,2:3,4-Di-*O*-isopropylidene-α-D-galactopyranose (proGal-OH).

The dendritic initiators were utilised in the methanolic Cu-catalysed ATRP of *n*BuMA at 60 °C, targeting DP_n = 60, 80, 100 monomer units, with all polymerisations proceeding homogeneously to high conversion (≥ 98 %) to yield low dispersity polymers ($1.12 \leq Đ \leq 1.30$); although the observed dispersities were higher than those seen in Chapters 2 and 3, they are still highly indicative of a well-controlled polymerisation. ^{1}H-NMR analysis of the purified G2-proGal-*p*(*n*BuMA)$_{60}$ polymer showed resonances attributed to the protected galactose functionalities, thereby confirming that *retro*-Michael additions had not taken place during the polymerisation; however, the analysis did suggest that the MeOH solvent may have trans-esterified to the dendritic chain end functionality.

Despite the possibility of transesterification reactions having taken place, the same reaction conditions were utilised to synthesise *hyp*-glycopolydendrons using each of the dendritic initiators, targeting a DP_n = 30 *n*BuMA units; a low concentration of the divinyl branching monomer EGDMA was used to promote the statistical inter-chain branching of the primary polymer chains. Analysis by ^{1}H-NMR and triple-detection GPC (DMF) revealed that each of the branched polymerisations proceeded homogeneously to high conversion (99 %) to yield high molecular weight polymers with weight average molecular weight (M_w) values ranging from 102,650 g mol^{-1} to 159,450 g mol^{-1}.

Deprotection of the isopropylidene protecting groups from the dendritic chain end functionalities was very difficult to achieve, with many attempts following reported methods within the literature proving unsuccessful. However, successful deprotection was achieved using *para*-toluene sulfonic acid monohydrate (PTSA) in MeOH, utilising the co-solvency effect of the *n*BuMA monomer to solvate the branched polymers. ^{1}H-NMR analysis of the deprotected polymers showed the absence of resonances attributed to the protected galactose functionalities, but did not conclusively reveal resonances attributed to the deprotected galactose functionalities; the results of a proof-of-concept study involving the deprotection of the proGal-OH starting material indicated that these resonances are likely to reside beneath the large broad peak attributed to the CH_2 environment of the *p*(*n*BuMA) pendant groups. However, IR spectroscopy did reveal a small transmittance at 3,400 cm^{-1} attributed to the O-H stretch, indicating that deprotected galactose functionalities are present within

the polymer. Unfortunately, the ^{1}H-NMR analysis also revealed a significantly greater intensity for the unexpected peak at 3.65 ppm, which suggests a greater degree of transesterification reactions having occurred during the deprotection step, catalysed under the acidic reaction conditions.

Nanoprecipitations of both the protected and deprotected *hyp*-glycopolydendrons were performed to yield stable nanoparticles in aqueous media; DLS analysis and zeta potential measurements showed that nanoparticles with smaller hydrodynamic diameters and greater negative zeta potentials were obtained when nanoprecipitating the deprotected materials compared to their protected equivalents. These results strongly suggest that the deprotected galactose functionalities are present on the surface of the *hyp*-glycopolydendrons, providing charge stabilisation. It is important to note, however, that a significant amount of precipitate was observed for the deprotected G2 *hyp*-glycopolydendron, and the high attenuator and low derived count rate of the measurement suggested that the sample concentration was too low to provide a credible result. This is likely attributed to branched materials whose galactose functionalities have been displaced by the MeOH solvent during the deprotection step.

It is also worth noting that one of the key issues that prevent dendrimers gaining regulatory approval as drug-delivery vehicles is that the structural defects often introduced during the synthesis of high generation materials consequently cause batch-to-batch variability that have significant effects on the reproducibility of their pharmacological assessment. Therefore, despite the analysis suggesting that *hyp*-glycopolydendrons bearing deprotected galactose functionalities capable of targeting hepatic ASGPR receptors were successfully obtained, it is believed that the transesterification reactions during polymer synthesis and the deprotection step cannot guarantee reproducible results for numerous batches. For that reason, the deprotection strategy certainly requires further work; however, if the modified deprotection step still cannot guarantee batch-to-batch reproducibility, then an alternative synthesis of the galactosylated *hyp*-glycopolydendrons will be required.

6.1.4. Chapter 5

Chapter 5 demonstrated the successful synthesis of a G0 mannose functionalised ATRP initiator by a 3 step reaction procedure that involved protection of all hydroxyl groups, followed by the selective deprotection at the anomeric centre, and finally, a bromo-esterification reaction to introduce the tertiary bromide functionality that is required for the polymerisation.

Unfortunately, the synthesis of a G2 dendritic mannose-functionalised ATRP initiator using similar chemistry to that described in Chapter 4 was unsuccessful; ^{1}H-NMR and ^{13}C-NMR analysis strongly suggested that a series of side-reactions had taken place that initially involved a transesterification between the Mann-$(OAc)_4$-acrylate and the IPA solvent, yielding an isopropyl-acrylate compound that then reacted with the APAP AB_2 brancher *via* aza-Michael-type additions. This suggests that the position of functionalisation on the ring structure of the saccharide is critical to the successful synthesis of mannosylated dendritic compounds. Therefore, alternative protection and deprotection strategies may be required.

The methanolic Cu-catalysed ATRP of *n*BuMA was performed using the G0-Mann-Br initiator, using the same reaction conditions that have been utilised in previous chapters. Linear G0-Mann-*p*(*n*BuMA) polymers were synthesised at both 60 °C and 25 °C, targeting a DP_n = 60, 80, 100 monomer units, with all polymerisations achieving high conversions (≥ 91 %) to yield low dispersity polymers ($Đ \leq 1.08$); narrower molecular weight distributions and improved M_n targeting were observed when polymerising at the reduced temperature. However, phase separation did occur when polymerising at 25 °C, targeting a DP_n = 100 *n*BuMA units; this could either be due to contamination of the reaction solvent with H_2O, or the presence of the protected mannose chain-end functionalities having a significant effect on the UCST behaviour of the polymer within the methanolic environment.

Branched polymers were obtained by repeating the polymerisations in the presence of a low concentration of the divinyl branching monomer, EGDMA, with only the target DP_n changing to 30 monomer units; the reaction temperature was varied to study its effect on the degree of branching. Once again, phase separation occurred when polymerising at 25 °C, suggesting that the polymer architecture may also has an effect on the UCST behaviour of the polymer within the methanolic environment. Analysis

by ^{1}H-NMR and triple detection GPC (DMF) revealed that higher conversions were achieved and higher M_w values (M_w = 89 800 g mol^{-1}) obtained when polymerising at 60 °C.

Nanoprecipitations of each of the branched materials were performed to yield stable nanoparticles in aqueous media, where DLS analysis showed monomodal and symmetrical distributions with D_z values ranging from 120-140 nm, very low PDI values (≤ 0.074) and negative zeta potentials (≥ -18.4 mV). The large particle sizes show that the nanoparticles are formed *via* the proposed nucleation/growth mechanism that is associated with this technique, and the negative zeta potentials indicated the presence of charge stabilisation. Additionally, SEM images confirmed the presence of spherical nanoparticles with sizes that correlate well with the DLS data.

Unfortunately, deprotection of the mannose chain-end functionalities of the branched polymers were not attempted due to lack of time, but future attempts would involve reactions with PTSA; however, as described in Section 6.1.3, the deprotection strategy would require optimisation to avoid transesterification reactions with protic solvents.

Although mannosylated *hyp*-polydendrons were not obtained, it is believed that the mannose-functionalised branched polymers described within this chapter are still interesting materials that have the potential, once successfully deprotected, to actively target DC-SIGN and mannose receptors that are abundantly present on latent cellular reservoirs of HIV.

6.2. Future work

The results of Chapter 4 indicated that the polymerisations conducted at 60 °C resulted in - albeit on a small scale - transesterification reactions between the MeOH solvent and the dendritic chain end functionality. However, Chapter 5 demonstrated that by decreasing the temperature of the branched polymerisations to 25 °C resulted in phase separation at some point towards the latter stages of the reaction. Therefore, as part of future work, a study involving the methanolic Cu-catalysed ATRP of *n*BuMA would be performed at various reaction temperatures between the two temperatures demonstrated within this thesis (*i.e.* 30 - 55 °C) to attain optimal reaction conditions for the synthesis of *hyp*-glycopolydendrons that avoids both transesterification reactions and phase separation.

Another future study would involve increasing the hydrophobic *p*(*n*BuMA) block length of the branched copolymers by simply targeting greater DP_n values during polymer synthesis. This will consequently affect the aggregation of the branched copolymers within the aqueous media during nanoprecipitation, resulting in stable nanoparticles with greater hydrodynamic diameters than those seen within this thesis; this is particularly important for drug-delivery systems hoping to utilise the EPR effect to accumulate within solid tumours before actively targeting cancer cells.

It was concluded in Chapters 4 and 5 that if modified deprotection strategies could not provide batch-to-batch reproducibility regarding the formation and pharmacological assessment of amphiphilic nanoparticles capable of actively targeting various cellular receptors, then alternative synthesis may be required. An interesting approach would involve the synthesis of glycosylated dendritic initiators without utilising protection/deprotection strategies, which would enable the synthesis of *hyp*-glycopolydendrons that would no longer require deprotection, thereby preventing transesterification reactions and thus batch-to-batch variability. This could potentially be achieved by initially performing a Fischer glycosylation using hydrogen bromide (HBr), which would introduce an excellent bromide leaving group at the anomeric centre of reducing saccharides, thereby enabling nucleophilic substitution using amine/thiol functionalised nucleophiles (Scheme 6.1); the latter step could utilise either the APAP AB_2 branching unit used within this thesis, or alternatively, xanthate functional dendritic substrates, whose synthesis has already been developed within the Rannard research group.[10,11]

Furthermore, *in vitro* pharmacological studies would be performed to assess the viability of the PEGylated branched copolymers, galactosylated *hyp*-glycopolydendrons and mannosylated *hyp*-glycopolydendrons as drug-delivery vehicles. This would involve transwell plate assays using the Caco-2 cell line (human epithelial colorectal adenocarcinoma cells) to predict the permeability of the nanoparticles across the intestinal tract into systemic circulation, and cytotoxicity assays.

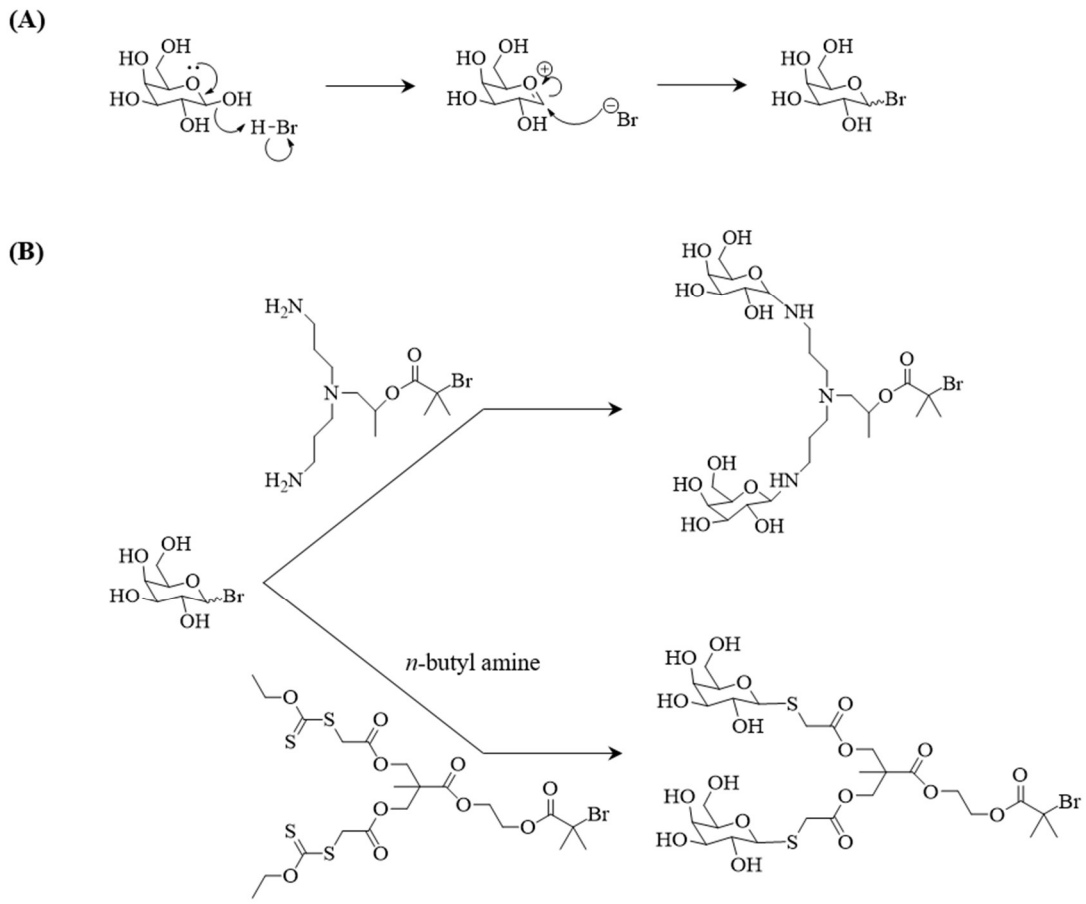

Scheme 6.1. Reaction scheme detailing the alternative synthesis of glycosylated dendritic ATRP initiators by: (A) introducing the bromide leaving group at the anomeric centre of the saccharide by a Fischer glycosylation, and (B) nucleophilic substitution at the anomeric centre using amine and thiol functionalised dendritic compounds.

Various reports within the literature have recently shown how nanoparticle shape can have a dramatic effect on the rate of cellular internalisation.[12–16] Furthermore, previous work has demonstrated the direct synthesis of polymer nanoparticles with targeted shapes without the need for functional groups that induce self-assembly.[17,18] Instead, well-defined "dumbbell" and "clover-leaf" shaped branched amphiphilic block copolymer nanoparticles were synthesised by introducing bifunctional and trifunctional initiators, respectively, into the initiating system of a branched ATRP reaction; these multifunctional initiators essentially generated tie-chains between branched polymer moieties to generate the targeted shape.

Preliminary studies regarding the synthesis of shaped *hyp*-glycopolydendrons have been conducted during this PhD, which involved the synthesis of G1 and G2 dendritic initiators bearing protected amines functionalities; these initiators were used in the

branched methanolic ATRP of HPMA at 40 °C, targeting a DP_n = 50 monomer units, in the presence of a bifunctional initiator; triple detection GPC (THF) analysis revealed yield high molecular weight polymers, with M_w values as high as 555,000 g mol^{-1}. Cleavage of the *t*BOC protecting groups under acidic conditions to liberate the amine surface functionality, followed by dialysis against H_2O, yielded dumbbell shaped nanoparticles in aqueous media, whose shape was confirmed by transmission electron microscopy (TEM) (Figure 6.1). Therefore, another interesting study would involve the synthesis of shaped *hyp*-glycopolydendrons *via* the methanolic ATRP of *n*BuMA, using mixed monofunctional dendritic glycosylated initiators and multifunctional initiators. The effect of their shape on the rate of cellular internalisation could be evaluated by *in vitro* pharmacological studies.

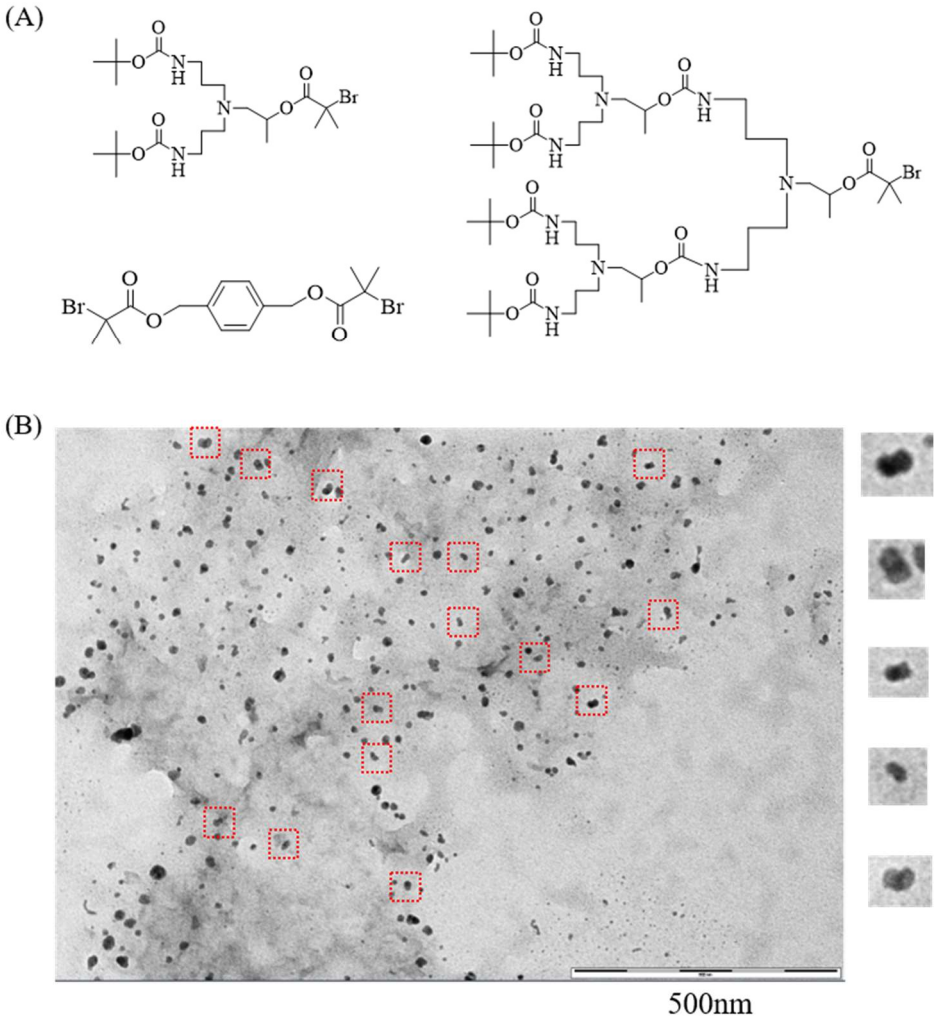

Figure 6.1. The synthesis of amine functionalised *hyp*-polydendrons with targeted dumbbell shape showing: (A) the monofunctional dendritic initiators and the bifunctional "tie-chain" initiator, and (B) a transmission electron microscopy (TEM) image of the shaped nanoparticles.

6.3. References

1 T. L. Doane and C. Burda, *Chem. Soc. Rev.*, 2012, **41**, 2885–2911.

2 H. Maeda, J. Wu, T. Sawa, Y. Matsumura and K. Hori, *J. Control. Release*, 2000, **65**, 271–284.

3 H. Hatakeyama, H. Akita and H. Harashima, *Biol. Pharm. Bull.*, 2013, **36**, 892–899.

4 F. Danhier, O. Feron and V. Préat, *J. Control. Release*, 2010, **148**, 135–146.

5 Z. Tang, D. Li, H. Sun, X. Guo, Y. Chen and S. Zhou, *Biomaterials*, 2014, **35**, 8015–8027.

6 J. Wang, S. Tian, R. a. Petros, M. E. Napier and J. M. Desimone, *J. Am. Chem. Soc.*, 2010, **132**, 11306–11313.

7 F. L. Hatton, P. Chambon, T. O. Mcdonald and S. P. Rannard, *Chem. Sci.*, 2014, **5**, 1844–1853.

8 F. L. Hatton, L. M. Tatham, L. R. Tidbury, P. Chambon, T. He, A. Owen and S. P. Rannard, *Chem. Sci.*, 2015, **6**, 326–334.

9 H. E. Rogers, P. Chambon, S. E. R. Auty, F. Y. Hern, A. Owen and S. P. Rannard, *Soft Matter*, 2015, **11**, 7005–7015.

10 S. E. R. Auty, O. Andrén, M. Malkoch and S. P. Rannard, *Chem. Commun.*, 2014, **50**, 6574.

11 S. E. R. Auty, O. C. J. Andrén, F. Y. Hern, M. Malkoch and S. P. Rannard, *Polym. Chem.*, 2014, **6**, 573–582.

12 P. Decuzzi, R. Pasqualini, W. Arap and M. Ferrari, *Pharm. Res.*, 2008, **26**, 235–243.

13 P. Decuzzi and M. Ferrari, *Biomaterials*, 2006, **27**, 5307–5314.

14 R. Vácha, F. J. Martinez-Veracoechea and D. Frenkel, *Nano Lett.*, 2011, **11**, 5391–5395.

15 J. a Champion and S. Mitragotri, *Proc. Natl. Acad. Sci. U. S. A.*, 2006, **103**, 4930–4934.

16 S. E. a Gratton, P. a Ropp, P. D. Pohlhaus, J. C. Luft, V. J. Madden, M. E. Napier and J. M. DeSimone, *Proc. Natl. Acad. Sci. U. S. A.*, 2008, **105**, 11613–11618.

17 T. He, D. J. Adams, M. F. Butler, T. Y. Chert, A. I. Cooper and S. P. Rannard, *Angew. Chemie - Int. Ed.*, 2007, **46**, 9243–9247.

18 T. He, D. J. Adams, M. F. Butler, A. I. Cooper and S. P. Rannard, *J. Am. Chem. Soc.*, 2009, **131**, 1495–1501.

Chapter 7

Experimental

7.1. Materials

Poly(ethylene glycol) methyl ether (average M_n 750, 2000, and 5000), *n*-Butyl methacrylate (BMA, 99%), toluene (anhydrous 99.8 %), methanol-d_4 (99.8 atom % D), N, N, N', N'', N'' pentamethyl diethylene triamine (PMDETA, 99%), triethylamine (99+%), α-bromoisobutyryl bromide (98 %), copper(I) chloride (Cu(I)Cl, 99%), $CDCl_3$ (99.8 atom % D), *para*-toluenesulfonic acid monohydrate (98.5%), methanol (MeOH, anhydrous 99.8%), ethylene diamine (99+), sodium thiosulfate (99%), iodine (99.8+%), 2,2'-bipyridine (bpy, 99%), *tert*-butanol (anhydrous), propylene oxide (99%), aluminium oxide (activated, neutral, Brockmann I), silica gel used for column chromatography, ethylene glycol dimethacrylate (EGDMA, 98 %), bis(3-aminopropyl)amine (BAPA, 98%), 1,2:3,4-Di-O-isopropylidene-α-D-galactopyranose (97%), methyl methacrylate (MMA, 99%), ethyl-α-bromoisobutyrate (EBiB, 98%), ethanolamine (99+%), *tert*-butyl methacrylate (*t*BMA, 98 %), DOWEX marathon ion-exchange resin (hydrogen form), 4,4'-azobis(4-cyanovaleric acid) (ACVA, 98 %) and 2-cyano-2-propyl benzodithioate (CPBD, 97 %) were purchased from Aldrich. 1,1'-Carbonyldi (1H-imidazole) (98%) was purchased from Apollo Scientific Ltd. Analytical TLC was performed on commercial Merck plates coated with silica gel. Tetrahydrofuran (THF, HPLC-grade), chloroform, dichloromethane, methanol (MeOH, analytical grade), diethyl ether, acetone (analytical grade), ethyl acetate, *n*-hexane, petroleum ether (analytical grade, bp 40-60 °C), propan-2-ol (IPA, HPLC grade) N,N-dimethylformamide (DMF, HPLC-grade) were purchased from Fisher. Poly(ethylene glycol) (average M_n 4000), acetic anhydride (99+%), 4-(dimethylamino)pyridine (DMAP, 99%), D-(+)-mannose (99%), sodium hydrogen carbonate (99%), acryloyl chloride (96%), Tris(2-dimethyl aminoethyl)amine (Me_6TREN, 99+%) was purchased from Alfa Aesar. All materials were used as received.

7.2. Characterisation

^{1}H nuclear magnetic resonance (NMR) spectra were recorded in $CDCl_3$ or MeOD using a Bruker Avance spectrometer operating at 400 MHz. ^{1}H-NMR were recorded at 400 MHz and ^{13}C-NMR were recorded at 100 MHz. Chemical shifts (δ) are reported in parts per million (ppm) and TMS was used as an internal standard for both ^{1}H and ^{13}C spectra.

Electrospray (ESI) mass spectrometry data were recorded in the Mass Spectrometry Laboratory at the University of Liverpool using a MicroMass LCT mass spectrometer using electron ionisation and direct infusion syringe pump sampling. All materials were diluted with methanol.

Dynamic light scattering (DLS) measurements were performed at 25 °C using a Malvern Zetasizer Nano ZS instrument (laser wavelength = 630 nm).

Scanning electron microscopy (SEM) images were obtained using a Hitachi S-4800 FE-SEM. Sample preparation involved dropping the aqueous samples on to silicon wafers mounted on an aluminium stub with a carbon tab. Samples were left to dry over several hours before being subjected to Au sputter at 20 mA for 2 mins prior to imaging.

Triple detection gel permeation chromatography (GPC) was performed using Malvern Viscotek instruments. One apparatus is equipped with a GPCmax VE2001 auto-sampler, two Viscotek D6000 columns (and a guard column) and a triple detector array TDA305 (refractive index, light scattering and viscometer) with a mobile phase of DMF containing 0.01 M lithium bromide at 60 °C and a flow-rate of 1 mL min^{-1}. The second instrument is equipped with a GPCmax VE2001 auto-sampler, two Viscotek T6000 columns (and a guard column), a refractive index (RI) detector VE3580 and a 270 Dual Detector (light scattering and viscometer) with a mobile phase of THF containing 2 v/v % of triethylamine and a flow-rate of 1 mL min^{-1}.

7.3. Methods

7.3.1. Chapter 2

All ATRP polymerisations were conducted at a constant ratio to initiator bromine atoms of [Br]:[Cu(I)Cl]:[Bpy] = 1:1:2.

7.3.1.1. Synthesis of *p*(*n*BuMA)$_x$ homopolymers in anhydrous MeOH

In a typical synthesis, targeting a DP_n = 60 monomer units, *p*(*n*BuMA)$_{60}$, *n*BuMA (0.85 g, 6 mmol) and bpy (31.2 mg, 0.2 mmol) were added to a 15 mL single-neck round bottom flask equipped with a magnetic stirrer bar. MeOH (1.07 mL; 50 wt%) (deoxygenated *via* N_2 purge prior to use) was added and the resulting solution was sparged with N_2 for 10 mins. Cu(I)Cl (9.9 mg, 0.1 mmol) was rapidly added to the

flask, instantly forming a brown coloured mixture and purged with N_2 for a further 5 mins. The flask was submerged into an oil bath pre- heated at 60 °C or 25 °C and ethyl α-bromoisobutyrate (14.7 mL, 0.1 mmol) was added under N_2 flow using a micro-syringe. The mixture was stirred at 60 °C for 24 hours before termination by dilution with MeOH until appearance of a blue/green colour. Upon cooling, the polymer precipitated and the supernatant containing the catalytic system was discarded. The polymer was dissolved in THF, passed through a neutral alumina column to remove residual catalyst and concentrated by rotary evaporation. The polymer was precipitated into cold MeOH to give a white solid.

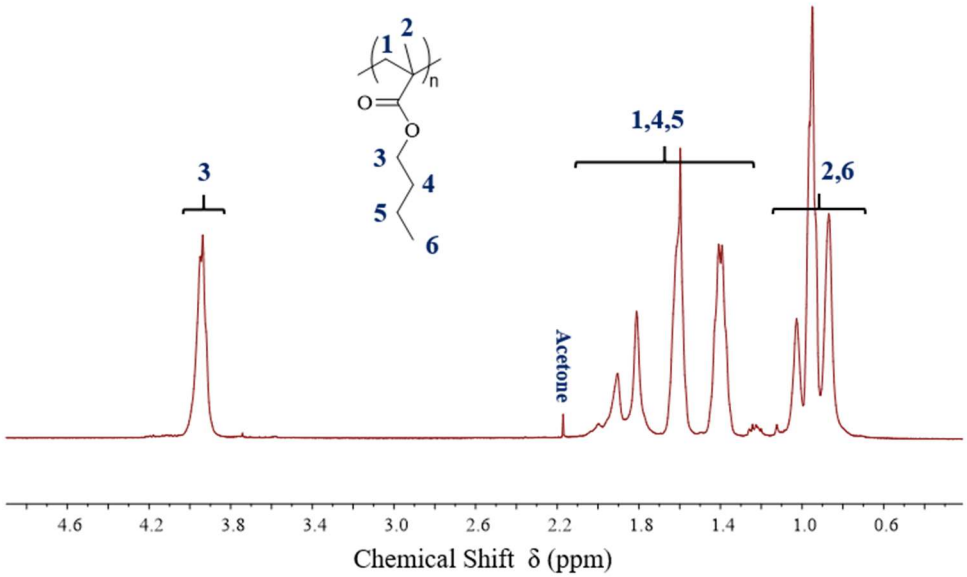

Figure 7.1. ^{1}H-NMR ($CDCl_3$) of $p(n\text{BuMA})_{100}$.

7.3.1.2. Determination of *p*(*n*BuMA) polymerisation kinetics

Kinetic studies were performed by taking samples from the reaction medium under positive N_2 pressure with subsequent analysis by ^{1}H NMR in $CDCl_3$ and triple detection GPC. Monomer conversion was determined by NMR spectroscopy using crude samples of the reaction medium. Integrals of the vinyl protons of the unreacted monomer (5.50 ppm and 6.05 ppm) were compared with integration of the CH_2 signal adjacent to the ester group of the both the polymer repeat units and the monomer (3.80 ppm and 4.30 ppm) to determine conversion. Catalyst was removed from the samples prior to GPC analysis by passing through a small alumina column.

7.3.1.3. Determination of *p*(*n*BuMA) UCST cloud point curves

Cloud points were determined by visual observation. Different *p*(*n*BuMA) weight fractions in anhydrous MeOH (MeOH–H_2O or MeOH–*n*BuMA mixtures) were dissolved in test tubes under stirring/heating and cooled at a rate of approximately 0.5 °C min^{-1}. Cloud points were determined as the first visual indication of turbidity and were performed in triplicate. Errors values were determined by considering the difference between the highest and lowest values obtained. Typically, $p(n\text{BuMA})_{60}$ (10 mg) and anhydrous MeOH (1.25 mL; 990 mg) was added to a test tube equipped with a magnetic flea and a rubber septum pierced with a long, small gauged, stainless steel needle. The tube was immersed in an oil bath fitted with a reference test tube containing pure MeOH and equipped with a thermocouple. The temperature was increased until total dissolution of the polymer followed by switching off of the heating element. For this example, three cloud points measurements were recorded (using the reference tube) at 52.8 °C, 52.9 °C and 52.9 °C.

7.3.1.4. Determination of *p*(*n*BuMA) UCST cloud point curves studying the monomer co-solvency effect

Cloud points were determined visually. *P*(*n*BuMA) was dissolved in anhydrous MeOH / *n*BuMA monomer mixtures within test tubes under stirring/heating, and cooled at a rate of approximately 0.5 °C min^{-1}. Cloud points were determined as the first visual indication of turbidity. The study began by adding $p(n\text{BuMA})_x$ (0.5 g) and anhydrous MeOH (0.63 mL; 0.5 g) to a test tube equipped with a magnetic flea and a rubber septum pierced with a long, small gauged, stainless steel needle. The tube was immersed in an oil bath fitted with a reference test tube containing pure MeOH and equipped with a thermocouple. The sample was heated, but it is important to note that dissolution within anhydrous MeOH could not be achieved in the absence of monomer. The *n*BuMA monomer was then added in increments of 10 μL and the polymer sample was heated; once total dissolution was achieved below the boiling point of MeOH, the heating element was switched off and the cloud point temperature was recorded. The same polymer sample was subjected to further heating/cooling cycles after each incremental 10 μL addition of *n*BuMA monomer and the cloud point temperatures were recorded at each point.

7.3.1.5. Synthesis of *p*(*n*BuMA)$_x$ homopolymers in IPA

In a typical synthesis, targeting a DP$_n$ = 60 monomer units, *p*(*n*BuMA)$_{60}$, *n*BuMA (0.85 g, 6 mmol) and bpy (31.2 mg, 0.2 mmol) were added to a 15 mL single-neck round bottom flask equipped with a magnetic stirrer bar. IPA (1.08 mL; 50 wt%) (deoxygenated *via* N_2 purge prior to use) was added and the resulting solution was sparged with N_2 for 10 mins. Cu(I)Cl (9.9 mg, 0.1 mmol) was rapidly added to the flask, instantly forming a brown coloured mixture and purged with N_2 for a further 5 mins. The flask was submerged into an oil bath pre-heated at 60 °C and ethyl α-bromoisobutyrate (14.7 μL, 0.1 mmol) was added under N_2 flow using a micro-syringe. The mixture was stirred at 60 °C for 24 hours before termination by dilution with THF until appearance of a blue/green colour. The solution was passed through a neutral alumina column to remove residual catalyst and concentrated by rotary evaporation. The polymer was precipitated into cold MeOH to give a white solid.

7.3.1.6. Synthesis of *p*(*n*BuMA)$_x$ homopolymers using PMDETA as catalyst ligand

In a typical synthesis, targeting a DP$_n$ = 60 monomer units, *p*(*n*BuMA)$_{60}$, *n*BuMA (1.7 g, 12 mmol) and PMDETA (41.6 μL, 0.2 mmol) were added to a 25 mL single-neck round bottom flask equipped with a magnetic stirrer bar. MeOH (2.15 mL; 50 wt%) (deoxygenated *via* N_2 purge prior to use) was added and the resulting solution was sparged with N_2 for 10 mins. Cu(I)Cl (19.8 mg, 0.2 mmol) was rapidly added to the flask, instantly forming a brown coloured mixture and purged with N_2 for a further 5 mins. The flask was submerged into an oil bath pre-heated at 60 °C and ethyl α-bromoisobutyrate (29.4 μL, 0.2 mmol) was added under N_2 flow using a micro-syringe. The mixture was stirred at 60 °C for 48 hours before termination by dilution with MeOH until appearance of a blue/green colour. Upon cooling, the polymer precipitated and the supernatant containing the catalytic system was discarded. The polymer was dissolved in THF, passed through a neutral alumina column to remove residual catalyst and concentrated by rotary evaporation. The polymer was precipitated into cold MeOH to give a white solid.

7.3.1.7. Synthesis of *p*(*n*BuMA)$_x$ homopolymers using Me$_6$TREN as catalyst ligand

In a typical synthesis, targeting a DP$_n$ = 60 monomer units, *p*(*n*BuMA)$_{60}$, *n*BuMA (1.7 g, 12 mmol) and Me$_6$TREN (53.5 µL, 0.2 mmol) were added to a 25 mL single-neck round bottom flask equipped with a magnetic stirrer bar. MeOH (2.15 mL; 50 wt%) (deoxygenated *via* N_2 purge prior to use) was added and the resulting solution was sparged with N_2 for 10 mins. Cu(I)Cl (19.8 mg, 0.2 mmol) was rapidly added to the flask, instantly forming a brown coloured mixture and purged with N_2 for a further 5 mins. The flask was submerged into an oil bath pre-heated at 60 °C and ethyl α-bromoisobutyrate (29.4 µL, 0.2 mmol) was added under N_2 flow using a micro-syringe. The mixture was stirred at 60 °C for 48 hours before termination by dilution with MeOH until appearance of a blue/green colour. Upon cooling, the polymer precipitated and the supernatant containing the catalytic system was discarded. The polymer was dissolved in THF, passed through a neutral alumina column to remove residual catalyst and concentrated by rotary evaporation. The polymer was precipitated into cold MeOH to give a white solid.

7.3.1.8. RAFT polymerisations

The DP$_n$ of homopolymers synthesised by RAFT were assessed by ^{1}H NMR spectroscopy in $CDCl_3$ of purified samples by comparison of the aromatic signal attributed to the CTA Z-group with clear resonances assigned to *n*BuMA monomer (e.g. -COO-C**H$_2$**-CH_2- 3.9 ppm and - C(C**H$_3$**)COO-$(CH_2)_3$-C**H$_3$** 0.5-1.25 ppm) and MMA residues (e.g. -C(CH_3)COO-C**H$_3$** 3.3- 3.8 ppm).

7.3.1.8.1. Synthesis of *p*(*n*BuMA)$_x$ homopolymers by methanolic RAFT at 60 ºC

In a typical synthesis, targeting a number average degree of polymerisation DP$_n$ = 60 monomer units, ACVA (17.2 mg, 0.06 mmol), CPBD (67.8 mg, 0.30 mmol) and *n*BuMA (2.55 g, 18.0 mmol) were added to a 25 mL single-neck round bottom flask equipped with a magnetic stirrer bar. Anhydrous MeOH (3.22 mL, 50 wt % wrt monomer, deoxygenated via N_2 purge) was added and the resulting solution was sparged with N_2 for 15 mins. The reaction flask was placed into a pre-heated oil-bath (60 ºC) and stirred for 24 hours after which the reaction medium was observed to be slightly turbid. The polymerisation was stopped by cooling the flask to room temperature causing the polymer to precipitate and sediment to the bottom of the flask.

The MeOH supernatant was decanted and the resultant polymer dissolved in THF. The solution was concentrated by rotary evaporation and precipitated into cold MeOH to give a pink solid.

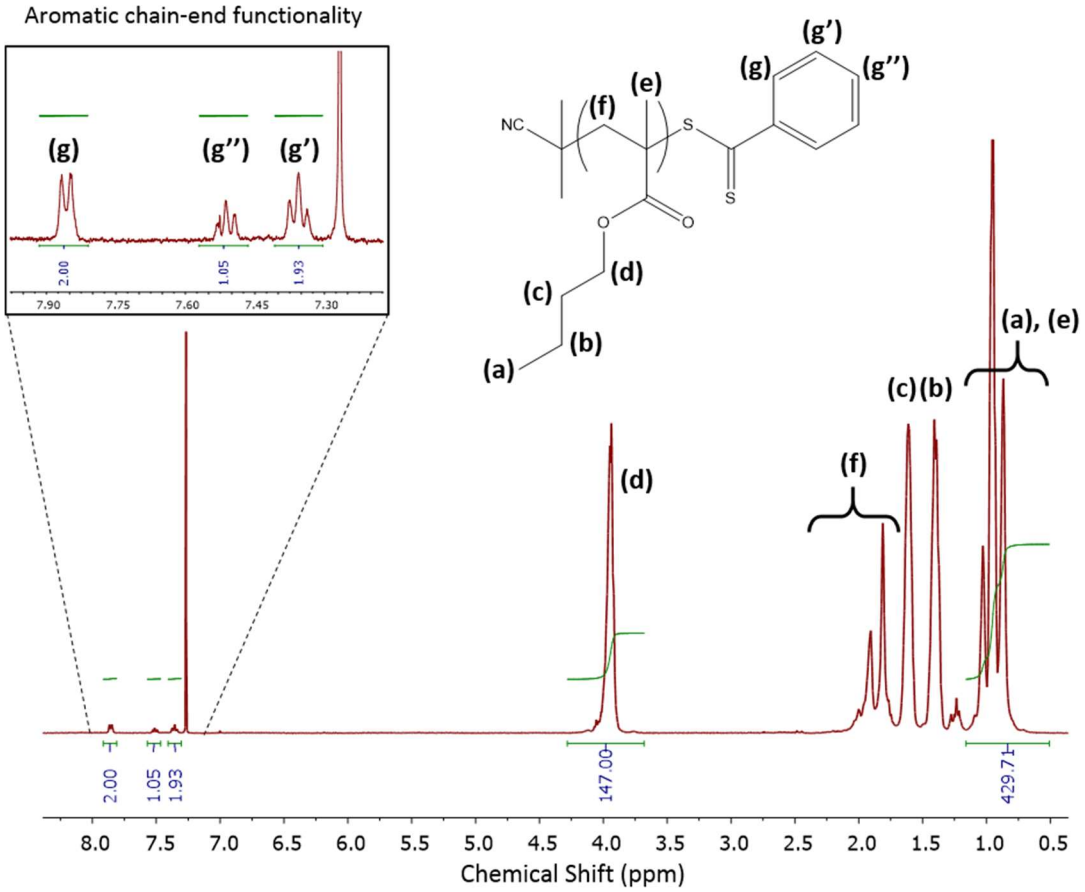

Figure 7.2: ^{1}H-NMR ($CDCl_3$) analysis of purified *p*(*n*BuMA)$_{60}$ obtained *via* RAFT to determine the DPn. Inset; magnification of the aromatic region of the spectrum showing resonances attributed to the CTA chain-end functionality.

7.3.1.8.2. Kinetic studies of the polymerisation of *n*BuMA using RAFT at 60 ºC

To avoid potential precipitation during sampling from a single reaction, multiple small reactions were initiated to model individual time points.

In a typical kinetic experiment, targeting DP_n = 100 monomer units, CPBD (98.40 mg, 0.422 mmol, 1 equivalent), ACVA (23.65 mg, 0.084 mmol, 0.2 equivalents) and *n*BuMA (6.00 g, 42.19 mmol, 100 equivalents) were placed in a single-neck round bottom flask fitted with a stirrer bar and a rubber septum. The reactor and its contents were degassed (N_2 sparge for 20 mins) after which anhydrous MeOH (7.58 mL,

50 wt %; degassed *via* N_2 sparge) was added to the round bottom flask under positive N_2 pressure. The reactor was flushed with argon for an additional 10 mins and the homogeneous reaction mixture transferred into several 1.5 mL vials fitted with stirrer bars under an argon blanket. The vials were sealed and placed in an oil bath at 60 ºC. The samples were removed successively over a period of 34 hours and analysed by ^{1}H NMR and triple detection GPC (THF). NB Kinetic experiments targeting a DP_n = 1000 monomer units utilised *n*BuMA (18.00 g) and the reaction was split across four 10 mL single-neck round bottom flasks fitted with stirrer bars and samples were removed over 50 hours.

7.3.1.8.3. Synthesis of poly(methyl methacrylate) *p*(MMA) homopolymers by methanolic RAFT at 60 °C

In a typical experiment, targeting a number average degree of polymerisation DP_n = 100 monomer units per chain, 31.13 mg of chain transfer agent CPBD (0.1406 mmol; 1 equivalent), 7.9 mg of ACVA (0.02812 mmol; 0.2 equivalents) and 1.4077 g of MMA (14.06 mmol; 100 equivalents) were placed in a single-neck round bottom flask fitted with a stirrer bar and a rubber septum. The reactor and its content were degassed by N_2 sparge for 15 mins, then 1.82 mL of anhydrous MeOH (50 wt %; thoroughly degassed via N_2 sparge prior to use) were added to the round bottom flask under positive pressure of N_2 using a syringe. The reaction mixture was flushed with N_2 for an additional 5 mins and the reactor was placed in an oil bath at 60 °C. After 27 hours, an aliquot of the crude material was taken for NMR analysis in order to assess the monomer conversion and the reactor was cooled down to room temperature resulting in the phase separation of polymer and MeOH. THF was added to the reaction mixture until obtaining a clear homogeneous solution and the material was purified by precipitation into MeOH (THF:MeOH = 1:10 v/v). The sample was collected by filtration and dried under vacuum at 40 °C overnight.

Monomer conversion was assessed using ^{1}H-NMR spectroscopy in $CDCl_3$ for the crude samples by comparing the integrated signals of the residual MMA at 5.5 ppm and 6 ppm with those due to the methacrylic backbone between 0.5 ppm and 2.5 ppm and/or - for comparison purposes - with the integrated signals from the pendant group (-O-C**H**$_3$, MMA + p(MMA)) between 3.5 ppm and 3.8 ppm.

^{1}H-NMR in $CDCl_3$ at 50 °C was also used to estimate the number average degree of polymerisation, DP_n, of the precipitated *p*(MMA) samples. Comparison of the integrated signals of the CTA chain-end "Z" group between 7.25 ppm and 7.9 ppm with those due to the methacrylic backbone between 0.5 ppm and 2.2 ppm and/or - for comparison purposes - with the integrated signals from the pendant group (-O- C**H**$_3$) between 3.3 ppm and 3.8 ppm allowed the assessment of the DP_n by NMR. Therefore, M_n NMR could be calculated using the following equation M_n NMR = (DP_n NMR * M_{MMA}) + M_{CTA} and making the assumption that all the polymer chains are initiated with the "R" group and terminated with the "Z" group of the CTA (which is evidently not the case due to the nature of the RAFT process but allowed a reasonable assessment of the molecular weight).

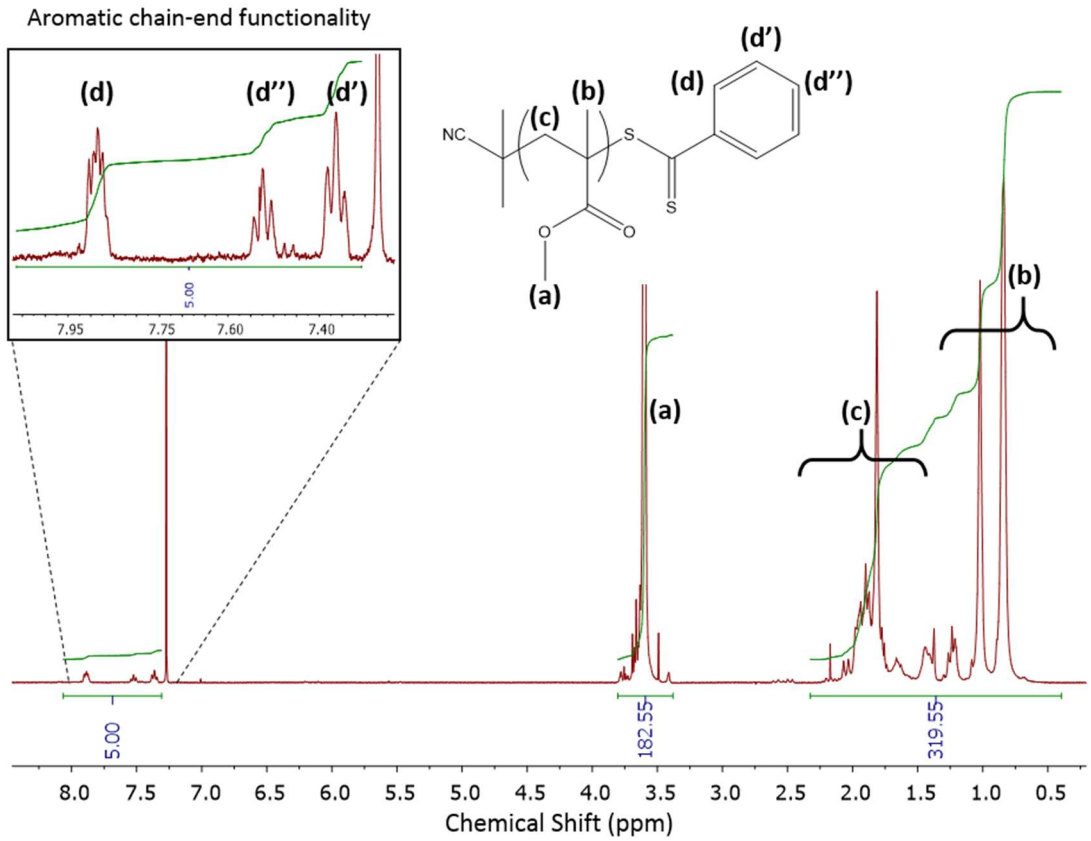

Figure 7.3; ^{1}H-NMR ($CDCl_3$) analysis of purified *p*(MMA)$_{60}$ obtained *via* RAFT to determine the DPn. Inset; magnification of the aromatic region of the spectrum showing resonances attributed to the CTA chain-end functionality.

7.3.1.9. Synthesis of *p*(MMA) homopolymers by methanolic ATRP

In a typical synthesis, targeting a number average degree of polymerisation DP_n = 60 monomer units and using ethyl-α-bromoisobutyrate (EBiB) as initiator, MMA (2.52g, 25.2 mmol) and bpy (130 mg, 0.8 mmol) were added to a 25 mL single-neck round bottom flask equipped with a magnetic stirrer bar. Anhydrous MeOH (3.16 mL, 50 wt % wrt. monomer) (deoxygenated *via* N_2 purge prior to use) was added and the resulting solution was sparged with N_2 for 15 mins. Cu(I)Cl (41.2 mg, 0.4 mmol) was rapidly added to the flask whilst maintaining a positive nitrogen flow, instantly forming a brown coloured mixture. EBiB (61.1 μL, 0.4 mmol) was added to the

reaction flask which was then submerged into an oil bath pre-heated at 60 °C and left to stir for 26 hours. The polymerisation was stopped by cooling the flask to room temperature, exposing its contents to air, and diluting the reaction medium with THF to poison the catalytic system. The polymer solution was then passed through a neutral alumina column to remove the catalytic system using THF as the mobile phase. The solution was concentrated by rotary evaporation and precipitated into cold MeOH to give a white solid. The sample was dried under vacuum at 40 °C and analysed by ^{1}H-NMR in $CDCl_3$ and triple-detection GPC with a mobile phase of THF.

7.3.1.10. Synthesis of poly(*tert*-butyl methacrylate) *p*(*t*BuMA) homopolymers by methanolic ATRP at 25 °C or 60 °C

In a typical synthesis, targeting a number average degree of polymerisation DP_n = 80 monomer units and using ethyl-α-bromoisobutyrate (EBiB) as initiator, *t*BuMA (1g, 7.03 mmol) and bpy (27.5 mg, 0.18 mmol) were added to a 25 mL single-neck round bottom flask equipped with a magnetic stirrer bar. Anhydrous MeOH (1.33 mL, 50 wt %) (deoxygenated *via* N_2 purge prior to use) was added and the resulting solution was sparged with N_2 for 15 mins. Cu(I)Cl (8.7 mg, 0.09 mmol) was rapidly added to the flask whilst maintaining a positive nitrogen flow, instantly forming a brown coloured mixture. EBiB (12.9 μL, 0.09 mmol) was added to the reaction flask which was then submerged into an oil bath pre-heated at 60 °C and left to stir for 25 hours. The polymerisation was stopped by cooling the flask to room temperature, exposing its contents to air, and diluting the reaction medium with THF to poison the catalytic system. The polymer solution was then passed through a neutral alumina

column to remove the catalytic system using THF as the mobile phase. The solution was concentrated by rotary evaporation, precipitated into cold MeOH/water (80/20), and washed with MeOH to give a white solid. The sample was dried under vacuum at 40 °C and analysed by ^{1}H-NMR in $CDCl_3$ and triple-detection GPC with a mobile phase of THF.

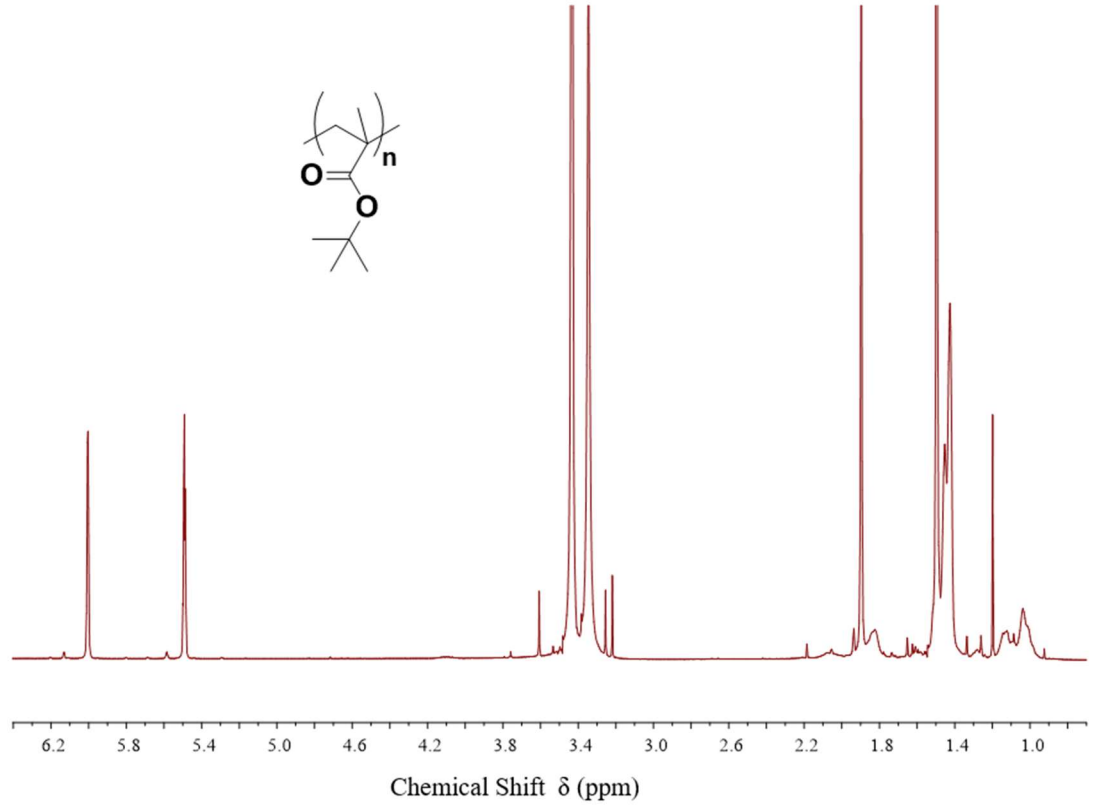

Figure 7.4. ^{1}H-NMR ($CDCl_3$) of the crude *p*(*t*BuMA)$_{60}$ sample before purification.

7.3.2. Chapter 3

7.3.2.1. Synthesis of poly(ethylene glycol) mono methyl ether-derived ATRP macro-initiators (PEG$_{17}$- Br, PEG$_{45}$-Br and PEG$_{113}$-Br)

In a typical synthesis, PEG$_{113}$-OH (30 g, 6 mmol) was dissolved in 100 mL of anhydrous toluene in the presence of triethylamine (0.91 g, 9 mmol) in a two-neck round bottom flask fitted with an addition funnel, a N_2 inlet/outlet and a stirrer bar. α-Bromoisobutytyl bromide (2.07 g, 9 mmol), diluted with 20 mL of anhydrous toluene, was placed in the addition funnel. Whilst stirring the contents of the flask, the α-bromoisobutyryl bromide solution was added slowly over a period of 20-30 min. After

the addition was completed, the reaction was left to stir for 24 hours at room temperature. The formation of a white precipitate (triethylammonium bromide salt) indicated the progress of the reaction. Once the reaction was complete, the reaction medium was warmed in a water bath at about 50 ºC, filtered and concentrated on the rotary evaporator. The resulting product was diluted in acetone and purified by precipitation in petroleum ether (40-60). The last step was repeated and the product was finally dried under vacuum at 40 ºC for 24 hours. The resulting macro-initiator was recovered with 70 % yield and its structure was confirmed by ^{1}H-NMR ($CDCl_3$) and triple detection GPC with a mobile phase of DMF.

7.3.2.2. Synthesis of poly(ethylene glycol) bi-functional ATRP macro-initiator (Br-PEG$_{91}$-Br)

PEG_{91}-diOH (20 g, 5 mmol) was dissolved in 100 mL of anhydrous toluene in the presence of triethylamine (1.52 g, 15 mmol) in a two-neck round bottom flask fitted with an addition funnel, a N_2 inlet/outlet and a stirrer bar. α-Bromoisobutytyl bromide (3.45 g, 15 mmol i.e. 1.5 eq. per hydroxyl group = 3 eq. per PEG chain) diluted with 20 mL of anhydrous toluene was placed in the addition funnel. Whilst stirring, the reactor was cooled to 0 °C in an ice bath and the α-bromoisobutyryl bromide solution was added slowly over a period of 20-30 min. After the addition was completed, the reactor was allowed to reach room temperature and left to stir for 24 hours. After purification by filtration and precipitation in petroleum ether (40-60), the structure of the resulting bi-functional macro-initiator was confirmed by ^{1}H-NMR in $CDCl_3$ and triple detection GPC with a mobile phase of DMF.

7.3.2.3. Synthesis of poly(ethylene glycol)-*b*-poly(*n*-butyl methacrylate) (*p*(PEG$_x$-*b*-*n*BuMA$_y$)) A-B block copolymers by methanolic ATRP

In a typical synthesis, targeting DP_n = 60 monomer units and using PEG_{113}–Br as the macro-initiator, PEG_{113}-Br (0.50 g, 0.1 mmol), *n*BuMA (0.85 g, 6 mmol) and bpy (31.20 mg, 0.2 mmol) were added to a 15 mL single-neck round bottom flask equipped with a magnetic stirrer bar. Anhydrous MeOH (1.07 mL, 50 wt % wrt. monomer; deoxygenated *via* N_2 purge) was added and the resulting solution was sparged with N_2 for 15 mins. Cu(I)Cl (9.90 mg, 0.1 mmol) was rapidly added to the flask whilst maintaining a positive N_2 flow, instantly forming a brown coloured mixture. The reactor was heated in an oil bath and left to stir. The polymerisation was stopped by

cooling the flask to room temperature, exposing its contents to air and diluting the reaction medium with THF. The polymer solution was passed through a neutral alumina column to remove the catalyst using THF as the mobile phase and the resulting solution was concentrated by rotary evaporation and precipitated into cold petroleum-ether (40-60) to give a white solid. The sample was dried under vacuum at 40 °C for 24 hours and analysed by ^{1}H-NMR in $CDCl_3$ (50 °C) and triple-detection GPC with a mobile phase of DMF.

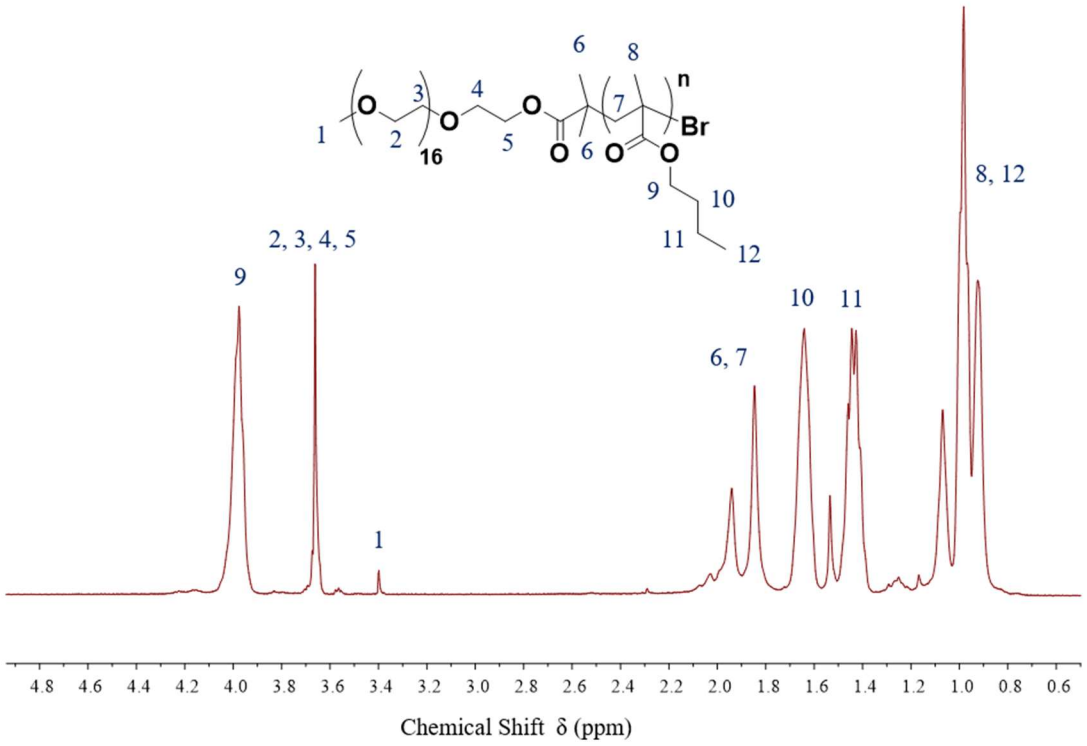

Figure 7.5. ^{1}H-NMR ($CDCl_3$) of PEG_{17}-*b*-*p*(*n*$BuMA_{60}$).

7.3.2.4. Synthesis of *p*(*n*BuMA)-PEG-*p*(*n*BuMA) A-B-A triblock copolymers

In a typical synthesis, targeting a number average degree of polymerisation DP_n = 80 monomer units on each side of the PEG bi-functional macro-initiator (in this specific case, DP_n total = 160 monomer units), Br-PEG_{91}-Br initiator (0.473 g, 0.11 mmol), *n*BuMA (2.5 g, 17.6 mmol), bpy (69 mg, 0.44 mmol) were placed into a 25 mL single-neck round bottom flask and deoxygenated *via* N_2 sparge for 10 mins under stirring. Anhydrous MeOH (3.75 mL, 50 wt %) (deoxygenated *via* N_2 purge prior to use) was added and the resulting solution was purged with N_2 for a further 5 mins. Finally, Cu(I)Cl (22 mg, 0.22 mmol) was added rapidly to the solution whilst maintaining a

positive N_2 flow and the reactor was placed in a preheated oil bath at 60 °C. After 27 hours, the reaction was stopped by exposure to air and addition of THF (approximately 10 mL) until appearance of a green colour which is evidence of the catalytic system being oxidised. The reaction medium was transferred into a larger container at room temperature, another addition of THF (approximately 50 mL) was performed and the catalytic system was removed by addition of ion-exchange resin beads followed by filtration. Finally, the resulting solution was concentrated on the rotary evaporator, diluted in THF and precipitated in cold petroleum ether (40-60). After collection, the sample was dried under vacuum at 40 °C for 24 hours and analysed by ^{1}H NMR in $CDCl_3$ and triple-detection GPC with a mobile phase of DMF.

For all the *p*(PEG-*block*-*n*BuMA) copolymers after purification, the DP_n of the *n*BuMA block could be assessed by ^{1}H-NMR spectroscopy in $CDCl_3$ at 50 °C. The proton signal due to the PEG block is apparent at 3.6 ppm. The intensity of this signal is proportional to the known DP_n of the PEG block. Comparison of this integrated signal with those due to the *p*(*n*BuMA) repeat units (e.g. -COO-C**H$_2$**- CH_2- at 3.9 ppm or -C(C**H$_3$**)COO-(CH2)3-C**H$_3$** between 0.5 ppm and 1.25 ppm) allowed the DP_n of the *p*(*n*BuMA) block to be calculated.

7.3.2.5. Kinetic studies of the polymerisation of *n*BuMA using the PEG macro-initiators

Kinetic studies (i.e. plots $\ln([M]_0/[M]) = f(t)$ and $M_n = f(\text{conversion})$) were performed by taking samples from the reaction medium under positive pressure of N_2 and analysing them by ^{1}H-NMR in $CDCl_3$ and triple detection GPC. The monomer conversion was determined by ^{1}H-NMR spectroscopy in $CDCl_3$ for crude samples of the reaction medium. The vinyl protons (C**H$_2$**=C(CH3)COO-*n*-Bu) due to the residual monomer can be seen at 5.5 ppm and 6.05 ppm. Comparison of these integrated signals with those due to the CH_2 next to the ester group for both the polymer repeat units and the monomer (between 3.8 ppm and 4.3 ppm) allowed the conversion to be estimated using the following equation: Conversion = [1 – (2*I6 / I4)] x 100, where I6 and I4 are respectively the integrals of the NMR signals at 5.5 ppm (or 6.05 ppm) and between 3.8 ppm and 4.3 ppm. Alternatively, it is also possible to calculate the conversion by comparing the signals due to the vinyl protons with those due to the 6 protons from the two methyl groups of the polymer repeat units (both backbone and

pendant group) between 0.5 ppm and 1.25 ppm. The catalytic system was removed from the kinetic samples prior to triple-detection GPC analysis by passing them through an alumina column.

7.3.2.6. Synthesis of branched poly(ethylene glycol)-*b*-poly(*n*-butyl methacrylate-*co*-ethylene glycol dimethacrylate) (*p*(PEG$_{113}$-*b*-(*n*BuMA-*co*-EGDMA)) copolymers by methanolic ATRP at 60 °C.

In a typical synthesis, targeting DP_n = 60 monomer units of *n*BuMA in the primary polymer chains, PEG$_{113}$-Br (0.50 g, 0.1 mmol), *n*BuMA (0.85 g, 6 mmol), EGDMA (16.80 mg, 0.085 mmol; 0.85 equiv. relative to initiator) and bpy (31.20 mg, 0.2 mmol) were added to a 15 mL single-neck round bottom flask equipped with a magnetic stirrer bar. Anhydrous MeOH (1.07 mL, 50 wt % wrt. monomer; deoxygenated *via* N_2 purge) was added and the resulting solution was sparged with N_2 for 15 mins. Cu(I)Cl (9.9 mg, 0.1 mmol) was rapidly added to the flask whilst maintaining a positive N_2 flow, instantly forming a brown coloured mixture. The reactor was submerged into an oil bath pre-heated at 60 °C, and left to stir. The polymerisation was stopped by cooling the flask to room temperature, exposing its contents to air, and diluting the reaction medium with THF. The polymer solution was passed through a neutral alumina column to remove the catalyst using THF as the mobile phase. The solution was concentrated by rotary evaporation and precipitated into cold petroleum-ether (40-60) to give a white solid. The sample was dried under vacuum at 40 °C for 24 hours and analysed by ^{1}H-NMR in $CDCl_3$ and triple-detection GPC with a mobile phase of DMF.

7.3.2.7. Nanoprecipitations of branched (*p*(PEG$_{113}$-*b*-(*n*BuMA-*co*-EGDMA)) copolymers

Nanoparticles were prepared following a rapid nanoprecipitation approach. The branched copolymers were dissolved in THF-H_2O (1/1) binary solution at a concentration of 5 mg mL^{-1}. Once fully dissolved, the polymer solution (1 mL, 5 mg mL^{-1}) was added rapidly to a vial of water (4.5 mL) stirring at ambient temperature. The solvent was allowed to evaporate overnight to give a final concentration of 1 mg mL^{-1} polymer in water.

7.3.3. Chapter 4

7.3.3.1. Synthesis of G0-proGal-Br [2]

In a typical synthesis, 1,2:3,4-Di-O-isopropylidene-α-D-galactopyranose (2g, 7.68 mmol) was dissolved in 20 mL of anhydrous dichloromethane in a two-neck round bottom flask fitted with an addition funnel, N_2 inlet/outlet and a stirrer bar. Triethylamine (1.61 mL, 11.5 mmol) was added to the reaction flask, followed by 4-dimethylamino)pyridine (94 mg, 0.768 mmol). The reaction flask was cooled in an ice-bath for approximately 10 min. α-Bromoisobutytyl bromide (1.42 mL, 11.5 mmol) was added to the addition funnel containing 10 mL of anhydrous dichloromethane, and the resulting solution was added dropwise over a period of 20 min to the reaction flask, instantly forming a precipitate upon addition. The reaction was left to stir overnight under an inert N_2 atmosphere at ambient temperature to form a brown coloured mixture. After reaction completion, the solvent was removed on the rotary evaporator to give a brown coloured oily residue. The crude product was extracted with diethyl ether (3 x 100 mL), with each extract filtered to remove the triethylammonium bromide ($Et_3N^+Br^-$) salt. The solvent was removed on the rotary evaporator, and the crude product was purified by normal phase flash chromatography using silica gel as the stationary phase and ethyl acetate/hexane (*gradient*: 10/90 to 20/80) as the mobile phase. The purified product was dried *in vacuo* to give G0-proGal-Br [2] as a white solid in 60 % yield. ^{1}H-NMR (400 MHz, $CDCl_3$): δ ppm = 1.34 (d, J = 4.5 Hz, 6H), 1.49 (d, J = 19.7 Hz, 6H), 1.95 (s, 6H), 4.06 (ddd, J = 7.7, 4.4, 1.8 Hz, 1H), 4.30 (m, 3H), 4.41 (dd, J = 11.5, 4.4 Hz, 1H), 4.63 (dd, J = 7.9, 2.5 Hz, 1H), 5.54 (d, J = 5.0 Hz, 1H). ^{13}C NMR (100 MHz, $CDCl_3$): δ ppm = 24.43, 24.99, 25.94, 26.02, 30.82, 55.68, 64.74, 65.92, 70.51, 70.72, 71.02, 96.27, 108.84, 109.72, 171.59. ESI-MS: $[M+Na]^+$ m/z = 433.1, required $[M]^+$ m/z = 408.08.

7.3.3.2. Synthesis of proGal-acrylate [3]

In a typical synthesis, 1,2:3,4-Di-O-isopropylidene-α-D-galactopyranose (12.78 g, 49.1 mmol) was dissolved in 80 mL of anhydrous dichloromethane in a two-neck round bottom flask fitted with an addition funnel, N_2 inlet/outlet and a stirrer bar. Triethylamine (17.1 mL, 123 mmol) was added to the reaction flask, followed by 4-(dimethylamino)pyridine (0.6 g, 4.91 mmol). The reaction flask was cooled in an ice-bath for approximately 10 min. Acryloyl chloride (7.98 mL, 98.2 mmol) was added to

the addition funnel containing 30 mL of anhydrous dichloromethane, and the resulting solution was added dropwise over a period of 20 min to the reaction flask, instantly forming a precipitate upon addition. The reaction was left to stir overnight under an inert N_2 atmosphere at ambient temperature to form an orange/brown coloured mixture. After reaction completion, the salt was filtered off and washed with cold dichloromethane, and the solvent was removed on the rotary evaporator (35 °C) to give a brown coloured oily residue. The crude product was extracted with diethyl ether (3 x 100 mL), with each extract filtered to remove residual triethylammonium chloride ($Et_3N^+Cl^-$) salt. The solvent was removed on the rotary evaporator (35 °C), and the crude product was purified by normal phase flash chromatography using silica gel as the stationary phase and ethyl acetate/hexane (*gradient*: 10/90 to 20/80) as the mobile phase, to give the proGal-acrylate [3] as a yellow coloured oil in 81 % yield. ^{1}H-NMR (400 MHz, $CDCl_3$): δ ppm = 1.34 (d, *J* = 5.4 Hz, 6H), 1.49 (d, *J* = 20.5 Hz, 6H), 4.08 (m, 1H), 4.32 (m, 4H), 4.63 (dd, *J* = 7.9, 2.5 Hz, 1H), 5.55 (d, *J* = 5.0 Hz, 1H), 5.84 (dd, *J* = 10.4, 1.4 Hz, 1H), 6.17 (dd, *J* = 17.3, 10.4 Hz, 1H), 6.43 (dd, *J* = 17.3, 1.4 Hz, 1H). ^{13}C NMR (100 MHz, $CDCl_3$): δ ppm = 24.47, 24.95, 25.94, 25.97, 63.50, 66.00, 70.46, 70.69, 71.07, 96.28, 108.77, 109.64, 128.19, 131.06, 166.03.

7.3.3.3. Synthesis of G1-proGal-OH [4]

In a typical synthesis, proGal-acrylate [3] (3 g, 9.54 mmol) was dissolved 15 mL of 2-propanol (IPA) in a single-neck round bottom flask equipped with a magnetic stirrer bar, to give a yellow coloured solution. Ethanolamine (0.144 mL, 2.39 mmol) was added to the reaction flask, and the solution was allowed to stir at ambient temperature for 4 days. After reaction completion, the solvent was removed on the rotary evaporator, and the crude product was purified by normal phase flash chromatography using silica gel as the stationary phase and ethyl acetate (100 %) as the mobile phase. The purified product was dried *in vacuo* to give G1-proGal-OH [4] as a yellow coloured viscous syrup in 74 % yield. ^{1}H-NMR (400 MHz, $CDCl_3$): δ ppm = 1.31 (d, *J* = 3.8 Hz, 12H), 1.48 (d, *J* = 27.6 Hz, 12H), 2.50 (t, *J* = 6.9 Hz, 4H), 2.58 (m, 2H), 2.82 (m, 4H), 2.91 (s, broad, 1H), 3.57 (m, 2H), 4.04 (m, 2H), 4.26 (m, 8H), 4.62 (dd, *J* = 7.9, 2.5 Hz, 2H), 5.53 (d, *J* = 5.0 Hz, 2H). ^{13}C NMR (100 MHz, $CDCl_3$): δ ppm = 24.42, 24.87, 25.84, 25.97, 48.96, 55.78, 59.07, 63.51, 65.82, 70.34, 70.62, 70.95, 96.21, 108.68, 109.57, 172.42. ESI-MS: $[M+H]^+$ m/z = 690.3, required $[M]^+$ m/z = 689.33.

7.3.3.4. Synthesis of G1-proGal-Br [5]

In a typical synthesis, G1-proGal-OH [4] (2.13 g, 3.09 mmol) was dissolved in 30 mL of anhydrous dichloromethane in a two-neck round bottom flask fitted with an addition funnel, N_2 inlet/outlet and a stirrer bar. Triethylamine (0.86 mL, 6.18 mmol) was added to the reaction flask, followed by 4-(dimethylamino)pyridine (37.8 mg, 3.09 mmol). The reaction flask was cooled in an ice-bath for approximately 10 min. α-Bromoisobutytyl bromide (0.57 mL, 4.63 mmol) was added to the addition funnel containing 10 mL of anhydrous dichloromethane, and the resulting solution was added dropwise over a period of 20 min to the reaction flask. The reaction was left to stir overnight under an inert N_2 atmosphere at ambient temperature to form a brown coloured mixture. After reaction completion, the solvent was removed on the rotary evaporator to give a brown coloured oily residue. The crude product was extracted with diethyl ether (3 x 100 mL), with each extract filtered to remove the triethylammonium bromide ($Et_3N^+Br^-$) salt. The solvent was removed on the rotary evaporator, and the crude product was purified by normal phase flash chromatography using silica gel as the stationary phase and ethyl acetate/hexane (40/60) as the mobile phase. The purified product was dried *in vacuo* to give G1-proGal-Br [5] as a yellow coloured viscous syrup in 82 % yield. ^{1}H-NMR (400 MHz, $CDCl_3$): δ ppm = 1.34 (d, J = 4.3 Hz, 12H), 1.48 (d, J = 26.7 Hz, 12H), 1.92 (s, 6H), 2.51 (t, J = 7 Hz, 4H), 2.78 (t, J = 5.7 Hz, 2H), 2.86 (t, J = 7.0 Hz, 4H), 4.03 (m, 2H), 4.25 (m, 10H), 4.62 (dd, J = 7.9, 2.4 Hz, 2H), 5.53 (d, J = 5.0 Hz, 2H). ^{13}C NMR (100 MHz, $CDCl_3$): δ ppm = 24.48, 24.94, 25.95, 26.03, 30.75, 49.67, 51.66, 55.71, 63.42, 65.85, 70.40, 70.66, 70.99, 96.26, 108.71, 109.58, 171.53, 172.14. ESI-MS: $[M+H]^+$ m/z = 838.3, required $[M]^+$ m/z = 837.28.

7.3.3.5. Synthesis of APAP [8]

7.3.3.5.1. Step 1 – synthesis of intermediate [6]

CDI (39.14 g, 241 mmol) was added to a 500 mL 2-neck round bottom flask equipped with magnetic stirrer, reflux condenser, and dry N_2 inlet. The flask was purged with N_2 for approximately 15 mins, and anhydrous toluene (350 mL) was added. Whilst stirring at 60 ºC, tertiary butanol (46 mL, 483 mmol) was added to the flask *via* a warm syringe, and the mixture was then stirred at 60 ºC for 6 hours under a positive flow of N_2, forming a pale-yellow coloured solution. Afterwards, BAPA (17.15 mL,

121 mmol) was added to the flask drop-wise whilst maintaining the temperature at 60 ºC. The reaction was allowed to stir for a further 18 hours at 60 ºC under a positive flow of N_2. The remaining solution was filtered to remove any solid imidazole, and the solvent removed *in vacuo* to give a yellow coloured oil. This was then dissolved in DCM (250 mL) and washed with distilled water (3 x 250 mL), followed by a saturated brine solution (100 mL). The organic layer was collected, dried over anhydrous $MgSO_4$, filtered and concentrated *in vacuo* to give a white solid in 84 % yield. ^{1}H-NMR (400 MHz, $CDCl_3$): δ ppm = 5.19 (s, br, NH), 3.21 (m, 4H), 2.65 (t, *J* = 6.5 Hz, 4H), 1.65 (q, *J* = 6.4 Hz, 4H), 1.44 (s, 18H). ^{13}C NMR (100 MHz, $CDCl_3$): δ ppm = 156.48, 79.34, 47.77, 39.29, 30.11, 28.79. *m/z* (ES MS) 332.3 $[M+H]^+$.

7.3.3.5.2. Step 2 – synthesis of intermediate [7]

Intermediate [6] (20 g, 60 mmol) was weighed out into a 500 mL 2-neck round bottom flask equipped with a magnetic stirrer, reflux condenser and dry N_2 inlet. The flask was purged with N_2 for approximately 15 mins, anhydrous ethanol was then added to the flask, which was then heated to 30 ºC. Propylene oxide (11.2 mL, 181 mmol) was added to the flask drop-wise, and the reaction was then left stirring for 24 hours at 30 ºC, under a positive flow of N_2, yielding a pale-yellow coloured solution. After reaction completion, the solvent was removed on the rotary evaporator and the crude product was purified by normal phase flash chromatography using silica gel as the stationary phase and ethyl acetate/methanol (75/25) as the mobile phase. The purified product was dried *in vacuo* to give the intermediate [7] in 85 % yield. ^{1}H-NMR (400 MHz, $CDCl_3$): δ ppm = 4.94 (s, broad, NH), 3.79 (m, 1H), 3.17 (m, 4H), 2.62 (m, 2H), 2.41 (m, 2H), 2.32 (d, *J* = 6.1 Hz, 2H), 1.65 (m, 4H), 1.44 (s, 18H), 1.13 (d, *J* = 6.2 Hz, 3H). ^{13}C NMR (100 MHz, $CDCl_3$): δ ppm = 156.08, 79.18, 63.45, 62.55, 51.77, 38.75, 27.48, 20.14. *m/z* (ES MS) 390.3 $[M+H]^+$, required $[M]^+$ m/z = 389.29.

7.3.3.5.3. Step 3 – synthesis of APAP [8]

The intermediate [7] (33.7 g, 86.5 mmol) was weighed out into a 1 L single-neck round bottom flask, and dissolved in ethyl acetate (300 mL). Concentrated hydrochloric acid (30 mL) was added drop-wise, causing significant effervescence to occur. The solution was allowed to stir at ambient temperature for 4 hours and then at 50 °C for 3 hours, whilst keeping the reaction flask open. The solvent was then removed *in vacuo* to give a yellow coloured viscous oil. The oil was then dissolved in 4M NaOH

(300 mL) and then the solvent was reduced down to approximately 150 mL. This was then transferred to a 500 mL separating funnel, and washed with chloroform (2 x 250 mL). The organic layers were then combined, dried over anhydrous $MgSO_4$, filtered and concentrated *in vacuo* to give the desired compound APAP [8] as a yellow coloured viscous oil in 82 % yield. Final product stored under an inert N_2 atmosphere. ^{1}H-NMR (400 MHz, $CDCl_3$): δ ppm = 3.78 (m, 1H), 2.75 (m, 4H), 2.62 (m, 2H), 2.44 (m, 2H), 2.32 (m, 2H), 1.89 (s, broad, 5H), 1.62 (m, 4H), 1.12 (d, J = 6.2 Hz, 3H). ^{13}C NMR (100 MHz, $CDCl_3$): δ ppm = 63.95, 62.56, 52.10, 40.31, 30.80, 20.03. ESI-MS: $[M+H]^+$ m/z = 190.3, required $[M]^+$ m/z = 189.18.

7.3.3.6. Synthesis of G2-proGal-OH [9]

In a typical synthesis, proGal-acrylate [3] (6 g, 19.1 mmol) was dissolved in 25 mL of 2-propanol (IPA) in a 100 mL single-neck round bottom flask equipped with a magnetic stirrer bar, to give a yellow coloured solution. APAP [8] (0.452 g, 2.39 mmol) was added to the reaction flask, and the solution was allowed to stir at ambient temperature for 7 days. After reaction completion, the solvent was removed on the rotary evaporator, and the crude product was purified by normal phase flash chromatography using silica gel as the stationary phase and dichloromethane/methanol (*gradient elution*: 95/5 to 90/10) as the mobile phase. The purified product was dried *in vacuo* to give G2-proGal-OH [9] as a yellow coloured viscous syrup in 86 % yield. ^{1}H-NMR (400 MHz, $CDCl_3$): δ ppm = 1.36 (m, 55H), 2.39 (m, 18H), 2.77 (t, J = 7.1 Hz, 8H), 3.69 (m, 1H), 4.03 (m, 4H), 4.25 (m, 16H), 4.62 (d, J = 7.8 Hz, 4H), 5.53 (d, J = 4.9 Hz, 4H). ^{13}C NMR (100 MHz, $CDCl_3$): δ ppm = 19.96, 24.50, 24.97, 25.97, 26.07, 32.10, 48.91, 51.56, 52.11, 62.20, 63.38, 65.90, 70.45, 70.68, 71.02, 96.27, 108.74, 109.59, 172.42. ESI-MS: $[M+H]^+$ m/z = 1446.7, required $[M]^+$ m/z = 1445.73.

7.3.3.7. Synthesis of G2-proGal-Br [10]

In a typical synthesis, G2-proGal-OH [9] (11.02 g, 7.62 mmol) was dissolved in 60 mL of anhydrous dichloromethane in a two-neck round bottom flask fitted with an addition funnel, N_2 inlet/outlet and a stirrer bar. Triethylamine (3.19 mL, 22.9 mmol) was added to the reaction flask, followed by 4-(dimethylamino)pyridine (93.1 mg, 0.76 mmol). The reaction flask was cooled in an ice-bath for approximately 10 min. α-Bromoisobutytyl bromide (1.88 mL, 15.2 mmol) was added to the addition funnel

containing 20 mL of anhydrous dichloromethane, and the resulting solution was added dropwise over a period of 20 min to the reaction flask. The reaction was left to stir overnight under an inert N_2 atmosphere at ambient temperature to form a brown coloured mixture. After reaction completion, the solvent was removed on the rotary evaporator to give a brown coloured oily residue. The crude product was extracted with diethyl ether (3 x 150 mL), with each extract filtered to remove the triethylammonium bromide ($Et_3N^+Br^-$) salt. The solvent was removed on the rotary evaporator, and the crude product was purified by normal phase flash chromatography using silica gel as the stationary phase and dichloromethane/methanol (*gradient elution*: 95/5 to 90/10) as the mobile phase. Further purification involved dissolving the compound in 60 mL of THF, to which 2 mL of 4M $NaOH_{aq}$ was added; the solution was stirred for 30 min before removing the solvent on the rotary evaporator and repeating the purification by flash chromatography. The purified product was dried *in vacuo* to give G2-proGal-Br [10] as a yellow coloured viscous syrup in 68 % yield. ^{1}H NMR (400 MHz, $CDCl_3$): δ ppm = 1.10-1.70 (m, 55H), 1.91 (m, 6H), 2.20-3.00 (m, 26H), 4.02 (m, 4H), 4.25 (m, 16H), 4.62 (d, J = 7.8 Hz, 4H), 4.99 (s, broad, 1H), 5.52 (d, J = 4.9 Hz, 4H). ^{13}C NMR (100 MHz, $CDCl_3$): δ ppm = 17.94, 24.51, 24.97, 25.97, 26.07, 30.77, 32.25, 49.04, 51.75, 52.71, 56.28, 60.22, 63.35, 65.90, 67.94, 70.47, 70.70, 71.03, 96.28, 108.73, 109.58, 171.04, 172.42. ESI-MS: $[M+H]^+$ m/z = 1596.7, required $[M]^+$ m/z = 1593.68.

7.3.3.8. Methanolic ATRP of *n*BuMA using galactosylated dendritic initiators (G0-proGal-Br [2], G1-proGal-Br [5] and G2-proGal-Br [10])

All ATRP polymerisations were conducted at a constant ratio to initiator bromine atoms of [Br]:[Cu(I)Cl]:[Bpy] = 1:1:2.

In a typical synthesis, targeting a DP_n = 60 monomer units and using G2-proGal-Br [10] as initiator, G2-proGal-Br [10] (187 mg, 0.117 mmol), *n*BuMA (1 g, 7.03 mmol) and bpy (36.5 mg, 0.234 mmol) were added to a 15 mL single-neck round bottom flask equipped with a magnetic stirrer bar. MeOH (1.56 mL; 50 wt%) (deoxygenated *via* N_2 purge prior to use) was added and the resulting solution was sparged with N_2 for 20 mins. Cu(I)Cl (11.6 mg, 0.117 mmol) was rapidly added to the flask, instantly forming a brown coloured mixture and purged with N_2 for a further 5 mins. The flask was submerged into an oil bath pre-heated at 60 °C. The mixture was

stirred at 60 °C for 22 hours before termination by exposing the reaction flask to air and diluting with THF until appearance of a green colour. The polymer solution was passed through a neutral alumina column (using THF as eluent) to remove residual catalyst and concentrated by rotary evaporation. The polymer was precipitated into cold hexane within a dry-ice bath to give a white solid.

Monomer conversion was assessed using ^{1}H-NMR spectroscopy in $CDCl_3$ for the crude samples by comparing the integrated signals of the residual *n*BuMA at 5.5 ppm and 6 ppm with those at 0.5-1.15 ppm due to the C(C**H**$_3$)COO-$(CH_2)_3$-C**H**$_3$ of *p*(*n*BuMA) and C(CH_3)COO-$(CH_2)_3$-C**H**$_3$ of *n*BuMA monomer.

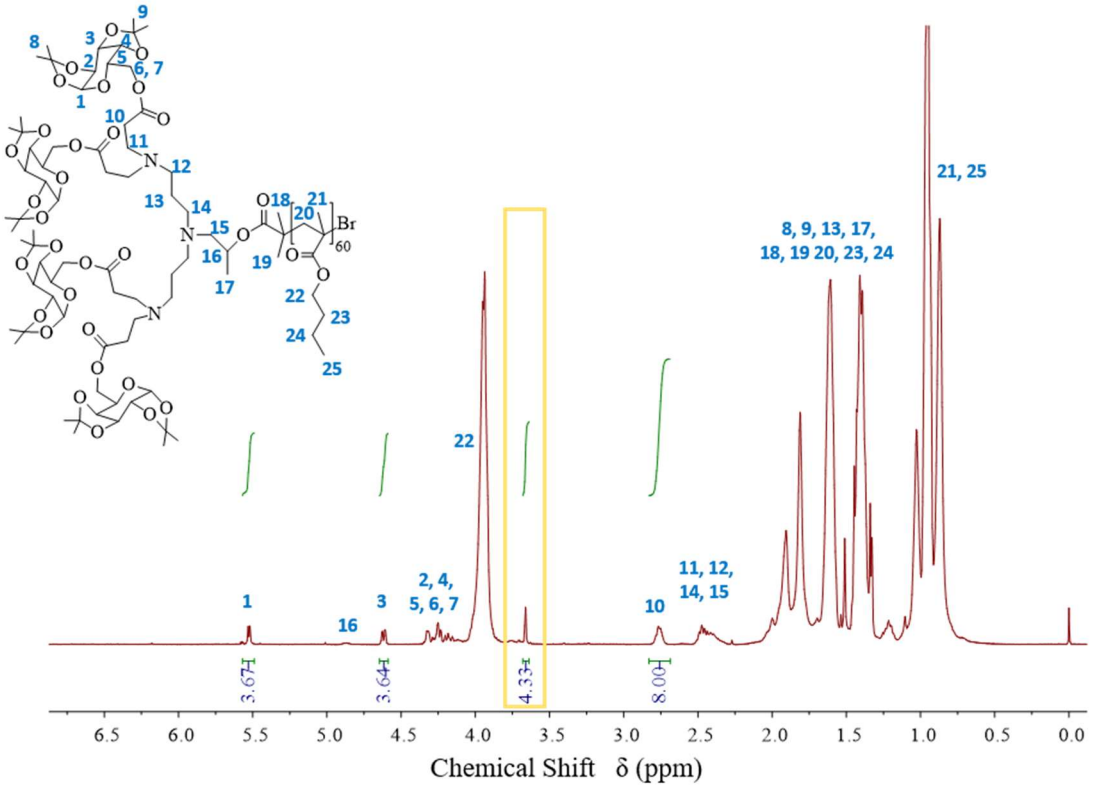

Figure 7.6. ^{1}H-NMR ($CDCl_3$) analysis of G2-proGal-*p*(*n*BuMA)$_{60}$ after purification; the resonance potentially due to transesterification reactions is highlighted by the yellow box.

7.3.3.9. Synthesis of *hyp*-glycopolydendrons by methanolic ATRP using galactosylated initiators (G0-proGal-Br [2], G1-proGal-Br [5] and G2-proGal-Br [10])

All ATRP polymerisations were conducted at a constant ratio to initiator bromine atoms of [Br]:[Cu(I)Cl]:[Bpy] = 1:1:2.

In a typical synthesis, targeting a DP_n = 30 monomer units and using G2-proGal-Br [10] as initiator, G2-proGal-Br [10] (493 mg, 0.309 mmol), EGDMA (49.0 mg, 0.247 mmol), *n*BuMA (1.32 g, 9.27 mmol) and bpy (96.5 mg, 0.618 mmol) were added to a 15 mL single-neck round bottom flask equipped with a magnetic stirrer bar. Anhydrous MeOH (2.52 mL; 50 wt%) (deoxygenated *via* N_2 purge prior to use) was added and the resulting solution was sparged with N_2 for 20 mins. Cu(I)Cl (30.6 mg, 0.309 mmol) was rapidly added to the flask, instantly forming a brown coloured mixture and purged with N_2 for a further 5 mins. The flask was submerged into an oil bath pre-heated at 60 °C. The mixture was stirred at 60 °C for 12 hours before termination by exposing the reaction flask to air and diluting with THF until appearance of a green colour. The polymer solution was passed through a neutral alumina column (using THF as eluent) to remove residual catalyst and concentrated by rotary evaporation. The polymer was precipitated into cold hexane within a dry-ice bath to give a white solid.

Monomer conversion was assessed using ^{1}H-NMR spectroscopy in $CDCl_3$ for the crude samples by comparing the integrated signals of the residual *n*BuMA at 5.5 ppm and 6 ppm with those at 0.5-1.15 ppm due to the C(C**H$_3$**)COO-$(CH_2)_3$-C**H$_3$** of *p*(*n*BuMA) and C(CH_3)COO-$(CH_2)_3$-C**H$_3$** of *n*BuMA monomer.

7.3.3.10. Deprotection of proGal-OH [1] using PTSA

In a typical synthesis, proGal-OH [1] (200 mg, 0.768 mmol) was dissolved in 2 mL of MeOH in a 10 mL single-neck round bottom flask, to which *para*-toluenesulfonic acid monohydrate (14.6 mg, 0.008 mmol) was then added. The reaction was stirred at 50 °C for 6 hours. The crude product was dried *in vacuo* and analysed by ^{1}H-NMR and infrared spectroscopy.

7.3.3.11. Deprotection of galactosylated *hyp*-glycopolydendrons

In a typical synthesis, G1-proGal-*p*(*n*$BuMA_{30}$-*co*-$EGDMA_{0.8}$) (100 mg) was dissolved in 1.5 mL of MeOH in a 10 mL single-neck round bottom flask. *Para*-toluenesulfonic acid monohydrate (15 mg) and *n*BuMA (0.3 mL) were added, and the reaction flask was submerged into a pre-heated oil bath at 50 °C. The reaction was stirred at 50 °C for 24 hours before cooling the reaction flask and removing the solvent on the rotary evaporator. The crude polymer was dissolved in 2 mL of THF, and 4M $NaOH_{aq}$ (20 μL) was added to neutralise the acid, forming a sodium *para*-toluenesulfonate

($PTSA^-Na^+$) salt that precipitated from solution. The salt was filtered off and washed with THF before dialysing the polymer-THF solution against THF for 48 hours using a regenerated cellulose dialysis tubing with a molecular weight cut-off of 2000 g mol^{-1}. The purified polymer was dried *in vacuo* and analysed by ^{1}H-NMR and infrared spectroscopy.

7.3.3.12. Nanoprecipitations of *hyp*-glycopolydendrons

Nanoparticles were prepared following a rapid nanoprecipitation approach. The *hyp*-glycopolydendrons were dissolved in THF at a concentration of 5 mg mL^{-1}. Once fully dissolved, the polymer solution (1 mL, 5 mg mL^{-1}) was added rapidly to a vial of water (5 mL) stirring at ambient temperature. The solvent was allowed to evaporate overnight to give a final concentration of 1 mg mL^{-1} polymer in water.

7.3.4. Chapter 5

7.3.4.1. Synthesis of Mann-$(OAc)_5$ [12]

In a typical synthesis, D-(+)-mannose (6g) and iodine (300 mg) were weighed out into a 100 mL single-neck round bottom flask equipped with a magnetic stirrer bar. The reaction flask was cooled in an ice-bath for 10 min before slowly adding acetic anhydride (40 mL). The reaction was stirred at ambient temperature for 30 min; initially, the reaction begun as a brown coloured mixture, but quickly formed a brown coloured solution as the acetylated mannose product formed. After reaction completion, a pressure-equalising dropping funnel was fitted to the reaction flask, to which 30 mL of water and crushed ice were added. The ice-water was added to the reaction flask drop-wise over 20 min to hydrolyse the remaining acetic anhydride, and the reaction media was stirred at ambient temperature for 2 hours. The contents of the flask were added to a 1 L separating funnel, diluted with 200 mL of chloroform and washed with 100 mL of 0.4M aqueous sodium thiosulfate solution to remove the iodine, where the organic phase changed colour from brown/purple to yellow. The organic phase was washed with (5 x 200 mL) saturated aqueous solution of sodium bicarbonate to remove the acetic acid by-product: it is important to note that the initial few washes produced a lot of CO_2 gas, and therefore extreme caution is required during this step. The organic phase was then washed with (2 x 100 mL) of water,

followed by 200 mL saturated brine solution. Finally the organic phase was dried over sodium sulfate, filtered and concentrated on the rotary evaporator to give the Mann-$(OAc)_5$ [12] as a pale yellow coloured syrup in 98 % yield. ^{1}H-NMR (400 MHz, $CDCl_3$): δ ppm = 1.96-2.20 (m, 15H), 4.00-4.40 (m, 3H), 5.00-5.50 (m, 3H), 5.80-6.30 (m, 1H). ^{13}C NMR (100 MHz, $CDCl_3$): δ ppm = 20.62, 20.64, 20.69, 20.75, 20.84, 62.06, 65.45, 68.24, 68.72, 70.61, 90.49, 168.04, 169.53, 169.74, 169.96, 170.61. ESI-MS: $[M+Na]^+$ m/z = 413.1, required $[M]^+$ m/z = 390.12.

7.3.4.2. Synthesis of Mann-$(OAc)_4$ [13]

In a typical synthesis, Mann-$(OAc)_5$ [12] (5.21 g, 13.3 mmol) was dissolved in 150 mL of THF in a 500 mL single-neck round bottom flask equipped with a magnetic stirrer. Acetic acid (1.23 mL, 21.4 mmol) and ethylene diamine (1.43 mL, 21.4 mmol) were added to the reaction flask, with the addition of the latter instantly forming a white coloured precipitate. The reaction mixture was allowed to stir overnight at ambient temperature. After reaction completion, the precipitate was filtered off and washed with THF before removing the solvent on the rotary evaporator to give a yellow coloured crude oil. The crude product was dissolved in 200 mL of chloroform, transferred to a 1L separating funnel and washed with: 120 mL 2M HCl_{aq}, 100 mL sat. $NaHCO_3$, 100 mL H_2O, and 100 mL sat. brine. The organic phase was dried over sodium sulfate, filtered and concentrated on the rotary evaporator. The crude product was purified further by normal phase flash chromatography using silica gel as the stationary phase and ethyl acetate/hexane (40/60) as the mobile phase. The purified product was dried *in vacuo* to give Mann-$(OAc)_4$ [13] as a yellow coloured oil in 56 % yield. ^{1}H-NMR (400 MHz, $CDCl_3$): δ ppm = 1.93 (s, 3H), 1.99 (s, 3H), 2.04 (s, 3H), 2.10 (s, 3H), 3.23 (d, J = 4.2 Hz, 1H), 4.13 (m, 3H), 5.24 (m, 4H). ^{13}C NMR (100 MHz, $CDCl_3$): δ ppm = 20.70, 20.73, 20.79, 20.92, 62.57, 66.16, 68.58, 68.71, 69.94, 92.24, 169.81, 170.02, 170.19, 170.82. ESI-MS: $[M+Na]^+$ m/z = 371.1, required $[M]^+$ m/z = 348.11.

7.3.4.3. Synthesis of G0-Mann-$(OAc)_4$-Br [14]

In a typical synthesis, Mann-$(OAc)_4$ [13] (7.1 g, 20.4 mmol) was dissolved in 100 mL of anhydrous dichloromethane in a two-neck round bottom flask fitted with an addition funnel, N_2 inlet/outlet and a stirrer bar. Triethylamine (5.69 mL, 40.8 mmol) was added to the reaction flask, followed by 4-(dimethylamino)pyridine (249 mg,

2.04 mmol). The reaction flask was cooled in an ice-bath for approximately 10 min. α-Bromoisobutytyl bromide (3.78 mL, 30.6 mmol) was added to the addition funnel containing 25 mL of anhydrous dichloromethane, and the resulting solution was added dropwise over a period of 20 min to the reaction flask. The reaction was left to stir overnight under an inert N_2 atmosphere at ambient temperature to form a brown coloured mixture. After reaction completion, the solvent was removed on the rotary evaporator to give a brown coloured oily residue. The crude product was extracted with diethyl ether (3 x 150 mL), with each extract filtered to remove the triethylammonium bromide ($Et_3N^+Br^-$) salt. The solvent was removed on the rotary evaporator, and the crude product was purified by normal phase flash chromatography using silica gel as the stationary phase and ethyl acetate/hexane (*gradient elution*: 30/70 to 40/60) as the mobile phase. The purified product was dried *in vacuo* to give G0-Mann-$(OAc)_4$-Br [14] as an orange coloured viscous syrup in 95 % yield. ^{1}H-NMR (400 MHz, $CDCl_3$): δ ppm = 1.80-2.30 (m), 3.87 (m), 3.95-4.70 (m), 4.90-5.60 (m), 5.70-6.30 (m). ESI-MS: $[M+Na]^+$ m/z = 519.0, required $[M]^+$ m/z = 496.06.

7.3.4.4. Synthesis of Mann-$(OAc)_4$-acrylate [15]

In a typical synthesis, Mann-$(OAc)_4$ [13] (6.67 g, 19.1 mmol) was dissolved in 50 mL of anhydrous dichloromethane in a two-neck round bottom flask fitted with an addition funnel, N_2 inlet/outlet and a stirrer bar. Triethylamine (6.68 mL, 47.9 mmol) was added to the reaction flask, followed by 4-(dimethylamino)pyridine (233 mg, 1.91 mmol). The reaction flask was cooled in an ice-bath for approximately 10 min. Acryloyl chloride (3.30 mL, 38.3 mmol) was added to the addition funnel containing 20 mL of anhydrous dichloromethane, and the resulting solution was added dropwise over a period of 20 min to the reaction flask, instantly forming a precipitate upon addition. The reaction was left to stir overnight under an inert N_2 atmosphere at ambient temperature to form an orange/brown coloured mixture. After reaction completion, the salt was filtered off and washed with cold dichloromethane, and the solvent was removed on the rotary evaporator (35 °C) to give a brown coloured oily residue. The crude product was extracted with diethyl ether (3 x 100 mL), with each extract filtered to remove residual triethylammonium chloride ($Et_3N^+Cl^-$) salt. The solvent was removed on the rotary evaporator (35 °C), and the crude product was purified by normal phase flash chromatography using silica gel as the stationary phase and ethyl acetate/hexane (40/60) as the mobile phase, to give the

Mann-$(OAc)_4$-acrylate [3] as a yellow coloured oil in 66 % yield. ^{1}H-NMR (400 MHz, $CDCl_3$): δ ppm = 2.02 (s, 3H), 2.05 (s, 3H), 2.09 (s, 3H), 2.19 (s, 3H), 3.90-4.40 (m, 3H), 5.10-5.60 (m, 3H), 5.98 (dd, *J* = 10.5, 1.1 Hz, 1H), 6.17 (m, 2H), 6.51 (dd, *J* = 17.3, 1.1 Hz, 1H). ^{13}C NMR (100 MHz, $CDCl_3$): δ ppm = 23.34, 23.37, 23.42, 23.49, 63.11, 64.76, 68.22, 71.08, 71.49, 93.54, 129.76, 136.20, 165.81, 172.25, 172.44, 172.69, 173.35. ESI-MS: $[M+Na]^+$ m/z = 425.1, required $[M]^+$ m/z = 402.12.

7.3.4.5. Methanolic ATRP of *n*BuMA using G0-Mann-$(OAc)_4$-Br [14]

All ATRP polymerisations were conducted at a constant ratio to initiator bromine atoms of [Br]:[Cu(I)Cl]:[Bpy] = 1:1:2.

In a typical synthesis, targeting a DP_n = 60 monomer units and using G0-Mann-$(OAc)_4$-Br [14] as initiator, G0-Mann-$(OAc)_4$-Br [14] (58.3 mg, 0.117 mmol), *n*BuMA (1 g, 7.03 mmol) and bpy (36.5 mg, 0.234 mmol) were added to a 15 mL single-neck round bottom flask equipped with a magnetic stirrer bar. MeOH (1.40 mL; 50 wt%) (deoxygenated *via* N_2 purge prior to use) was added and the resulting solution was sparged with N_2 for 20 mins. Cu(I)Cl (11.6 mg, 0.117 mmol) was rapidly added to the flask, instantly forming a brown coloured mixture and purged with N_2 for a further 5 mins. The flask was submerged into an oil bath pre-heated at 60 °C. The mixture was stirred at 60 °C for 24 hours before termination by exposing the reaction flask to air and diluting with THF until appearance of a green colour. The polymer solution was passed through a neutral alumina column (using THF as eluent) to remove residual catalyst and concentrated by rotary evaporation. The polymer was precipitated into cold hexane within a dry-ice bath to give a white solid.

Monomer conversion was assessed using ^{1}H-NMR spectroscopy in $CDCl_3$ for the crude samples by comparing the integrated signals of the residual *n*BuMA at 5.5 ppm and 6 ppm with those at 0.5-1.15 ppm due to the C(C**H**$_3$)COO-$(CH_2)_3$-C**H**$_3$ of *p*(*n*BuMA) and C(CH_3)COO-$(CH_2)_3$-C**H**$_3$ of *n*BuMA monomer.

7.3.4.6. Branched methanolic ATRP using G0-Mann-$(OAc)_4$-Br [14]

All ATRP polymerisations were conducted at a constant ratio to initiator bromine atoms of [Br]:[Cu(I)Cl]:[Bpy] = 1:1:2.

In a typical synthesis, targeting a DP_n = 30 monomer units and using G0-Mann-$(OAc)_4$-Br [14] as initiator, G0-Mann-$(OAc)_4$-Br [14] (233 mg,

0.469 mmol), EGDMA (74.3 mg, 0.375 mmol), *n*BuMA (2 g, 14.1 mmol) and bpy (146.5 mg, 0.938 mmol) were added to a 15 mL single-neck round bottom flask equipped with a magnetic stirrer bar. Anhydrous MeOH (3.16 mL; 50 wt%) (deoxygenated *via* N_2 purge prior to use) was added and the resulting solution was sparged with N_2 for 20 mins. Cu(I)Cl (46.4 mg, 0.469 mmol) was rapidly added to the flask, instantly forming a brown coloured mixture and purged with N_2 for a further 5 mins. The flask was submerged into an oil bath pre-heated at 60 °C. The mixture was stirred at 60 °C for 21 hours before termination by exposing the reaction flask to air and diluting with THF until appearance of a green colour. The polymer solution was passed through a neutral alumina column (using THF as eluent) to remove residual catalyst and concentrated by rotary evaporation. The polymer was precipitated into cold hexane within a dry-ice bath to give a white solid.

Monomer conversion was assessed using ^{1}H-NMR spectroscopy in $CDCl_3$ for the crude samples by comparing the integrated signals of the residual *n*BuMA at 5.5 ppm and 6 ppm with those at 0.5-1.15 ppm due to the C(C**H$_3$**)COO-(CH$_2$)$_3$-C**H$_3$** of *p*(*n*BuMA) and C(CH$_3$)COO-(CH$_2$)$_3$-C**H$_3$** of *n*BuMA monomer.

7.3.4.7. Nanoprecipitations of G0-Mann-*p*(*n*BuMA$_{30}$-*co*-EGDMA$_{0.8}$)

Nanoparticles were prepared following a rapid nanoprecipitation approach. The branched copolymers were dissolved in THF at a concentration of 5 mg mL^{-1}. Once fully dissolved, the polymer solution (1 mL, 5 mg mL^{-1}) was added rapidly to a vial of water (5 mL) stirring at ambient temperature. The solvent was allowed to evaporate overnight to give a final concentration of 1 mg mL^{-1} polymer in water.

Appendix

Chapter 2

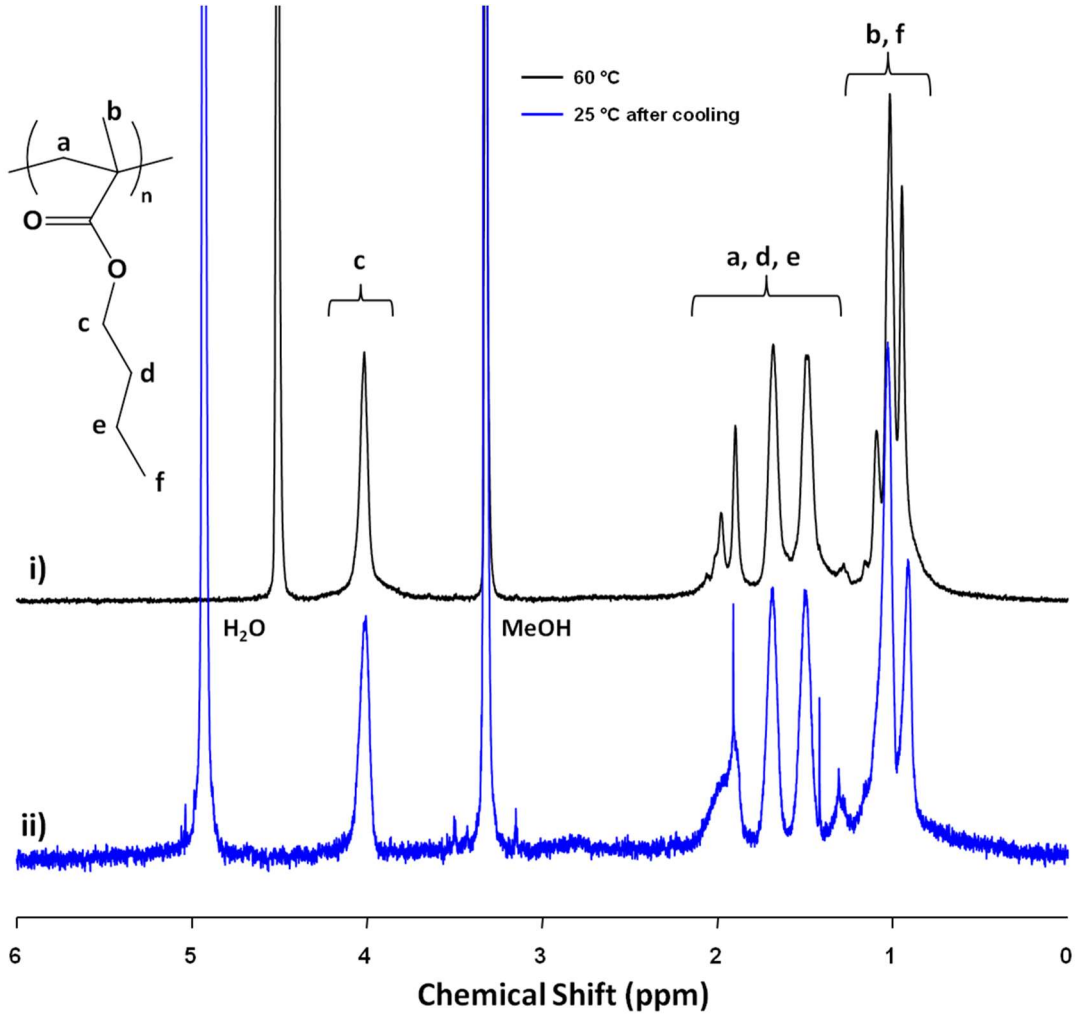

Figure A1: Studies of *p*(*n*BuMA) solubility in MeOH-d_4. ^{1}H NMR spectra of i) *p*(*n*BuMA) heated to 60 °C, ii) *p*(*n*BuMA) after heating and cooling to 25 °C. In ii) the intensity of the peaks owing to residual polymer in solution has been increased in order to compare the resolution to that in spectrum i).

Table A1: Cloud point temperatures for *p*(*n*BuMA) in MeOH with varying water content within the organic solvent. Measurements recorded in triplicate for each composition.

	Anhyd. MeOH			Analytical Grade MeOH			Anhyd. MeOH:H_20 (1wt %)		
	Cloud Point Temperature (°C)			Cloud Point Temperature (°C)			Cloud Point Temperature (°C)		
Composition (wt %)	**#1**	**#2**	**#3**	**#1**	**#2**	**#3**	**#1**	**#2**	**#3**
0.5	47.6	47.5	47.5	47.7	47.5	47.4	52.1	52.2	52.1
1	52.8	52.9	52.9	53.1	53.1	53.2	58.3	58.2	58.4
1.5	56.1	56.0	56.0	56.7	56.4	56.5	62.1	62.1	62.0
2	57.9	57.7	58.0	58.1	58.3	58.1	63.8	63.7	63.7
2.5	59.6	59.7	59.8	59.9	59.6	59.8	---	---	---
3	61.2	61.4	61.4	61.8	61.8	61.7	---	---	---
3.5	62.1	62.0	61.9	62.7	62.5	62.5	---	---	---
4	62.9	62.9	62.8	63.9	63.8	63.7	---	---	---
4.5	64.0	64.0	63.9	64.1	64.2	64.1	---	---	---
5	64.6	64.6	64.7	---	---	---	---	---	---

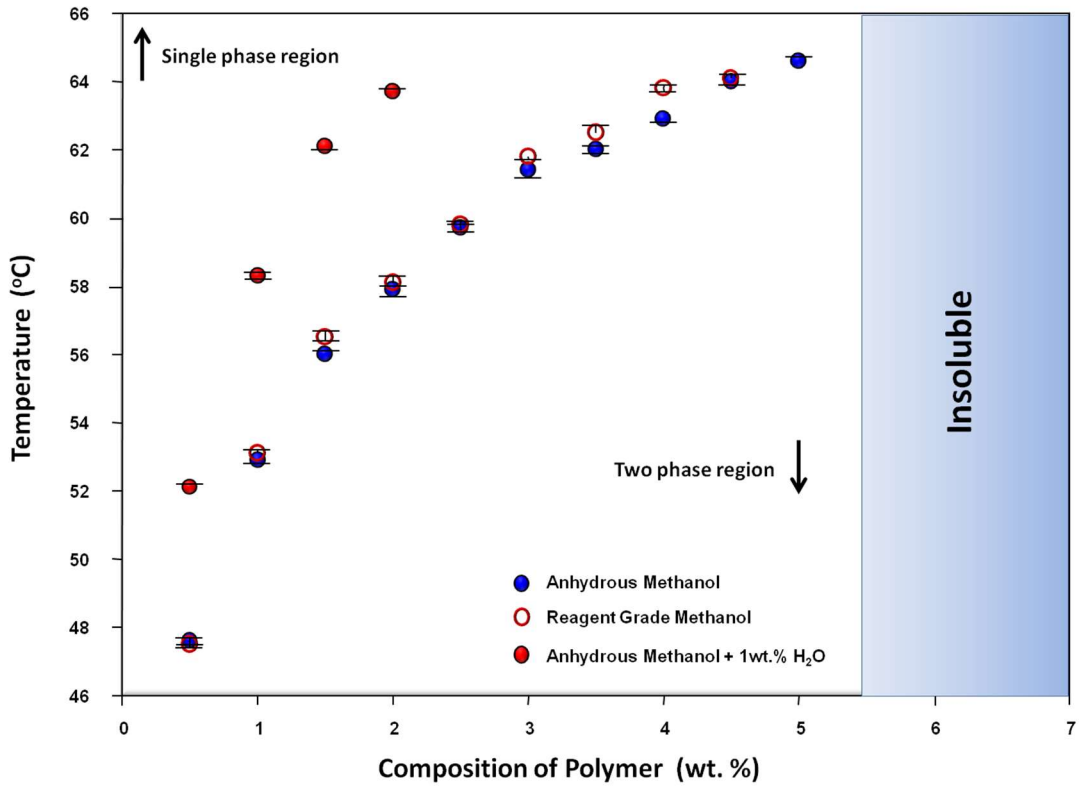

Figure A2: Cloud Point behaviour for *p*(*n*BuMA) in MeOH with varying water content within the organic solvent. The reagent grade methanol was reported by the supplier to contain < 0.05 % H_2O content. Asymmetric error bars shown.

Table A2: Calculation of an average *dn/dc* value obtained over 18 samples of *p*(*n*BuMA) analysed *via* THF triple-detection GPC.

Target DP_n	***dn/dc***
60	0.0809
80	0.0786
100	0.0848
100	0.0712
150	0.0787
200	0.0763
300	0.076
400	0.0772
500	0.0865
1000	0.0901
60	0.0755
100	0.0747
200	0.0683
60	0.0709
100	0.0688
200	0.0697
60	0.0734
200	0.0708
Average	**0.0762**

Table A3: Cu-catalysed methanolic ATRP of *n*BuMA at 60 °C, targeting DP_n = 60 monomer units; reactions were performed over 2, 7, 10 and 14 days to determine whether termination reactions, either by combination or disproportionation, take place.

				Triple-detection GPC[c] (THF)		
Target[a] DP_n	Conversion [actual DP_n]	Time (days)	M_n theory[b]	M_n (g mol^{-1})	M_w (g mol^{-1})	Đ
60	99 % [59]	2	8 675	13 550	13 950	1.03
60	99 % [59]	7	8 675	13 200	13 750	1.04
60	99 % [59]	10	8 675	13 550	14 150	1.05
60	99 % [59]	14	8 675	13 100	13 650	1.04

[a] Target DP_n calculated as [*n*BuMA]/[initiator]. [b] Theoretical M_n calculated as (target DP_n x actual conversion achieved and includes initiator residue. [c] Triple-detection GPC utilising THF eluent and d*n*/d*c* = 0.0762 mL g^{-1} (averaged across 18 samples; Table A2, Appendix).

Table A4: Cloud point temperatures for *p*(*n*BuMA)$_x$ (0.5 g) in anhydrous MeOH (0.5 g) with increasing concentrations of *n*(BuMA) monomer.

Monomer Addition (µL)	Mass of monomer / mass of solvent	Cloud Point Temperature (°C)		
		***p*(*n*BuMA)$_{60}$**	***p*(*n*BuMA)$_{200}$**	***p*(*n*BuMA)$_{300}$**
50	**0.089**	**53.6**	**61.3**	**insoluble**
60	**0.107**	**51.5**	**---**	**---**
70	**0.125**	**49.3**	**---**	**---**
80	**0.143**	**47.0**	**---**	**---**
90	**0.161**	**44.9**	**---**	**---**
100	**0.179**	**43.0**	**54.5**	**56.9**
110	**0.197**	**40.8**	**---**	**---**
120	**0.215**	**39.1**	**---**	**---**
130	**0.232**	**37.0**	**---**	**---**
140	**0.250**	**35.4**	**---**	**---**
150	**0.268**	**33.4**	**45.2**	**47.6**
160	**0.286**	**31.7**	**---**	**---**
170	**0.304**	**30.9**	**---**	**---**
180	**0.323**	**28.8**	**---**	**---**
190	**0.340**	**27.2**	**---**	**---**
210	**0.376**	**24.4**	**---**	**---**

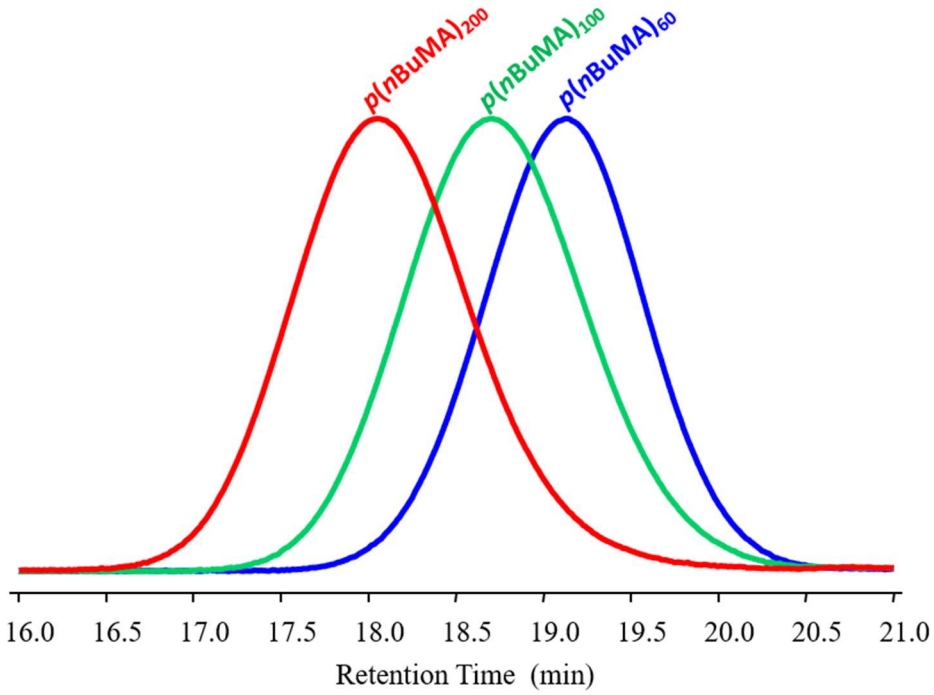

Figure A3: GPC chromatograms (RI) showing *p*(*n*BuMA) molecular weight distributions across targeted DP_n = 60 – 200 monomer units; polymerised in IPA at 60 °C.

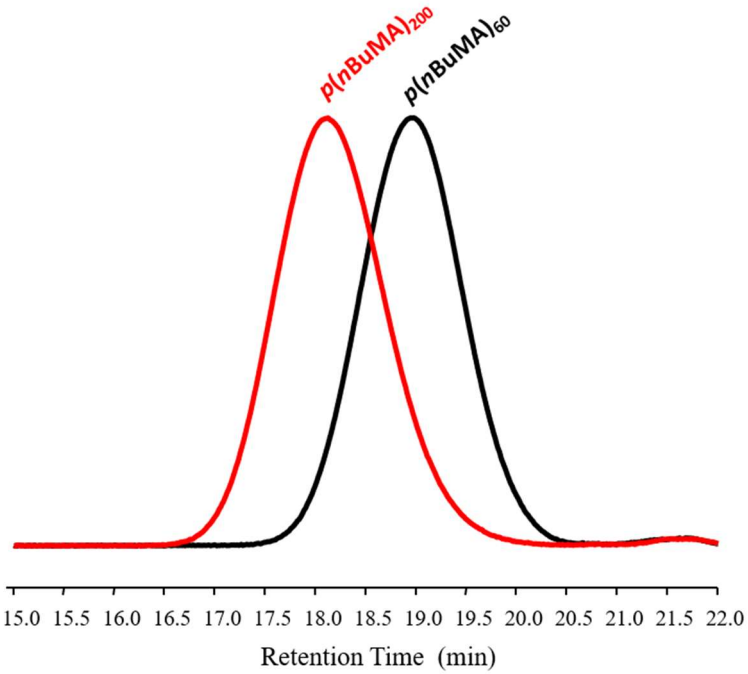

Figure A4: GPC chromatograms (RI) showing *p*(*n*BuMA) molecular weight distributions across targeted DP_n = 60 – 200 monomer units; polymerised in IPA at 25 °C.

Table A5: Cu-catalysed ATRP of *n*BuMA at 60 °C in IPA, targeting DP_n = 60 monomer units; reactions were performed over 2 and 7 days to determine whether termination reactions, either by combination or disproportionation, take place.

				Triple-detection GPC[c] (THF)		
Target[a] DP_n	Conversion [actual DP_n]	Time (days)	M_n theory[b]	M_n (g mol^{-1})	M_w (g mol^{-1})	Đ
60	99 % [59]	2	8 675	11 850	13 500	1.14
60	99 % [59]	7	8 675	14 400	16 950	1.18

[a] Target DP_n calculated as [*n*BuMA]/[initiator]. [b] Theoretical M_n calculated as (target DP_n x actual conversion achieved and includes initiator residue. [c] Triple-detection GPC utilising THF eluent and d*n*/d*c* = 0.0762 mL g^{-1} (averaged across 18 samples; Table A2, Appendix).

Table A6: Methanolic ATRP of *n*BuMA at 60 °C using various catalyst ligands

				Triple-detection GPC (THF)[c]		
Target[a] DP_n	Ligand	Conversion (%)	M_n Theory[b]	M_n (g/mol)	M_w (g/mol)	Đ
60	Bpy	99	8640	13570	13950	1.03
60	PMDETA	99	8640	20350	29800	1.46
60	Me_6TREN	87	7620	38550	44550	1.16

[a] Target DP_n calculated as [*n*BuMA]/[initiator]; [b] Theoretical M_n calculated as (Target DP_n x 142.2 gmol^{-1})*actual fractional conversion achieved and includes initiator residue; [c] Triple-detection GPC utilising THF eluent and *dn/dc* = 0.0762 (averaged across 18 samples; Table A2, Appendix).

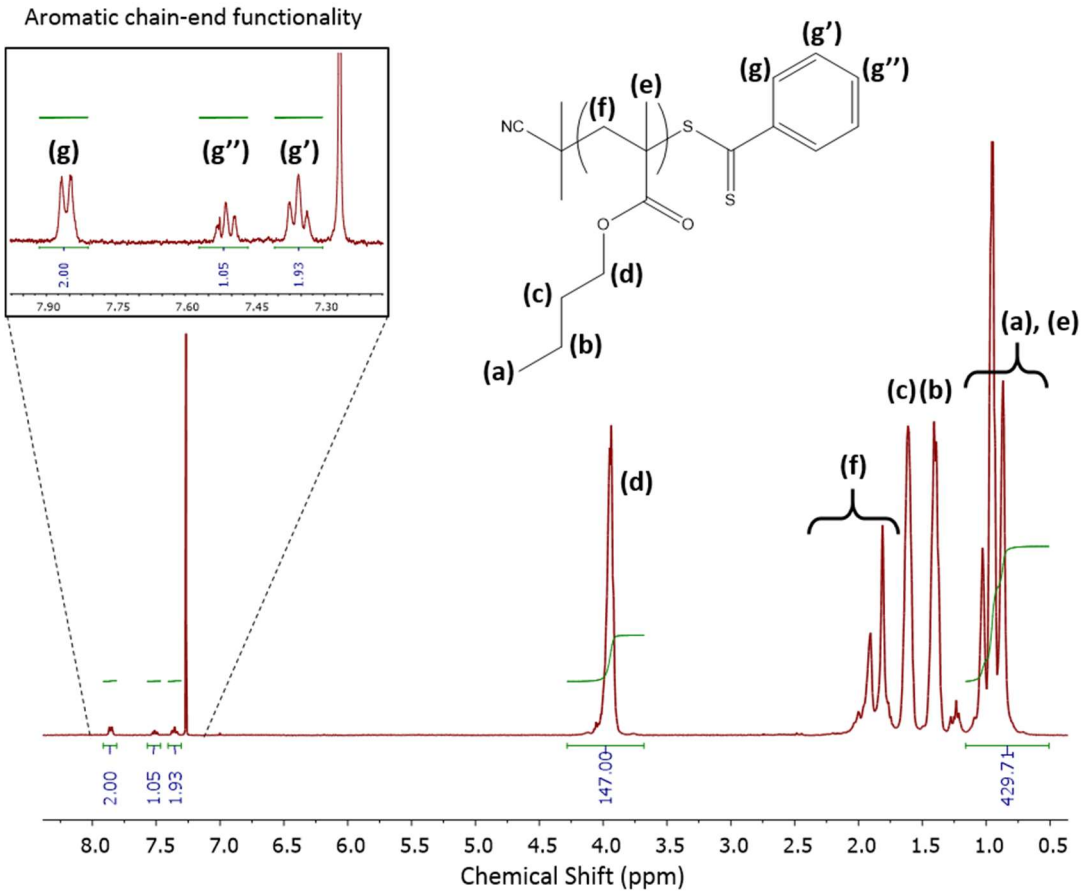

Figure A5: ^{1}H-NMR ($CDCl_3$) analysis of purified $p(n\text{BuMA})_{60}$ obtained *via* RAFT to determine the DPn. Inset; magnification of the aromatic region of the spectrum showing resonances attributed to the CTA chain-end functionality.

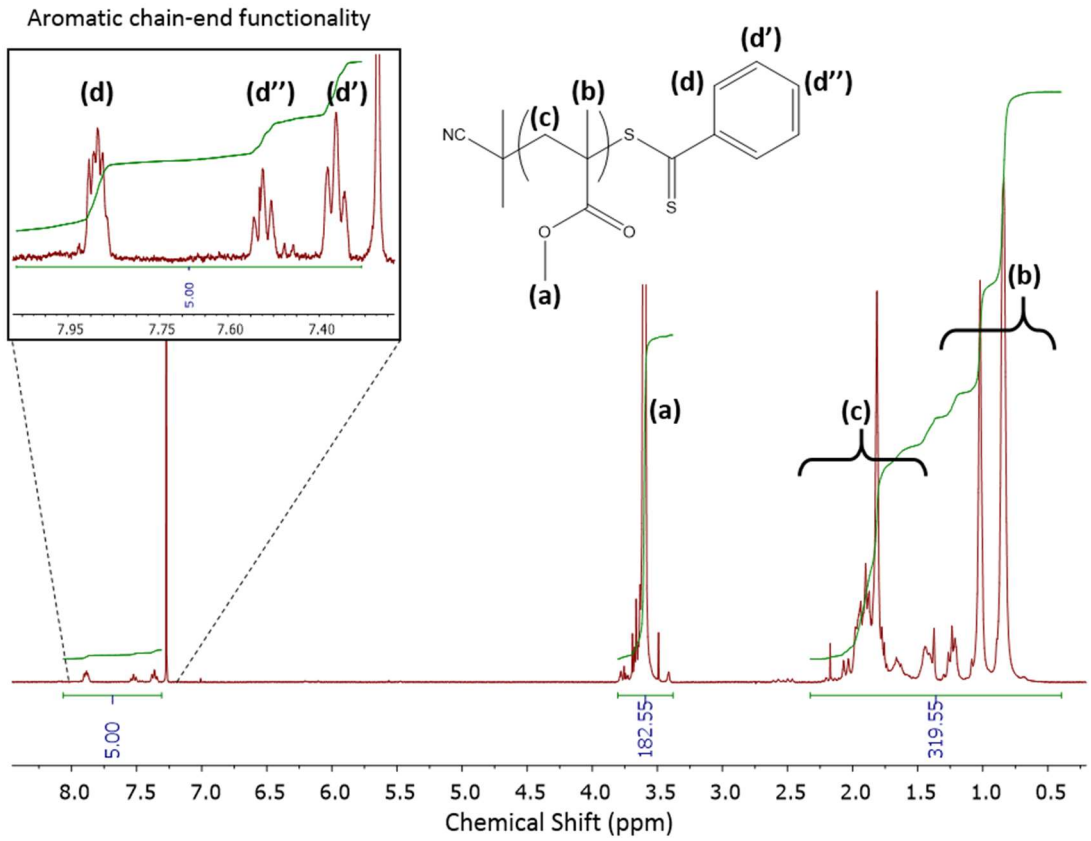

Figure A6; ^{1}H-NMR ($CDCl_3$) analysis of purified *p*(MMA)$_{60}$ obtained *via* RAFT to determine the DPn. Inset; magnification of the aromatic region of the spectrum showing resonances attributed to the CTA chain-end functionality.

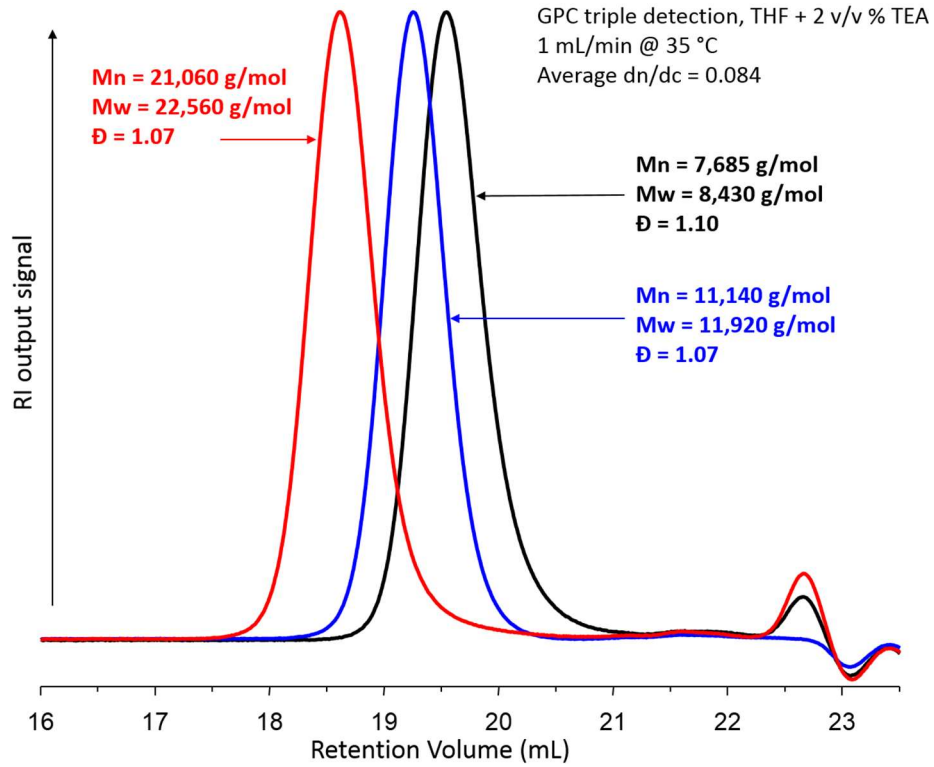

Figure A7; RAFT polymerisation of MMA in anhydrous methanol at 60°C. SEC chromatograms (RI) showing *p*(MMA) molecular weight distributions across targeted DPn = 60-200 monomer units. Analysis performed in THF (+ 2 v/v % TEA) at 1 mL/min, 35 °C.

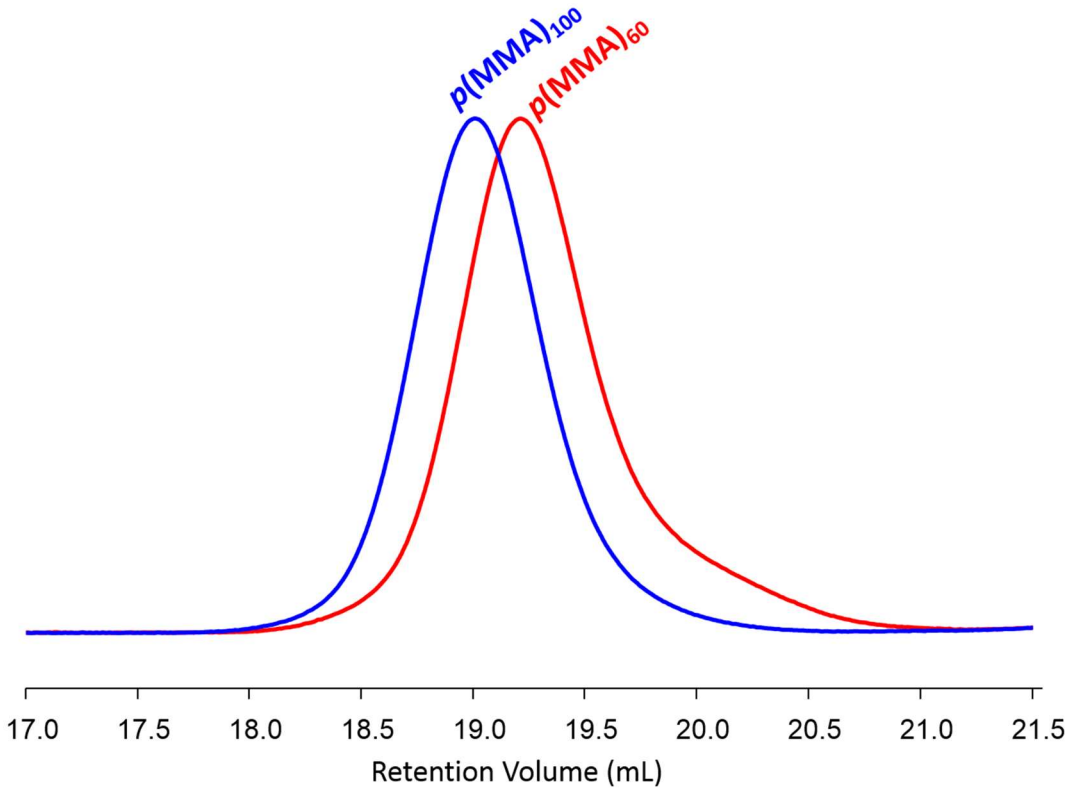

Figure A8; Cu-catalysed ATRP of MMA in anhydrous methanol at 60 °C. SEC chromatograms (RI) showing *p*(MMA) molecular weight distributions across targeted DPn = 60-100 monomer units. Analysis performed in THF (+ 2 v/v % TEA) at 1mL/min, 35 °C.

Table A7; Calculation of an average dn/dc value obtained over 6 samples of *p*(MMA) analysed *via* triple-detection SEC (THF).

		Triple-detection GPC (THF) [a]	
Sample	**Technique**	**dn/dc**	**Average dn/dc**
***p*(MMA)$_{105}$ Standard**		**0.0865**	**0.084**
***p*(MMA)$_{60}$**	**RAFT**	**0.0825**	
***p*(MMA)$_{100}$**		**0.0941**	
***p*(MMA)$_{200}$**		**0.0731**	
***p*(MMA)$_{60}$**	**ATRP**	**0.0810**	
***p*(MMA)$_{100}$**		**0.0853**	

[a]Determined by triple detection GPC (THF (+ 2 v/v % TEA), 1mL/min, 35 °C).

Chapter 3

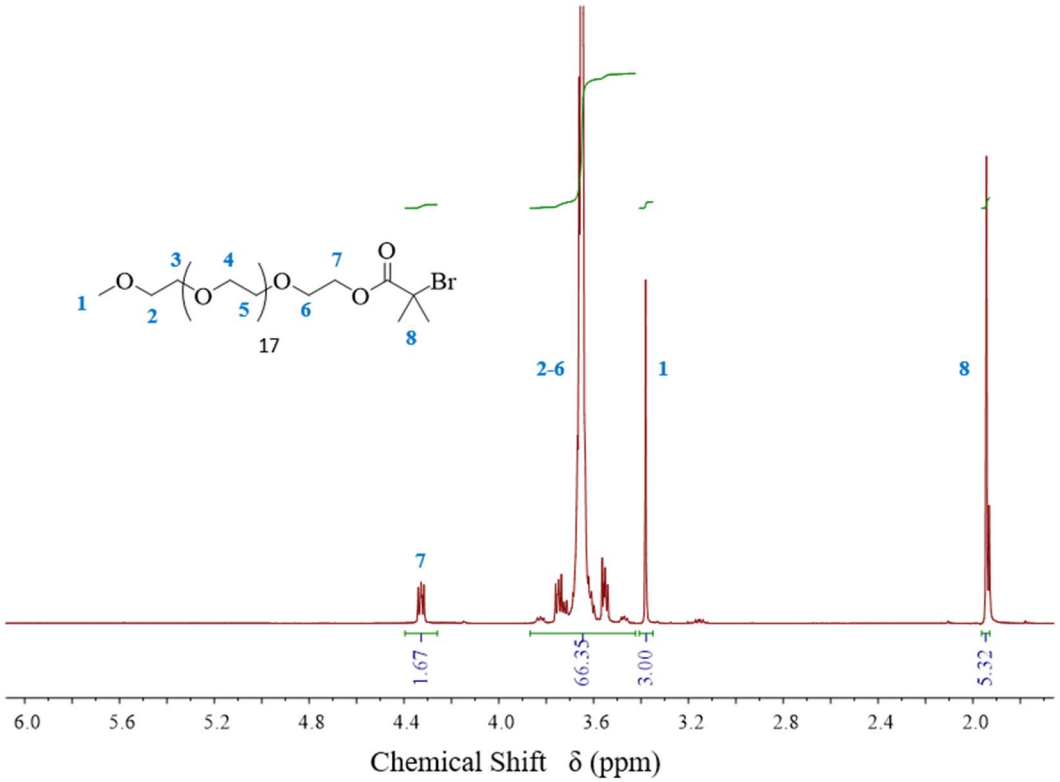

Figure A9; ^{1}H-NMR ($CDCl_3$) analysis of $PEG_{17}Br$ macro-initiator.

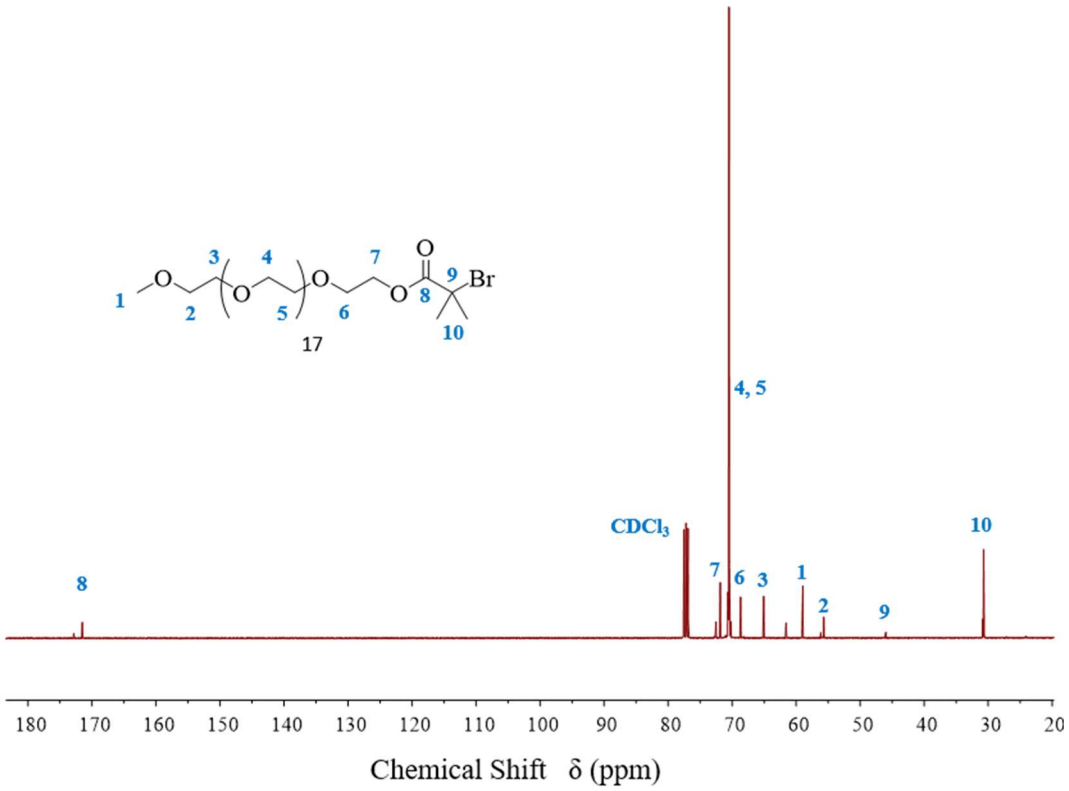

Figure A10; ^{13}C-NMR ($CDCl_3$) analysis of $PEG_{17}Br$ macro-initiator.

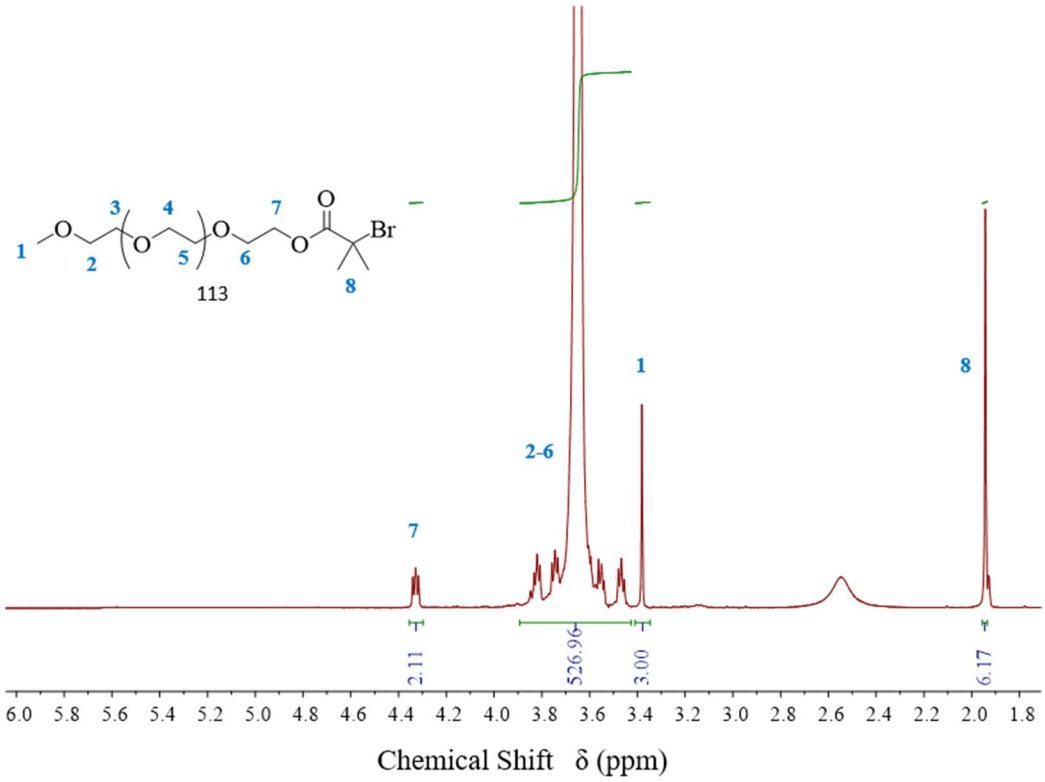

Figure A11; ^{1}H-NMR ($CDCl_3$) analysis of $PEG_{113}Br$ macro-initiator.

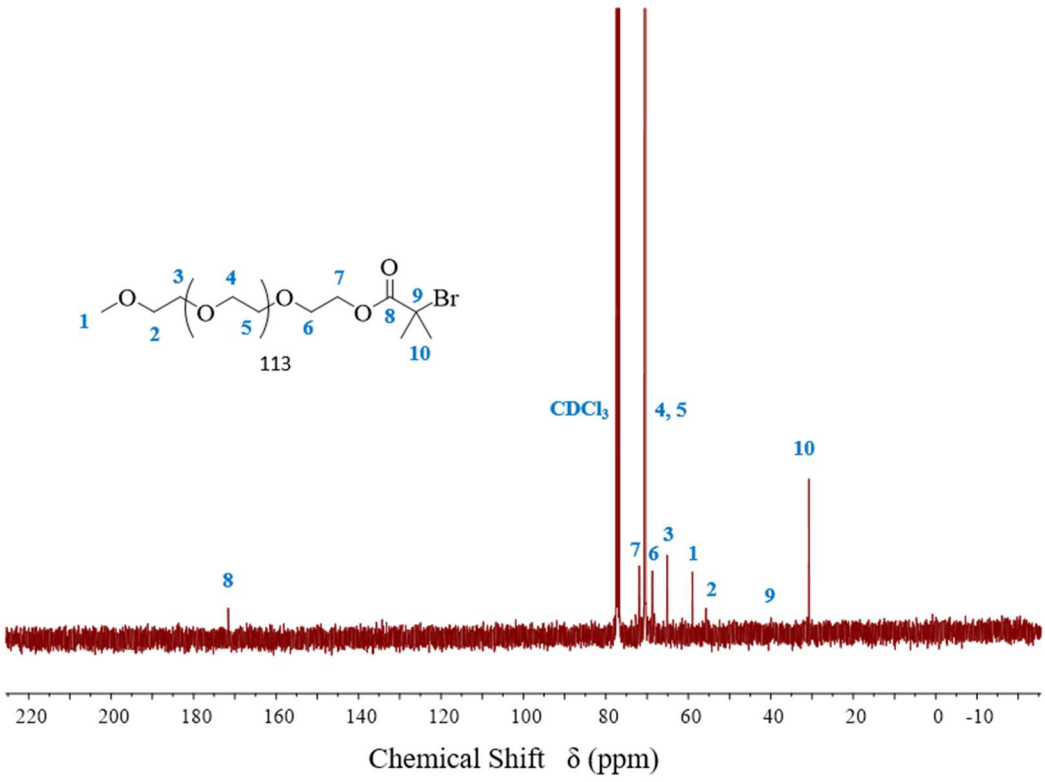

Figure A12; ^{13}C-NMR ($CDCl_3$) analysis of $PEG_{113}Br$ macro-initiator.

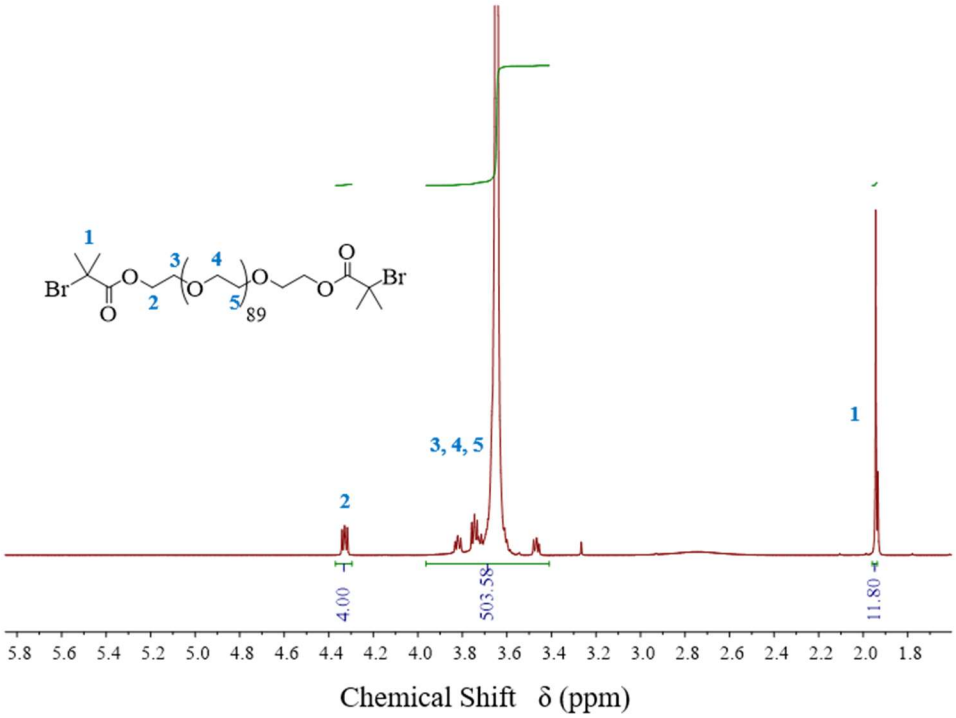

Figure A13: ^{1}H-NMR ($CDCl_3$) analysis of $PEG_{91}Br_2$ α,ω-bifunctional macro-initiator.

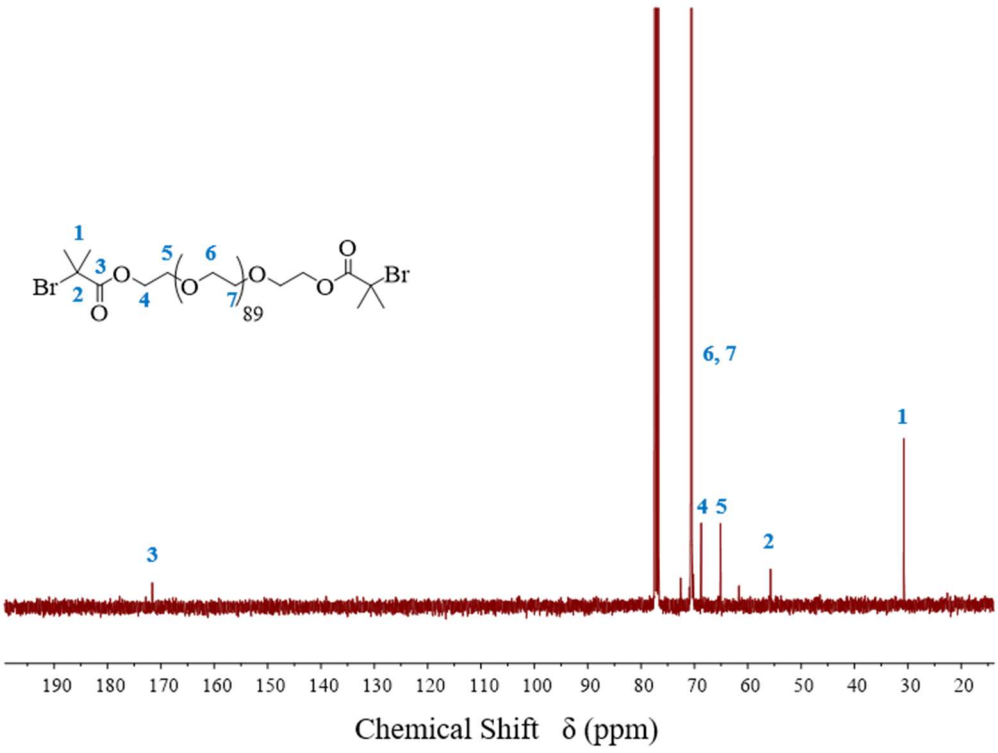

Figure A14; ^{13}C-NMR ($CDCl_3$) analysis of $PEG_{91}Br_2$ α,ω-bifunctional macro-initiator.

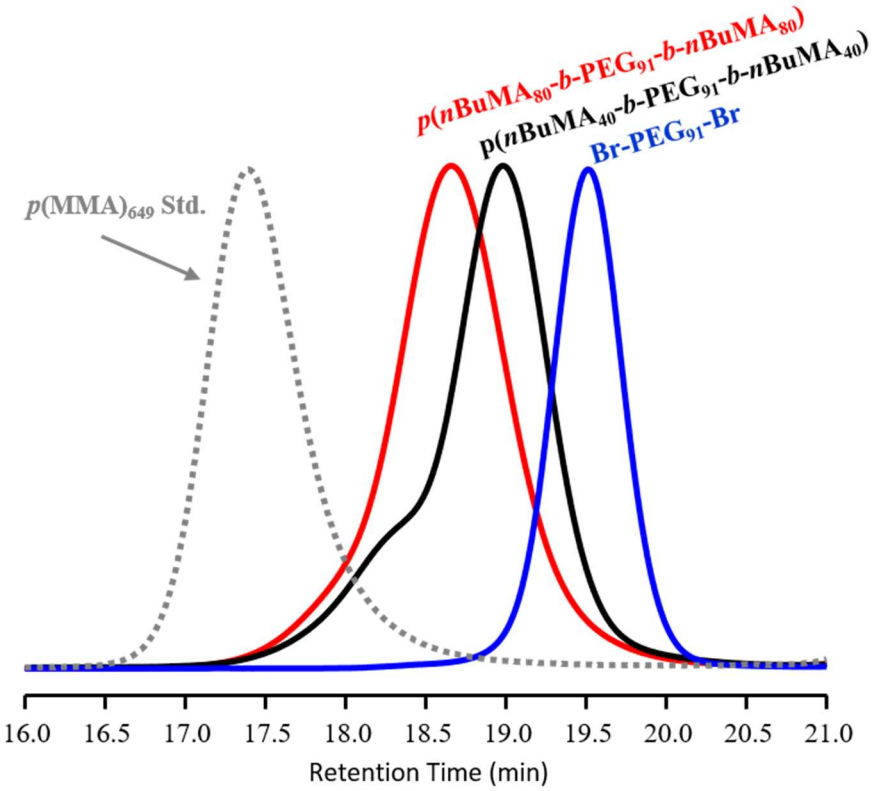

Figure A15; Cu-catalysed ATRP of *n*BuMA in anhydrous methanol at 60 °C using the Br-PEG$_{113}$-Br macroinitiator. SEC chromatograms (RI) showing *p*(*n*BuMA-*b*-PEG$_{91}$-*b*-*n*BuMA) molecular weight distributions across targeted DPn = 80-160 monomer units – Br-PEG$_{91}$-Br macroinitiator and *p*(MMA)$_{649}$ standard shown for comparison. Analysis performed in DMF (+ 0.01M LiBr) at 1 mL/min, 60 °C.

Table A8; Calculation of an average dn/dc value for PEG (averaged over 3 polymer standards) and for *p*(*n*BuMA) (averaged over three polymer samples) for use in equation [1] in order to generate a (dn/dc)$_{copolym.}$ for the *p*(PEG-*b*-*n*BuMA) A-B block copolymers. Analysed by triple-detection GPC (DMF).

	Triple-detection GPC (DMF) [a]	
Sample	**dn/dc**	**Average dn/dc**
PEO 19kDa	**0.0571**	
PEO 32.6 kDa	**0.0553**	**0.0566**
PEO 32.6 kDa	**0.0573**	
***p*(*n*BuMA)$_{80}$**	**0.0616**	
***p*(*n*BuMA)$_{80}$**	**0.0627**	**0.0624**
***p*(*n*BuMA)$_{80}$**	**0.0630**	

[a] Determined by triple detection GPC (DMF (+ 0.01M LiBr), 1 mL/min, 60 °C).

Table A9: Methanolic Cu-catalysed ATRP of MMA at 60 °C and 25 °C using $PEG_{113}Br$

Target[a] DP_n	Conv. (%)	Time (hrs)	M_n Theory[b]	M_n ^1H NMR	Triple-detection GPC (DMF) M_n (g/mol)	M_w (g/mol)	Đ
60 °C							
60	99+	29	11100	11250	14600	17000	1.16
80	99+	49	13100	12050	14900	18200	1.22
100	99+	67	15100	15050	18200	22300	1.23
25 °C							
80	91	27	12400	12950	12800	15750	1.23

[a] Theoretical M_n includes initiator residue and was calculated as [(Target DP_n x 100.12 g mol^{-1}) x experimental monomer conversion.

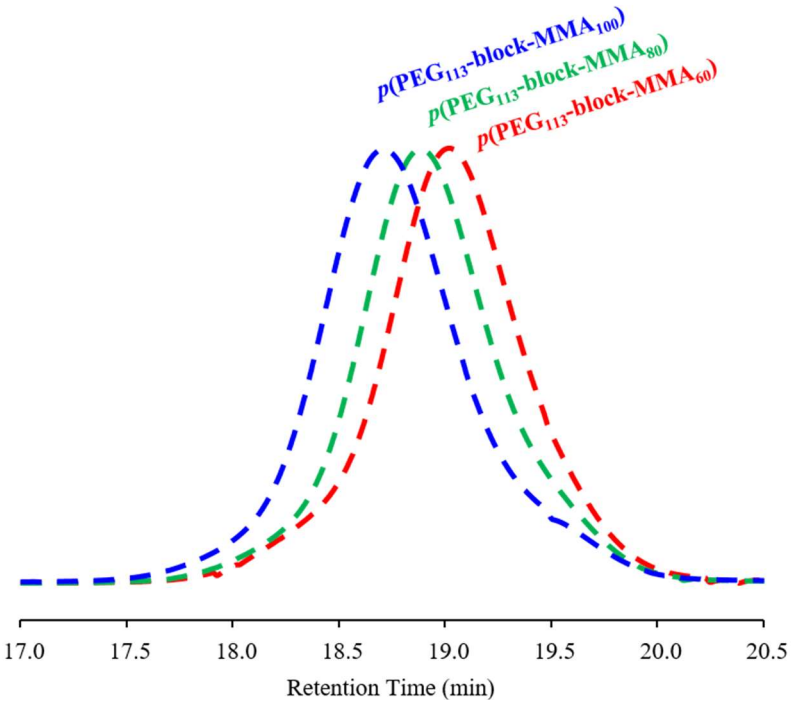

Figure A16; Cu-catalysed ATRP of MMA in anhydrous methanol at 60 °C using the $PEG_{113}Br$ macroinitiator. SEC chromatograms (RI) showing *p*(PEG_{113}-*b*-MMA) molecular weight distributions across targeted DPn = 60-100 monomer units. Analysis performed in DMF (+ 0.01M LiBr) at 1 mL/min, 60 °C.

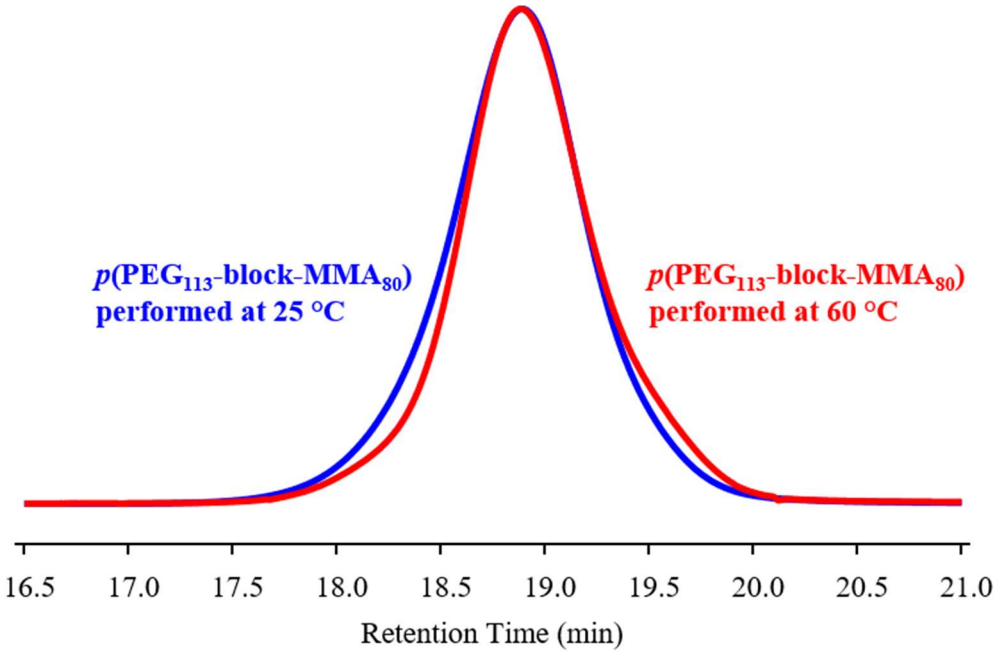

Figure A17; Cu-catalysed ATRP of MMA (target DPn = 80 monomer units) in anhydrous methanol performed at 25 °C and 60 °C using the $PEG_{113}Br$ macroinitiator. GPC chromatograms (RI) showing *p*(PEG_{113}-*b*-MMA_{80}) molecular weight distributions for each A-B block copolymer. Analysis performed in DMF (+ 0.01M LiBr) at 1 mL/min, 60 °C.

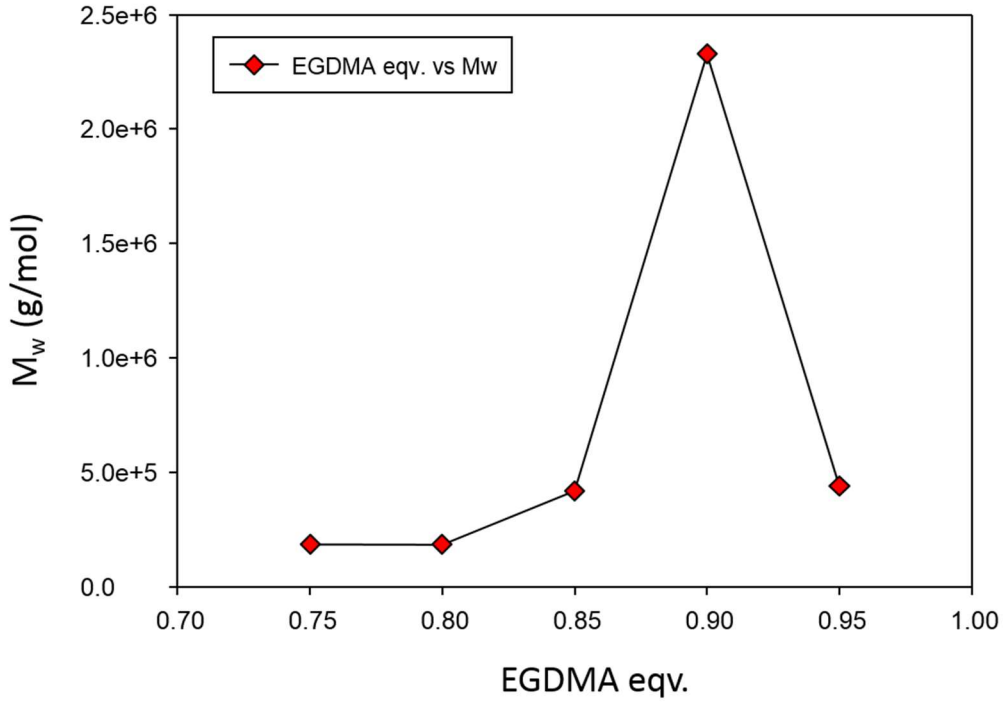

Figure A18; Cu-catalysed branched methanolic ATRP of *n*BuMA (target DPn = 60 monomer units) at 60 °C using the $PEG_{113}Br$ macroinitiator and varying equivalents (0.75-0.95 wrt, initiator) of divinyl monomer, EGDMA. A graph showing the evolution of molecular weight with increasing levels of EGDMA – M_w decreases when using 0.95eqv. EGDMA due to partial microgelation which was filtered off prior to SEC (DMF) analysis.

Chapter 4

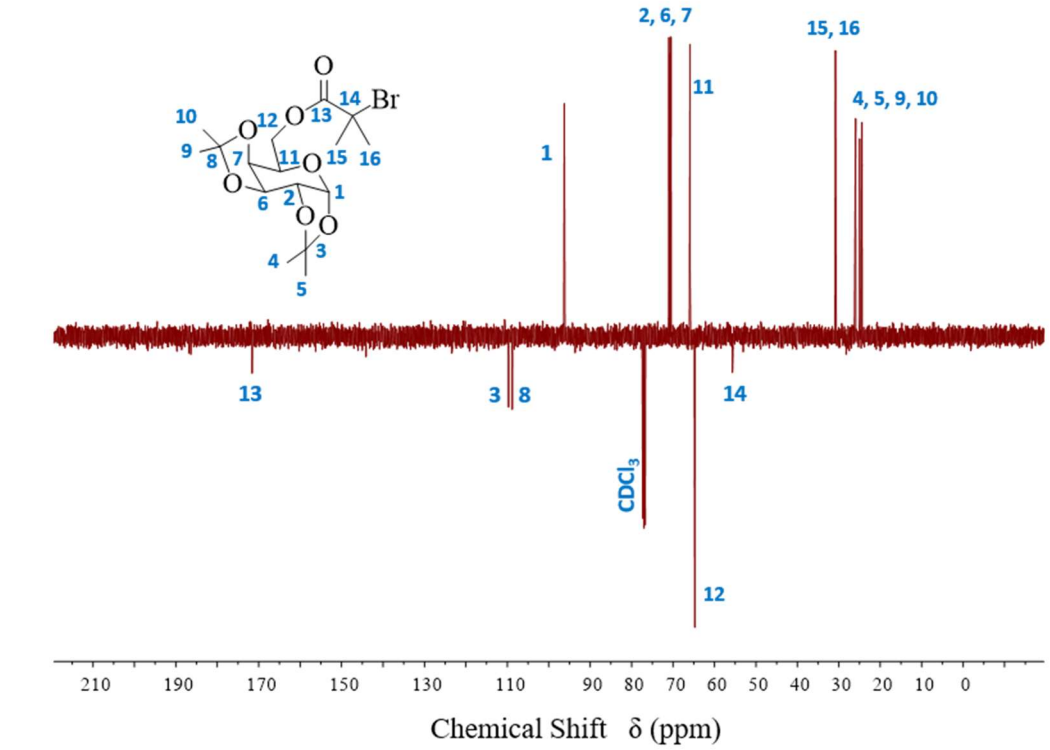

Figure A19: ^{13}C-NMR ($CDCl_3$) APT spectrum of G0-proGal-Br [2].

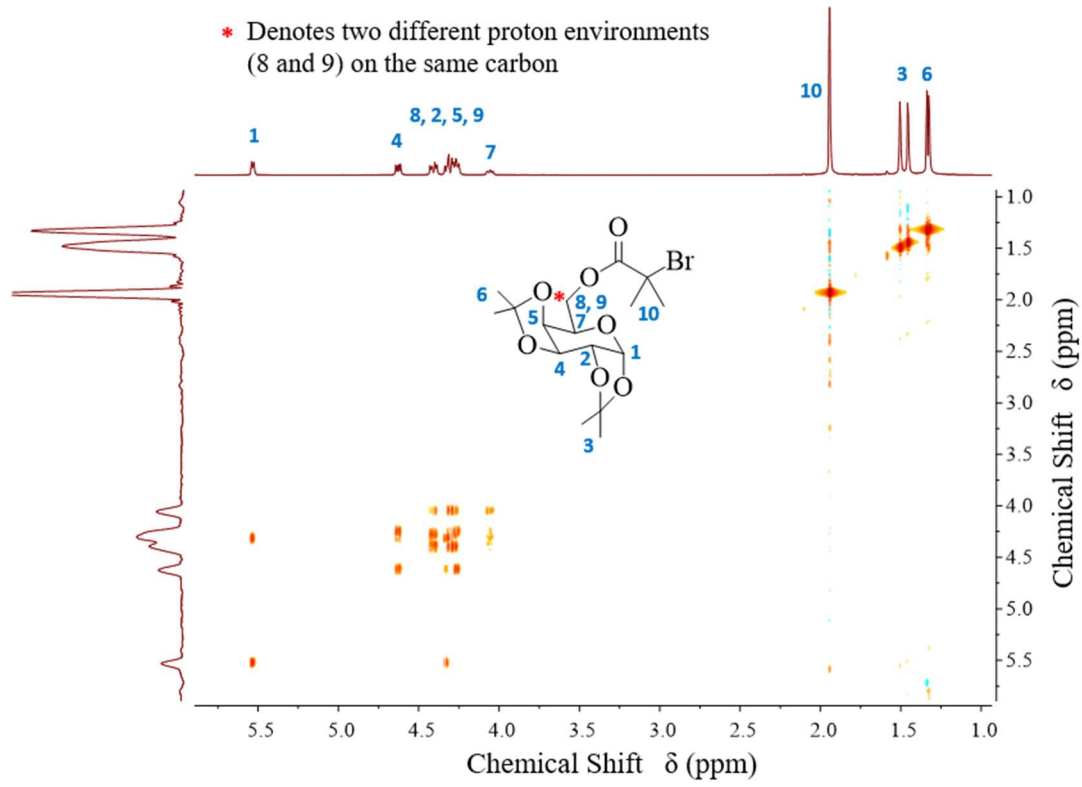

Figure A20: 2-Dimensional ^{1}H-NMR ($CDCl_3$) COSY spectrum of G0-proGal-Br [2].

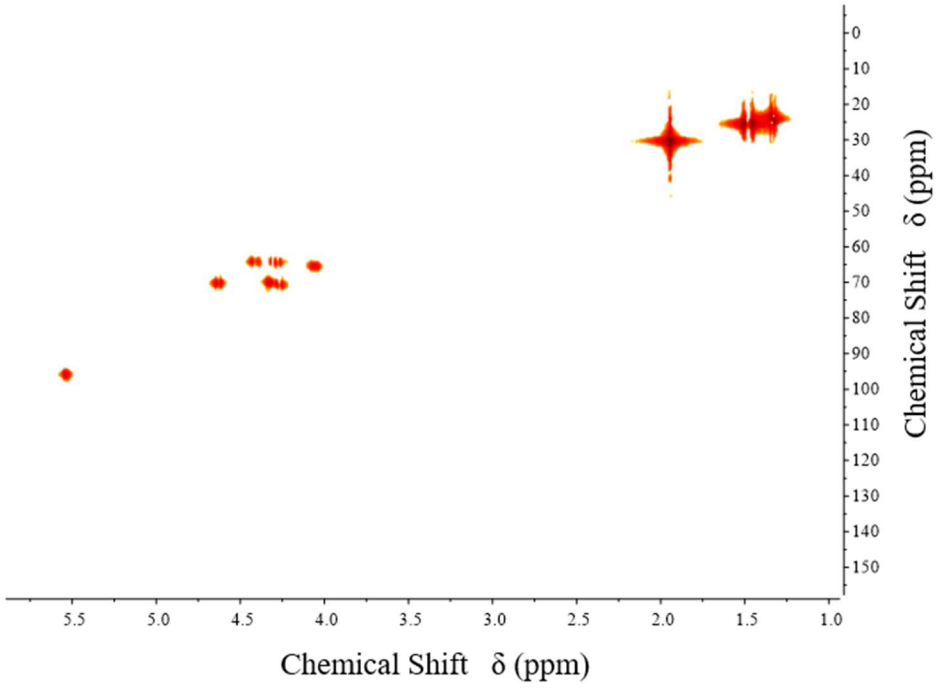

Figure A21: 2-Dimensional ^{1}H-^{13}C HSQC ($CDCl_3$) spectrum of G0-proGal-Br [2].

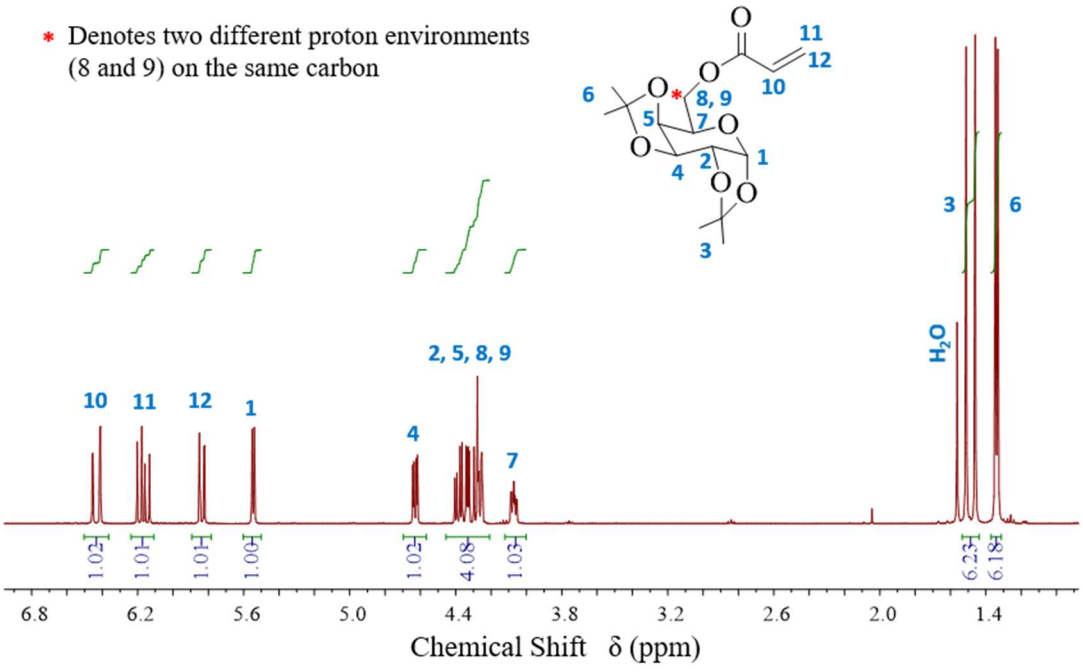

Figure A22: ^{1}H-NMR ($CDCl_3$) of proGal-acrylate [3], showing the assignment and integrations of each environment after normalising the integration of the anomeric proton (1) to 1H.

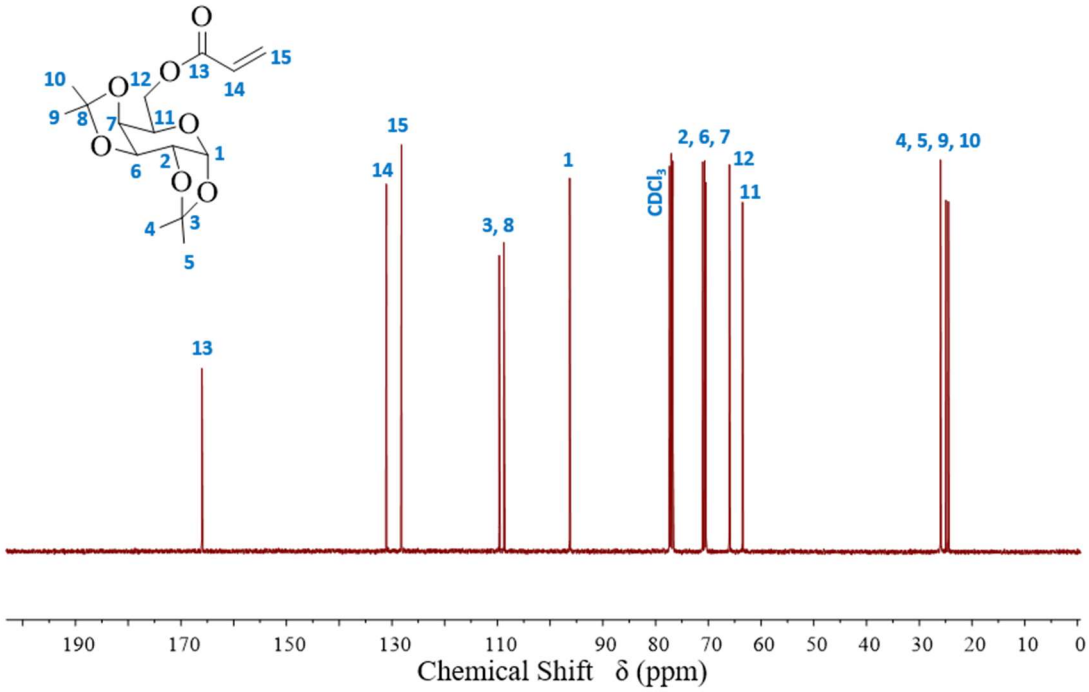

Figure A23: ^{13}C-NMR ($CDCl_3$) of proGal-acrylate [3], showing the assignment of each carbon environment.

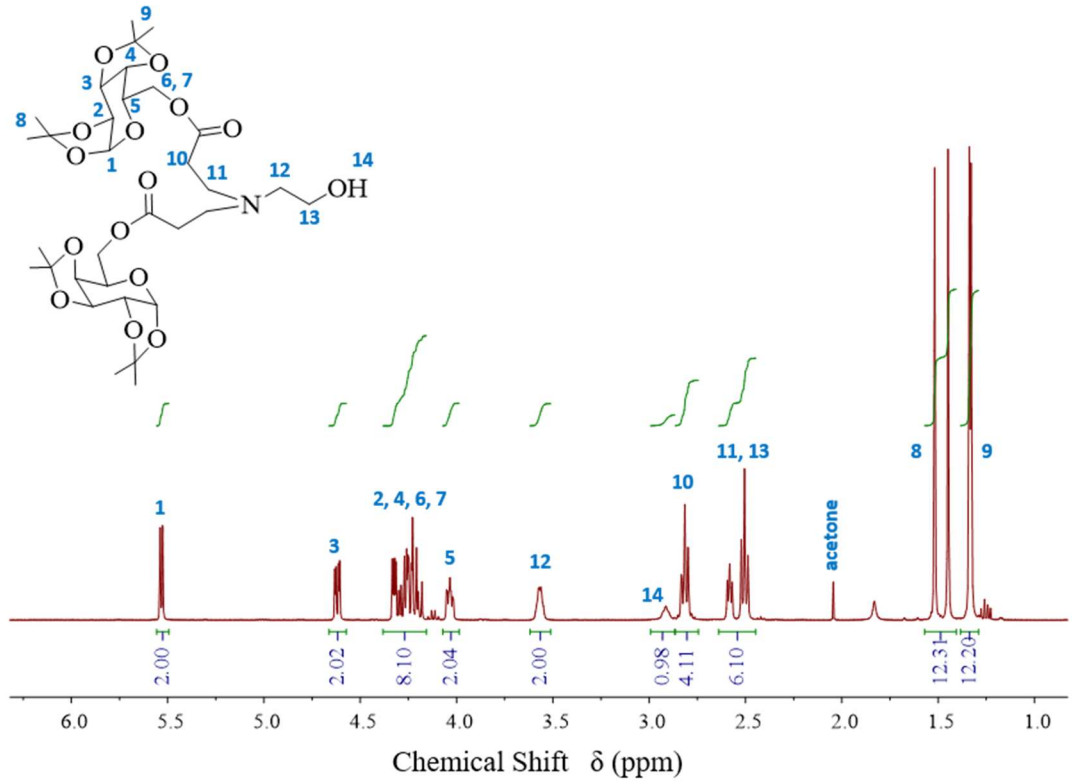

Figure A24: ^{1}H-NMR ($CDCl_3$) of G1-proGal-OH [4], showing the assignment and integrations of each environment after normalising the integration of the anomeric protons (1) to 2H.

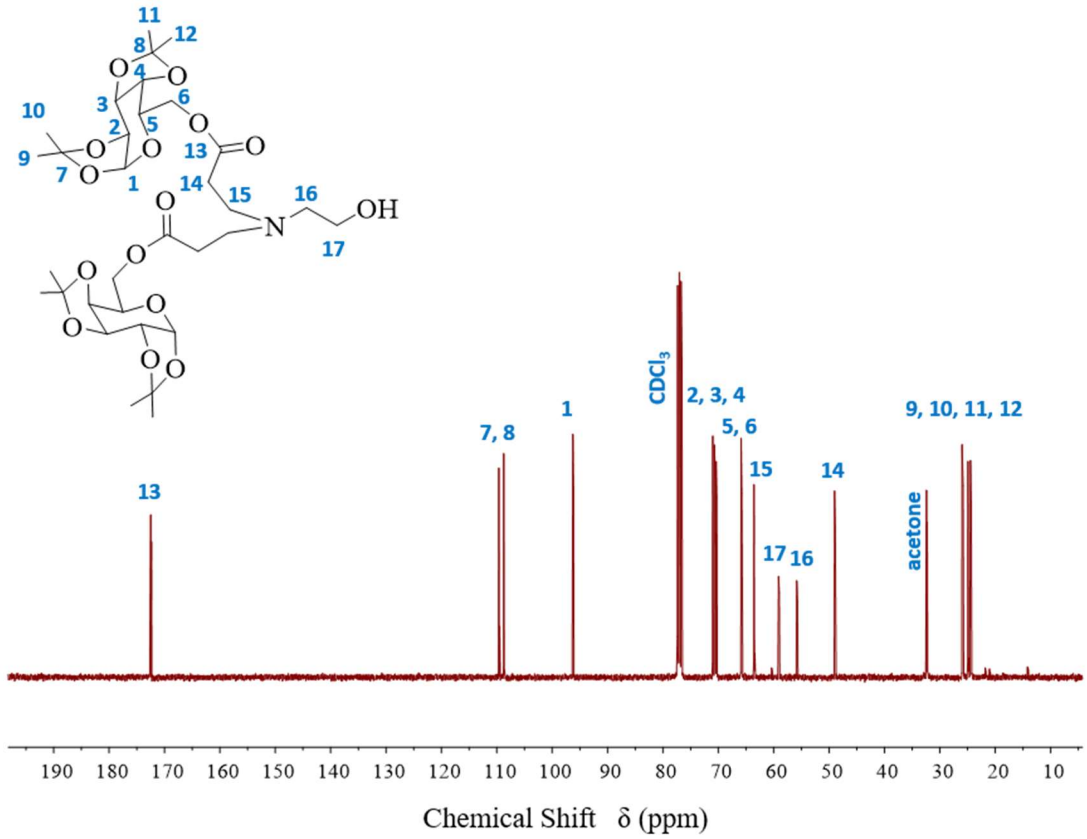

Figure A25: ^{13}C-NMR ($CDCl_3$) of G1-proGal-OH [4], showing the assignment of each carbon environment.

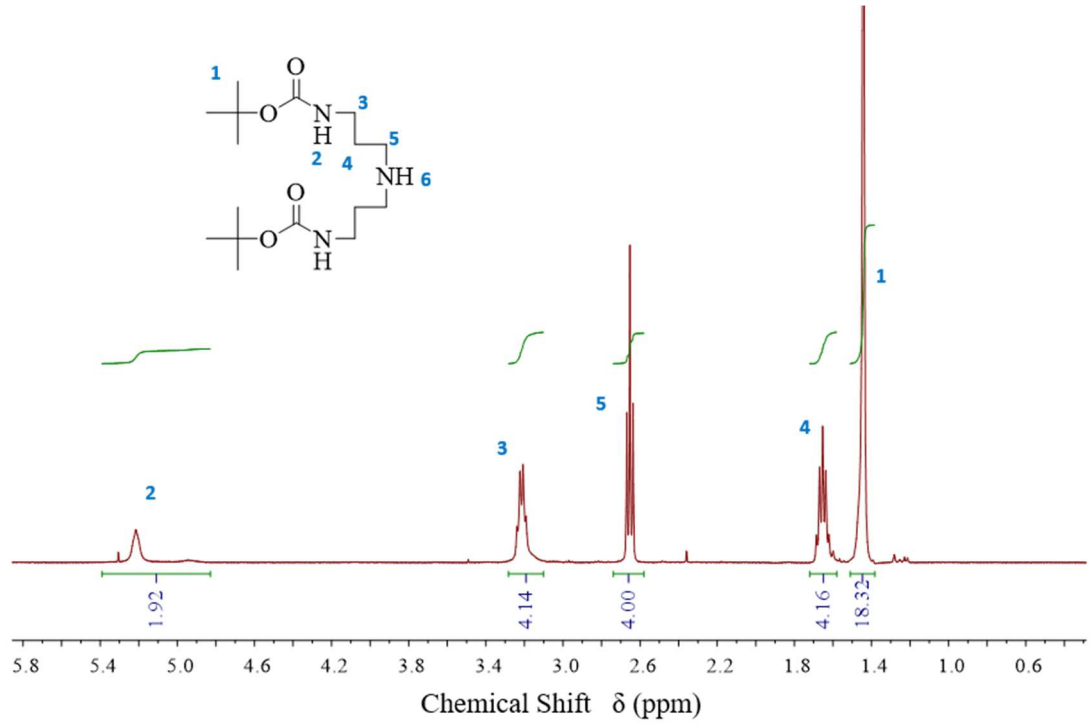

Figure A26: ^{1}H-NMR ($CDCl_3$) of intermediate [6] of the APAP synthesis, showing the assignment and integrations of each environment after normalising the integration of the proton environment (5) to 4H.

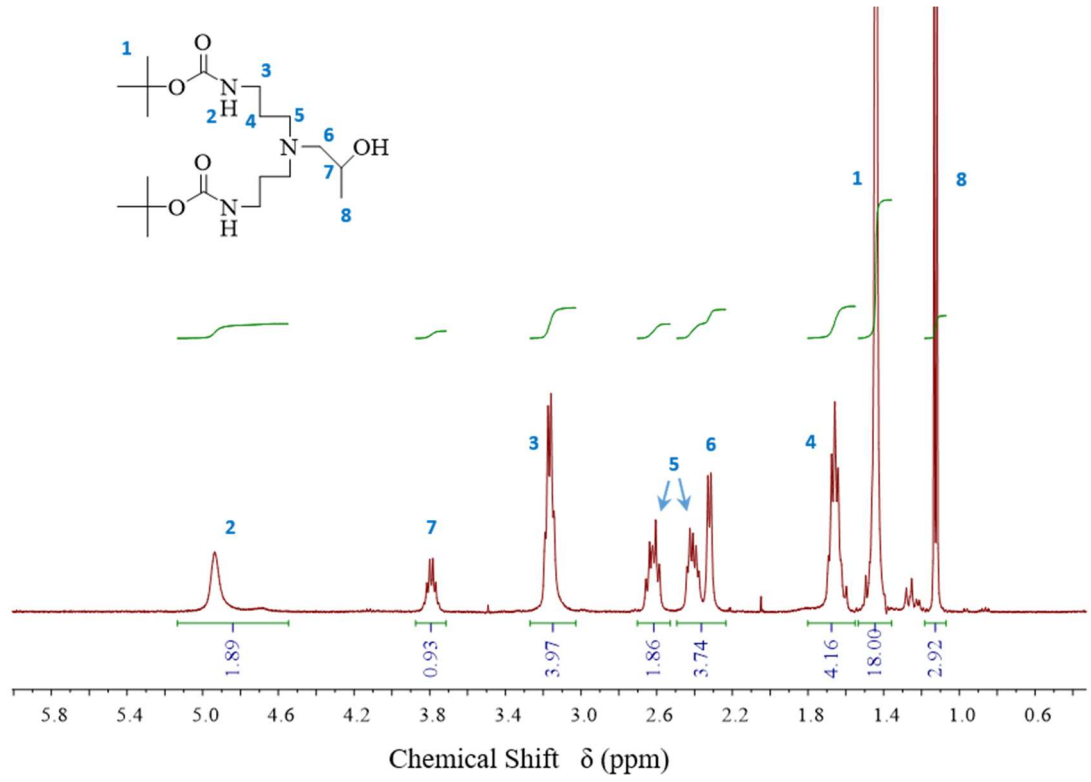

Figure A27: ^{1}H-NMR ($CDCl_3$) of intermediate [7] of the APAP synthesis, showing the assignment and integrations of each environment after normalising the integration of the *t*BOC protons (1) to 18H.

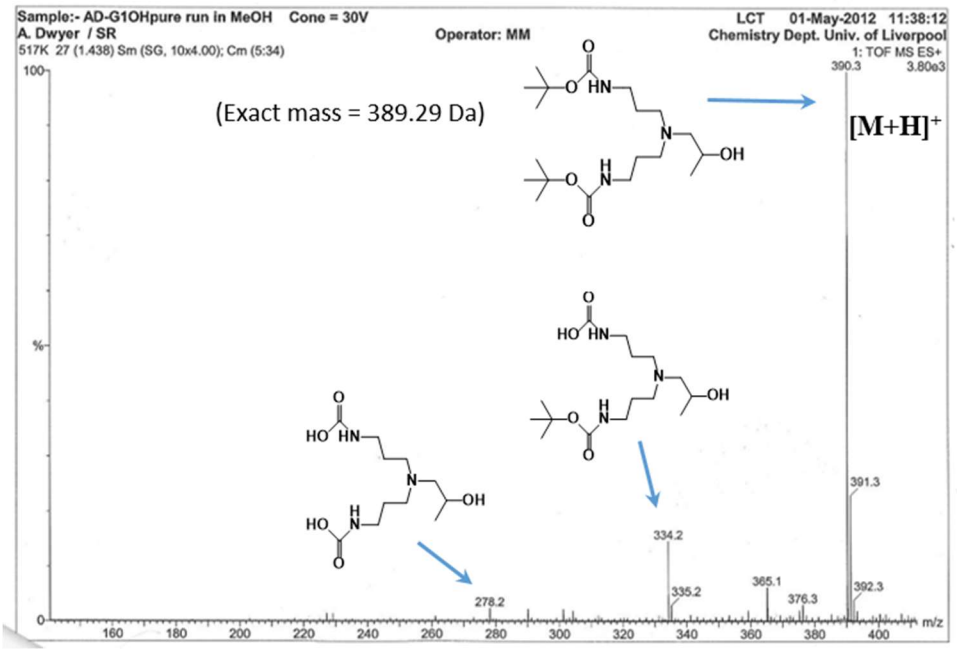

Figure A28: ESI mass spectrometry analysis of intermediate [7] of the APAP synthesis showing the $[M+H]^+$ molecular ion peak, and its fragments.

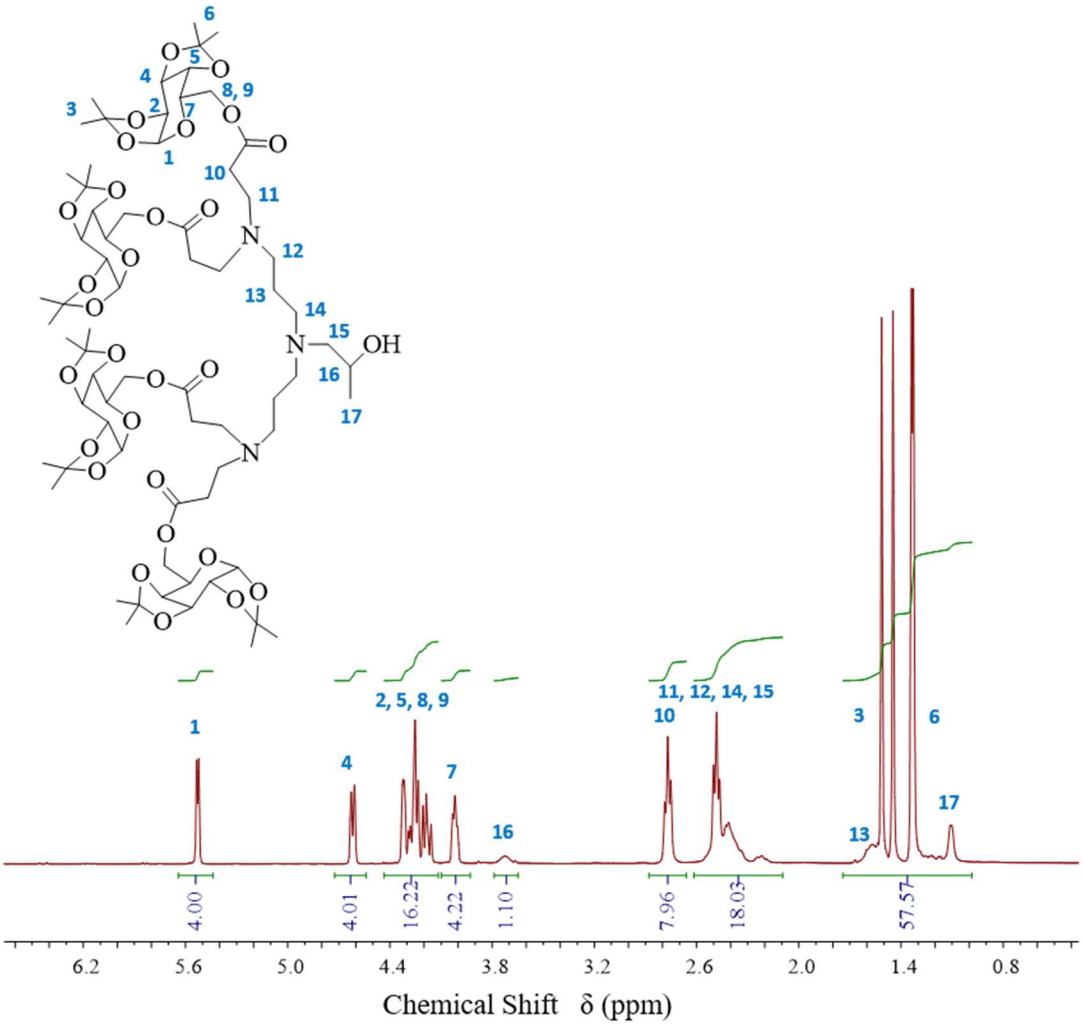

Figure A29: ^{1}H-NMR ($CDCl_3$) of G2-proGal-OH [9], showing the assignment and integrations of each environment after normalising the integration of the anomeric protons (1) to 4H.

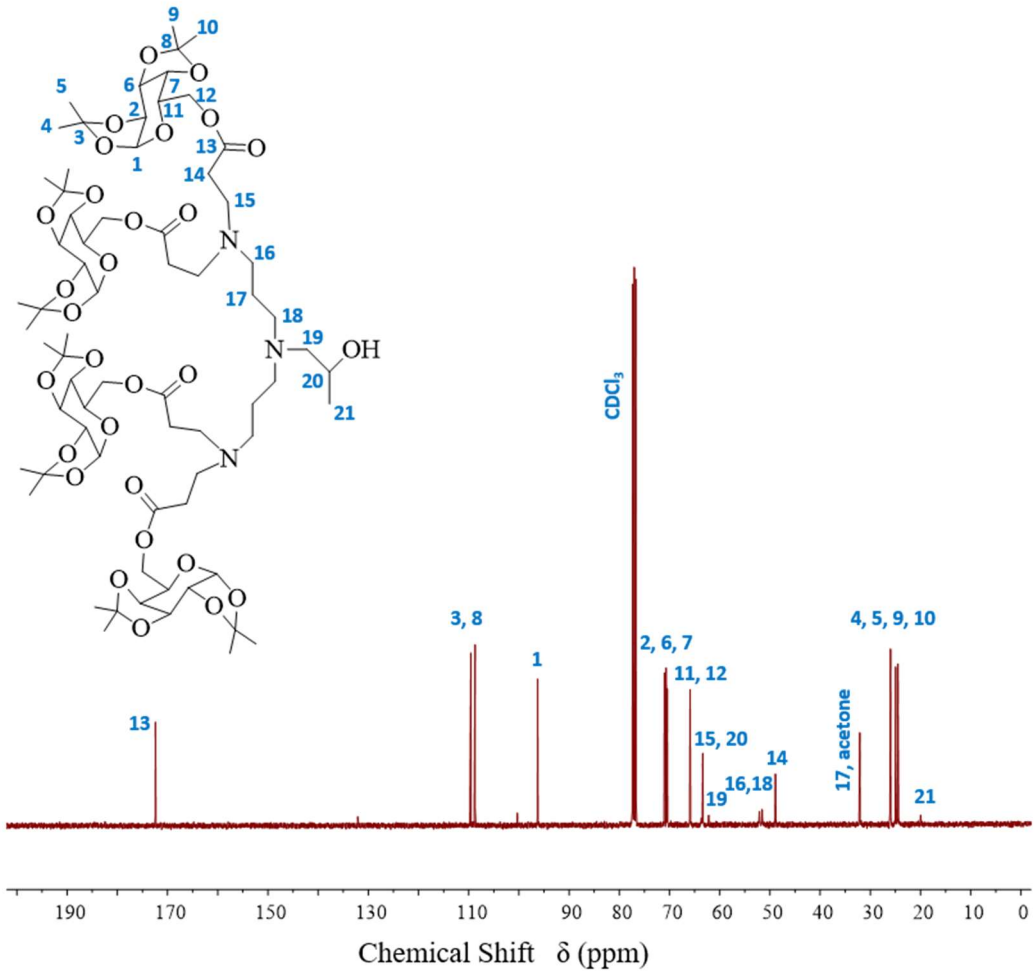

Figure A30: ^{13}C-NMR ($CDCl_3$) of G2-proGal-OH [9], showing the assignment of each carbon environment.

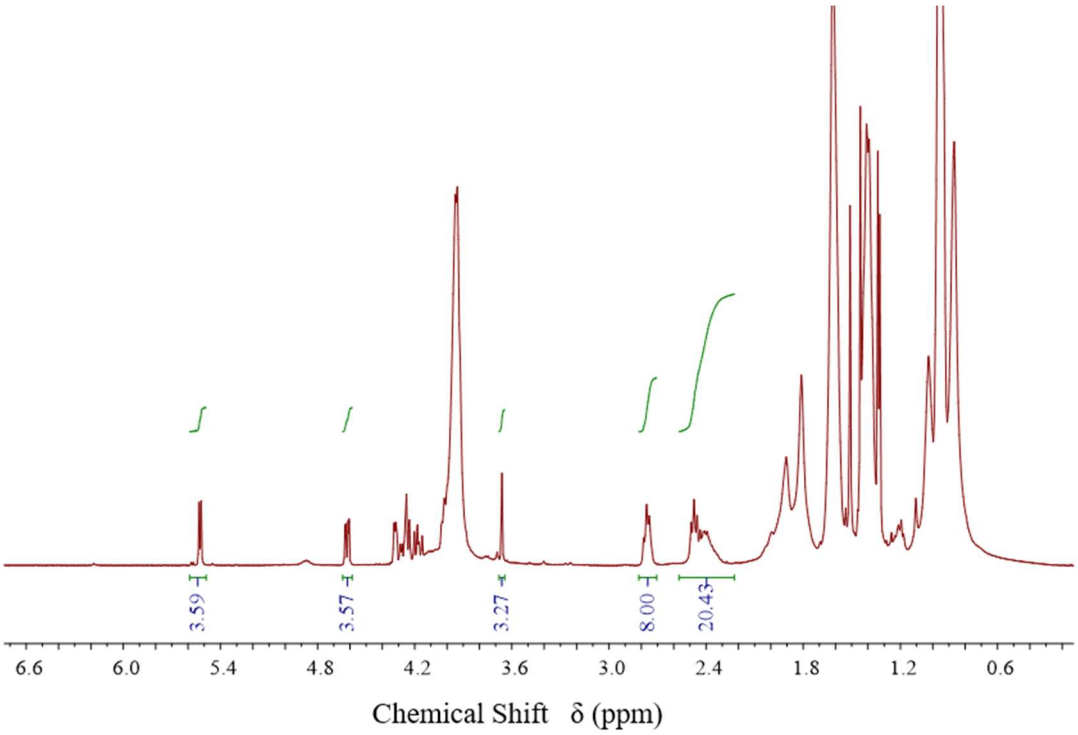

Figure A31: ^{1}H-NMR ($CDCl_3$) analysis of G2-proGal-*p*(*n*BuMA$_{30}$-*co*-EGDMA$_{0.8}$) after purification; the resonance potentially due to transesterification reactions can be seen at approximately 3.65 ppm, integrating to 3.27H.

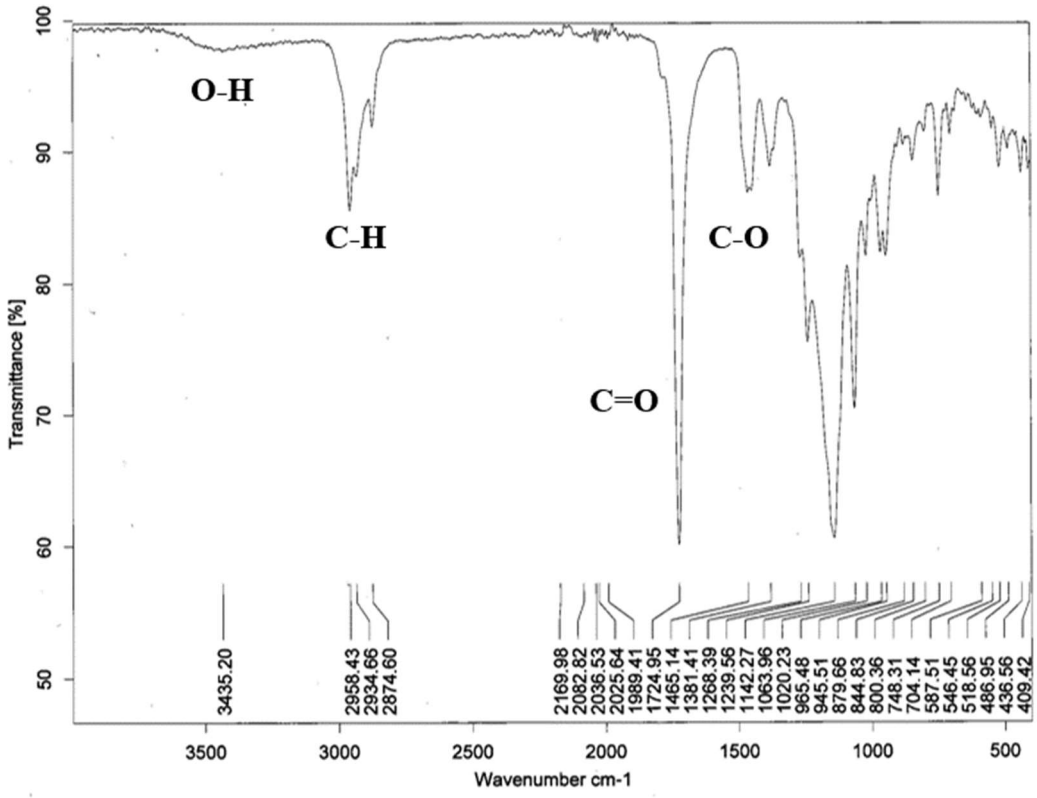

Figure A32: IR spectroscopy analysis of G2-Gal-*p*(*n*BuMA$_{30}$-*co*-EGDMA$_{0.8}$) showing a small transmittance at approximately 3,400 cm^{-1} (attributed to the O-H stretch) after deprotection.

Chapter 5

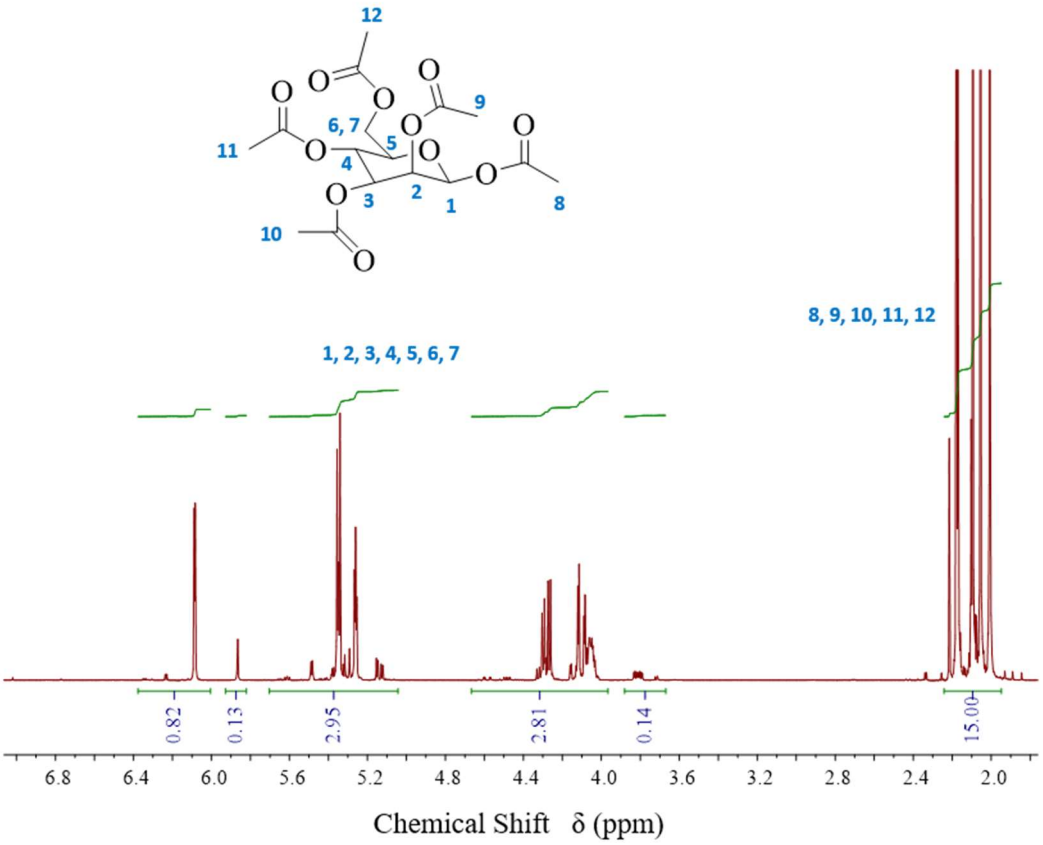

Figure A33: ^{1}H-NMR ($CDCl_3$) of Mann-$(OAc)_5$ [12], showing the assignment and integrations of the environments after normalising the integration of the acetyl protons (8, 9, 10, 11, 12) to 15H.

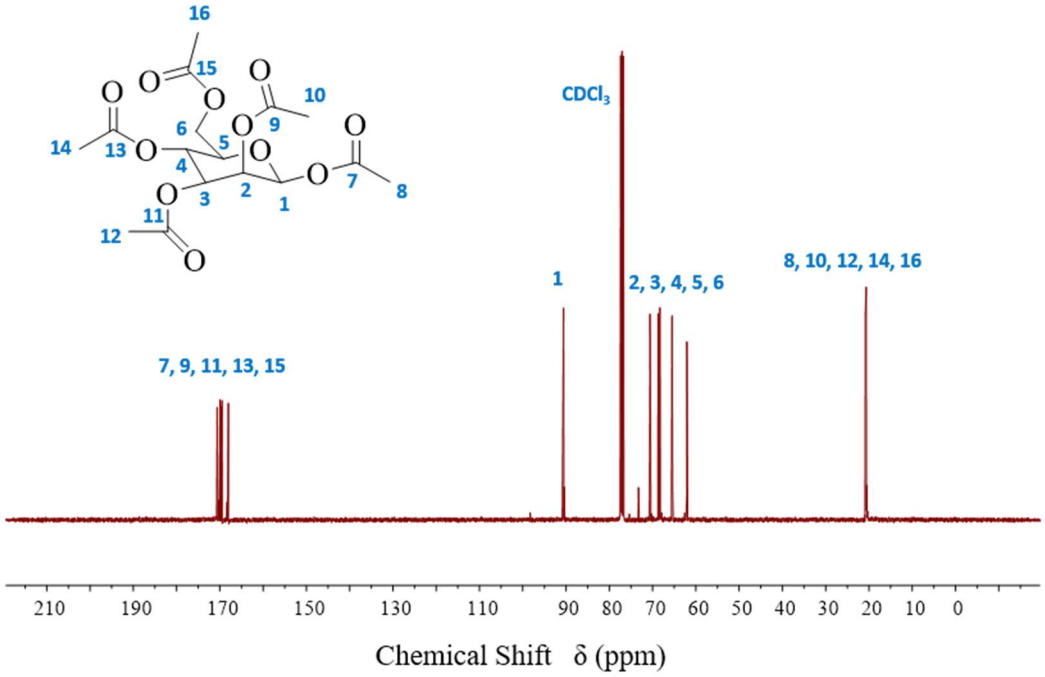

Figure A34: ^{13}C-NMR ($CDCl_3$) of Mann-$(OAc)_5$ [12], showing the assignment of the carbon environments.

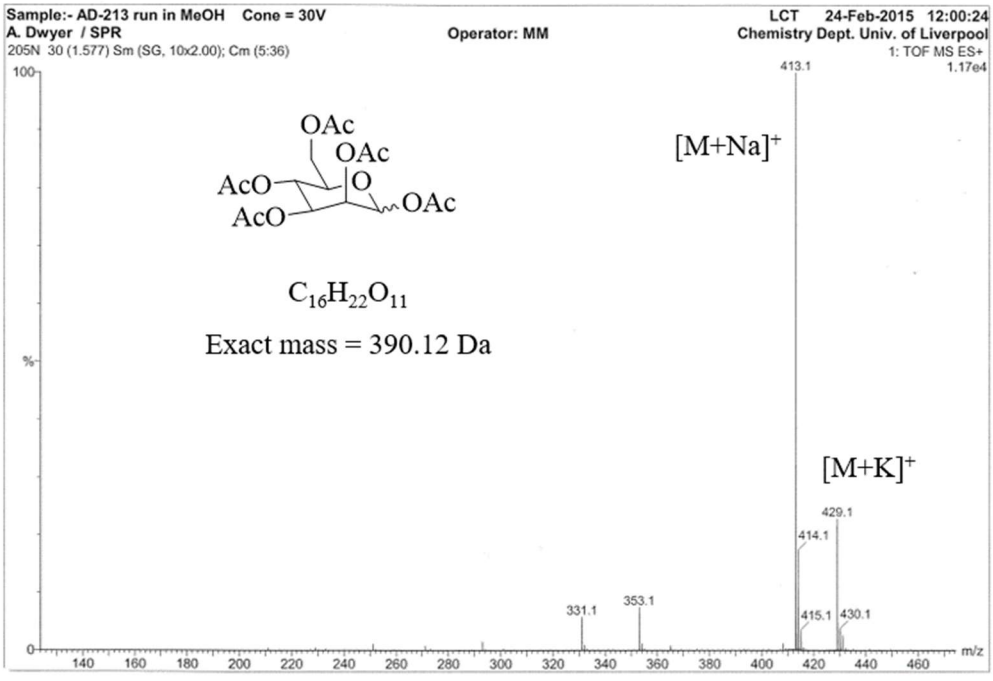

Figure A35: ESI mass spectrometry analysis of Mann-$(OAc)_5$ [12], showing the $[M+Na]^+$ and $[M+K]^+$ molecular ion peaks.

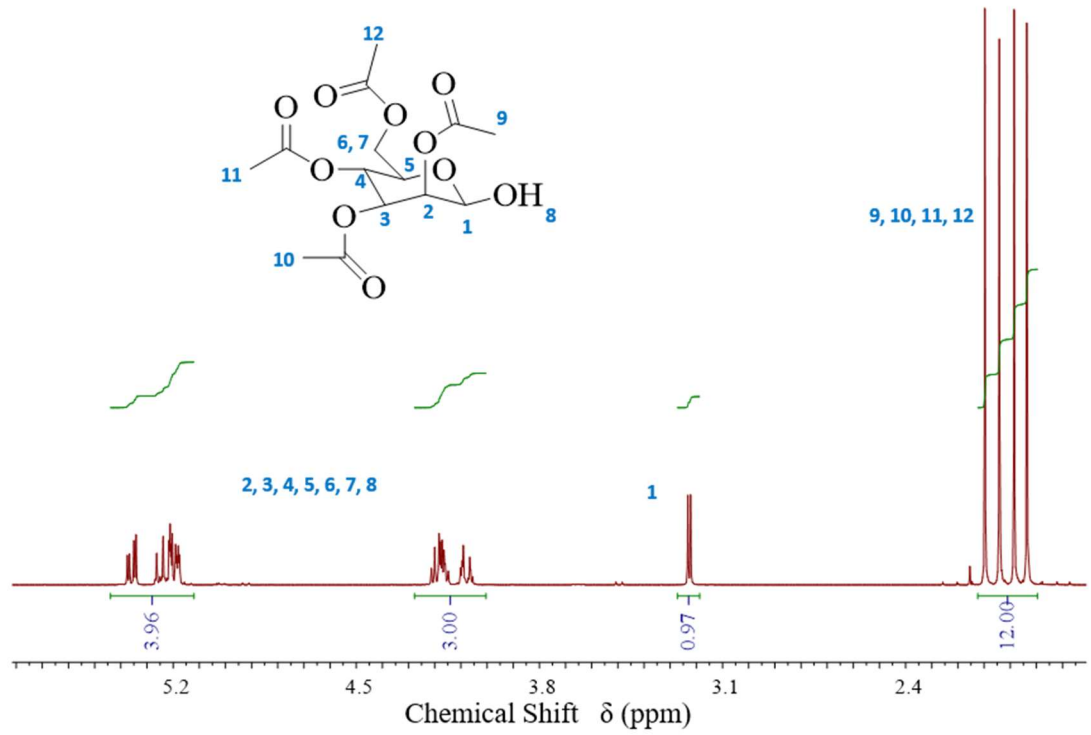

Figure A36: ^{1}H-NMR ($CDCl_3$) of Mann-$(OAc)_4$ [13], showing the assignment and integrations of the environments after normalising the integration of the acetyl protons (9, 10, 11, 12) to 12H.

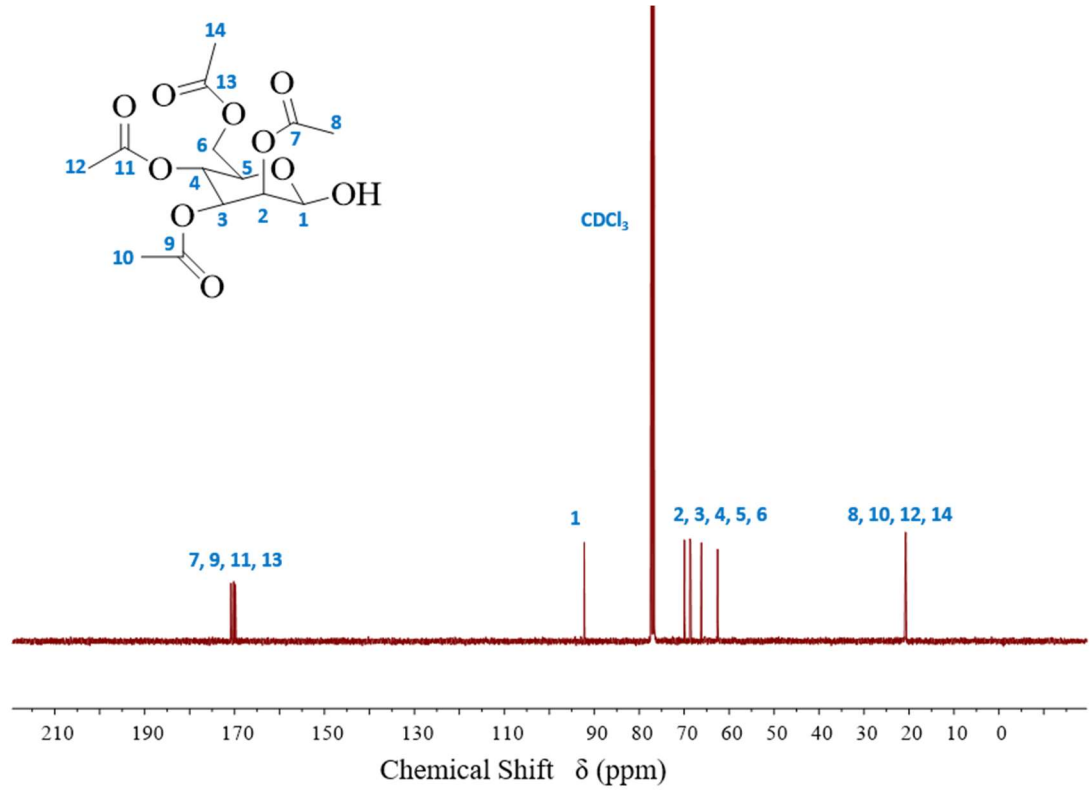

Figure A37: ^{13}C-NMR ($CDCl_3$) of Mann-$(OAc)_4$ [13], showing the assignment of the carbon environments.

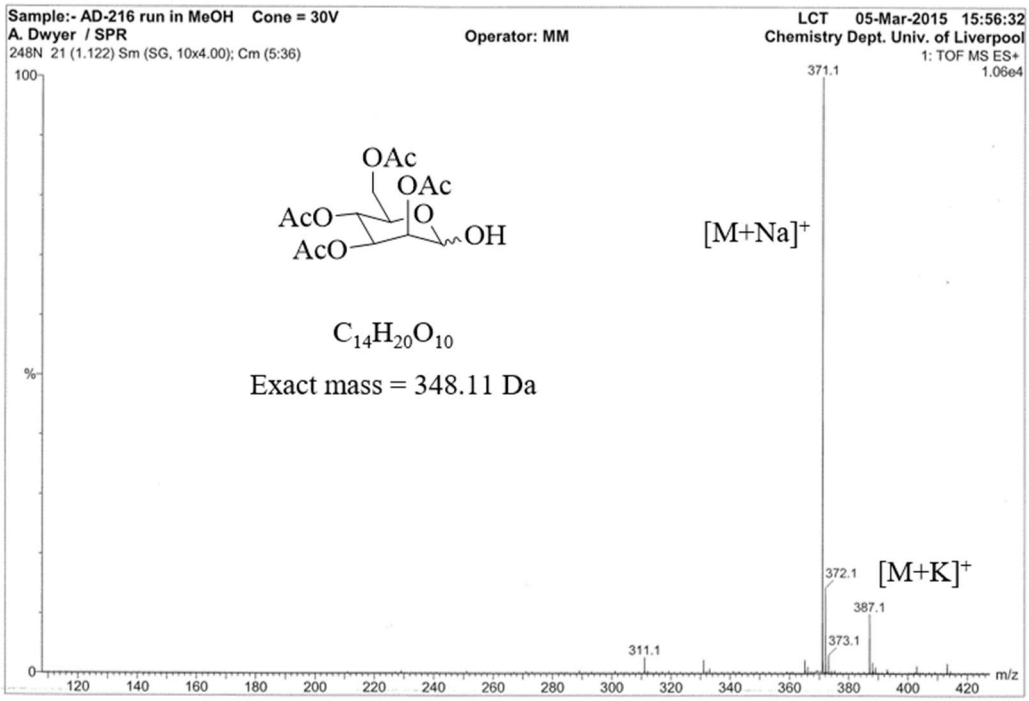

Figure A38: ESI mass spectrometry analysis of Mann-$(OAc)_4$ [13], showing the $[M+Na]^+$ and $[M+K]^+$ molecular ion peaks.

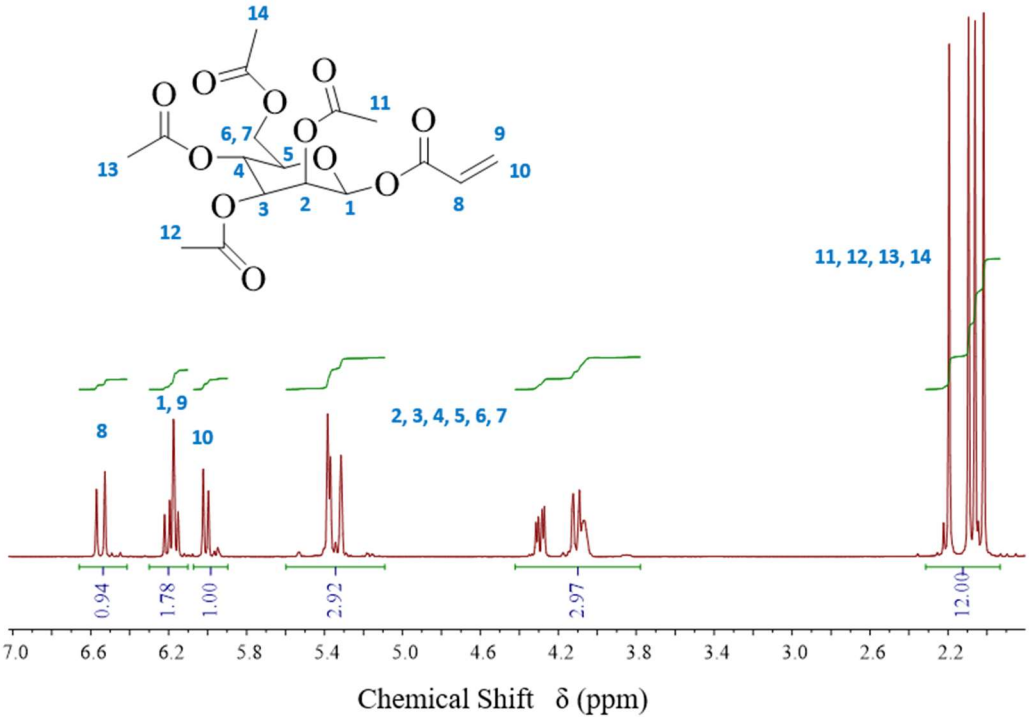

Figure A39: ^{1}H-NMR ($CDCl_3$) of Mann-$(OAc)_4$-acrylate [15], showing the assignment and integrations of the environments after normalising the integration of the acetyl protons (11, 12, 13, 14) to 12H.

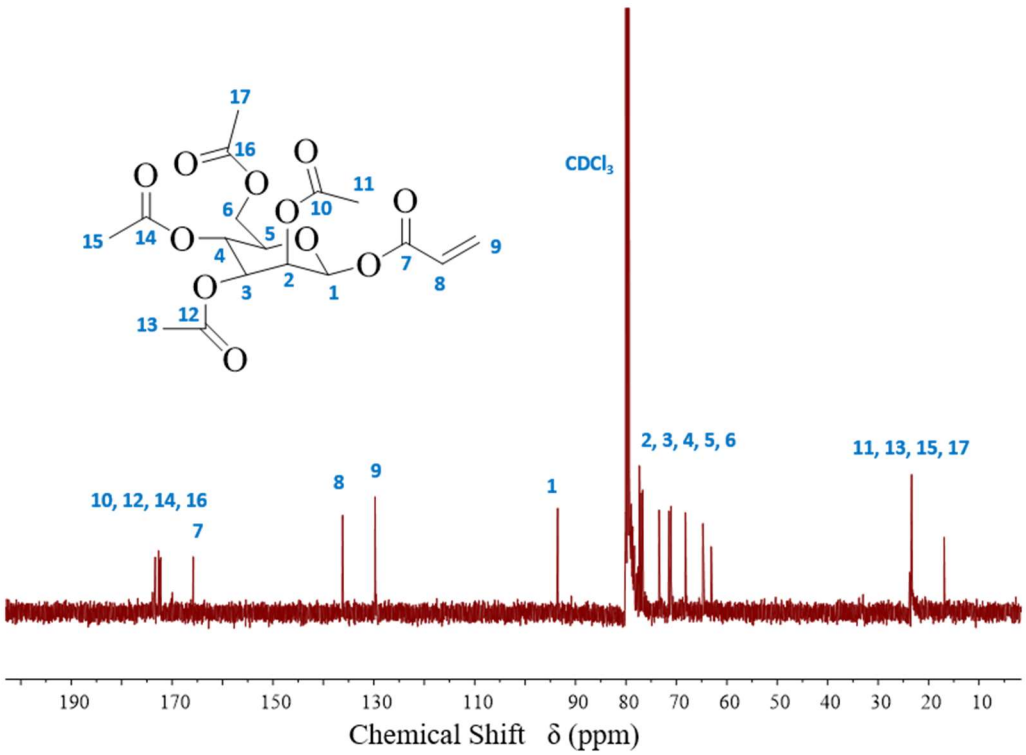

Figure A40: ^{13}C-NMR ($CDCl_3$) of Mann-$(OAc)_4$-acrylate [15], showing the assignment of the carbon environments.

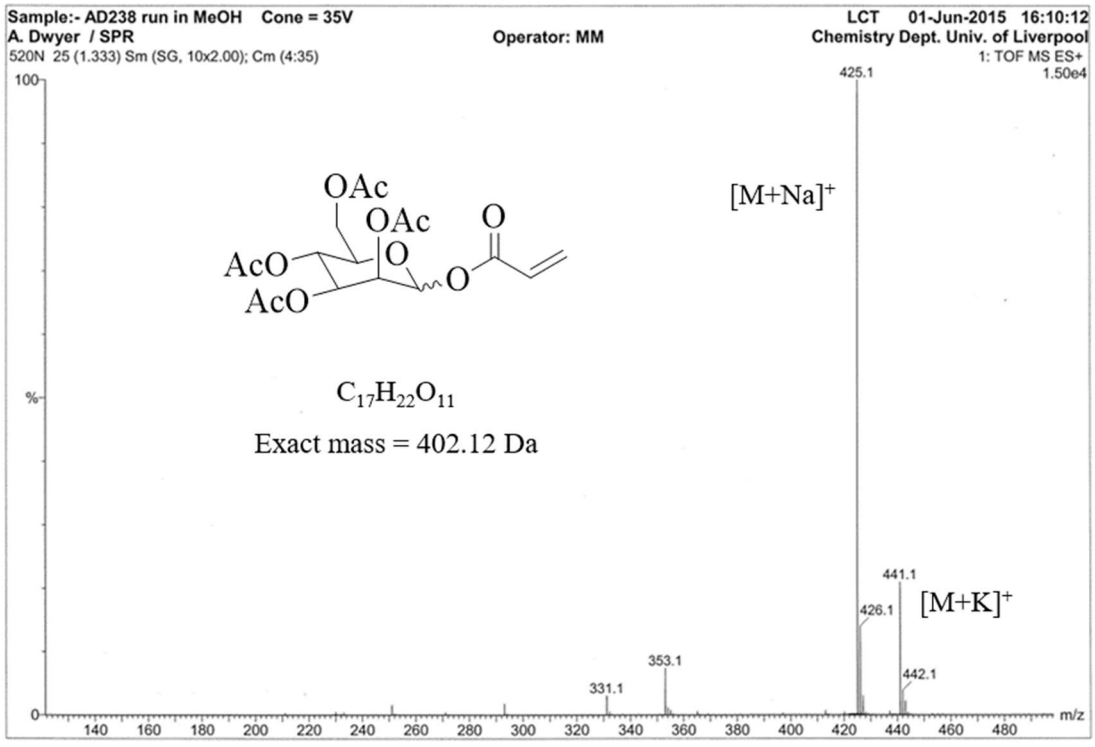

Figure A41: ESI mass spectrometry analysis of Mann-$(OAc)_4$-acrylate [15], showing the $[M+Na]^+$ and $[M+K]^+$ molecular ion peaks.